Fundamental Biomedical Technologies

Alessandra Giuliani
Alessia Cedola *Editors*

Advanced High-Resolution Tomography in Regenerative Medicine

Three-Dimensional Exploration into the Interactions between Tissues, Cells, and Biomaterials

Springer

Fundamental Biomedical Technologies

Series Editor
Mauro Ferrari
The University of Texas
Houston, TX, USA

More information about this series at http://www.springer.com/series/7045

Alessandra Giuliani • Alessia Cedola
Editors

Advanced High-Resolution Tomography in Regenerative Medicine

Three-Dimensional Exploration into the Interactions between Tissues, Cells, and Biomaterials

Springer

Editors
Alessandra Giuliani
Department of Clinical Sciences
Polytechnic University of Marche
Ancona, Italy

Alessia Cedola
Institute of Nanotechnology - CNR
c/o Sapienza University
Rome, Italy

ISSN 1559-7083
Fundamental Biomedical Technologies
ISBN 978-3-030-00367-8 ISBN 978-3-030-00368-5 (eBook)
https://doi.org/10.1007/978-3-030-00368-5

Library of Congress Control Number: 2018961740

This Springer imprint is published by the registered company Springer Nature Switzerland AG
The registered company address is: Gewerbestrasse 11, 6330 Cham, Switzerland

Alis volat propriis

It is used as the motto of the US state of Oregon and its official English version is "She flies with her wings," in line with the tradition of considering countries and territories as women.

In fact, this book comes from an idea of the two female co-editors and is the product of high-level scientists, many of whom are young women starting to fly with their wings in the complex world of the scientific research.

Preface

In the international scene over the last 20 years, the published papers related to the many and varied studies of tissue engineering and regenerative medicine are countless. Worthy of note are the two most authoritative journals in the sector, the three sets of *Tissue Engineering* (Mary Ann Liebert Inc., USA) and the *Journal of Tissue Engineering and Regenerative Medicine* (John Wiley & Sons Ltd., UK). Just as wide and varied are the books produced. We should mention *Fundamentals of Tissue Engineering and Regenerative Medicine* (Springer, 2009), *Tissue Engineering and Regenerative Medicine: A Nano Approach* (CRC Press, 2012), and the open-access productions of INTECH, but these are just a few non-exhaustive examples of the international offer.

Among these productions, a certain number also contains imaging studies performed using high-resolution tomography, but the information is usually extremely synthesized into individual sections of volumes (as in Zhang Zhiyong, Jerry KY Chan, and Teoh Swee Hin's *Computer Tomography and Micro-CT for Tissue Engineering Application, on Imaging in Cellular and Tissue Engineering*, edited by Hanry Yu, Nur Aida Abdul Rahim, 2012) or often refers to high-resolution tomography analysis of samples of interest for tissue engineering of specific anatomical districts (like in Zehbe Rolf, Haibel Astrid, Franziska Schmidt, Riesemeier Heinrich, James C. Kirkpatrick, Helmut Schubert, and Christoph Brochhausen's *High Resolution X-Ray Tomography: 3D Imaging for Tissue Engineering Applications, on Methods in Tissue Engineering*, edited by Daniel Eberli, 2010).

There are also a fair number of books that focus on microtomography technique and its applications; two notable examples are *MicroComputed Tomography: Methodology and Applications*, edited by Stock, Stuart R., CRC Press 2009, and *Advanced Tomographic Methods in Materials Research and Engineering*, edited by John Banhart, Oxford University Press, 2008. Even in these cases, the information related to regenerative medicine and tissue engineering applications is very limited, often focused on the sole bone district.

An even more reduced number of scientific studies include results deriving from synchrotron radiation experiments. Again, we are predominantly referring to

journal papers or to individual chapters within broader treatises related to specific, engineered sites that are focused on the techniques based on the use of synchrotron radiation or, in numbers still lower, on the specific microtomography technique.

We have personally contributed, over the last 10 years, to some of these volumes with chapters related to regenerative studies based on synchrotron radiation microtomography. Among these works, we would like to mention Cedola A. et al., X-ray Micro and Nano-Probes: Fundamentals and Applications, Recent *Res. Devel. Applied Phys*., 9(2006): 169–196; Fiori F. et al., Synchrotron Radiation and Nanotechnology for Stem Cell Researchers, in *Adult and Embryonic Stem Cells*, 2012, New York, Dordrecht, Heidelberg, London, 81–102; Giuliani A. et al., Synchrotron Radiation and Nanotechnology for Stem Cell Research, in *Stem Cells in Clinic and Research*, 2011, 683–708; and Giuliani A., Analysis of Bone Response to Dental Bone Grafts by Advanced Physical Techniques, in *Bone Response to Dental Implant Materials*, edited by A. Piattelli, 2016.

From this fragmentation of information forcefully emerges the need to produce a book exclusively dealing with microtomography studies, mainly (but not exclusively) based on synchrotron radiation, related to problems of regenerative medicine and tissue engineering of several anatomical districts. De facto, there is the lack of a volume, similarly conceived, in the international scene, putting this book as a novelty in the book market.

The goal of this book is even more ambitious: we would like to stimulate the reader toward scientific and experimental multidisciplinary paths in regenerative medicine. In fact, the project involves, as authors of the various chapters, highly selected scientists with great experience at Synchrotron Facilities, some of them working for years at the microtomography-dedicated beamlines. Furthermore, the authors involved in this project have gained, over the years and within international projects of scientific and popularizing character, great educational skills, mainly directed at a heterogeneous audience. We believe that this is a solid premise to achieve, in the multidisciplinary direction, an easy language that is also understandable for readers with different educational backgrounds compared to physics, biology, and clinical medicine. In fact, modern science teaches us that, without the creation of a common and transversal language between the basic disciplines, further progress will not be possible. This is convincingly demonstrated in Chap. 1, authored by Prof. Franco Rustichelli, which we strongly wanted to start the full set of chapters, being that it is a prerequisite for understanding the rationale behind this project. Indeed, Prof. Rustichelli is an eminent scientist who, perhaps among the first in Europe, believes in the importance of multidisciplinarity in science and in the role played by the huge machines of physics in this context. It is no coincidence that, in the last eight years, he scientifically coordinated two European COST Actions focused on multidisciplinarity in regenerative medicine, i.e., the *MP1005 – From nano to macro biomaterials (design, processing, characterization, modelling) and applications to stem cells regenerative orthopedics and dental medicine (NAMABIO),* and the *CA16122 – Biomaterials and advanced physical techniques for regenerative cardiology and neurology (BIONECA).*

This book is a key manual for easy consultation that is intended for clinicians, biologists, physicists, and biomedical engineers, but also for students who want to continue their studies in the field of Regenerative Medicine and for ordinary people who are intrigued by the fascinating world that revolves around synchrotron structures and their possible use in research, diagnostics, and medical therapy.

Ancona, Italy — Alessandra Giuliani
Rome, Italy — Alessia Cedola

Contents

Contributors

Sam Bayat Department of Clinical Physiology, Sleep and Exercise, Université de Grenoble Alpes & Grenoble University Hospital, Grenoble, France

Department of Anaesthesia, Pharmacology and Intensive Care, Geneva University Hospital, Geneva, Switzerland

Rossella Bedini National Center of Innovative Technologies in Public Health, Italian National Institute of Health, Rome, Italy

Francesco Brun Department of Engineering and Architecture, University of Trieste, Trieste, Italy

National Institute for Nuclear Physics (INFN) – Trieste Division, Trieste, Italy

Inna Bukreeva Institute of Nanotechnology, CNR, Rome, Italy

Christian Dullin Institute for Diagnostic and Interventional Radiology, University Hospital Goettingen, Goettingen, Germany

Italian Synchrotron Light Source "Elettra", Trieste, Italy

Translational Molecular Imaging, Max-Plank-Institute for Experimental Medicine, Goettingen, Germany

Fabrizio Fiori Department of Clinical Science, Polytechnic University of Marche, Ancona, Italy

Michela Fratini Institute of Nanotechnology, CNR, Rome, Italy

Santa Lucia Foundation, Rome, Italy

Alessandra Giuliani Department of Clinical Sciences, Polytechnic University of Marche, Ancona, Italy

Charlotte K. Hagen Department of Medical Physics and Biomedical Engineering, University College London, London, UK

Annie Horng RZM – Radiologische Zentrum München, Pasing, Germany

Marcus J. Kitchen School of Physics and Astronomy, Monash University, Clayton, VIC, Australia

Max Langer Creatis, CNRS UMR 5220, INSERM U1206, INSA-Lyon, Université Claude Bernard Lyon 1, Université de Lyon, Villeurbanne, France

Goran Lovric Swiss Light Source, Paul Scherrer Institut, Villigen, Switzerland

Milena Mastrogiacomo Department of Experimental Medicine, University of Genoa, Genoa, Italy

Serena Mazzoni Department of Clinical Sciences, Polytechnic University of Marche, Ancona, Italy

Deborah Meleo Rome, Italy

Mara Mencarelli Department of Clinical Sciences, Polytechnic University of Marche, Ancona, Italy

M. Nardini Department of Experimental Medicine, University of Genoa, Genoa, Italy

Serena Pacilè Department of Engineering and Architecture, University of Trieste, Trieste, Italy

Elettra-Sincrotrone Trieste S.C.p.A., Trieste, Italy

M. E. F. Palamà Department of Experimental Medicine, University of Genoa, Genoa, Italy

Raffaella Pecci National Center of Innovative Technologies in Public Health, Italian National Institute of Health, Rome, Italy

Nicola Pieroni Institute of Nanotechnology, CNR, Rome, Italy

Ginevra Begani Provinciali Institute of Nanotechnology, CNR, Rome, Italy

A. Romaldini Department of Experimental Medicine, University of Genoa, Genoa, Italy

Franco Rustichelli National Institute of Biostructures and Biosystems, Rome, Italy

Giuliana Tromba Elettra-Sincrotrone Trieste S.C.p.A., Trieste, Italy

Kerstin Zehbe University of Potsdam, Department of Chemistry, Potsdam, Germany

Rolf Zehbe University of Potsdam, Institute of Physics and Astronomy, Potsdam, Germany

Chapter 1
The Huge Machines of Physics: The Bet of the Multidisciplinary Research Teams in Regenerative Medicine

Franco Rustichelli

There are more things in heaven and earth, Horatio,
Than are dreamt in your philosophy.

– Hamlet Act 1, William Shakespeare

Abstract In the last decades the biology and medicine made great progresses thanks, on one side to the expoitation of basic discoveries of physical phenomena, and on the other side on the development of physical techniques applied to the medical diagnostic area, like for instance the Nuclear Magnetic Resonance. This chapter presents the Huge Machines of Physics, starting with large accelerators for sub-nuclear physics, like the Large Hadron Collider, and continuing with synchrotrons and free-electron lasers. It will be shown that the last two types of facilities can provide very useful information both for biology and medicine. In particular it will be emphasized the great help provided by the X-ray synchrotron radiation to the regenerative medicine, with examples of tracking of stem cells in investigations of pathologies of cardiological and neurological nature.

Many persons believe that, as the twentieth century was characterized by the splendour of the discoveries in the field of Physics, with their numerous consequences in our practical life, the twenty-first century will be characterized by the discoveries in the field of biology, with a straightforward impact on Medicine and human health.

Actually already in the last decades, the biology (and as a consequence the medicine) made surprising progresses, very often thanks to the basic knowledges produced by Physics and to the help provided by the innovative physical experimental techniques.

F. Rustichelli (✉)
National Institute of Biostructures and Biosystems, Rome, Italy
e-mail: f.rustichelli@univpm.it

A. Giuliani, A. Cedola (eds.), *Advanced High-Resolution Tomography in Regenerative Medicine*, Fundamental Biomedical Technologies,
https://doi.org/10.1007/978-3-030-00368-5_1

In this context, we will mention only two examples of milestone discoveries in the field of biology, which were possible thanks to the use of a classical physical technique, namely, the X-ray diffraction.

The first discovery was performed by Perutz and Kendrew, who were able to elucidate for the first time the structure, at atomic level, of a protein, namely, the haemoglobin, for which they received in 1962 the Nobel Prize in Chemistry. In the same year, the Nobel Prize in Medicine was assigned to Watson, Wilkins and Crick for having discovered the double helix structure of DNA, which was based on the X-ray diffraction experiment performed by Franklin in the Physics laboratory of Wilkins. Also if the paternity of this epoch-making discovery is often attributed only to Watson and Crick, we must be aware that without the experimental contribution of the two physicists Franklin and Wilkins, and in particular without their complex mathematical elaboration of the data, this leap forward in biological science would have been impossible.

Since the time of Archimedes, humans, fascinated by the unknown, tried to enter the mysteries of our real world.

Paradoxically, the scientific instrumentation has become bigger as the objects to be studied have become smaller. Thus, the huge machines of Physics were generated, like tower of Babel or Pyramids in Egypt, which were erected to pursue the eternal dream of immortality.

Many advances in the discovery of the physical properties of the world have been made in the last few decades by building huge machines, some of which have allowed the development of very useful characterization techniques in interdisciplinary research, including regenerative medicine, as will be discussed in this book.

Large accelerators built by physicists can be divided into two categories:

(a) Machines for producing high-energy collisions between subnuclear particles in order to understand the microscopic world.
(b) Machines for the production of very intense X-rays to perform basic scientific experiments and applied in various scientific disciplines, including biology and medicine.

Although this book is focused on the second type of machines, we consider it useful, for the sake of completeness and in some way for historical reasons, to spend some words also on the first category of machines.

Let us consider the Large Hadron Collider (LHC) at the European Organization for Nuclear Research Centre in Geneva, Switzerland (Figs. 1.1 and 1.2), which has been realized to reach a new knowledge frontier on subnuclear elementary particles [1].

It is a huge ring, 27 km long, where protons with incredibly high energy are made to turn in opposite directions at nearly the speed of light and are then made to collide. The existence of atoms, the first step to understanding the structure of matter, had been foreseen and advocated already at the time of ancient Greece (BC IV sec), but only more than 2000 years later, atomic theory began to encounter scientifically clear evidence.

Fig. 1.1 The Large Hadron Collider (LHC) at the European Organization for Nuclear Research Centre in Geneva. (Courtesy CERN)

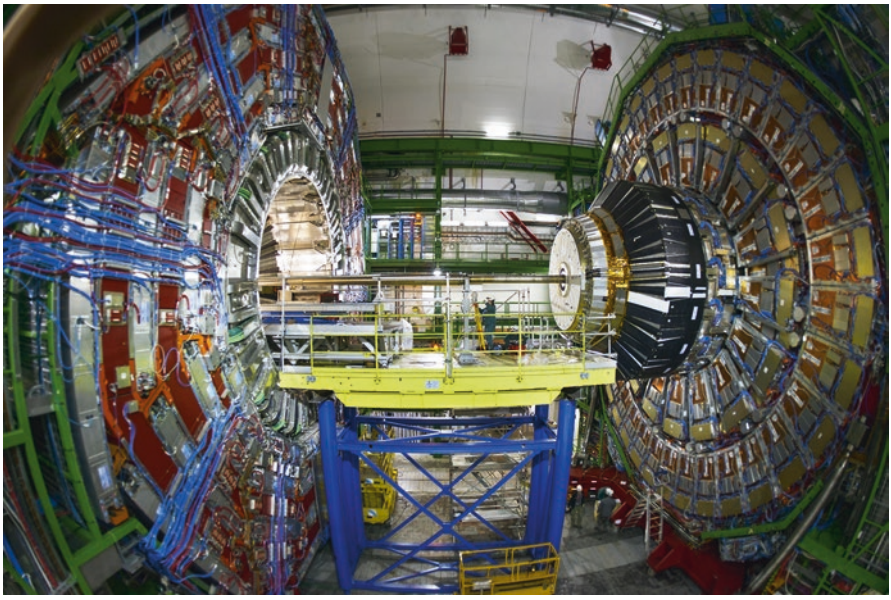

Fig. 1.2 Internal view of the LHC in Geneva. (Courtesy CERN)

Now, after a century of unwavering research in atomic and nuclear physics, we hope to obtain fundamental information on the interaction forces of particles at distances much smaller than the size of atomic nuclei, through these proton collisions.

The study of the smallest interaction distance, in fact, can bring us information about the most basic features of matter in our universe: the aim is to understand the origin of the atomic nuclei components and then of all existing matter.

We still do not know the origin of the mysterious energy associated with mass, as described by the hundred-year-old, well-known equation $E = mc^2$. We also have no clear idea as to the origin of energy and invisible matter, which contribute to 96% of the total mass of the universe. Maybe even our numbers and the present mathematics are not adequate to describe the infinitesimal forms of our world. So something new must happen when these proton collide in the gigantic accelerator of Geneva! From such collisions a myriad of unstable elementary particles are obtained. A very important experiment was already performed, namely, the discovery of the Higgs boson [2], which was foreseen theoretically several decades ago by the physicist, who gave to it his name and who was awarded recently by the Nobel Prize in Physics (Fig. 1.3).

Qualitative leaps in physical knowledge have always been the origin of innovative technological applications. Future experiments at the LHC could help us to answer important questions and perhaps to understand the fundamental rules governing the evolution of the entire universe. Probably we will also learn more about the nature of space itself, making a qualitative leap in our knowledge of nature.

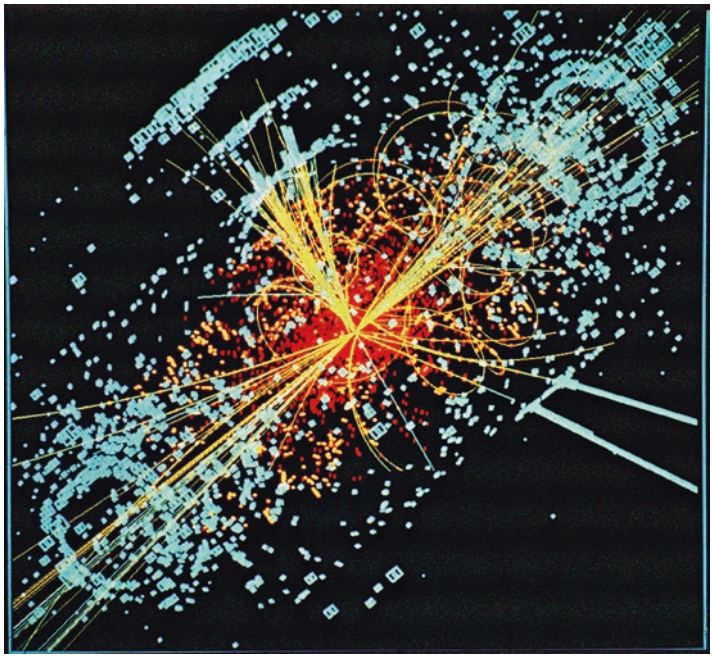

Fig. 1.3 Image related to the discovery of the Higgs boson at the LHC. (Courtesy CERN)

Geneva's machine is indeed an incredible effort to push ahead the frontiers of knowledge. Whether you consider it a proud Babel Tower or a cathedral to celebrate the mysteries of nature, the researches carried out there will certainly have great cultural implications, impossible to foresee four centuries ago when we were discussing whether the sun was turning around the earth or vice versa.

Now in Geneva, we can make discoveries that are fulfilling at large extent the dream of Einstein: *I want to know God's thoughts. The rest are details*, also if somebody like Woody Allen seems to have said: *Can we actually know the Universe? My God, it's hard enough finding your way around Chinatown.*

However, very important scientific contributions are continuously produced also by machines devoted to basic and applied science experiments, through the X-ray radiation delivered by large accelerating machines called synchrotrons. A relevant example is the European Synchrotron Radiation Facility (ESRF), built in Grenoble (France) and shown in Fig. 1.4, constituting the most intense and brilliant X-ray source existing today worldwide [3].

ESRF consists in a ring (called storage ring) which is a tube having a circumference of 844 m, where the electrons travel for hours at a velocity close to that of light (300 km/s). If they travelled around the earth, they would complete the circle more than seven times per second. During their ultrafast travel, the electrons emit X-Ray radiation of very large intensity, which is extracted through several tens of tangential beams, as reported in the scheme of Fig. 1.5. In any beam, several experimental facilities are installed.

Fig. 1.4 The European Synchrotron Radiation Facility (ESRF) in Grenoble

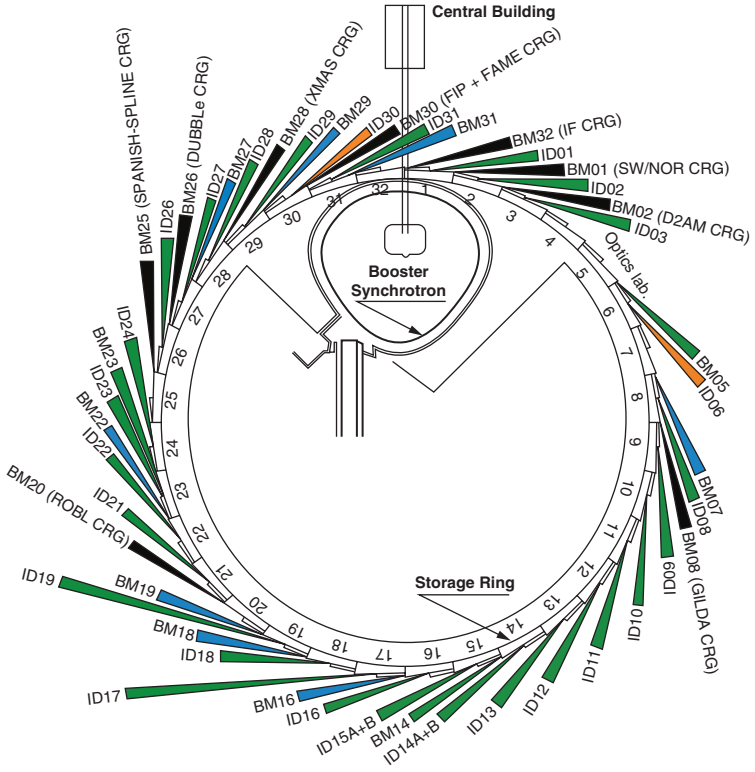

Fig. 1.5 Scheme of the tangential X-ray beams at ESRF

Synchrotron light in addition to very high intensity and brilliance offer the advantage of covering a wide range of frequencies through the electromagnetic spectrum from the infrared, through the ultraviolet, to the X-ray region, allowing also time-resolved experiments in the sub-nanosecond range.

The ESRF is used by several thousands of scientists every year, coming mainly, but not only, from all Europe, operating in the fields of physics, chemistry, biology, medicine (in particular in different areas of regenerative medicine as we will see below), Earth sciences, material sciences and engineering, nanosciences and nanotechnologies.

Another Synchrotron Facility, built very recently, is the Synchrotron-Light for Experimental Science and Applications in the Middle East (SESAME). It is located in Jordan and is the largest international scientific laboratory existing in this area. Its members are Jordan, Iran, Pakistan, Israel, Turkey, Cyprus, Egypt, the Palestinian Authority and Bahrain [4].

It is an installation of great social interest because its existence shows that it is possible to build scientific and cultural bridges between different countries in a region often tormented by violence, conflict and extremism, contributing to a culture of peace through international scientific cooperation.

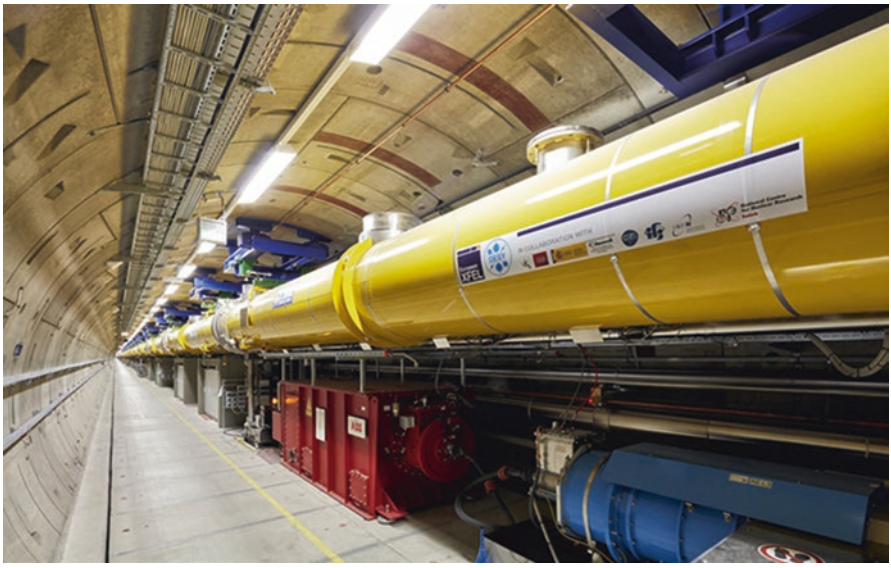

Fig. 1.6 Inner view of the European X-ray free-electron laser (XFEL) in Hamburg

It is expected that, by fostering scientific and technical development in the Middle East and neighbouring countries, the brain drain will reverse in the near future. The SESAME creation was sponsored by UNESCO, the general director of which was present together with the King of Jordan to its inauguration on May 16, 2017. On November 22, 2017, scientists saw the first monochromatic X-ray radiation, signalling the start of the laboratory experimental program. In SESAME, like in ESRF, electrons circulate around a circular tube (having a circumference of 130 m), guided by magnets and other equipment, close to the speed of light.

The electrons produce X-rays, having an energy of 2.5 GeV, which are extracted through tangential beams, where several experimental facilities can be located allowing researches in structure of matter, material science, cultural heritage, archaeometry, biology and medical sciences. In the future 20 beamlines are foreseen but, at present, only 3 of them are operative: they are mainly devoted to study living cells and tissues, protein crystallography, structure of viruses and developing of drugs.

Another category of huge machines are X-ray free-electron lasers (Fig. 1.6), which constitute extremely bright X-ray sources, having an enormous impact also on biological research. They generate very short X-ray pulses, of a few hundred femtoseconds, which are billions of times more intense than synchrotron radiation. The succession of these very short pulses of radiation impinging very rapidly moving molecules allows to obtain, in spite of their high speed, a series of snapshots of them, like they would be frozen in time, as it happens in discotheques when the dancers of rock and roll are illuminated by stroboscopic light and appear frozen. By using this technique, the Pearson American Dance Company obtained recently very impressive effects by showing dancers appearing suddenly in the dark sus-

pended and immobile at a considerable height above the floor, giving the illusion of a levitation.

Moreover, the wavelength of the produced X-ray pulses is small enough allowing to obtain pictures of the investigated samples at atomic resolution.

At the end of 2017, the 3.4-km-long European X-ray free-electron laser (XFEL) started running near Hamburg (Germany), and it is, at present, the most performant one of the world, producing 27,000 pulses per second [5]. The intensity of its pulses is so high that they destroy the investigated sample; however, before sample destruction, enough photons are diffused in the detector, allowing to study the 3D atomic structure of the sample.

In a second, it is possible to collect more than 3000 X-ray pictures compared to about 100 of other facilities. In structure-determination experiments based on conventional X-ray sources, one must obtain a single crystal of the investigated molecule. Indeed, the pulses of XFEL are so bright that it sufficient to obtain single crystals of very reduced sizes, up to the order of magnitude of few nanometres. In addition, even non-crystalline clusters of molecules (for instance, in the case of proteins difficult to crystallize, like some membrane proteins) are suitable. The XFEL facilities allow investigations of the structure and dynamics of atomic and molecular systems, previously not accessible. Indeed, by XFEL it is possible to obtain movies showing the movements of enzymes and viruses by combining thousands of snapshots and even investigating the dynamical aspects of catalysts.

X-rays are electromagnetic waves, like visible light, but characterized by a much smaller wavelength, that is, of the order of tenths of nanometre, which corresponds to the atomic diameter.

The *nanometre* is defined as 1 billionth of a metre. To remember this definition and better understand the meaning of many frequently used words like Nanoscience, Nanotechnology and Nanomedicine, let us consider the following practical example.

Suppose that shortly before the presentation ceremony of this book at the University of Rome by editors Alessia Cedola and Alessandra Giuliani, they receive a call from the Ambassador of China to Rome who says that one billion Chinese would like to participate in this very interesting event. It is possible to satisfy the request by hosting the Chinese in the hills around Rome and using large screens, but the problem arises of how to feed them at lunchtime. It is very easy to buy an Italian salami “mortadella”, 1 m long, and cut a billion slices, producing an equal number of sandwiches. The thickness of each slice is 1 nm!

Using X-ray diffraction it was possible to determine the atomic-level structure of the different chemical compounds and therefore also of biological molecules. To understand why X-rays can “see” the position of atoms, while radiation with a longer wavelength, such as visible light, cannot, let us imagine having a row of watermelons on a table.

If we enter the room with an eye patch so that we cannot see anything and try to guess the structure of the line of objects on the table by touching the line with a 1-m-long bar, we will discover a flat structure. On the other hand, if we use a pencil (roughly with the same length as the diameter of the watermelons) as a probe, we

1901	Wilhelm Conrad Röntgen	Physics	has rendered by the discovery of the remarkable rays subsequently named after him"
1902	Hendrik Antoon Lorentz and Pieter Zeeman	Physics	"In recognition of the extraordinary service they rendered by their researches into the influence of magnetism upon radiation phenomena"
1914	Max von Laue	Physics	"For his discovery of diffraction of x rays by Crystals"
1915	Sir William Henry Bragg and William Lawrence Bragg	Physics	"For their services in analysis of crystal structure by means of X rays"
1917	Charles Glover Barkla	Physics	"For his discovery of characteristic roentgen radiation of elements"
1924	Karl Manne Georg Siegbahn	Physics	"For discoveries and research in field of X ray spectroscopy"
1927	Arthur Holly Compton	Physics	"For the discovery of the Compton Effect that bears his name"
1936	Petrus (Peter) Josephus Wilhelmus Debye	Chemistry	"For his contributions to our knowledge of molecular structure through his investigations on dipole moments and on the diffraction of X-rays and electrons in gases"
1962	Max Ferdinand Perutz and John Cowdery Kendrew	Chemistry	"For their studies of the structures of globular proteins"
1962	Francis Harry Compton Crick, James Dewey Watson and Maurice Hugh Frederick Wilkins	Medicine	"For their discoveries concerning the molecular structure of nucleic acids and its significance for information transfer in living material"
1979	Allan M. Cormack and Godfrey N. Hounsfield	Medicine	"For the development of computed axial tomography"
1981	Kai M. Siegbahn	Physics	"For his contribution to the development of high-resolution electron spectroscopy"
1985	Herbert A. Hauptman and Jerome Karle	Chemistry	"For their outstanding achievements in the development of direct methods for the determination of crystal structures"
1988	Johann Deisenhofer, Robert Huber and Hartmut Michel	Chemistry	"For the determination of the three-dimensional structure of a photosynthetic reaction centre"
2006	Roger D. Kornberg	Chemistry	"For his studies on molecular bases of eukaryotic transcription"
2009	Venkatraman Ramakrishnan, Thomas A. Steitz and Ada E. Yonath	Chemistry	"For studies of the structure and function of the ribosome"

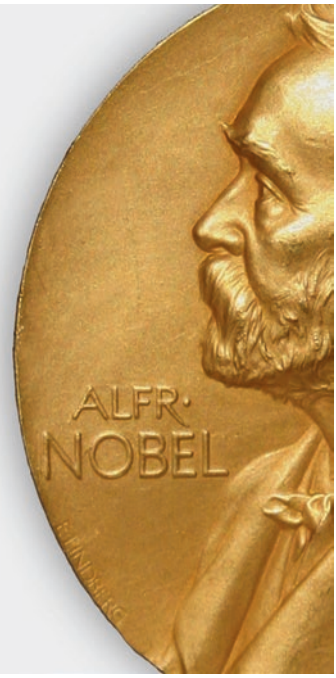

Fig. 1.7 Nobel Prizes obtained by experiments based on X-rays

will obtain a correct structural information on the curvature and on the position of the watermelons.

In practice, the position in space of the different atoms of a given compound or molecule is obtained by first recording the X-ray intensities diffused in the different directions of space by the electrons belonging to all the atoms contained in the sample studied, then performing very complex mathematical treatments.

Figure 1.7 reports the list of Nobel Prizes assigned before 2009 for researches using X-rays. The physicist W.C. Roentgen discovered such type of radiation in 1895 and performed the first radiography on the hand of his wife.

Von Laue and Knipping obtained the first X-ray image diffracted by a crystal in 1912. Fifty years later, the Nobel Prize in Chemistry was assigned to Perutz and Kendrew, as previously mentioned, for having clarified for the first time the structure of a protein, i.e. the haemoglobin, after a very intense work due to the high number of atoms contained in it. Since then, the structure of a large number of increasingly complex proteins has been determined.

In the same year, the Nobel Prize in Medicine was awarded to Watson, Wilkins and Crick for discovering the double helix structure of DNA.

Several structural biology experiments have been performed at the European Synchrotron Radiation Facility (ESRF) over the past 15 years. We will mention some examples, in detail what we consider the most brilliant, namely, the determination of the structure, at the atomic level, of the ribosome, which was awarded

with the Nobel Prize in Chemistry awarded in 2009 to Yonath, Steitz and Ramakrishnan [6].

The ribosome has the fundamental role of reading the information contained in the RNA messenger and using it to produce proteins.

Ribosomes exist in all living systems, from bacteria to humans, and are ideal targets in bacteria for antibiotic drugs. The adventure of this extraordinary discovery began at the end of the seventh decade of the twentieth century, when an Israeli researcher, Ada Yonath, decided to bravely face this challenge, overcoming a series of problems that were considered impossible to solve by the great majority of the scientific community. In fact, the ribosome is one of the most complex proteins/RNA, consisting of a "small subunit" and a "large subunit". In the human ribosome, the "small subunit" consists of a DNA molecule surrounded by 32 proteins, while the "large unit" is made up of 3 DNA molecules surrounded by 46 proteins. Therefore, each subunit is made up of thousands of nucleotides and thousands of amino acids, for a total of hundreds of thousands of atoms: the challenge for Ada was to find for each of these atoms the exact values of its Cartesian coordinates.

The first critical problem which Ada was obliged to solve was the production of a single crystal, of good quality, in which the ribosomes must be located in space in an extremely ordered way, namely, according to a triply periodic structure along the three Cartesian axes. After 10 years of intense research, she succeeded to obtain a perfect crystal from the thermophilic bacteria of the Dead Sea.

However, 10 years more were necessary to overcome other important difficulties, also of mathematical–physical nature, for which she took advantage of the cooperation with other outstanding scientists. Finally, in 2000, they were able to publish the structures at atomic level, obtained at the ESRF, of the "large subunit" of ribosome of the *Haloarcula marismortui* and of the "small subunit" from the *Thermus thermophilus* [6].

It is known that to combat bacteria, which are becoming progressively more resistant, it is necessary to produce new antibiotics. Researchers from the various pharmaceutical companies take advantage of the knowledge of the ribosome structure to understand the mechanisms of action of antibiotics and to develop new drugs [7].

In addition to the studies mentioned above, related to the structure of the ribosome, other researches carried out at the ESRF, many essentially related to the area of biology, have allowed the involved scientists to be awarded, some of them with Nobel Prizes, as a result of the exceptional experimental opportunities offered by this European instrument. For example, the Nobel Prize awarded to Kobilka and Lefkowitz for *having elucidated the structure of "G-protein-coupled receptors"* [8] or the Nobel Prize in Chemistry assigned in 2003 to Roderick Mackinnon for *structural and mechanistic studies of ion channels in cell membranes* [9].

In the last section of this chapter, I would like to present the potential offered by X-ray synchrotron radiation for investigations related to regenerative medicine.

Since the numerous chapters of this book deal with, also from a theoretical point of view, the different tomographic opportunities available for the different areas of the medical sciences, here only a general sample of these potentials is presented,

supported by some examples, with the objective to convince the reader to continue the immersion in reading the topics of specific interest.

Most of the examples presented in this book are based on the use of X-ray microtomography, in particular in phase-contrast microtomography, for applications in regenerative orthopaedics, regenerative dentistry, degenerative neurology and regenerative cardiology.

A revolution occurred in the area of imaging for medical diagnostic purposes when, at the beginning of the 1970s, the first equipment for X-ray computed tomography became available in hospitals [10]. The new technique presented enormous advantages as compared to the conventional X-ray radiography technique, by delivering 3D structural information on the investigated organ, as compared to the projection on the 2D photographic plate of the inner structures of the organ.

The principle of this imaging technique is very simple: hundreds of conventional 2D projection radiographs are recorded, in correspondence to an equal number of rotation angles of the sample with respect to the direction of the impinging X-ray beam. The obtained images are based on the absorption contrast. Then, by using proper mathematical algorithms, the so-called tomographic image reconstruction is performed, delivering volumetric structural information on the investigated sample.

A crucial problem in regenerative orthopaedics is the repair and the regeneration of damaged tissues produced by different causes, including diseases like cancer. The classical approach for repairing the bone lesions makes use of ceramic scaffolds loaded with bone marrow stromal cells (BMSCs). Several studies [11–14] have shown that this procedure generates new-engineered bone in a shorter time than with cells or scaffold alone.

These experiments had the objective to find scaffolds with ideal characteristics, namely, enough large surface area and pores for bone growth and high interconnectivity in order to achieve the blood vessels penetration into the pores [15–25].

Several scaffolds materials were considered: metals, ceramics, glasses, natural and artificial polymers, combinations to form composites and recently nanostructured materials.

X-ray microCT was shown to provide not only interesting images of the internal microstructure but also quantitative structural data, applying different parametrization methods [23–25]. In particular, scaffold surface, volume, pore wall thickness and diameter were evaluated.

The microCT technique was also used to investigated in non-destructive way tissue-engineered constructs obtaining quantitative information on the newly formed bone. Pioneer experiments were performed in small animal models [15, 26]. For instance, at the microCT beamlines of ESRF, the kinetics of bone growth in an immunodeficient murine model was determined by analysing the structural parameters at different time points after implantation.

Moreover, more recently, microCT was also used to quantify the resorption rate of the scaffolds by engineered bone [27].

The same team of scientists was able to visualize, without the need for any contrast agent, the microvascular network of an engineered bone derived from 24 weeks of implantation in a mouse [28]. The used technique, based on phase contrast, is

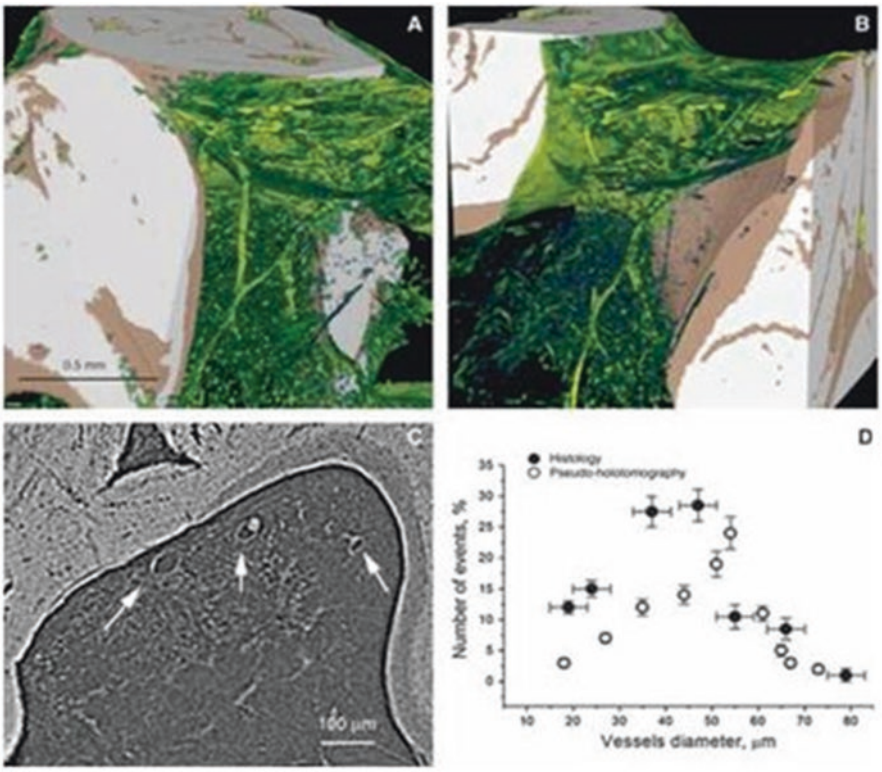

Fig. 1.8 (**a**, **b**) MicroCT imaging of the 3D vessel network and (**c**) 2D microCT sampling slice. (**d**) Histogram of the vessel diameter distribution measured by phase-contrast-based microCT (open circle) and histology (solid circle). (From Ref. [28])

able to image thin low absorbing structures, like blood vessels, which are transparent when using conventional microCT based on X-ray absorption contrast. Figure 1.8 shows the 3D blood vessel network and the histogram of the vessel diameter distribution in comparison with the data obtained by histology.

An application of the phase-sensitive microCT for a clinical investigation related to regenerative dentistry was recently performed at ESRF [29]. Mesenchymal stem cells derived from human dental pulp were seeded on collagen I scaffolds and grafted in human mandible defects. Three years after grafting, some biopsies were extracted from these sites and investigated by conventional methods and by propagation-based phase-contrast microCT. The regenerated tissue appeared more compact than the control alveolar bone. Figure 1.9 shows a microCT 3D reconstruction where the regenerated bone (white) and the blood vessels (red) are clearly visible.

It should be noted that both of the dental research mentioned above were conducted in the context of the European Project "MPNS Action COST MP1005 – *From nano to macro biomaterials (design, processing, characterization, modelling) and applications to stem cells regenerative orthopaedic and dental medicine* (NAMABIO)".

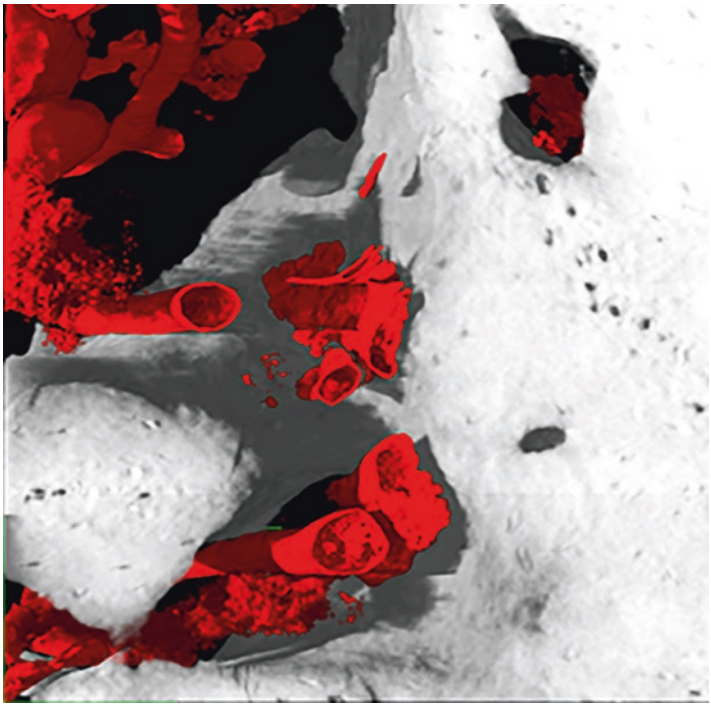

Fig. 1.9 Three-dimensional image of a portion of human regenerated mandible observed by synchrotron radiation-based phase-contrast microCT. The newly formed bone is virtually rendered in white and the newly formed blood vessels in red

Another European Project recently funded and deserving to be mentioned in this context is the COST Action CA16122 "BIONECA – *Biomaterials and advanced physical techniques for regenerative cardiology and neurology*".

The principal BIONECA challenge is to establish an intensive interaction among the top-level European institutions of different scientific background, with the main goal to reduce the number of deaths and costs associated with neurological and cardiological diseases.

Indeed, in the field of neurological disorders, cell-based treatment appeared as a very promising approach to ameliorate (or at least to slow) the course of different diseases. Positive results were obtained by using the primary foetal tissue for clinical trials related to the Parkinson's disease. Moreover, recent in vivo studies have shown that neural stem/precursors cells show a satisfactory survival, counteracting different neurological pathologies.

Another type of adult stem cells, the mesenchymal stem cells (MSC), show great promise in controlling the inflammatory activity and repairing of damaged tissues in the presence of different pathologies, including ALS, Huntington's, Alzheimer's and Parkinson's diseases, as well as spinal cord injuries, stroke and multiple sclerosis.

In this context, one of the major challenges is the treatment of Duchenne muscular dystrophy, a pathology inducing severe muscular damage in the affected patients.

Recent pioneering investigations [30, 31] demonstrated that cellular therapy is able to produce an improvement of the pathology by repairing the muscle damage. In particular, it was observed in muscular dystrophy mice models that a subpopulation of human stem cells, through an arterial route delivering, can reach the sites of muscle regeneration more efficiently than using myogenic progenitors.

After a first ex vivo experiment [32], another in vivo investigation [33] was performed by using microCT at ESRF, having labelled the injected stem cells with highly radiopaque iron oxide nanoparticles. This study allowed to elucidate the kinetics of the diffusion of the stem cells from the blood stream to the different skeletal muscle sites, obtaining results undoubtedly of great interest to attempt cellular treatment for muscular tissue repair.

Recently, the X-ray high-resolution phase-contrast tomography was also used to investigate, in ex vivo conditions, the microstructure of spinal cord in mice [34]. In particular, the 3D vascular and neuronal systems were imaged at scales from millimetres to hundreds of nanometres. Similar investigations were also performed by comparing the healthy mouse neuronal architecture with one of the mouse models of multiple sclerosis [35].

Finally, the same team was able to investigate, by phase-contrast nanotomography, the alterations induced by autoimmune encephalomyelitis in the vascular and neuronal networks of mice and possible treatments with mesenchymal stem cells [36].

Cardiovascular diseases (CDVs), in particular congestive heart failure (CHF), are other leading causes of death worldwide, in a population progressively aged.

Indeed, in spite of important advances in the treatment of ischemic and non-ischemic cardiovascular diseases [37], a poor understanding exists of the basic mechanism of CHF, justifying the search for new therapeutic options.

In this context, the regenerative cardiology constitutes one of the most promising strategies, where a key role is played by stem cells, with their unique ability of self-renewal and multipotency. Stem cell-based treatments to regenerate the myocardium can be accomplished by local injection of cells in the myocardium and systemic mobilization by cytokines and by tissue engineering strategies [38–42].

Primitive cells, with stem/progenitor characteristics, were isolated and expanded. Several clinical trials have shown that they represent a suitable autologous source to repair damaged myocardium by cellular therapy [43, 44].

In preclinical research, high-resolution tomographic imaging based on the synchrotron radiation was shown to offer a valid support in cell tracking, as demonstrated by a pioneering experiment performed at the ESRF [45]. This study, based on cellular therapy [46], showed that X-ray microCT is able to visualize, with high resolution and definition, the 3D spatial distribution of rat cardiac progenitor cells inside the infarcted heart, in ex vivo conditions and after short time from their injection. Thus, microCT imaging represents a considerable stride forward as compared to 2D histological analysis and constitutes a promising tool in view of future clinical experiments.

All of these studies, most of which will be reported in more detail in the next chapters of this book, demonstrate the prospective usefulness of the considered

tomographic techniques in the study of the damage induced by various diseases and traumas and their repair with regenerative medicine approaches.

In conclusion, a first paradoxical consideration that springs from this first chapter is the need to build ever larger machines, the modern cathedrals of these last two centuries, to explore the secrets of nature and life on an ever smaller scale.

A second consideration is linked to the importance of X-rays and in recent times of synchrotron radiation, to provide experimental instruments more and more suitable to produce knowledge not only in the fields of structure and dynamics of matter but also in more complex areas such as biology and medicine that even led to the awarding of the Nobel Prize in several brilliant discoveries!

The last consideration is for the Physics' discipline that, beyond the importance that it has in the interdisciplinary research, is at the base of all this magical world of enormous machines and scientific applications. If we just restrict our considerations to the brilliant results already obtained in biology and to the enormous prospects of the contributions of synchrotron radiation for clinical progress in the innovative area of regenerative medicine, we can conclude that we are operating in accordance with the philosophy of one of the first great physicists of modern time, Galileo Galilei, who said:

I am looking for the light of science and its benefits.
La Luce della Scienza cerco e 'l Beneficio
Galileo Galilei

Acknowledgements It is a pleasure to thank Prof. Federico Quaini and Dr. Mario Stefanon for their precious scientific contributions and to Mr. Mario Pergolini for his outstanding technical support.

References

1. https://home.cern/
2. Chatrchyan S et al (2012) Observation of a new boson at a mass of 125 GeV with the CMS experiment at the LHC. Phys Lett B 716:30–61
3. http://www.esrf.fr
4. Kamel G, Lefrancois S, Al-Najdawi M, Abu-Hanieh T, Saleh I, Momani Y, Dumas P (2017) EMIRA: the infrared synchrotron radiation beamline at SESAME. Synchrotron Radiat News 30(4):8–10. https://doi.org/10.1080/08940886.2017.1338415
5. Schwandt J, Fretwurst E, Klanner R, Poehlsen T, Zhang J (2013) Design of the AGIPD sensor for the European XFEL. Nucl Inst Methods Phys Res Sect A 731:252–254
6. Ramakrishnan V (2002) Ribosome structure and the mechanism of translation. Cell 108:557–572
7. Nobel Prizes in Chemistry (2002) The Royal Swedish Academy of Science. http://KVA.SE
8. Kobilka B (2007) G protein coupled receptor structure and activation. Biochim Biophys Acta Biomembr 1768:794–807
9. MacKinnon R (2003) Potassium channels. FEBS Lett 555:62–65
10. Claesson T (2001) A medical imaging demonstrator of computed tomography and bone mineral densitometry. Universitetsservice US AB, Stockholm

11. Salomè M, Peyrin F, Cloetens P, Baruchel J, Spanne P, Suorti P, Laval-Jeantot AM (1997) Assessment of bone micro-architecture using 3D computed microtomography. ESRF Newslett 28:26
12. Ozawa S, Kasugai S (1966) Evaluation of implant materials (hydroxyapatite, glass-ceramics, titanium) in rat bone marrow stromal cell culture. Biomaterials 17:23
13. Marcacci M, Kon M, Zaffagnini S, Giardino R, Rocca M, Corsi A, Benvenuti A, Bianco P, Quarto R, Martin I, Cancedda R (1999) Reconstruction of extensive long bone defects in sheep using porous hydroxyapatite sponges. Calcif Tissue Int 64:83
14. Kon E, Muraglia A, Corsi A, Bianco P, Marcacci M, Martin I, Boyde A, Ruspantini I, Chistolini P, Rocca M, Giardino R, Cancedda R, Quarto R (2000) Autologous bone marrow stromal cells loaded onto porous hydroxyapatite ceramic accelerate bone repair in critical defects of sheep long bones. J Biomed Mater Res 49:328
15. Mastrogiacomo M, Komlev VS, Hausard M, Peyrin F, Turquier F, Casari S, Cedola A, Rustichelli F, Cancedda R (2004) Synchrotron radiation microtomography of bone engineered from bone marrow stromal cells. Tissue Eng 10:1767–1774
16. Atwood RC, Jones JR, Lee PD, Hench LL (2004) Analysis of pore interconnectivity in bioactive glass foams using X-ray microtomography. Scr Mater 51:1029–1033
17. Williams JM, Adewunmi A, Schek RM, Flanagan CL, Krebsbach PH, Feinberg SE et al (2005) Bone tissue engineering using polycaprolactone scaffolds fabricated via selective laser sintering. Biomaterials 226:4817–4827
18. Ho ST, Hutmacher DW (2005) Application of micro CT and computation modeling in bone tissue engineering. Comput Aid Des 37:1151–1161
19. Shao XX, Hutmacher DW, Ho ST, Goh JCH, Lee EH (2005) Evaluation of a hybrid scaffold/cell construct in repair of high-load-bearing osteochondral defects in rabbits. Biomaterials 27:1071–1080
20. Jones AC, Milthorpe B, Averdunk H, Limaye A, Senden TJ, Sakellariou A et al (2004) Analysis of 3D bone ingrowth into polymer scaffolds via micro-computed tomography imaging. Biomaterials 25:4947–4954
21. Mathieua LM, Muellerb TL, Bourbana PE, Piolettic DP, Mullerb R, Mansona JAE (2006) Architecture and properties of anisotropic polymer composite scaffolds for bone-tissue engineering. Biomaterials 27:905–916
22. Baruchel J, Lodini A, Romanzetti S, Rustichelli F, Scrivani A (2001) Phase-contrast imaging of thin biomaterials. Biomaterials 22:1515–1520
23. Wellington SL, Vinegar HJ (1987) X-ray computerized tomography. J Pet Technol 39(8):885–898
24. Bonse U, Busch F (1999) X-ray computed microtomography (mCT) using synchrotron radiation (SR). Prog Biophys Mol Biol 65(1/2):133–169
25. Cancedda R, Cedola A, Giuliani A, Komlev V, Lagomarsino S, Mastrogiacomo M, Peyrin F, Rustichelli F (2007) Bulk and interface investigations of scaffolds and tissue-engineered bones by X-ray microtomography and X-ray microdiffraction. Biomaterials 28:2505–2524
26. Komlev VS, Peyrin F, Mastrogiacomo M, Cedola A, Papadimitropoulos A, Rustichelli F et al (2006) Kinetics of in vivo bone deposition by bone marrow stromal cells into porous calcium phosphate scaffolds: a X-ray computed microtomography study. Tissue Eng 12:3449–3458
27. Papadimitropoulos A, Mastrogiacomo M, Peyrin F, Molinari E, Komlev V, Rustichelli F, Cancedda R (2007) Kinetics of in vivo bone deposition by bone marrow stromal cells within a resorbable porous calcium phosphate scaffold: an x-ray computed microtomography study. Biotechnol Bioeng 98(1):271–281
28. Komlev V, Mastrogiacomo M, Peyrin F, Cancedda R, Rustichelli F (2009) X-ray synchrotron radiation pseudo-holotomography as a new imaging technique to investigate angio-and microvasculogenesis with no usage of contrast agents. Tissue Eng 15(3):425–430
29. Giuliani A, Manescu A, Langer M, Rustichelli F, Desiderio V, Paino NF, De Rosa A, Laino L, D'Aquino R, Tirino V, Papaccio G (2013) Three years after transplants in human mandibles, histological and in line holotomography revealed that stem cells regenerate a compact rather

than a spongy bone: biological and clinical implications. Stem Cells Transl Med 2(4):316–324. https://doi.org/10.5966/sctm.2012-0136
30. Torrente Y, Belicchi M, Sampaolesi M et al (2004) Human circulating AC133+ stem cells restore dystrophin expression and ameliorate function in dystrophic skeletal muscle. J Clin Investig 114(2):182–195. https://doi.org/10.1172/JCI200420325
31. Sampaolesi M et al (2003) Cell therapy of alpha-sarcoglycan null dystrophic mice through intra-arterial delivery of mesoangioblast. Science 301:487–492
32. Torrente Y, Gavina M, Belicchi M, Fiori F, Komlev V, Bresolin N, Rustichelli F (2006) High-resolution X-ray microtomography for three-dimensional visualization of human stem cell muscle homing. FEBS Lett 580:5759–5764
33. Farini A, Villa C, Manescu A, Fiori F, Giuliani A, Razini P, Sitzia C, Del Fraro G, Belicchi M, Meregalli M, Rustichelli F, Torrente Y (2012) Novel insight into stem cell trafficking in dystrophic muscles. Int J Nanomed 7:3059–3067
34. Fratini M et al (2015) Simultaneous submicrometric 3D imaging of the micro-vascular network and the neuronal system in a mouse spinal cord. Sci Rep 5:8514
35. Bukreeva I et al (2017) Quantitative 3D investigation of neuronal network in mouse spinal cord model. Sci Rep 7:41054
36. Cedola A et al (2017) X-ray phase contrast tomography reveals early vascular alterations and neuronal loss in a multiple sclerosis model. Sci Rep 7:5890
37. Benjamin EJ et al (2018) Heart disease and stroke statistics update: a report from the American Heart Association. Circulation 137(10):e67–e492. https://doi.org/10.1161/CIR.0000000000000558
38. Stamm C et al (2003) Autologous bone-marrow stem-cell transplantation for myocardial regeneration. Lancet 361:45–46
39. Assmus B, Schachinger V, Teupe C et al (2002) Transplantation of progenitor cells and regeneration enhancement in acute myocardial infarction (TOPCARE-AMI). Circulation 106:3009–3017
40. Tse HF, Kwong YL, Chan JKF, Lo G, Ho CL, Lau CP (2003) Angiogenesis in ischaemic myocardium by intramyocardial autologous bone marrow mononuclear cell implantation. Lancet 361:47–49
41. Kang HJ, Kim HS, Zhang SY, Park KW, Cho HJ, Koo BK et al (2004) Effects of intracoronary infusion of peripheral blood stem-cells mobilised with granulocyte-colony stimulating factor on left ventricular systolic function and restenosis after coronary stenting in myocardial infarction: the MAGIC cell randomised clinical trial. Lancet 363:751–756
42. Menasche P, Hagege AA, Scorsin M, Pouzet B, Desnos M, Duboc D, Schwartz K, Vilquin JT, Marolleau JP (2001) Myoblast transplantation for heart failure. Lancet 357:279–280
43. Bolli R, Chugh AR, D'Amario D, Loughran JH, Stoddard MF, Ikram S et al (2011) Cardiac stem cells in patients with ischaemic cardiomyopathy: initial results of the SCIPIO trial. Lancet 378:1847–1857
44. Makkar RR, Smith RR, Cheng K, Malliaras K, Thomson LE, Berman D et al (2012) Intracoronary cardiosphere-derived cells for heart regeneration after myocardial infarction (CADUCEUS): a prospective, randomised phase 1 trial. Lancet 379:895–904
45. Giuliani A, Frati C, Rossini A, Komlev V, Lagrasta C, Savi M et al (2011) High-resolution X-ray microtomography for three-dimensional imaging of cardiac progenitor cell homing in infarcted rat hearts. J Tissue Eng Regen Med 5(8):e168–e178. https://doi.org/10.1002/term.409
46. Leri A, Kajstura J, Anversa P, Frishman WH (2008) Myocardial regeneration and stem cells repair. Curr Probl Cardiol 33:91–15

Chapter 2
Introduction to X-Ray Micro-tomography

Serena Pacilè and Giuliana Tromba

Abstract X-ray computed tomography (CT) represents one of the most powerful 3D non-destructive imaging techniques exploited in clinics to help the diagnostic process of many diseases. The progress achieved in the realization of detectors, in x-ray tube technology, and in the computational power of modern hardware has led to its translation toward micrometer and sub-micrometer range resolution applications.

Micro-CT and nano-CT systems based on conventional micro-focus x-ray tubes or newest generation liquid-metal-jet anode (MetalJet) systems are, today, available and largely applied in biomedical research for in vitro studies of biomaterials, scaffolds, bones, teeth, etc. as well as for morphologic and functional studies on excised organs and small animals.

Absorption-based imaging is the basis for the most common modality of CT scanners; however, the recent developments of x-ray sources based on synchrotron laboratories and capable to reach unprecedented characteristics of brilliance and intensity have allowed the implementation of innovative imaging approaches. These techniques exploit the refraction of x-rays in the matter instead of their absorption, overcoming the intrinsic limitation of conventional techniques and broadening the utility of micro-CT.

In this chapter an overview of the basics of micro-CT will be given, starting from the sources characteristics, then describing the x-ray interactions with matter, and finally addressing the image formation principles. In this latter paragraph, particular attention will be reserved to phase-sensitive techniques, highlighting their potentials to improve biomedical research.

S. Pacilè (✉)
Department of Engineering and Architecture, University of Trieste, Trieste, Italy

Elettra-Sincrotrone Trieste S.C.p.A., Trieste, Italy
e-mail: serena.pacile@elettra.eu

G. Tromba
Elettra-Sincrotrone Trieste S.C.p.A., Trieste, Italy
e-mail: giuliana.tromba@elettra.eu

A. Giuliani, A. Cedola (eds.), *Advanced High-Resolution Tomography in Regenerative Medicine*, Fundamental Biomedical Technologies,
https://doi.org/10.1007/978-3-030-00368-5_2

1 Introduction

In medical diagnostics, x-ray imaging is a fundamental tool for observing the inside of the human body in a noninvasive way. From the very beginning, shortly after the discovery of x-rays in 1895, this technology was used to image bones [1], opening the way to a new kind of medical examination. As an evolution of the x-ray radiography, where the overlapping structures cannot unambiguously be discerned in a single image, computed tomography (CT) has been developed in 1972 by Godfrey Newbold Hounsfield (Nobel Prize winner in 1979 for Physiology and Medicine), with the first prototype of medical CT scanner [2]. CT was the first method able to produce images of trans-axial planes through the human body (slices) without being biased by superimposition of distinct anatomical structures. From the first clinical CT scanners to date, the enormous technological developments involving the x-ray sources and the new detectors have led to substantial improvements, in terms of delivered dose and image quality. CT technology has evolved toward higher resolution setups, with x-ray computed micro-tomography (μ-CT) systems able to reach a micrometric spatial resolution on centimeter-sized samples and a sub-micrometer spatial resolution on samples at the scale of 1–2 mm (nano-tomography). Nowadays, it is employed in a wide range of research areas, from medicine to biology and from geology to archaeology and material sciences.

Dedicated μ-CT setups have been developed for preclinical research, involving ex vivo and in vivo studies on small animal models. On the other hand, the development of new methods for x-ray production based on particle accelerators (synchrotrons) allowed to obtain sources with new characteristics in terms of high spatial coherence and brilliance, opening the way to the use of new imaging approaches, the so-called phase-sensitive techniques.

Some basic aspects of x-ray μ-CT are described in this chapter, from the generation of x-rays to their interaction with matter and image formation.

2 Basic Principles

During a μ-CT scan, the object is illuminated by x-rays in transmission geometry. The beam, after passing through the object, is collected by a detector. A series of bi-dimensional projections are taken, usually at a fixed angular increment. While in clinical CTs, source and detector are rotating around the patient to produce the different projections, for preclinical and industrial applications, very often source and detector are fixed, and the sample is placed on a rotating stage. The total rotational angle depends on the system geometry but typically is 180° when a parallel beam is used or 360° when a cone-beam geometry is used. Starting from the totality of projections, the 3D tomographic slices (i.e., images of the internal structure of the object in a plane parallel to the beam propagation direction) are then reconstructed. The reconstruction process and the visualization of the 3D data are discussed more in detail in Chap. 5. The principle on which relies the image formation can be either

absorption or phase-contrast effect. In conventional x-ray imaging, the image formation is based on the differences in x-ray absorption of the sample details, i.e., dense structures like bones absorb more than lighter elements comprising soft tissues; therefore μ-CT is based on the mapping of the linear attenuation coefficient of x-ray crossing the investigated sample [3], and the attenuation depends upon the composition and density of the object. However, if structures with a weak absorption, or with similar absorption properties, are observed, the overall image contrast may be insufficient to obtain a meaningful image. Notwithstanding, as x-rays are electromagnetic waves, not only their absorption but also the relative phase shifts can carry information about an object. Thus, *phase contrast* becomes an essential modality to obtain sufficient image contrast for hard x-ray imaging of soft biological tissues and biological samples, where conventional absorption radiography fails [4, 5]. There are several techniques able to exploit this latter mechanism; three main approaches to x-ray phase-contrast imaging currently attract the most attention, and these are propagation-based, analyzer-based, and grating-based imaging [6–9]. Recent quantitative studies [10] have shown that all these methods can deliver comparable outcomes, depending on the specific parameters of the experiment.

3 X-Ray Sources and Beam Geometry

According to the x-ray production modality, we distinguish between conventional systems based on tubes emitting x-rays with a typical conic emission and synchrotron radiation setups typically fed with intense, laminar x-ray beams with a nearby parallel beam geometry. Figure 2.1 shows a schematic representation of the main components (i.e., x-ray source, sample rotator stage, and detector) of a μ-CT setup in both cases.

3.1 Conventional Sources

The most common way to perform a μ-CT on biological samples employs a conventional micro-focus-based x-ray tube. Like all x-ray tubes, these sources generate x-rays when highly energetic electrons are stopped in a solid metal anode: x-rays result from the conversion of the kinetic energy attained by electrons accelerated under a potential difference into electromagnetic radiation, as a result of collisional and radiative interactions. A polychromatic divergent beam is generated, from which a conical solid angle is selected. Many benchtop μ-CT systems are today able to reach very high-resolution level, in the range of 1 μm with a voxel size below 0.1 μm. The position of the sample with respect to the source and the detector can be changed to adjust the magnification and the resolution; however, as the sample has to stay inside the field of view, the optimal position is always a compromise between sample size and spatial resolution.

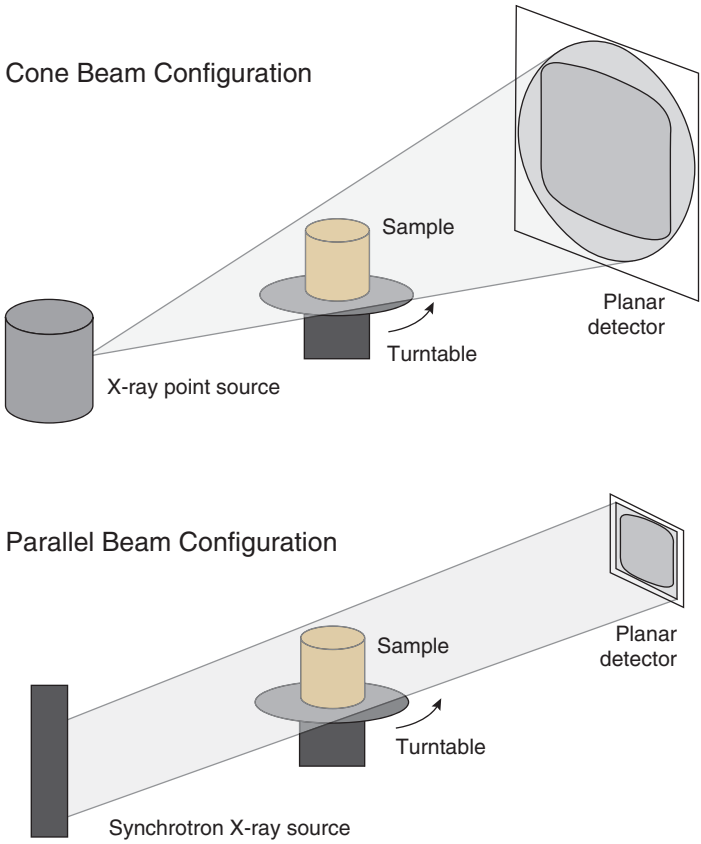

Fig. 2.1 Illustration of different beam configuration geometries

The mainly diffused usage of conventional μ-CT sources is in absorption mode as the produced beam is not always enough coherent to obtain phase contrast; however, more recently, technical developments have enabled the translation of some of the phase-contrast techniques to laboratories sources [11, 12], as described in Chap. 15.

The detector cameras used for μ-CT systems can be grouped into two categories, according to their ability to discriminate x-ray energy or not. In the first case, we speak about spectral CT, a promising technique recently introduced in last-generation μ-CT systems thanks to the progress achieved by single-photon counting detectors [11–13]. In most of the cases, the detector simply integrates all the x-ray energies.

In general μ-CT systems adopt digital flat 2D detectors; the most commonly used are charged-coupled device (CCD) systems using scintillator screens coupled via fiber-optic bundles for conversion of x-rays into visible photons [14, 15].

Table 2.1 Overview of laboratory sub-micro and nano-CT-systems with resolutions and voxel sizes <1 μm

CT-device	Best resolution [μm]	Minimum voxel size [nm^3]	Max. sample size [mm]	Ref./source
GE phoenix nanotom m	~1.0	300	250 × 240	www.ge-mcs.com/download/x-ray.phoenix-x-ray/nanotom_m_ s_DE_GE1T-0113
Bruker Skyscan 2211	~0.9	100	Diameter: 204 Length: 200	www.skyscan.be/products/2211
Zeiss Xradia 510 Versa	~0.7$^-$	70	Up to 300	www.xradia.com/versaxrm-510
NanoXCT	-	50	Several mm	www.nanoxct.eu, demonstrator available at RayScan
Zeiss Xradia 810 Ultra	~0.05	16	0.065 (FOV)	www.xradia.com/zeiss-xradia-810-ultra

Reproduced from Ref. [18]

More recently, new detectors based on complementary metal oxide semiconductor (CMOS) technology became available and are implemented in systems for in vivo imaging of small animals [16, 17]. The following table contains a list of laboratory sub-micro and nano-CT systems with resolution and voxel size <1 μm (Table 2.1).

An issue limiting the brightness for electron impact x-ray sources is the heat load at the anode that can bring to its local melting. This problem has been solved with the introduction of the liquid-metal-jet anode (MetalJet) technology that overcomes this limit by replacing the traditional anode by a thin high-speed jet of liquid metal (Fig. 2.2). In such a way, melting of the anode is no longer a problem as it is already molten. Usually, with these systems, the obtained brilliance is one order of magnitude higher than a solid anode x-ray tube [19], the electron beam power density can be ten times higher, and a sufficient grade of spatial coherence is achieved, thus allowing the use of phase-contrast imaging techniques [20].

3.2 Synchrotron Light Sources and Compact Sources

Synchrotron radiation (SR) is generated by an electron traveling at relativistic speed changing its direction of movement. SR covers a large spectrum of electromagnetic waves, from infrared to hard x-rays. Its main characteristics are the high intensity (three to four orders of magnitude higher than conventional x-ray tubes), the high brilliance, and the low-divergence emission. SR is produced in large accelerator-based facilities equipped with different magnetic structures (bending magnets and insertion devices) optimized to maximize radiation production for the different experimental purposes and user requirements (see Fig. 2.3). SR is extracted from the accelerators and transported to the experimental stations through the so-called beamlines.

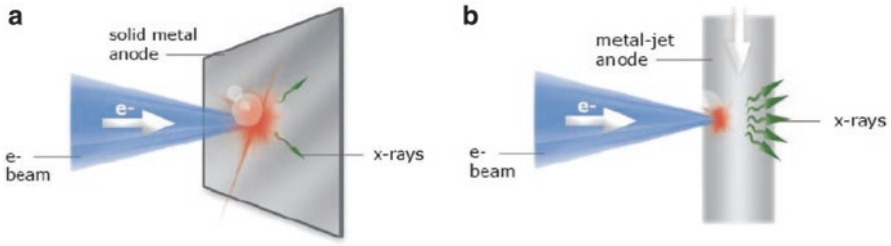

Fig. 2.2 Principle of a solid anode x-ray tube (**a**) and a liquid-metal-jet x-ray tube (**b**). (Reproduced from Ref. [21])

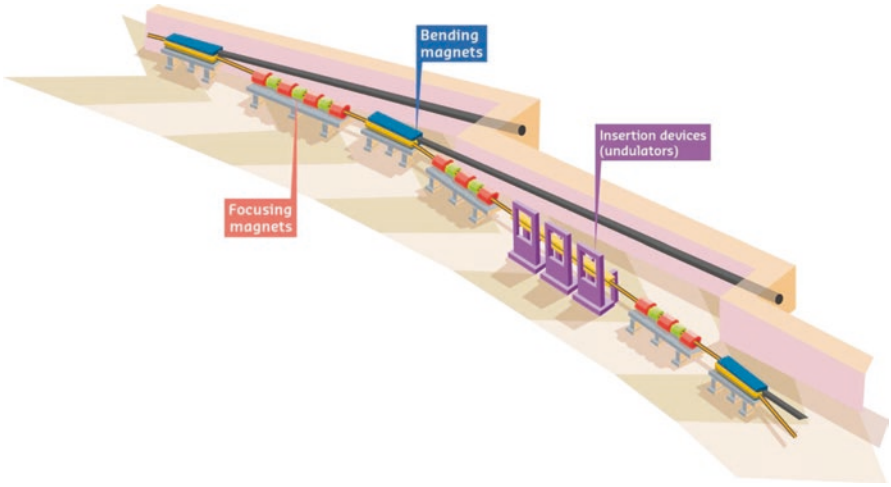

Fig. 2.3 Sketch of a curved section showing a bending magnet and an insertion device. (Reproduced from www.esrf.eu)

Imaging beamlines are made up of several components used for beam shaping, focusing/defocusing, filtering, and monochromatization. Experimental stations at hard x-ray imaging beamlines are generally located at high distance from the source and are, usually, designed and equipped to handle specific experiments, according to the samples under study, taking into account the photon flux, the energy range, the focus, and the collimation of the x-rays. The SR beam is characterized by a high level of spatial coherence; this allows to exploit the phase shift effects occurring to transmitted x-ray waves as a further mechanism contributing to image formation.

Contrary to the x-ray tubes, natively synchrotrons provide laminar, nearby parallel geometry, so there is low magnification of the object on the detector, and scatter contribution to image formation is negligible. The use of monochromatic x-rays makes negligible the beam hardening artifacts, which is fundamental to extract quantitative information about the sample (such as composition, density, morphology, etc.).

Table 2.2 List of some of the ICS sources in operation or under study/development worldwide

Project/source name	Type	Energy (keV)	Flux (10% bandwidth)	Source size(μm)
PLEIADES (LLNL)	LINAC	10–100	10^7 (10 Hz)	18
SLAC	LINAC	20–85		
Waseda University	LINAC	0.25–0.5	2.5×10^4 (5 Hz)	
AIST, Japan	LINAC	10–40	10^6	30
Tsinguha University	LINAC	4.6	1.7×10^4	
LUCX (KEK)	LINAC	33	5×10^4 (12.5 Hz)	80
MIT project	LINAC	3–30	3×10^{12} (100 MHz)	2
SPARC-PLASMONX	LINAC	20–380	$2 \times 10^8 - 2 \times 10^{10}$	0.5–13
TERAS (AIST)	Storage ring	1–40	5×10^4	2
Lyncean Tech	Storage ring	7–35	10^{12}	30
TTX (THU China)	Storage ring	20–80	10^{12}	35
ThomX, France	Storage ring	50	10^{13} (25 MHz)	70

Reproduced from Ref. [29]

Monochromaticity is also essential for dual-energy applications such as the K-edge subtraction (KES) imaging. This technique exploits the large difference in x-ray absorption of elements at energies around the K-absorption edge. In biomedical imaging, since the first application by B. Jacobson in 1953 [22], KES has been widely employed in vascular studies where a contrast agent with high Z like Iodine is injected into the blood vessels. Two images acquired at two energies, i.e., one above the K edge and one below the K edge, are logarithmically subtracted, and an image with the iodine distribution is obtained. The KES approach has been more recently adopted in preclinical research for lung functional studies on rabbits. In this case, the used contrast agent was Xenon gas inhaled by the animal during a controlled respiratory cycle. An updated review of recent results obtained with KES is available in [23].

Exploiting the high intensity of SR beam, recent achievements showed the possibility to shorten as much as possible the scan times, enabling fast, real time studies (4DCT) of dynamic processes [24].

In the last decade, a considerable effort has been devoted to the development of alternative x-ray sources, less expensive and smaller than synchrotron facilities, known as "compact x-ray light sources (CXLS)," able to produce high-intensity x-ray beams that mimic the features of SR. Some of these sources are in operation, and others are under construction in Europe (e.g., MuCLS, ThomX, STAR) [25–27] and worldwide (see Table 2.2). For most of them, the physical principle relies on the inverse Compton scattering (ICS), where an ultra-relativistic electron bunch, colliding with a laser pulse, is back-scattered as hard x-rays. The emission cone has an opening of a few mrad, and the energy bandwidth is a few percent. The produced x-ray beam rises in the same direction as the electrons. The energy required for the electrons is of the order of 50 MeV, and accelerator schemes are based on linear accelerators or small storage rings less than 5 m in circumference (Fig. 2.4), whereas synchrotrons need a circumference of nearly 1000 m [28].

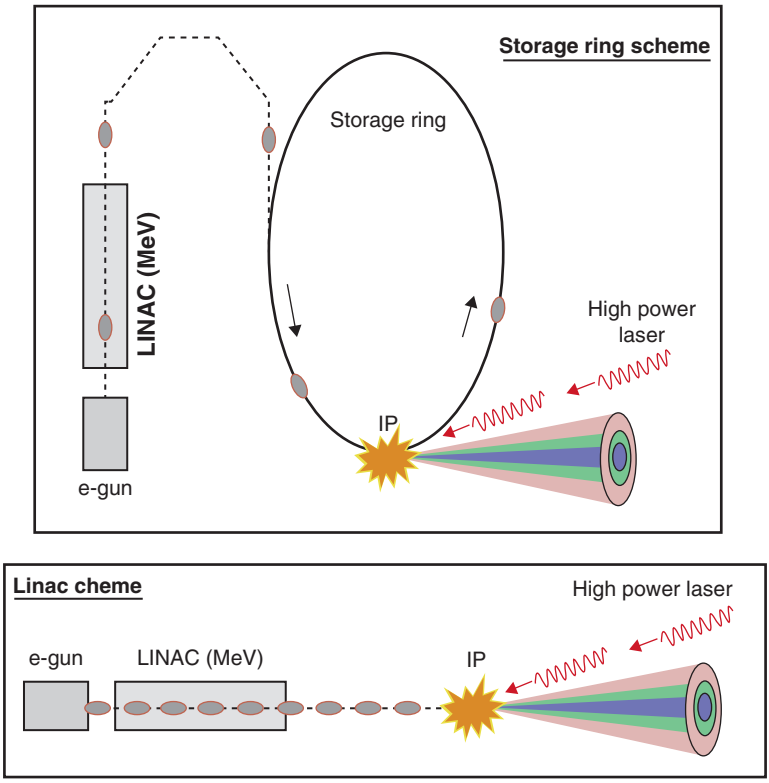

Fig. 2.4 Basic schemes of compact Compton sources. (Copyright 2015, with kind permission from Elsevier [29])

4 Image Formation Principles (X-ray Interaction with Matter)

At microscopic level, the interaction between x-rays and matter occurs in three fundamental ways: the photoelectric effect, the Compton effect, and coherent scattering.

The photoelectric effect occurs when an incident x-ray photon, of a certain energy $E = h\nu$ (where h is Planck's constant and ν is frequency), hits an atom in which the binding energy of the electrons is lower than E, so that it is absorbed by the atom. The interacting electron is raised to a state of the continuous spectrum, i.e., the electron of a lower shell is kicked off the atom and travels through the material as a free photoelectron. Then the photon is absorbed. The hole created in the deep shell is filled by an outer-shell electron. Since the outer-shell electron is at a higher energy state than the inner shell, the so-called characteristic radiation is emitted. Thus, the photoelectric effect produces a positive ion (the affected atom lacks an electron to be electrically neutral), a photoelectron, and a photon of characteristic radiation (Fig. 2.5).

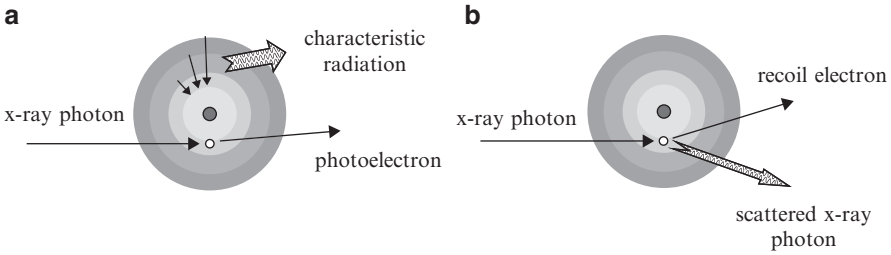

Fig. 2.5 Illustration of (**a**) photoelectric interaction and (**b**) Compton interaction. (Reproduced from Ref. [32])

The second interaction, i.e., the Compton scattering, occurs when the x-ray photon energy is higher than the electron binding energy. In this case, the x-ray photon frees the electron from the atom and is scattered losing a part of its initial energy.

An interaction of this kind produces a scattered photon and a positive ion. The photon can be deflected at any angle from 0 to 180°, according to a certain angle distribution depending of photon energy and sample composition.

In the coherent scattering, there is not an ionization process. The incident electromagnetic wave, with its oscillating electric field, induces a momentary vibration on the target atom, and the oscillating electrons emit radiation of the same wavelength (energy) as the incident one. Therefore, the scattered photon has the same energy on the primary one.

The overall result of these three interactions is that the x-ray photons, passing through a material, are either absorbed or scattered. Scattering is detrimental in the image formation as it contributes to increase the noise level.

4.1 Absorption Law

To describe the image formation, it is necessary to pass from interaction processes of a single x-ray photon to the quantitative attenuation of an x-ray beam taking into account absorption and scattering. In general, the mechanisms behind x-ray imaging can be explained by the complex refractive index of the sample. At macroscopic level, the absorption of a monoenergetic incident x-ray beam in a homogeneous material (i.e., with uniform density and atomic number Z) can be described by:

$$I = I_0 e^{-\mu \Delta x} \tag{2.1}$$

where I is the intensity of the beam after running through the matter and I_0 is the incident intensity; Δx is the thickness of the material. μ is known as linear attenuation coefficient, and it is given by a linear combination of the photoelectric, Compton, and coherent scattering effect. Equation 2.1 is called Beer–Lambert

law [30]. Clearly, a high value of μ means that materials are able to attenuate the x-ray more than objects with low μ values. As an example, in medical imaging, x-ray photons are more attenuated by bones (high μ) than by soft tissues (low μ). When dealing with a nonuniform object, i.e., an object made of several smaller homogeneous elements with different absorption coefficient, the incident intensity of a single element is given by the outgoing intensity of the previous one. Applying this concept to every single element repeatedly in a cascade fashion, the result is:

$$I = I_0 e^{-\mu_1 \Delta x} e^{-\mu_2 \Delta x} \ldots e^{-\mu_n \Delta x} = I_0 e^{-\sum_{n=1}^{N} \mu_n \Delta x} \tag{2.2}$$

Dividing both sides by I_0 and taking the negative logarithm, Eq. 2.2 becomes:

$$p = -\ln\left(\frac{I}{I_0}\right) = \sum_{n=1}^{N} \mu_n \Delta x \tag{2.3}$$

Assuming that Δx is approaching to zero, the summation in this latter equation can be written as an integral over the length of the object in the following way:

$$p = -\ln\left(\frac{I}{I_0}\right) = \int_L \mu(x)\,\mathrm{d}x \tag{2.4}$$

This equation says that the logarithm of the ratio of the entrance x-ray intensity over the transmitted x-ray intensity represents the line integral of the absorption coefficient along the x-ray path. The term p in CT is usually known as projection: it represents the starting point for the image reconstruction process that is discussed in Chap. 5.

4.2 Phase-Based Techniques for X-ray Imaging

As specified before, x-ray propagation through matter can be described by mean of the complex refractive index, expressed as:

$$n = 1 - \delta + i\beta \tag{2.5}$$

δ represents the refractive index decrement, which is related to the phase shifts of the electromagnetic wave in the matter and, therefore, its deviation from the incident direction [31]. β is the absorption term which is linked to the absorption of x-rays into the matter, due to the photoelectric effect and scattering. The absorption index is linked to the linear absorption coefficient μ, by means of the following relation [33]:

$$\mu = \frac{2\pi\beta}{\lambda} \tag{2.6}$$

where λ is the x-ray wavelength. In the diagnostic x-ray energy range, the refractive decrement δ is up to three orders of magnitudes higher than the absorption term β. Consequently, the phase shift effects can be much larger than the absorption effects, on which conventional techniques are based. Therefore, thanks to the phase shifts contributions, the sensitivity of the imaging system can be greatly enhanced, particularly when the contrast rising from the differences in absorption are not sufficient to distinguish tiny details from the background, as in the case of breast tumor lesions embedded in glandular tissue.

Moreover, since phase-based x-ray imaging methods can provide good quality images even with low x-ray absorption, energies higher than those typically used in radio-diagnostic imaging can be used. This means that, by selecting a suitable energy, it is possible to ensure a low radiation dose to the patient (keeping low the imaginary part β) and at the same time obtain good phase-contrast images (with well-discriminated features), being the refractive index decrement sufficiently large.

In the last 20 years, different approaches for phase-based x-ray imaging methods have been explored and are nowadays widely applied. In the following paragraphs, the most diffused phase-sensitive methods will be briefly described, namely, propagation-based imaging (PBI), analyzer-based imaging (ABI), edge illumination (EI), and Talbot (or grating) x-ray interferometry (GI). Several reviews partially or fully dedicated to these topics have appeared quite regularly in the recent scientific literature, such as Fitzgerald [34], Suortti and Thomlinson [35], Lewis [36], Momose [5], Bravin et al. [6], and Zhou and Brahme [37]. Moreover, Olivo [38] focused on the patents and intellectual property issues related to phase-sensitive techniques; finally, wider more general works were published by Nugent [39] and Paganin [40].

4.2.1 Propagation-Based Imaging Technique

The propagation-based imaging (PBI) is the simplest kind of phase-contrast technique as no optical elements are needed in the beam, and there is no constraint for beam monochromaticity. With this modality, as the beam passes through the object, parts of the wave front, having done different deflections, interfere producing a characteristic pattern that is registered by a detector placed at a suitable distance (Fig. 2.6) from the sample itself [41, 42]. Due to the Fresnel diffraction, the phase shifts are then converted into detectable intensity variations [43]. In order to achieve interference of the propagating beam, a very high degree of spatial coherence is required, and a high-resolution detector is needed to observe the fringes.

The PBI modality can be included in the differential phase-contrast imaging methods, as the image signal depends on the spatial variation of the phase shift induced by the sample rather than directly on it. The image contrast signal in this method is,

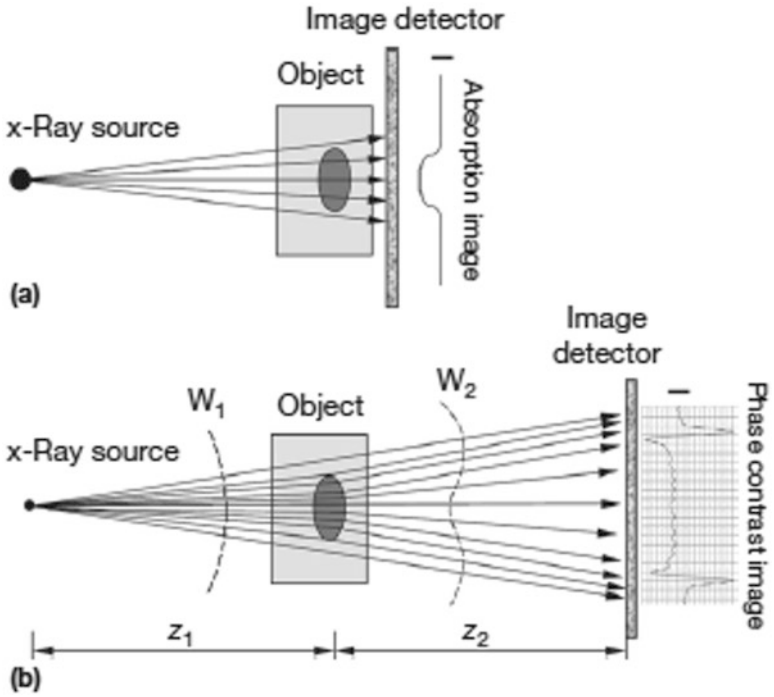

Fig. 2.6 Comparison between (**a**) conventional attenuation imaging, where the detector is in contact with the sample, and (**b**) PPCI, where the detector is placed at a suitable distance in order to allow the detection of a typical edge-enhanced image profile. (Reproduced from Ref. [37])

at a first approximation, proportional to the Laplacian of the phase shift in a plane perpendicular to the optical axis. The phase signal is strongly dependent on the effective propagation distance (called *defocus distance*) defined as $D = z_1\, z_2/(z_1 + z_2)$, where z_1 and z_2 are the source-to-sample and the sample-to-detector distances, respectively. For $z_1 \gg z_2$ the effective distance is mainly dominated by the propagation distance, so $D \simeq z_2$. This is a usual condition found in synchrotron beamlines.

Varying the defocus distance, considering a monochromatic plane wave, and considering the transverse characteristic length scale h of the sample (the size of the smallest present feature), four *regimes* can be defined [44, 45]:

- Absorption regime: the sample-to-detector distance is close to zero.
- Near-field diffraction regime: the effective propagation distance is relatively small, such that $r_F^2 = \lambda D \ll h^2$. The term r_F is the radius in the sample plane of the so-called Fresnel zone, and it determines the finite region in the object that contributes to a point P in the image. In these conditions, the contrast is formed locally around specific object features. The boundaries of details inside the object are strongly enhanced (well-known effect of "edge enhancement"), and a distinct interference pattern corresponds to each edge, giving reliable information on the object morphology. To express the above condition for the near-field regime, a Fresnel number must be defined as $N_F \equiv h^2/(\lambda D)$, so that $N_F \gg 1$.

- Fresnel regime: here the defocus distance is $r_F^2 = \lambda D \approx h^2$, which is equivalent to $N_F \approx 1$.
- Fraunhofer regime: the effective propagation distance is quite large and is $r_F^2 = \lambda D \gg h^2$, and then $N_F \ll 1$. In this condition, the interference fringes can be well detected, but they cannot be related to a specific edge of the sample, so that the sample morphology is not recognized.

Thus, based on the different experimental setups, the Fresnel diffraction pattern highlights different features of the object. It can be demonstrated that the image is most sensitive to a given frequency range f of a particular phase feature at a distance D defined as $D \approx 1/(2\lambda f^2)$. At this distance, the phase-contrast contribution is maximized.

In order to retrieve a quantitative information on the absorption and on the phase shift caused by the object on the beam, a series of algorithms have been studied. This inverse problem is usually solved by coupling a set of Fresnel diffraction patterns recorded at different distances z. A simplified algorithm based on the transfer of intensity equation (TIE) and using a single PB distance is widely applied, with the near-field regime for homogeneous samples, to decouple phase from absorption effects [46–50]. This algorithm is also applied to increase image contrast and facilitate analysis in propagation-based images, where the obtained edge enhancement effects improve the visibility of structure details but hamper further quantitative analysis relying on threshold-based segmentation of the data sets.

As an example, an application of TIE phase-retrieval algorithm (PhR) in comparison with PBI is shown in Fig. 2.7. The sample was a mouse lung studied at a distance of 30 cm at a beam energy of 22 keV. As indicated in the detailed views, PBI (Fig. 2.7a) presents strong edge effects when compared with PhR (Fig. 2.7b). However, on the basis of gray value histograms, it can be seen that these effects prevent a clear image segmentation, while, in the PhR image, different tissue structures were clearly segmented with respect to air, being the gray level histogram clearly composed of two peaks.

4.2.2 Analyzer-Based Imaging

Analyzer-based technique (ABI) makes use of an analyzer crystal placed between the sample and the detector (Fig. 2.8) in combination with a monochromatic and collimated x-ray beam. The sample produces a deviation (refraction) of the transmitted beam according to the real part δ of the refractive index. The crystal acts as an angular band-pass filter, selectively accepting or rejecting such photons. According to its orientation, only a narrow angular range of x-rays, those satisfying the Bragg law for diffraction, are transmitted to the detector and contribute to the image [52]. Thus, working with different orientations of the analyzer crystal with respect to the direction of primary beam, different refraction effects can be exploited, providing extra contrast in addition to x-ray absorption.

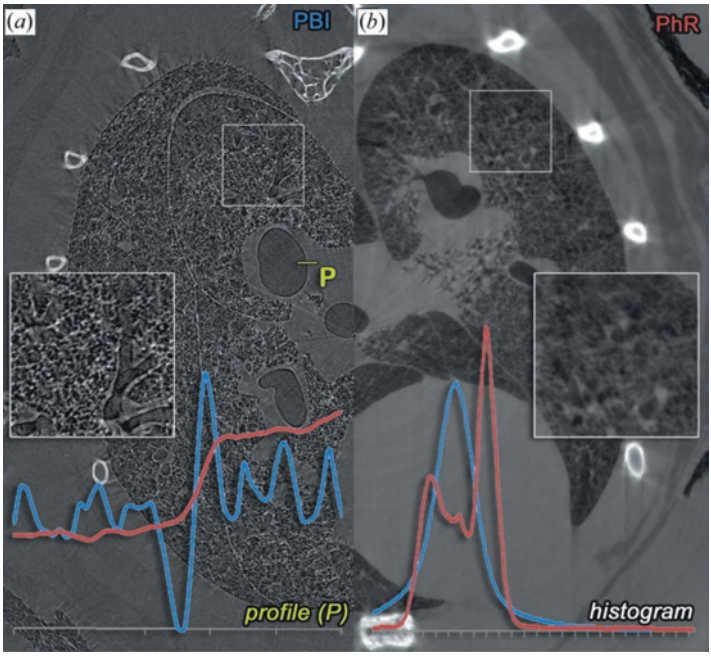

Fig. 2.7 Reconstructed slice from a micro-CT scan of a mouse lung using PBI (**a**) and the TIE PhR (**b**). Corresponding profiles in point P obtained are shown together with the overall gray level distribution histogram. (Reproduced from Ref. [51])

By the nature of the method, ABI produces images of the gradient of the refractive index in the sample. It has to be noticed that, in Fig. 2.8, all the crystals are used in Bragg geometry, but alternative arrangements have been developed using the Laue diffraction [53, 54].

The basic principle relies on the fact that, when the analyzer crystal reaches perfectly the peak of its reflectivity curve (known as rocking curve), it acts as an anti-scattering grid, giving a well-defined pure absorption image. According to the crystal orientation with respect to the primary x-ray beam, it is possible to study additional phase effects. ABI images, indeed, are usually represented by a mixture of absorption, refraction, and small and ultra-small angle scattering effects that can be extracted by combining images produced at different positions of the crystal rocking curve.

4.2.3 Edge Illumination Imaging

Similar to ABI, edge illumination (EI) method is based on the detection of the refraction angles suffered by photons when crossing the sample. Different from ABI, EI does not make use of a crystal but is based on two systems of collimated slits placed just behind the sample and in front of the detector, to detect refraction effects. In the simplest technique implementation used at a synchrotron, shown in

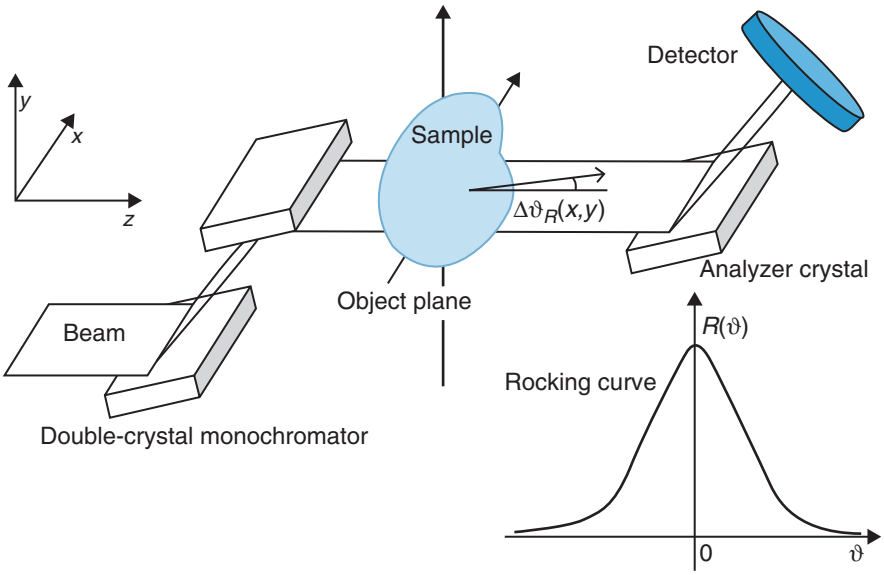

Fig. 2.8 Sketch of an ABI setup. The rocking curve is obtained with no sample in the beam. When the sample is put onto the beam, the rocking curve acts as an angular band-pass filter, and the analyzer crystal selectively diffracts photons according to their deviation angle *DyR* (*x*,*y*) upon exiting the sample. (Reproduced from Ref. [55])

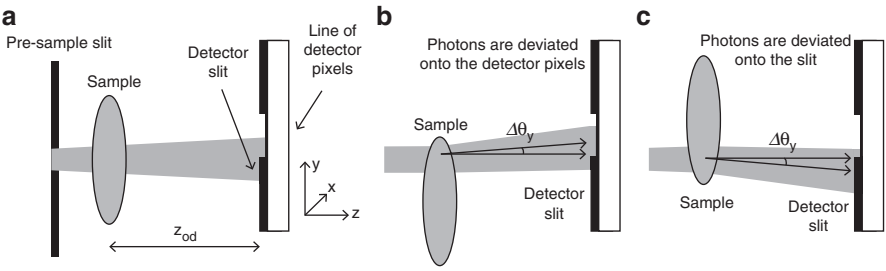

Fig. 2.9 Scheme of a typical synchrotron EI setup based on the use of two slits (not to scale). (**a**) No refraction from the object, (**b**) photons refracted onto the detector pixels increase the detector signal, and (**c**) photons deviated out of the detector pixels decrease the detector signal. (Reproduced from Ref. [29])

Fig. 2.9 [56–58], the setup is composed of a first slit placed before the sample (called pre-sample slit), used to collimate the beam, and a second slit, called detector slit, that is aligned with one pixel's row of the detector. The two slits have the same opening (some tens micrometers), but they are slightly misaligned.

In this way, the beam exiting from the first slit reaches the edge of the detector slit and is partially stopped by the second slit (partial illumination condition). If there is a sample in the system, the beam is refracted; thus the small portion of the beam falling on the detector slit is shifted by the quantity $\Delta y = z_{od} \tan(\Delta\theta_y)$, where z_{od} represents the distance between the sample and the detector slit and $\Delta\theta_y$ is the

component of the refraction angle in the direction orthogonal to the slits. For small refraction angles, in the order of microradians, the shift can be approximated to $\Delta y \approx z_{od}\,(\Delta\theta_y)$; the displacement is typically less than few micrometers for propagation distances of about 1 m. If the beam is shifted toward the aperture, the counts on the detector increase and vice versa; if the deviation goes toward the slits, the counts on the detector are less. In this way, it is possible to translate the refraction angles caused by the object into a modulation of the intensity on the detector. Like for ABI, EI produces images of the gradient of the refractive index in the sample. The whole image of the sample can be obtained scanning the sample, step by step, in the direction orthogonal to the slits and then pasting together all the single lines.

A modified setup has been developed for conventional x-ray tubes, as the technique does not require a coherent source [59, 60]. In this case, the above described working principle can be achieved by substituting the two slits with two masks (Fig. 2.10), characterized by several apertures, and the vertical sample scan is no more needed [61].

4.2.4 Grating X-Ray Interferometry

Grating-based imaging (GI) system bases its functioning on the use of grating interferometers. The technique is based on the optical phenomenon discovered by Talbot in the 1830s and foresees the use of a phase grating and an analyzer grating [62]. According to this phenomenon, under x-ray illumination, the image reproducing the grating is repeated at regular distances $d_T = 2p^2/\lambda$, where p is the period of the grating. The object causes absorption, refraction, and scattering effect on the x-ray beam, modifying the interference pattern produced by the grid. Accordingly, the

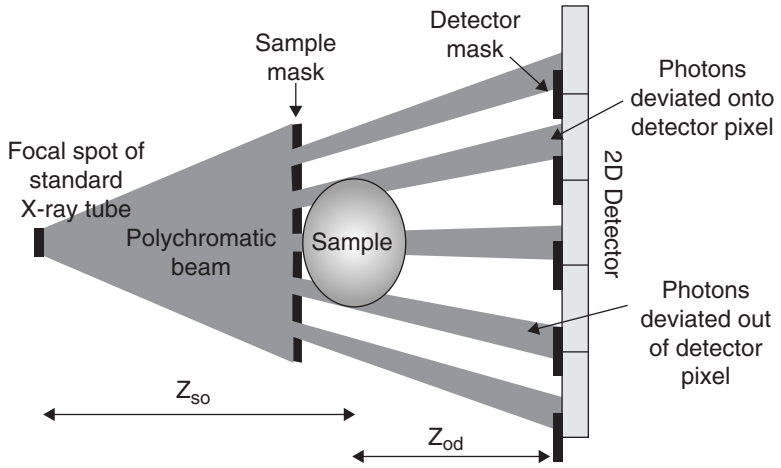

Fig. 2.10 Scheme of laboratory EI setup based on the use of an x-ray tube and a pair of masks. (Reproduced from Ref. [29])

angular shifting can be exploited as an intensity modulation on the detector, measuring the changes in the interference pattern with and without the sample. The second grating is placed at a fractional Talbot length distance (d_T) and is needed to analyze the interference pattern (Fig. 2.11). Allowing a direct registration of the x-ray phase shifts, the technique gives access to the measure of sample refractive index and produces optimal results for small or smooth phase gradients.

There are two methods to discriminate the different contributions to the signal: the phase-stepping technique and the method making use of the Moiré fringes.

Both of them can be used to obtain planar and tomographic images and are able to produce information about both real and imaginary component of the complex refractive index [64, 65].

The described setup is the one typically used in synchrotron facilities, as it requires a high degree of spatial coherence of the x-ray beam. However, the GI method can be implemented in conventional x-ray tubes, using a third additional grating, called Talbot-Lau interferometer.

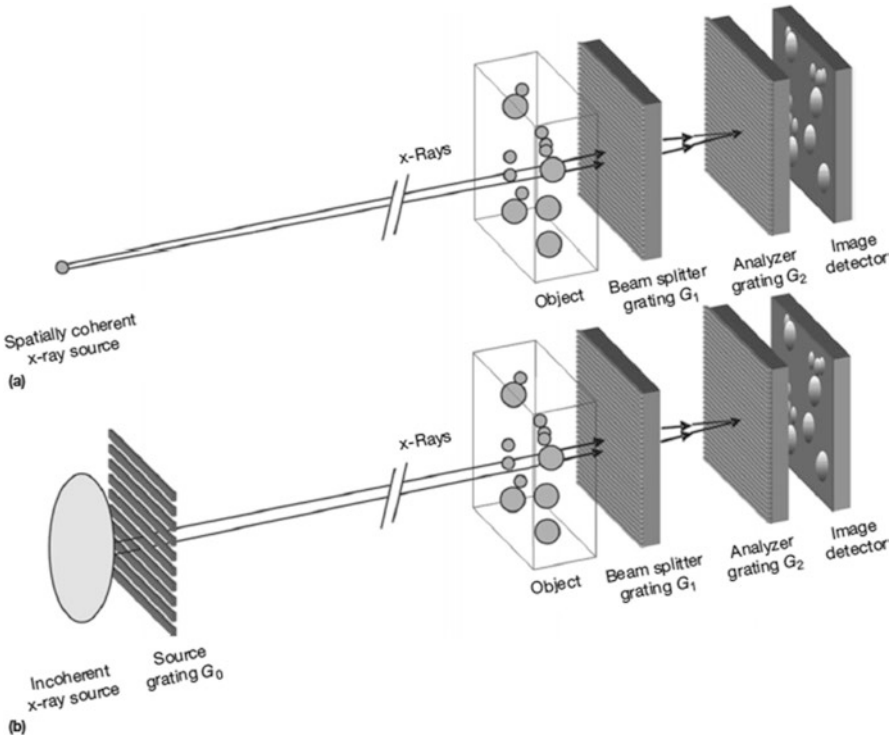

Fig. 2.11 Sketch of the typical grating interferometer. (**a**) Talbot interferometer (two-grating setup) used with spatially coherent sources such as synchrotron radiation. (**b**) Talbot–Lau interferometer (three-grating setup) used with incoherent radiation, for example, from a standard x-ray tube. (Reproduced from Ref. [63])

Conventional polychromatic x-ray sources can be efficiently used with the phase-stepping configuration, as the position of the interference fringes arising behind the source grating is independent of the wavelength over a wide x-ray energy range [64]. On the contrary, the Moiré configuration allows the use of a moderate polychromaticity, as a wide bandwidth of energies decreases the visibility of the Moiré fringes and worsens the image quality [66].

References

1. Röntgen WC (1949) About a new kind of rays, original text [Internet]. Springer, Berlin [cited 2018 May 8]. Available from: www.springer.com/de/book/9783662132470
2. The Nobel Prize in Physiology or Medicine (1979) [Internet]. [Cited 2018 May 8]. Available from: https://www.nobelprize.org/nobel_prizes/medicine/laureates/1979/index.html
3. X-Ray Tomography in Material Science | Tomography | Interferometry [Internet]. Scribd. [Cited 2018 May 8]. Available from: https://www.scribd.com/document/301859575/X-Ray-Tomography-in-Material-Science
4. Atsushi M, Jun F (1995) Phase-contrast radiographs of nonstained rat cerebellar specimen. Med Phys 22(4):375–379
5. Momose A (2005) Recent advances in X-ray phase imaging. Jpn J Appl Phys Part 1 Regular Pap Short Notes Rev Pap 44(9 A):6355–6367
6. Bravin A, Coan P, Suortti P (2013) X-ray phase-contrast imaging: from pre-clinical applications towards clinics. Phys Med Biol 58(1):R1–R35
7. Wilkins SW, Nesterets YI, Gureyev TE, Mayo SC, Pogany A, Stevenson AW (2014) On the evolution and relative merits of hard X-ray phase-contrast imaging methods. Philos Trans R Soc A Math Phys Eng Sci 372(2010):20130021
8. Krenkel M, Markus A, Bartels M, Dullin C, Alves F, Salditt T (2015) Phase-contrast zoom tomography reveals precise locations of macrophages in mouse lungs. Sci Rep 5:9973
9. Auweter SD, Herzen J, Willner M, Grandl S, Scherer K, Bamberg F et al (2014) X-ray phase-contrast imaging of the breast – advances towards clinical implementation. Br J Radiol 87(1034):20130606
10. Diemoz PC, Bravin A, Coan P (2012) Theoretical comparison of three X-ray phase-contrast imaging techniques: propagation-based imaging, analyzer-based imaging and grating interferometry. Opt Express 20(3):2789–2805
11. Alessio Adam M, MacDonald Lawrence R (2013) Quantitative material characterization from multi-energy photon counting CT. Med Phys 40(3):031108
12. Paul RJ, Zainon R, Agnes SNJ, Paul GS, Butler Anthony P, Butler Philip H et al (2012) Toward quantifying the composition of soft tissues by spectral CT with Medipix3. Med Phys 39(11):6847–6857
13. Wang X, Meier D, Mikkelsen S, Maehlum GE, Wagenaar DJ, Tsui BMW et al (2011) MicroCT with energy-resolved photon-counting detectors. Phys Med Biol 56(9):2791–2816
14. Paulus MJ, Gleason SS, Kennel SJ, Hunsicker PR, Johnson DK (2000) High resolution X-ray computed tomography: an emerging tool for small animal cancer research. Neoplasia 2(1):62–70
15. Goertzen AL, Nagarkar V, Street RA, Paulus MJ, Boone JM, Cherry SR (2004) A comparison of x-ray detectors for mouse CT imaging. Phys Med Biol 49(23):5251
16. Lee TH (2003) The design of CMOS radio-frequency integrated circuits. Cambridge University Press, Cambridge. 826 p
17. Kalender WA, Kyriakou Y (2007) Flat-detector computed tomography (FD-CT). Eur Radiol 17(11):2767–2779

18. Salvo L, Cloetens P, Maire E, Zabler S, Blandin JJ, Buffière JY et al (2003) X-ray micro-tomography an attractive characterisation technique in materials science. Nucl Instrum Methods Phys Res Sect B Beam Interact Mater Atoms 200:273–286
19. Kastner J, Plank B, Heinzl C (2015) Advanced X-ray computed tomography methods: high resolution CT, quantitative CT, 4 DCT and phase contrast CT.:13
20. Kastner J, Harrer B, Requena G, Brunke O (2010) A comparative study of high resolution cone beam X-ray tomography and synchrotron tomography applied to Fe- and Al-alloys. NDT & E Int 43(7):599–605
21. Kastner J, Heinzl C (2015) X-ray computed tomography for non-destructive testing and materials characterization. In: Integrated imaging and vision techniques for industrial inspection [Internet]. Springer, London. [Cited 2018 May 8]. pp 227–250. (Advances in Computer Vision and Pattern Recognition). Available from: https://link.springer.com/chapter/10.1007/978-1-4471-6741-9_8
22. Jacobson B (1953) Dichromatic absorption radiography. Dichromography. Acta Radiol os-39(6):437–452
23. Thomlinson W, Elleaume H, Porra L, Suortti P (2018) K-edge subtraction synchrotron X-ray imaging in bio-medical research. Phys Med 49:58–76
24. Mokso R, Schwyn DA, Walker SM, Doube M, Wicklein M, Müller T et al (2015) Four-dimensional in vivo X-ray microscopy with projection-guided gating. Sci Rep 5:8727
25. Physics Department, TUM | MuCLS [Internet]. [Cited 2018 May 7]. Available from: https://www.ph.tum.de/latest/news/MuCLS/?language%EF%BB%BF=%EF%BB%BFen
26. Favier P, Amoudry L, Cassou K, Dupraz K, Martens A, Monard H, et al (2017) The compact x-ray source ThomX. In: Advances in laboratory-based X-ray sources, optics, and applications VI [Internet]. International Society for Optics and Photonics. [Cited 2018 May 8]. p 1038708. Available from: https://www.spiedigitallibrary.org/conference-proceedings-of-spie/10387/1038708/The-compact-x-ray-source-ThomX/10.1117/12.2280921.short
27. Reda S (2016) …A new star is born… [Internet]. INFN-LNF. [Cited 2018 May 7]. Available from: http://w3.lnf.infn.it/a-new-star-is-born/?lang=en
28. Compact X-ray Sources | MIT Nuclear Reactor Laboratory [Internet]. [Cited 2018 May 7]. Available from: https://nrl.mit.edu/research/compact-x-ray
29. Handbook of X-ray imaging: physics and technology. [Internet] (2018) CRC Press. [Cited 2018 May 7]. Available from: https://www.crcpress.com/Handbook-of-X-ray-Imaging-Physics-and-Technology/Russo/p/book/9781498741521
30. Swinehart DF. The Beer-Lambert law. p 3
31. Computed tomography principles, design, artifacts, and recent advances, 2nd edn. [Internet]. Wiley.com. [Cited 2018 May 7]. Available from: https://www.wiley.com/en-us/Computed+Tomography+Principles%2C+Design%2C+Artifacts%2C+and+Recent+Advances%2C+2nd+Edition-p-9780470563533
32. Suplee C (2009) X-ray mass attenuation coefficients. [Internet]. NIST. [Cited 2018 May 8]. Available from: https://www.nist.gov/pml/x-ray-mass-attenuation-coefficients
33. Raven C, Snigirev A, Snigireva I, Spanne P, Souvorov A, Kohn V (1996) Phase-contrast microtomography with coherent high-energy synchrotron x rays. Appl Phys Lett 69(13):1826–1828
34. Fitzgerald R (2007) Phase-sensitive X-ray imaging. Physics Today 53(7):23
35. Suortti P, Thomlinson W (2003) Medical applications of synchrotron radiation. Phys Med Biol 48(13):R1–R35
36. Lewis RA (2004) Medical phase contrast x-ray imaging: current status and future prospects. Phys Med Biol 49(16):3573–3583
37. Zhou S-A, Brahme A (2008) Development of phase-contrast X-ray imaging techniques and potential medical applications. Phys Med 24(3):129–148
38. Olivo A (2010) Recent patents in X-ray phase contrast imaging. Recent Patents Biomed Eng 3(2):95–106
39. Nugent KA (2010) Coherent methods in the X-ray sciences. Adv Phys 59(1):1–99
40. Paganin D (2013. 424 p) Coherent X-ray optics, Oxford Series on Synchrotron Radiation. Oxford University Press, Oxford

41. Snigirev A, Snigireva I, Kohn V, Kuznetsov S, Schelokov I (1995) On the possibilities of x-ray phase contrast microimaging by coherent high-energy synchrotron radiation. Rev Sci Instrum 66(12):5486–5492
42. Cloetens P, Barrett R, Baruchel J, Guigay J-P, Schlenker M (1996) Phase objects in synchrotron radiation hard x-ray imaging. J Phys D Appl Phys 29(1):133–146
43. [Born-Wolf, 1999] Principles of optics, 7th edn. [Internet]. Scribd. [Cited 2017 Nov 27]. Available from: https://www.scribd.com/doc/23494793/Born-Wolf-1999-Principles-of-Optics-7th-Ed
44. Mayo S, Miller P, Wilkins S, Davis T, Gao D, Gureyev T et al (2002) Phase-contrast X-ray projection microscopy for materials characterisation. Mater Forum 26:15–19
45. Gureyev TE (2003) Composite techniques for phase retrieval in the Fresnel region. Opt Commun 220(1):49–58
46. Gureyev TE, Roberts A, Nugent KA (1995) Partially coherent fields, the transport-of-intensity equation, and phase uniqueness. J Opt Soc Am A JOSAA 12(9):1942–1946
47. Bronnikov AV (1999) Reconstruction formulas in phase-contrast tomography. Opt Commun 171(4):239–244
48. Paganin D, Mayo SC, Gureyev TE, Miller PR, Wilkins SW (2002) Simultaneous phase and amplitude extraction from a single defocused image of a homogeneous object. J Microsc 206(Pt 1):33–40
49. Gureyev TE, Davis TJ, Pogany A, Mayo SC, Wilkins SW (2004) Optical phase retrieval by use of first Born- and Rytov-type approximations. Appl Opt AO 43(12):2418–2430
50. Beltran MA, Paganin DM, Uesugi K, Kitchen MJ (2010) 2D and 3D X-ray phase retrieval of multi-material objects using a single defocus distance. Opt Express OE 18(7):6423–6436
51. Mohammadi S, Larsson E, Alves F, Dal Monego S, Biffi S, Garrovo C et al (2014) Quantitative evaluation of a single-distance phase-retrieval method applied on in-line phase-contrast images of a mouse lung. J Synchrotron Radiat 21(4):784–789
52. Chapman D, Thomlinson W, Johnston RE, Washburn D, Pisano E, Gmur N et al (1997) Diffraction enhanced x-ray imaging. Phys Med Biol 42:2015
53. Chapman D, Thomlinson W, Arfelli F, Gmür N, Zhong Z, Menk R et al (1996) Mammography imaging studies using a Laue crystal analyzer. Rev Sci Instrum 67(9):3360–3360
54. Kitchen MJ, Paganin DM, Uesugi K, Allison BJ, Lewis RA, Hooper SB et al (2011) Phase contrast image segmentation using a Laue analyser crystal. Phys Med Biol 56(3):515
55. Rigon L (2014) 2.08 – x-ray imaging with coherent sources. In: Brahme A (ed) Comprehensive biomedical physics [Internet]. Elsevier, Oxford, pp 193–220 [cited 2017 Nov 27]. Available from: https://www.sciencedirect.com/science/article/pii/B9780444536327002094
56. Olivo A, Ignatyev K, Munro PRT, Speller RD (2011) A coded-aperture based method allowing non-interferometric phase contrast imaging with incoherent X-ray sources. Nucl Instrum Methods Phys Res Sect A Accel Spectrometers Detectors Assoc Equip 648(Supplement 1):S28–S31
57. Olivo A, Diemoz PC, Bravin A (2012) Amplification of the phase contrast signal at very high x-ray energies. Opt Lett OL 37(5):915–917
58. Olivo A, Gkoumas S, Endrizzi M, Hagen CK, Szafraniec MB, Diemoz PC et al (2013) Low-dose phase contrast mammography with conventional x-ray sources. Med Phys 40(9):090701
59. Olivo A, Speller R (2007) A coded-aperture technique allowing x-ray phase contrast imaging with conventional sources. Appl Phys Lett 91(7):074106
60. Olivo A, Speller R (2007) Modelling of a novel x-ray phase contrast imaging technique based on coded apertures. Phys Med Biol 52(22):6555
61. Krejci F, Jakubek J, Kroupa M (2010) Hard x-ray phase contrast imaging using single absorption grating and hybrid semiconductor pixel detector. Rev Sci Instrum 81(11):113702
62. Momose A (2003) Phase-sensitive imaging and phase tomography using X-ray interferometers. Opt Express OE 11(19):2303–2314
63. David C, Bruder J, Rohbeck T, Grünzweig C, Kottler C, Diaz A et al (2007) Fabrication of diffraction gratings for hard X-ray phase contrast imaging. Microelectron Eng 84(5–8):1172–1177

64. Weitkamp T, Diaz A, David C, Pfeiffer F, Stampanoni M, Cloetens P et al (2005) X-ray phase imaging with a grating interferometer. Opt Express OE 13(16):6296–6304
65. Momose A, Yashiro W, Maikusa H, Takeda Y (2009) High-speed X-ray phase imaging and X-ray phase tomography with Talbot interferometer and white synchrotron radiation. Opt Express OE 17(15):12540–12545
66. Momose A, Yashiro W, Takeda Y, Suzuki Y, Hattori T (2006) Phase tomography by X-ray Talbot interferometry for biological imaging. Jpn J Appl Phys 45(6R):5254

Chapter 3
Role of Benchtop Microtomographic Systems in Tissue Engineering

Rossella Bedini, Deborah Meleo, and Raffaella Pecci

Abstract Microtomographic system for laboratory (microCT) is a miniaturized form of the traditional computerized tomography. It allows for three-dimensional (3D) investigations of small radiopaque objects, with a high resolution of few micrometers, in a noninvasive and nondestructive way. Compared with the conventional electron microscopy techniques that produce only bidimensional images, the microCT is used to obtain a three-dimensional analysis of a sample with no need to cut and no need of particular surface treatments at all. Therefore, the microCT may satisfy the ideal requirements of 3D microscopy.

In this chapter, through a clinical research work of bone tissue regenerative medicine, we want to highlight the peculiar characteristics of this laboratory instrumentation for 3D imaging.

Three different bone substitute biomaterials were implanted in the human bone in an in vivo clinical study. Subsequently, human bone samples grafted with the aforementioned biomaterials were studied by microCT and histology analysis.

Then, 2D histological and 3D microCT images of these samples have been obtained, together with morphometric analysis performed on the microCT data. Although the microCT analysis shows better results for investigating bone substitute biomaterials implanted in human bone tissue, the histological analysis is still to be complementarily coupled for the observation of soft tissues and blood vessels.

Therefore, the main objective of this research work was to provide surgeons with the most suitable bone substitute to be used as scaffolds in specific clinical applications.

In tissue engineering, the benchtop microCT can then contribute to the design of a 3D biocompatible scaffold for the in vitro growth of autologous cells and, more generally, for wound repair and tissue regeneration.

R. Bedini (✉) · R. Pecci
National Centre of Innovative Technologies in Public Health,
Italian National Institute of Health, Rome, Italy
e-mail: rossella.bedini@iss.it; raffaella.pecci@iss.it

D. Meleo
Freelancer, Rome, Italy

A. Giuliani, A. Cedola (eds.), *Advanced High-Resolution Tomography in Regenerative Medicine*, Fundamental Biomedical Technologies,
https://doi.org/10.1007/978-3-030-00368-5_3

1 Introduction

In biomedical research, nowadays, with the developing of new electronic techniques and the evolution of dedicated software, it is possible through algorithms to virtually reconstruct an object by means of data acquired by different diagnostic techniques (i.e., X-rays, ultrasounds, etc.).

This is the main feature of the three-dimensional (3D) X-ray microtomography (microCT), a technology reproducing 3D images of the inner/outer structure of a sample that, in turn, does not need to be treated or cut before the investigation, providing a more reliable result due to the non-alteration of the sample itself.

In fact, other techniques, such as electron microscopy and histology analysis, usually require sample treatment before observation; this may influence its conditions, providing poorly reliable results. Furthermore, in order to observe the internal structure of the samples, it is sometimes necessary to cut them, which can lead to predictable damaging consequences.

The microCT, on the other hand, allows original sample preservation by running of various tests on the same object and, if necessary, by observation of the differences between its initial and final condition. This procedure is impossible to achieve with traditional microscopy methods, because it would be necessary to construct different sets of samples, one for electron microscopy observations and another for histological analysis.

Moreover, it has been demonstrated that the microCT can provide qualitative and quantitative information on 3D morphology and microarchitecture of a sample, sometimes in a more effective way than the abovementioned traditional methods.

The microCT is, in fact, similar to conventional computed tomography (CT), but, while CT shows images at a maximum spatial resolution of about 0.5 mm, microCT can go down to some hundreds of nanometers.

For these reasons, the microCT is used in many studies in order to analyze the details of the original structure of different biomaterials and devices, focusing on dimensions, shape, internal density gradients, and total porosity and studying the distribution and dimension of pores or gaps and their possible interconnections.

However, despite its numerous applications and capabilities, the use of benchtop microCT has not reached its full potential. Most likely, this is due to the fact that researchers in biological sciences are often unfamiliar with the technique and its process, including sample preparation, the scanning process, and the 3D reconstruction.

Here, we provide the evidence, approaching step-by-step the analysis protocol, that the use of the microCT is a valid imaging method, also compared to traditional ones. More specifically, the final goal is to support the role of benchtop microCT technique in the biomedical field of tissue engineering and regenerative medicine.

2 Bone Tissue Engineering: A Clinical Study Step-By-Step

Since one of the most important issues in bone tissue regeneration strategy is the use of scaffolds, an important step to design and optimize this kind of implantable devices is to define their morphometric and architectural characteristics through a powerful investigative technique like the benchtop microCT [1–15].

Indeed, an ideal bone substitute biomaterial should have the following main features: high porosity, large surface area for cell adhesion, and pores large enough to achieve the penetration of newly formed vascular structures [6, 14–24].

Here, we describe the microCT imaging and morphometric characterization of human bone samples grafted with different bone substitute biomaterials within a clinical in vivo study.

Three different cancellous hydroxyapatite biomaterials, commonly used as bone substitute, were selected according to the following list:

- BS1, bovine hydroxyapatite, (Bio-Oss, Geistlich Biomaterials, Italy);
- BS2, dehydrated and deantigenated equine bone (Bio-Gen, Biotek Srl, Milano, Italy);
- BS3, synthetic bioceramic hydroxyapatite, (ENGIpore, Fin-Ceramica S.p.A, Faenza, Italy).

BS1 is derived from the mineral portion of bovine bone and is used by dental and oral surgeons in order to generate new bone. This material is used in implantology, in periodontology (for diseases affecting the tissue supporting the teeth) and for large bone defects in oral and maxillofacial surgery. It supports the body's natural healing processes because it closely mimics the human bone tissue.

BS2 is a biomaterial of equine origin that also acts as osteoconductive material to be used in bone regeneration surgery. As it is enzyme deantigenized, it is fully remodeled and replaced by patient endogenous tissue. The time required for a complete replacement depends on the anatomical variables (i.e., the ratio between vital bone surface and graft site volume) and on other individual factors that vary from patient to patient.

BS3 is an innovative synthetic porous bioceramic hydroxyapatite with a trabecular structure similar to natural bone. It is a ready available bone graft, manufactured with highly controlled specifications and free of disease transmission risk. Different shapes have been designed to provide surgeons with a full range of products to meet the specific bone grafting needs. Its particular structure with highly porosity defines its resistance to compression forces, mimicking natural cancellous bone. Once grafted in situ, the material rapidly absorbs all bioactive proteins, growth factors, and bone precursor cells contained in the physiological fluids. This is the starting point of the process leading to an effective bone regeneration.

The clinical in vivo study has been performed on three patients, aged 18–30 and in good health conditions, who needed surgical bilateral extraction of totally impacted lower third molars.

An informed consent has been discussed and signed by patients, in accordance with the Declaration of Helsinki. The clinical in vivo study was approved by the Ethics Committee of the Sapienza University of Rome (Policlinico Hospital Umberto I of Rome, Rif.2134/28.04.2011).

Orthopantomography and intraoral pre-surgery examination confirmed the presence of total inclusion of the lower third molar.

In each patient the post-extraction site of one side was sutured and healed by means of clot formation (control site – Ctr), while the other (test site – Test) was grafted with chips of one of the bone substitute biomaterials selected for this clinical study.

Each biomaterial has been compacted inside the post-extraction socket, protected on the surface by the application of a collagen sponge (Condress, ABIOGEN PHARMA SpA, Pisa, Italy), and the flaps were then closed and sutured into their original position.

Sixteen weeks after grafting, after raising a small flap, samples from grafted (Test) and non-grafted (Ctr) sites were extracted with a steel surgical trephine drill of 3 mm internal diameter (DRILL-300, FMD S.r.l. Medical Devices, Rome, Italy).

Test- and Ctr-samples were obtained in the shape of carrots of bone with a height of about 5 mm. They were immediately placed in formalin to be processed through microCT.

The benchtop microCT system used in the present investigation is the Skyscan 1072 (Bruker MicroCT, Kontich, Belgium). This system include a microfocus tube generating a cone beam of X-rays, a rotating specimen stub to place the sample onto and an electronic detecting system which acquires the images.

The X-ray source was a 10 W microfocus tube (tungsten), which can operate at currents up to 98 μA and voltages of 100 kV. The sample can rotate around a vertical axis with an angular step normally that was fixed to 0.45° to complete the acquisition on 180° in a total time of about 2 h.

Resolution can be chosen ranging from 5 to 20 μm, depending on the sample transversal dimensions. In this case, for all Test- and Ctr-samples, a magnification (cross-section pixel size) of 95X (corresponding to 3.1 μm) was used to allow comparison (qualitative and quantitative) between samples.

This system was equipped with a 1 mm-thick aluminum plate, placed in front of the scintillator, used as beam-hardening filter [3, 7–9, 14, 15].

After the microCT acquisition phase, the cross-section axial slices were reconstructed using the dedicated software *Cone_rec* (ver. 2.23, Bruker MicroCT, Kontich, Belgium), which is based on the cone beam algorithm [25]. The projection images, acquired in TIFF format, were reconstructed in slice images in the BMP format. Then, these slices were evaluated with the *CTAnalyser* software (ver. 1.11, Bruker MicroCT, Kontich, Belgium) in order to obtain the 3D structure imaging and the quantification of the morphometric parameters.

The quantitative analysis requires, with the CTAnalyser software, the binarization of the set of slices. The process of binarization requires the choice of a threshold value in order to transform the images in new ones composed only of black pixels

(bone) and white pixels (non-bone). After binarization, the CTAnalyser software allows to calculate the morphometric parameters and to create 3D virtual reconstructions of the internal structure of the analyzed samples.

An internal *region of interest* (ROI) was selected for each sample and histomorphometric parameters for the corresponding *volume of interest* (VOI) were calculated. Primary morphometric indices (volume density – BV/TV and bone surface density – BS/BV) [1–18] and secondary indices (trabecular thickness – Tb.Th and trabecular separation – Tb.Sp.) were obtained [11, 14, 16, 18] for the quantification of bone architecture.

By means of the *3D Creator* software (v. 2.5, Bruker MicroCT, Kontich, Belgium), it was possible to investigate the inner 3D structure of the samples. This software includes several functions for 3D image treatment, achieving by complex algorithms an improved imaging of the observed ultrastructures [13, 16, 18]. In particular, the range of values corresponding to the gray-scale image varies according to the X-ray absorption coefficient of the different structures/tissues, in turn linearly dependent, as discussed in the previous chapter, on their mass density. Thus, X-rays were more attenuated by high-density materials, which appeared in light gray, than by low-density ones, depicted in dark gray in the reconstructed volumes.

After microCT analysis, the bone samples were immersed again in sterile physiological solution for about 10 min for rehydration, and then in 10% formalin, to store them for histological investigations.

For histological analysis, each bone sample was embedded in paraffin, and 7 mm sections were prepared and stained with hematoxylin and eosin and treated according to traditional techniques (no-decalcified samples; hematoxylin and eosin staining; 100X magnification).

2.1 Results and Discussion

3D reconstructions of the inner structure have been obtained for each Ctr- and Test-samples by means of the software *3D Creator*. Morphometric parameters were also extracted using the *CTAnalyser* software. The results are reported in Table 3.1.

Table. 3.1 MicroCT-derived morphometric data, expressed as *mean (standard deviation)*

	BS1		BS2		BS3	
Parameter	Test	Ctr	Test	Ctr	Test	Ctr
BV/TV (%)	19.80 (0.05)	28.17 (0.13)	15.07 (0.05)	31.69 (0.13)	23.35 (0.02)	39.25 (0.12)
BS/BV (mm^{-1})	95.59 (0.05)	90.22 (0.05)	52.25 (0.03)	28.30 (0.03)	84.13 (0.03)	81.06 (0.03)
Porosity (%)	80.20 (0.03)	72.20 (0.05)	84.93 (0.03)	68.31 (0.03)	76.65 (0.03)	60.75 (0.03)
Tb.Th. (mm)	0.08 (0.01)	0.06 (0.01)	0.12 (0.02)	0.08 (0.01)	0.07 (0.01)	0.06 (0.01)
Tb.Sp. (mm)	0.37 (0.03)	0.22 (0.02)	0.70 (0.03)	0.28 (0.02)	0.17 (0.03)	0.09 (0.01)

The Test-samples showed, for each biomaterial group, BV/TV ratios lower and BS/BV ratios higher than the Ctr-samples. Porosity percentages were significantly higher in Test-samples than Ctr-samples. Slight mismatches (not significant) were obtained comparing the mean Tb.Th., while Test-samples showed higher Tb.Sp. values than the respective Ctr-samples.

These data suggest that, after the same grafting time (16 weeks), samples grafted with a biomaterial (Test-samples) showed a minor formation of bone than samples healed with blood clot (Ctr-samples). This is independent on the bone substitute biomaterial origin (bovine, equine, or synthetic) and is possibly explained by the healing delay introduced by the scaffold that, on the other hand, guarantees better mechanical stability and resistance during the time necessary for a complete healing.

The full 3D reconstruction, in longitudinal (left) and transversal (right) view, of the same sample is shown in Figs. 3.1, 3.2, and 3.3 for the BS1, BS2, and BS3 samples, respectively. In each figure, different colors were selected to discriminate structures with different mass density: white to indicate the less radiopaque bone portion, pink for the areas that reached a first stage of calcification, and fuchsia for the areas that showed a highest level of mineralization.

By comparison of the 3D color maps, it is possible to observe that Test-samples showed more areas with high levels of mineralization than Ctr-samples.

This is in agreement with the histological results (data not shown) that evidenced an interesting quantity of newly formed bone in Ctr-samples. The newly formed bone in Test-samples seems to be lower than in Ctr-samples. Moreover, in

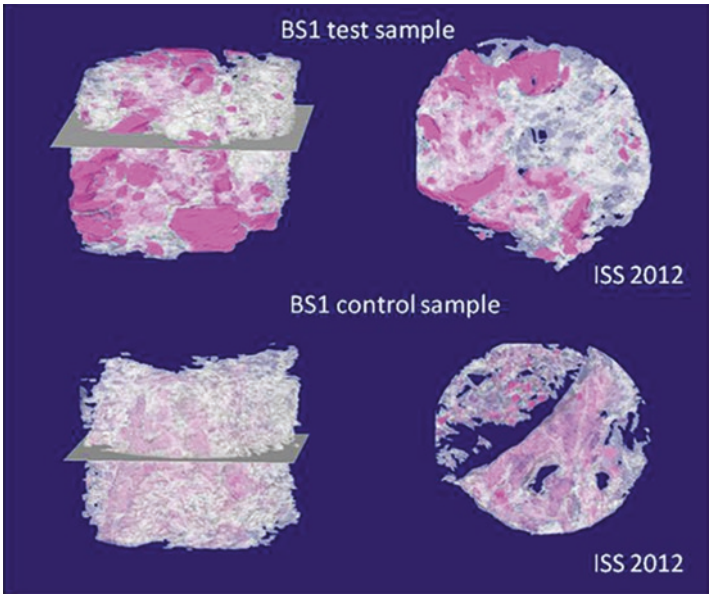

Fig. 3.1 Bovine-derived hydroxyapatite – BS1. 3D reconstruction, in longitudinal (left) and transversal (right) view, of Test (top)- and Ctr (bottom)-samples

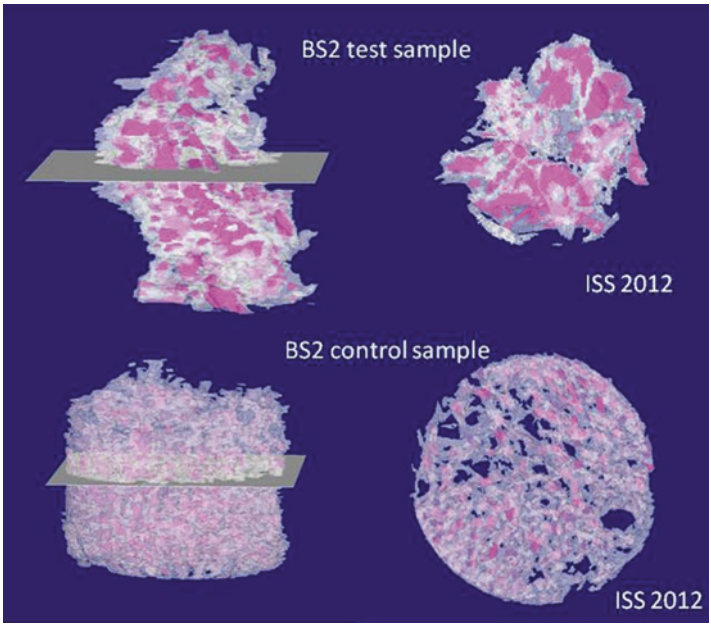

Fig. 3.2 Dehydrated and deantigenated equine bone – BS2. 3D reconstruction, in longitudinal (left) and transversal (right) view, of Test (top)- and Ctr (bottom)-samples

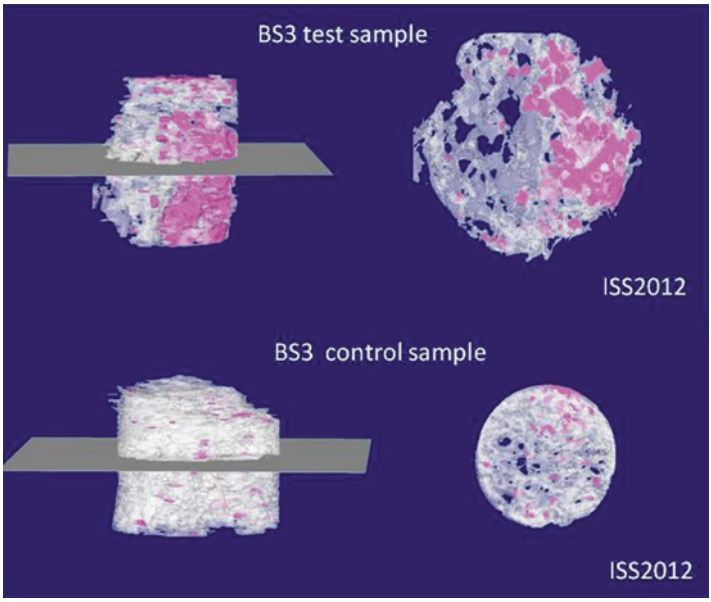

Fig. 3.3 Synthetic bioceramic hydroxyapatite – BS3. 3D reconstruction, in longitudinal (left) and transversal (right) view, of Test (top)- and Ctr (bottom)-samples

Test-samples it was observed also a relevant amount of fibrous connective tissue together scaffold residues.

In conclusion, after the same healing time (16 weeks), samples healed with blood clot (Ctr-samples) showed a greater formation of bone tissue than samples healed with a biomaterial (Test-samples), with widespread areas of mineralization.

This evidence suggests that, regardless of the its chemical and morphometric nature, the presence of the biomaterial delays the formation of new bone. This result, already known in the literature, thanks to several studies conducted in vitro [27, 28] and on animal models [29], is shown in this study on humans with the fundamental support of the benchtop microCT.

Furthermore, it is interesting to note that the microCT can also accurately identify the residues of the biomaterial particles in the grafted bone tissue, especially in the case of the use of very radiopaque bone substitutes, such as the biomaterials used in the clinical study described above.

3 Conclusions

The microCT is a 3D imaging technique that was shown, in the experience described in the previous paragraph and in several other cases, to be suitable to study the histomorphometric characteristics of a biologic tissue in a nondestructive and noninvasive way. It allows the analysis of a sample by means of a stack of 2D slices obtained at different sample depths, by means of a software dedicated to the 3D reconstruction [16, 17].

Using this technique, we have shown in the previous paragraph, step-by-step, a clinical study aiming to find the most suitable bone substitute biomaterial for a specific dental issue.

This clinical study was shown as an example of benchtop microCT technology application in biomedical engineering and surgical treatments [6, 7, 26, 29–33].

It has to be stressed that tissue engineering is increasingly oriented toward production of 3D biocompatible matrices, allowing the ex vivo cultivation of stem/progenitor cells.

Moreover, nowadays, several studies are focused on developing scaffolds doped with tissue-inductive factors to increase the graft performance [1–4, 8, 16, 24, 26, 27, 29]. Indeed, even if the homologous grafts continue to be the gold standard in regenerative medicine, the use of heterologous grafts is expected to reduce the infection risks in patients.

In this direction, the benchtop microCT could be a powerful tool in selecting the best scaffold structure for each tissue engineering application, giving fundamental contribution for the morphometric characterization of the grafted site, also with the final goal of supporting the industrial manufacturing of the aforementioned biomaterials.

Acknowledgments The authors acknowledge and thank Prof. G. Soda of Sapienza, University of Rome, Experimental Medicine Dept., for having supported the microCT observation with histological analysis.

References

1. Chiapasco M, Romeo E (2002) La riabilitazione implantoprotesica nei casi complessi. UTET, Milan
2. Mastrogiacomo M, Muraglia A, Komlev V, Peyrin F, Rustichelli F, Crovace A, Cancedda R (2005) Tissue engineering of bone: search for a better scaffold. Orthod Craniofac Res 8(4):277–284
3. Perilli E, Baruffaldi F, Visentin M, Bordini B, Traina F, Cappello A, Viceconti M (2007) MicroCT examination of human bone specimens: effects of polymethylmethacrylate embedding on structural parameters. J Microsc 225(Pt 2):192–200
4. Gielkens PF, Schortinghuis J, de Jong JR, Raghoebar GM, Stegenga B, Bos RR (2008) Vivosorb, Bio-Gide, and Gore-Tex as barrier membranes in rat mandibular defects: an evaluation by microradiography and micro-CT. Clin Oral Implants Res 19(5):516–521
5. Haıat G, Padilla F, Peyrin F, Laugier P (2007) Variation of ultrasonic parameters with microstructure and material properties of trabecular bone: a 3D model simulation. J Bone Miner Res 22(5):665–674
6. Jones JR, Poologasundarampillai G, Atwood RC, Bernard D, Lee PD (2007) Non-destructive quantitative 3D analysis for the optimisation of tissue scaffolds. Biomaterials 28(7):1404–1413
7. Kachelrieb M (2008) Micro-CT. Handb Exp Pharmacol 185(1):23–52 (Review)
8. Kamburoglu K, Barenboim SF, Ariturk T, Kaffe I (2008) Quantitative measurements obtained by micro-computed tomography and confocal laser scanning microscopy. Dentomaxillofac Radiol 37(7):385–391
9. Kerckhofs G, Schrooten J, Van Cleynenbreugel T, Lomov SV, Wevers M (2008) Validation of x-ray microfocus computed tomography as an imaging tool for porous structures. Rev Sci Instrum 79(1):013711
10. Lin-Gibson S, Cooper JA, Landis FA, Cicerone MT (2007) Systematic investigation of porogen size and content on scaffold morphometric parameters and properties. Biomacromolecules 8(5):1511–1518 (Epub 2007 Mar 24)
11. Maréchal M, Luyten F, Nijs J, Postnov A, Schepers E, van Steenberghe D (2005) Histomorphometry and micro-computed tomography of bone augmentation under a titanium membrane. Clin Oral Implants Res 16(6):708–714
12. Papadimitropoulos A, Mastrogiacomo M, Peyrin F, Molinari E, Komlev VS, Rustichelli F, Cancedda R (2007) Kinetics of in vivo bone deposition by bone marrow stromal cells within a resorbable porous calcium phosphate scaffold: an X-ray computed microtomography study. Biotechnol Bioeng 98(1):271–281
13. Parkinson IH, Badiei A, Fazzalari NL (2008) Variation in segmentation of bone from micro-CT imaging: implications for quantitative morphometric analysis. Australas Phys Eng Sci Med 31(2):160–164
14. Stauber M, Muller R (2008) Micro-computed tomography: a method for the non-destructive evaluation of the three-dimensional structure of biological specimens. Methods Mol Biol 455:273–292
15. van Lenthe HG, Hagenmuller H, Bohner M, Hollister SJ, Meinel L, Muller R (2007) Non destructive micro-computed tomography for biological imaging and quantification of scaffold-bone interaction in vivo. Biomaterials 28:2479–2490
16. Waarsing JH, Day JS, Weinans H (2004) An improved segmentation method for in vivo microCT imaging. J Bone Miner Res 19(10):1640–1650 (Epub 2004 Jul 12)
17. Cowan CM, Aghaloo T, Chou YF, Walder B, Zhang X, Soo C, Ting K, Wu B (2007) MicroCT evaluation of three-dimensional mineralization in response to BMP-2 doses in vitro and in critical sized rat calvarial defects. Tissue Eng 3(3):501–512
18. Burchardt H (1983) The biology of bone graft repair. Clin Orthop Relat Res 174:28–42
19. Komlev VS, Peyrin F, Mastrogiacomo M, Cedola A, Papadimitropoulos A, Rustichelli F, Cancedda R (2006) Kinetics of in vivo bone deposition by bone marrow stromal cells into porous calcium phosphate scaffolds: an X-ray computed microtomography study. Tissue Eng 12(12):3449–3458

20. Hofmann S, Hilbe M, Fajardo RJ, Hagenmüller H, Nuss K, Arras M, Müller R, von Rechenberg B, Kaplan DL, Merkle HP, Meinel L (2013) Remodeling of tissue-engineered bone structures in vivo. Eur J Pharm Biopharm Sep 85(1):119–129
21. Feldkamp LA, Davis LC, Kress JW (1984) Practical cone-beam algorithm. J Opt Soc Am A 1:612–619
22. Urist MR (1965) Bone: formation by autoinduction. Science 150:893–899
23. Guldberg RE, Duvall CL, Peister A, Oest ME, Lin AS, Palmer AW, Levenston ME (2008) 3D imaging of tissue integration with porous biomaterials. Biomaterials 29(28):3757–3761 (Epub2008 Jul 16).
24. Chu TM, Warden SJ, Turner CH, Stewart RL (2007) Segmental bone regeneration using a load bearing biodegradable carrier of bone morphogenetic protein-2. Biomaterials 28(3):459–467
25. Feldkamp LA, Goldstein SA, Parfitt AM, Jesion G, Kleerekoper M (1989) The direct examination of three-dimensional bone architecture in vitro by computed tomography. J Bone Miner Res 4(1):3–11
26. Manescu A, Giuliani A, Mazzoni S, Mohammadi S, Tromba G, Diomede F, Zini N, Piattelli A, Trubiani O (2016) Osteogenic potential of dual-blocks cultured with periodontal ligament stem cells: in-vitro and synchrotron microtomography study. J Periodontal Res 51(1):112–124
27. Mazzoni S, Mohammadi S, Tromba G, Diomede F, Piattelli A, Trubiani O, Giuliani A (2017) Role of cortico-cancellous heterologous bone in human periodontal ligament stem cell xeno-free culture studied by synchrotron radiation phase-contrast microtomography. Int J Mol Sci 18(2):364
28. Manescu A, Oancea R, Todea C, Rusu LC, Mazzoni S, Negrutiu ML, Sinescu C, Giuliani A. (2016) On long term effects of low power laser therapy on bone repair: a demonstrative study by synchrotron radiation-based phase-contrast microtomography. Int J Radiol Imaging Technol. 2:010, 2(1)
29. Freed LE, Guilak F, Guo XE, Grey ML, Tranquillo R, Holmes JW, Radisic M, Sefton MV, Kaplan D, Vunjak-Novakovic G (2006) Advanced tools for tissue engineering: scaffolds, bioreactors and signaling. Tissue Eng 12:3285–3305
30. Bedini R, Meleo D, Pecci R, Pacifici L (2009) The use of microtomography in bone tissue and biomaterial three-dimensional analysis. Ann Ist Super Sanita 45(2):178–184
31. Meleo D, Bedini R, Pecci R, Mangione F, Pacifici L (2012) Microtomographic and morphometric characterization of a bioceramic bone substitute in dental implantology. Ann Ist Super Sanita 48(1):59–64
32. Bedini R (2012) A new technology in biomedical engineering analysis: the 3Dimensional microtomography. Preface Ann Ist Super Sanita 48(1):7–9
33. Barbetta A, Bedini R, Pecci R, Dentini M (2012) Role of x-ray microtomography in tissue engineering. Ann Ist Super Sanita 48(1):10–18

Chapter 4
Synchrotron Radiation X-Ray Phase-Contrast Microtomography: What Opportunities More for Regenerative Medicine?

Ginevra Begani Provinciali, Nicola Pieroni, and Inna Bukreeva

Abstract In regenerative medicine 3D X-ray imaging is indispensable for characterizing damaged tissue, for measuring the efficacy of the treatment, and for monitoring adverse reactions.

Among the X-ray imaging techniques, high-resolution X-Ray Phase Contrast Tomography (XRPCT) allows simultaneous three-dimensional visualization of both dense (e.g. bone) and soft objects (e.g. soft tissues) on scale of length ranging from millimeters to hundreds of nanometers, without the use of contrast agent, sectioning or destructive preparation of the sample. XRPCT overcomes the problem of incomplete spatial coverage of conventional 2D imaging (histology or electron microscopy), while reaches a higher resolution and contrast than standard 3D computer tomographic imaging.

It can be used as a prominent tool in regenerative medicine field, where a crucial step after artificial tissue implantation is to monitor its correct functioning and connection with the surrounding tissue.

1 Introduction

Regenerative medicine is the application of treatments developed to replace tissues damaged by injury or disease. This technique creates living, functional tissues to repair or replace tissue function lost due to age, disease, damage, or congenital defects. These treatments involve the use of biochemical techniques to induce tissue regeneration directly at the site of damage or the use of transplantation techniques

G. Begani Provinciali (✉) · N. Pieroni · I. Bukreeva
Institute of Nanotechnology, CNR, Rome, Italy
e-mail: inna.bukreeva@cnr.it

A. Giuliani, A. Cedola (eds.), *Advanced High-Resolution Tomography in Regenerative Medicine*, Fundamental Biomedical Technologies,
https://doi.org/10.1007/978-3-030-00368-5_4

using stem cells or differentiated cells, either alone or as part of a bio artificial tissue [1, 2].

Although regenerative medicine is a large field and includes several topics as stem cell therapy (SCT) and synthetic organs, here we will focus primarily on tissue engineering (TE). In particular one of the most promising research areas within tissue engineering is bone substitute biomaterials (BSB) [3, 4]: complex and unique tissues, such as the bone, cartilage, and tendons that act as the internal support of the body. Since the long-term function of three-dimensional (3D) bone substitute biomaterials (BSB) is strongly dependent on adequate vascularization after grafting, it is crucial to develop imaging methods capable of providing detailed three-dimensional information on tissue structure.

However, full comprehension of the bone vascularization pathways is still hindered by limitations in the use of imaging techniques to monitor these processes. Nowadays, new advanced imaging modes are available. Upputuri et al. [5] recently classified the imaging approaches into three groups: nonoptical techniques (X-ray, magnetic resonance, ultrasound, and positron emission imaging), optical techniques (optical coherence, fluorescence, multiphoton, and laser speckle imaging), and hybrid techniques (photoacoustic imaging). In this regard, high-resolution microtomography (microCT) is able to provide much higher-resolution (∼1 μm) imaging, than ultrasound (∼30 μm) and MRI (∼100 μm), allowing the 3D visualization and quantification of microvasculature and bone tissues.

Within X-rays techniques, we will focus on X-ray phase-contrast tomography (XRPC) that overcomes limitations of conventional absorption-based X-ray imaging using alternative X-ray contrast mechanisms. In fact, conventional 2D imaging (histology, electron microscopy, etc.) produces an incomplete spatial coverage of the sample that leads to possible data misinterpretation, while standard absorption 3D computed tomographic imaging reaches insufficient resolution and contrast in soft tissue visualization. XRPCT enables the 3D imaging of biomaterial and soft tissue structures, as well as vascularization, with spatial resolution ranging from microns to tens of nanometers, without the use of contrast agents and without destructive sample preparation.

XRPCT is very promising in regenerative medicine field, due to the large penetration depth, excellent spatial and contrast resolution and simultaneous visualization of calcified and soft tissue. In particular, XRPC allows monitoring the regeneration of damaged tissues being able to discriminate between newly formed bone and connective tissue.

2 Physical Principles of X-Ray Phase-Contrast Imaging

The potentiality of X-ray phase-contrast tomography for different biomedical applications has been proved in numerous studies [6–15]. Since X-ray phase-contrast imaging (XPCI) exploits wave coherence, requirements on the X-ray source are necessary, despite some specific cases discussed in Chap. 15. In particular, highly

coherent X-ray radiation from bright synchrotron sources offers great opportunities for many cutting-edge medical applications including regenerative medicine, in particular for bone regenerative engineering [2, 16–18]. Synchrotron-based XPCI is particularly attractive for biomedicine applications since it provides high-resolution, high signal-to-noise ratio in the image at shorter acquisition time with respect to other conventional imaging techniques. To introduce the principle of XPCI, let us start from the optical properties of an object, which can be described by

$$n = 1 - \delta + i\beta, \tag{4.1}$$

where δ is the refractive index decrement responsible for the phase shift of X-ray wave propagating through the object and β is the extinction coefficient related with X-ray attenuation in the sample. The coefficient β is proportional to the linear attenuation coefficient μ:

$$\mu = \frac{4\pi}{\lambda}\beta, \tag{4.2}$$

where λ is the wavelength of X-ray radiation.

In particular, conventional radiography is based on absorption contrast, i.e., the imaginary part of the refraction index, and it is obtained from X-rays attenuation through the object. Phase-contrast technique exploits the real part of the complex refractive index.

Radiography and tomography for biomedical application require high X-ray penetration depth in the (thick) sample, and typically hard X-rays with energies $E \sim 10$–100 keV are used for image formation. Due to the weak interaction of hard

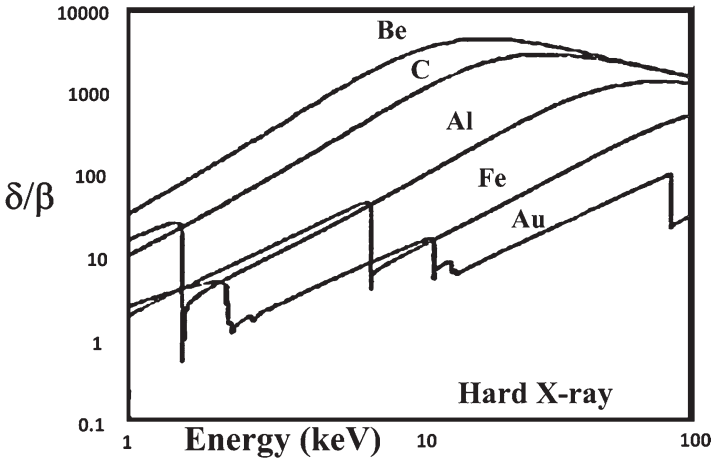

Fig. 4.1 The phase-attenuation ratio δ/β as a function of energy. The ratio δ/β for carbon (the main constituent of biological tissue) increases by a factor of 1000 in the hard X-rays region. The term δ is related to the phase variation and the term β is responsible for X-ray attenuation

X-rays with matter the refractive index is close to one ($|n-1| << 1$). The values of both indexes δ and β are several orders of magnitude below unity ($|n-1| \approx 10^{-6}$). At energies far from absorption edges δ and β can be approximated as

$$\delta \sim \frac{\rho_a Z}{E^2} \tag{4.3}$$

$$\beta \sim \frac{\rho_a Z^4}{E^4}, \tag{4.4}$$

where ρ_a is the atomic number density of a material, Z is the atomic number, and E is the X-ray photons energy [19, 20].Taking into account Eq. (4.3) and Eq. (4.4), the phase-attenuation ratio δ/β is given by

$$\frac{\delta}{\beta} \sim \frac{E^2}{Z^3} \tag{4.5}$$

In the Hard X-ray Region, the ratio of δ/β is in the range of 10^2–10^3 (Fig. 4.1) for different elements, typically contained in biological tissues. Therefore, at short wavelengths phase contrast is a predominant effect over absorption contrast. In particular, the advantage of phase contrast becomes more evident for low-absorbing materials (low atomic number Z) such as soft tissue in biological samples.

According to Eqs. (4.3 and 4.4), phase contrast decreases slower than absorption contrast as X-ray energy increases; thus, the absorbed dose and therefore potential damage of tissues can be decreased by using higher X-ray energies [11].

3 Image Formation

Layout of image formation in a XPCI setup includes (1) X-ray radiation source and X-ray optics for shaping the beam, (2) rotation and translation stages for the sample (the sample is shifted and rotated during tomographic scan), (3) X-ray phase-contrast optical equipment (except for free-space propagation mode), and (4) detector [21].

3.1 X-Ray Source

X-ray beam from synchrotron radiation facility is used to investigate object internal structure. In synchrotron facilities, the incident beam is formed by incoherent superposition of waves emitted by synchrotron electrons bunch in the storage ring [22]. The transverse coherence of the generated X-ray radiation increases with X-rays propagation distance. Due to the small bunch size and long source-sample distance,

synchrotron X-ray source has a high degree of transverse coherence. The emitted radiation has a specific energy spectrum; crystal monochromator allows to select a very narrow band of the spectrum ($\Delta E/E \approx 10^{-4}$) providing high degree of longitudinal coherence when it is required.

3.2 Object and Transmission Function

X-ray synchrotron radiation, approximated by a plane wave, illuminates the sample and passes through the object producing a distortion of the wave front. At the contact plane, the object is characterized by a transmission function (TF) defined as the E/E_0, the input/output complex amplitudes ratio. We assume a linear relationship between the incident wavefield (input signal E_0) and the transmitted wavefield (output signal E) [23]:

$$E = \mathrm{TF}\, E_0 \tag{4.6}$$

The transmission function TF depends on both the sample structure and the incident field. A variety of different processes participating in interaction between X-rays and sample significantly complicates the rigorous definition of TF, and some approximations are usually applied to simplify the description of X-ray transmission through the object. Commonly used approximations in phase-contrast imaging are *weak object* approximation, *slowly varying phase* approximation, and *homogeneous object* approximation [24, 25]. Due to the weak interaction of X-rays with matter, it is assumed that each element of the object interacts only with the incident wave and not with the refracted one, and diffraction phenomena within the scattering volume are neglected. In this case the object can be considered thin enough to treat the properties of a three-dimensional sample with a two-dimensional transmission function. In the so-called projection or thin object approximation TF is considered as a simple object projection into the contact plane [26]:

$$\mathrm{TF}(x,y) = A(x,y)\, e^{i\phi(x,y)} \tag{4.7}$$

The amplitude modulation A and the phase shift ϕ are given as the integrals along the optic axis:

$$A(x,y) = e^{-\frac{1}{2}\int_{\text{object}} \mu(x,y,z)\mathrm{d}z} = e^{-\mu_z} \tag{4.8}$$

$$\phi(x,y) = -\frac{2\pi}{\lambda} \int_{\text{object}} \delta(x,y,z)\,\mathrm{d}z, \tag{4.9}$$

where μ_z is the projection of the attenuation coefficient μ on the contact plane (x, y, z=0) divided by two.

Week object approximation is valid when both attenuation and phase shift in the object are small:

$$\mu_z \ll 1,\ \phi \ll 1 \tag{4.10}$$

For weakly interacting X-rays, the exponential function in Eq. (4.7) can be rewritten as a first term of the Taylor series expansion [27], leading to the next simple expression for TF:

$$\mathrm{TF} \approx 1 - \mu_z + i\phi \tag{4.11}$$

The assumption of slowly varying phase is given by the following expression:

$$\left|\phi\left(\boldsymbol{r} + \lambda z \boldsymbol{f}_m\right) - \phi\left(\boldsymbol{r}\right)\right| \ll 1, \tag{4.12}$$

where $\boldsymbol{r}=(x,y)$ and $\boldsymbol{f}=(p, q)$ are space coordinates at the contact plane and the transverse Fourier space coordinates reciprocal to $\boldsymbol{r}$, respectively; $|\boldsymbol{f}_m=(p_m, q_m)|$ is the highest frequency of the object to be included in the computation, λ is wavelength. This approximation partially relaxes the strict weak object condition of Eq. (4.10). In particular Eq. (4.12) is used to solve the propagation problem for a pure phase object with zero absorption ($\mu = 0$) and for a homogenous object with non-negligible absorption ($\mu \neq 0$) and $\delta \propto \beta$ [28].

Homogeneous object approximation supposes that the object contains only one material and air. In the object with non-negligible absorption ($\mu \neq 0$), the coefficients β and δ are proportional $\delta \propto \beta$ [28]. In this case the projected thickness of the object can be found from a single-distance image. More details on this issue will be discussed in Sect. 4.1.2.

4 Phase-Contrast Imaging Techniques

Since detector can only measure the intensity, the phase shift induced by the object in the X-ray beam cannot be directly revealed and therefore the phase information is lost. In order to detect the phase, different experimental approaches have been developed in order to transform the phase modulation into intensity modulation, directly detectable by the detector.

In the past years, a variety of techniques have been developed to detect phase contrast and to enhance the visibility of small and/or low contrast details in the sample image.

Phase-contrast imaging techniques can be grouped into four main categories: in-line phase-contrast imaging (ILPC), diffraction-enhanced imaging (DEI), analyzer-based imaging (ABI), and grating-based differential phase-contrast imaging (GBI) (see Fig. 4.2) [29–33].

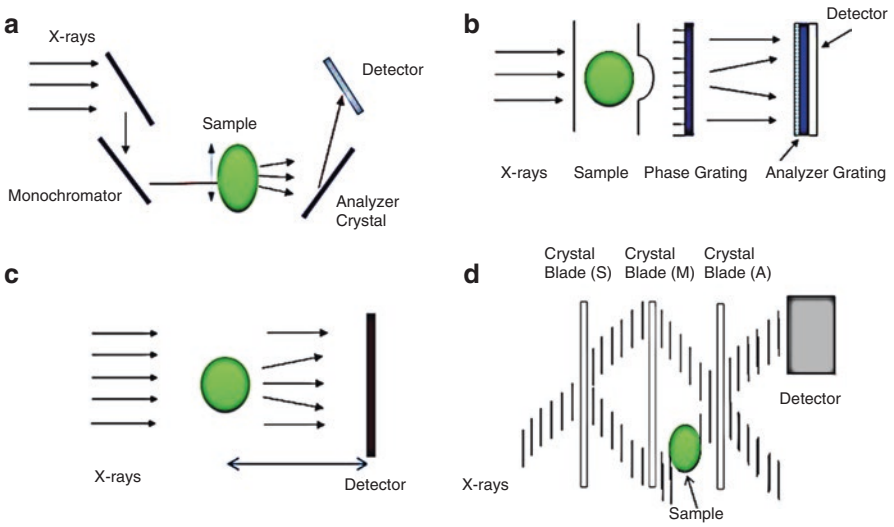

Fig. 4.2 Schematic representation of phase-contrast imaging experimental setup (**a**) analyzer-based imaging (ABI), (**b**) grating-based differential phase-contrast imaging (GBI), (**c**) in-line phase-contrast imaging (ILPC), (**d**) diffraction-enhanced imaging (DEI)

4.1 Free Space Propagation Imaging

X-ray in-line phase-contrast imaging (ILPC) or free space propagation imaging (XPI) exploits the propagation of a coherent X-ray beam to generate image contrast [33]. The experimental setup of X-ray in-line phase-contrast imaging (XPCI) is similar to conventional radiography but with larger sample-detector distance. The layout of this method includes the in-line arrangement of an X-ray source, the sample, and an X-ray detector and does not need any additional optical element. The simple experimental setup and high stability make this technique very attractive for biomedical applications. Because of its simplicity and relatively low sensitivity to misalignments, it is suitable to be combined with tomography techniques.

4.1.1 Direct Problem: Contrast Formation

Some conventional approaches for analytical and numerical solutions of direct and inverse imaging problems in single-distance XPCI are here described.The *direct problem* of wave propagation aims to define the wavefield at a distance $z = D$, given the value of the field at the contact plane ($z = 0$). The sample induces both amplitude and phase variations in the transmitted field, but at the contact plane, only absorption contrast can be detected. The propagation of the wave in free space transforms phase modulation into detectable intensity variations. The image obtained is called

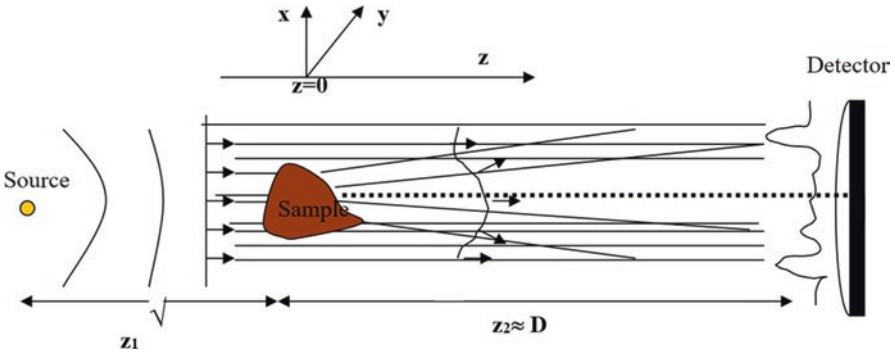

Fig. 4.3 Schematic representation of the setup used to record the defocused image. The incoming plane wave is deformed by the modulation of the index of refraction inside the sample. The interference pattern is acquired by the detector

defocused image: in fact, it is recorded out of focus due to the propagation from the sample to the detector. The defocusing distance D expresses the amount of defocusing in the image [34]:

$$D = \frac{z_1 z_2}{z_1 + z_2}, \tag{4.13}$$

where z_1 and z_2 are defined in Fig. 4.3.
In synchrotron facilities the distance z_1 of the sample from the source is much larger than the propagation distance z_2, and thus the defocusing distance Eq. (4.13) simply corresponds to the sample-to-detector distance:

$$D \approx z_2, \tag{4.14}$$

The analytical description of wavefield evolution in space is based on the solution of Maxwell's equations or electromagnetic wave equation in vacuum [35]. Due to the weak interaction of X-rays with matter, the typical refraction angles for hard X-rays interacting with the sample are very small. Therefore, X-ray photons of highly coherent low divergent synchrotron beam, even after scattering in the sample, are still propagating at small angle with respect to the z optical axis. This allows most theoretical analysis to adopt the paraxial approximation, which assumes $k_x^2 + k_y^2 \ll k^2$, where k is the wave vector number. Wave equation in the paraxial approximation for monochromatic wave has the name of homogeneous paraxial Helmholtz equation, and it is written as

$$i\frac{\partial}{dz}E(x,y,z) - \frac{1}{2k}\nabla_\perp^2 E(x,y,z) = 0 \tag{4.15}$$

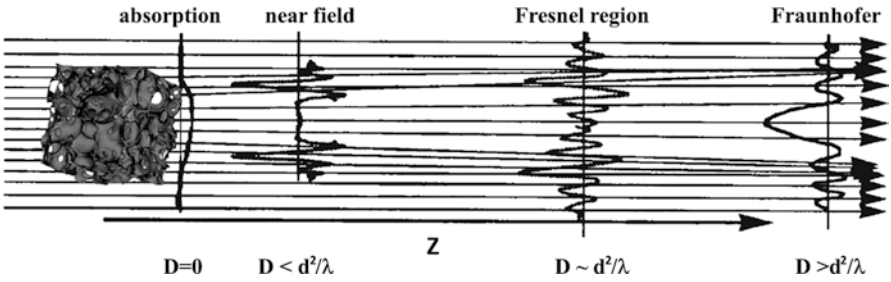

Fig. 4.4 Schematic representation of the diffraction regions according to the distance D from the object

The solution of Eq. (4.15) is given by the Fresnel–Kirchhoff integral (Fresnel diffraction integral):

$$E(x,y,z=D)=-\frac{ik\exp(ikD)}{2\pi D}\iint_{-\infty}^{\infty}E(x',y',z=0)\exp\left\{\frac{ik}{2D}\left[(x-x')^2+(y-y')^2\right]\right\}dx'dy' \quad (4.16)$$

Diffraction integral reveals that evolution of the diffraction pattern during the wave propagation is characterized with the length scale:

$$D_{\mathrm{F}}=\frac{d^2}{\lambda}, \quad (4.17)$$

where d is the typical transverse linear size of the object or of the object details we want to detect.

Four different diffraction regimes can be distinguished by the parameter D_F. The diffraction pattern varies with the distance D as it is shown in Fig. 4.4.

1. At the contact plane $z = D = 0$ only absorbing features of the object are detectable. This is the case of classic radiography and absorption-based tomography.
2. At near-field region $\lambda D \ll d^2$ locally object irregularities at any internal boundaries and interfaces of the sample (where the phase variation in high) form interference fringes highlighting the edges. Morphological details of the sample with low spatial frequencies are not yet subject to diffraction. In this region the diffraction regime is called edge enhancement because edges produce high contrast. The image of the sample at the detector still resembles the direct image of the real object (weak defocusing).
3. In the intermediate diffraction region (propagation distance $D \approx D_{\mathrm{F}}$), the recorded image shows more evident diffraction characteristics. The image of the real sample is almost lost, and distinct interference patterns are produced. This is so-called holographic regime that can be divided into near and far holographic regime for distances $D \approx D_{\mathrm{F}}$ and $D > D_{\mathrm{F}}$, respectively.
4. Far field is reached increasing propagation distance up to $D \gg D_{\mathrm{F}}$. In far field region the interference fringes cannot be associated with a specific sample

edge, and the resemblance between the original and the detected image is completely lost. The intensity recorded by the detector is defined by Fraunhofer diffraction law.

The wave propagation problem can be solved in different way. The straightforward approach is the direct analytical or/and numerical solution of Eq. (4.15) or to diffraction integral Eq. (4.16). Fourier transform method (FTM) or angular spectrum method is another conventional method that has been extensively applied in the field of XPCI [27]. Another way to specify the attenuation and the phase shift in wavefield propagation relies on the transport-of-intensity equation as the solution of Eq. (4.15) [36].

We will discuss two methods commonly used in XPI: FTM-based approach and transport-of-intensity equation-based approach.

The simplest solution of Helmholtz equation Eq. (4.15) is the plane wave solution. Because of the linearity of Maxwell's equations in vacuum, the general solution of the wave equation in free space can be obtained by linear superposition of elementary plane waves solution. This is the basis for so-called Fourier transform method (FTM) or angular spectrum method for the Helmholtz equation. The Fresnel–Kirchhoff integral Eq. (4.16) in FTM approach is given by equation [27]:

$$E\left(x,y,z=D\right)=\exp\left(ikD\right)F^{-1}\left[P\cdot F\left[E_0\left(x,y,z=0\right)\right]\right], \tag{4.18}$$

where F and F^{-1} are the 2D direct and inverse Fourier transforms, respectively, the term $P=\exp\left[-\dfrac{iD\left(k_x^2+k_y^2\right)}{2k}\right]$ is the Fresnel propagator. Since the propagation distance D is included in the numerator of the phase factor, the Fresnel FTM

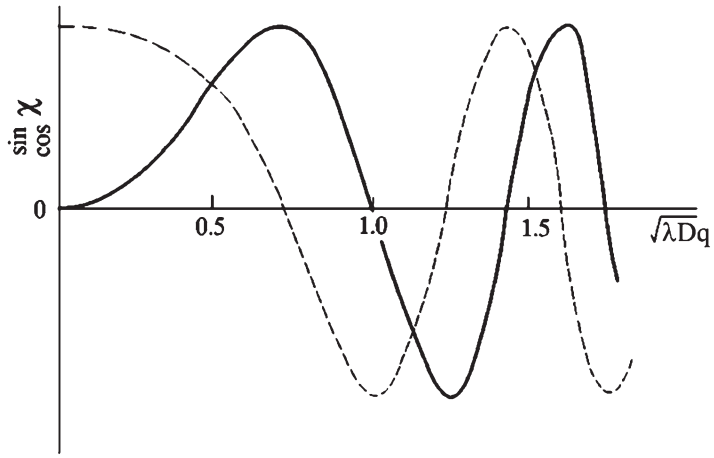

Fig. 4.5 Real (dashed) and imaginary (solid line) parts of the Fresnel transfer function as a function of the reduced spatial frequency

approach is more suitable for small distances $D \lesssim D_F$. For weakly interacting objects (see Eq. (4.11)) the wavefield at a distance D can be written as [27]:

$$E \approx F^{-1}\left[\Delta(f) - F\left[\mu_z\right]\cos\chi - F\left[\phi\right]\sin\chi\right] \tag{4.19}$$

where $\Delta(f)$ is the delta function. According to Eq. (4.19), the amplitude and phase of the transmitted wavefield are filtered by the terms $\sin\chi$ and $\cos\chi$ in Fourier space. The functions $\sin\chi$ and $\cos\chi$ are called the phase-contrast transmission function and the amplitude contrast transmission function, respectively, (PCTF and ACTF). The terms $\sin\chi$ and $\cos\chi$ are shown in Fig. 4.5 as a functions of radial spatial frequency $u = (\chi/\pi)^{1/2} = (\lambda D)^{1/2}q$. Equation (4.19) and Fig. 4.5 show that phase and absorption contrast are mixed in the image. They have different evolution with wavefield propagation. In the contact plane when $u = 0$, phase contrast in the image is near to zero, but the absorption image has maximum contrast.

As it follows from Eq. (4.19) for a pure phase object ($m_z = 0$) in the near-field diffraction regime $u = (\lambda D)^{1/2}/d \ll 1$, the wavefield intensity at the detector plane is proportional to the second derivative of the phase function [37]:

$$I\left(x,y,z=D\right) \approx 1 - \frac{D}{k}\nabla_\perp^2\phi\left(x,y\right) \tag{4.20}$$

Therefore high spatial frequencies originated from the edges of the object vastly contribute to the interference pattern formation. The object interference fringes delineate the edges and any internal boundary of the sample.

Increasing spatial frequency, phase, and amplitude CTFs oscillate. The functions reach the near holographic regime at $u \approx (\lambda D_F)^{1/2} q$ and the far holographic regime at $u > (\lambda D_F)^{1/2} q$, respectively. As CTF oscillate around zero value, only spatial frequencies far from the zeros of the oscillating functions contribute to the image formation.

Transport-of-intensity equation (TIE) [28, 38, 39] is another common XPCI approach to describe image contrast formation in free space propagation. Writing the homogeneous paraxial Helmholtz equation (Eq. 4.15) in terms of intensity and phase of the propagating wave and taking the imaginary part of the final equation, one receives the transport-of-intensity equation:

$$\nabla_\perp\left(I\left(r_\perp,z\right)\nabla_\perp\phi\left(r_\perp,z\right)\right) = -\frac{2\pi}{\lambda}\partial_z I\left(r_\perp,z\right) \tag{4.21}$$

TIE describes the intensity evolution of a paraxial monochromatic scalar electromagnetic wave on propagation, and it relates the phase and the derivative of the image intensity along propagation direction. TIE has a unique solution and does not require the phase unwrapping.

In general case TIE-based approaches in XPCI assume a short propagation distance $D < D_F$ to linearize the propagation model and finally to solve the inverse

phase problem. In case of pure phase object, TIE gives the same expression for the intensity as in FTM approach (see Eq. (4.20)).

Non-negligible absorption in the sample requires addition assumptions for the sample properties such as sample material homogeneity or the weak absorption approximation. This problem will be discussed in the next Sect. 4.1.2.

4.1.2 Inverse Problem: Phase Retrieval

Propagation-based imaging combined with computed tomography enables access to a sample's three-dimensional (3D) micro- or nanostructure. However, phase contrast, as it is discussed in Sect. 4.1.1, is not directly related with amplitude and phase of the object transmission function. The phase retrieval step must be performed to recover the sample refraction index.

The phase retrieval problem consists in the object phase estimation from intensity measurements accounting a priori information about the object. Different approaches are used to solve the phase retrieval problem [25, 40]. At distances close to the near-field regime, Fresnel and TIE-based methods are commonly used for phase shift reconstruction of objects at micro and sub micro-level resolution [28, 38–39, 41–43]. In Fresnel diffraction regime, holotomography method for multiple images at different propagation distances proved to be efficient for nanoscale resolution imaging [44]. In far-field zone the iterative image Fourier transform-based reconstruction algorithms are broadly applied to create high-resolution diffraction images [45].

Phase-contrast imaging in near field is particularly attractive for different medical application due to its ability to provide with acceptable resolution the richness of information about internal features and fine detail in the sample without a strong restriction on the sample dimension, as it takes place for other imaging techniques. In addition to that, this imaging technique has relative simple experimental setup and enables non-iterative implementation of single-image phase retrieval procedure.

In general, image at the detector contains both absorption and phase-contrast contribution; therefore information about δ and β is mixed. The different evolution of absorption and phase contrast in space allows to untangle these two parameters, but, generally, at least two intensity measurements at different distances or different energies are required [11]. The high radiation dose is a critical issue for biological samples since tomographic scan requires several successive sample acquisitions, while it is rotating. Multiple distance/energy measurements of the object additionally increase X-ray exposure time, and therefore the dose delivered to the sample. Thus, single-distance/energy image acquisition for each tomographic projection is preferable.

Phase reconstruction algorithms for single-distance image acquisition usually require a priori information about the object to solve the inverse problem and to ensure the unique solution for the problem.

The most common approximation about object material properties are:

1. Material has no absorption, or the absorption is constant [39].
2. Absorption and phase coefficients β and δ are proportional to each other, then a homogeneous object composed of the single material can be characterized by ratio δ/β, and the projected thickness of the sample can be found from single-distance image [28, 41–42].

Since often biological samples produce both phase and absorption contrast, the absorption contribution in the material cannot be neglected. Phase retrieval at homogeneous object approximation developed by D. Paganin [28] does not impose a strong restriction on the absorption phenomenon in the object. Moreover, it was shown that the algorithm can be applied for multi-material objects, for objects with homogeneous elemental composition, but varying density and for objects in which absorption is negligibly weak. The algorithm has been successfully applied in large number of experiments, and it gained wide recognition due to its stability with respect to noise, computational speed, and simplicity of implementation [46–50]. Paganin's algorithm derivation starts with the transport intensity equation Eq. (4.21). The method assumes that an optically thin object is composed of a single material. For plane wave illumination the intensity and phase of the wavefield at the object plane is given by the projection approximation. Application of TIE in near field allows to find the reconstructed phase map of the object from the equation:

$$\phi(x,y) = \frac{1}{2}\ln\left\{\mathcal{F}^{-1}\left(\frac{\mathcal{F}\left[\frac{I(x,y)}{I_0(x,y)}\right]}{\frac{\beta}{\delta}+\left[\frac{\lambda D}{4\pi}\right]\left(p^2+q^2\right)}\right)\right\} \tag{4.22}$$

where I/I_0 is the ratio between the measured intensity and the reference beam intensity, at distance $z = D$, F and F^{-1} are the 2D forward and inverse Fourier transforms, p and q are the Fourier coordinates, and D is the object–detector distance.

The Paganin's algorithm retrieves the phase information at the contact plane from two-dimensional phase radiograph images at the detector (called projections). Application of the phase retrieval algorithm to all radiographs taken at different illumination angles of the object during tomographic scan gives a set of projected images at the contact plane, with 2D phase information. These images are combined to provide 3D internal structure of the object with appropriate tomographic reconstruction method. The most commonly used tomographic reconstruction algorithm is Filtered Back-projection (FBP) method. Different alternative non-iterative and iterative algorithms have been proposed for tomographic reconstruction. This topic is well studied in CT, and a review on this topic can be find elsewhere [51].

5 Imaging Techniques in Regenerative Medicine

Regenerative medicine holds great promise for the treatment of a multitude of diseases for which there is no cure and that present many complications. Besides replacing what is malfunctioning, the aim of regenerative medicine is to provide the elements required for in vivo repair. It allows to devise replacements that seamlessly integrate with the living body and to stimulate and support the body's intrinsic capacities to heal itself.

Periodic monitoring of a regenerating tissue as it develops is one of the key steps as well as challenges. Clinical imaging is indispensable for characterizing damaged tissue, for measuring the efficacy of the treatment, and for monitoring adverse reactions [1]. Moreover clinical imaging is able to differentiate pathological and regenerative responses to the therapy. A growing emphasis is being placed on noninvasive in vivo imaging techniques to address concerns and limitations with traditional histological methods that are time-consuming, painful to the patients, and expensive in preclinical studies [52].

Among all the applications of regenerative engineering, we will focus on bone engineering because a deeper comprehension of bone formation process is at the basis of tissue engineering and regenerative medicine developments.

5.1 Bone Regenerative Engineering

Bone engineering aims to achieve functional recovery of damaged tissues by providing specific cell populations, alone or incorporated in biomaterial scaffolds, that enhance the body's intrinsic healing capacity [1]. The bone is a natural composite of approximately 70% hydroxyapatite together with 30% collagen fibers in a strong, three-dimensional structure.

The traditional bone engineering (BE) approach is often described as a winning combination of cells, supportive material (scaffold), and growth factors (stem cells). Stem cells are required to establish a bridge between living tissues and scaffold materials. They have the potential to differentiate into every type of cell and tissue in the body and hold promise in the treatment of cardiovascular, neural, and connective tissue diseases. Scaffolds instead provide physical and chemical support, while damaged tissue is being regenerated [52].

Among the standard clinical imaging technologies and their function within regenerative medicine, phase-contrast tomography (PCT) is the most promising 3D imaging technique in bone tissue engineering [3], providing morphological and anatomical details for in vivo imaging.

The implementation of X-ray microtomography in phase-contrast mode (XRPCT) enables the investigation of the soft connective tissues, which are invisible to the absorption contrast while are readily observed in phase contrast. Thanks to high-resolution XRPCT it is possible to obtain an exhaustive identifi-

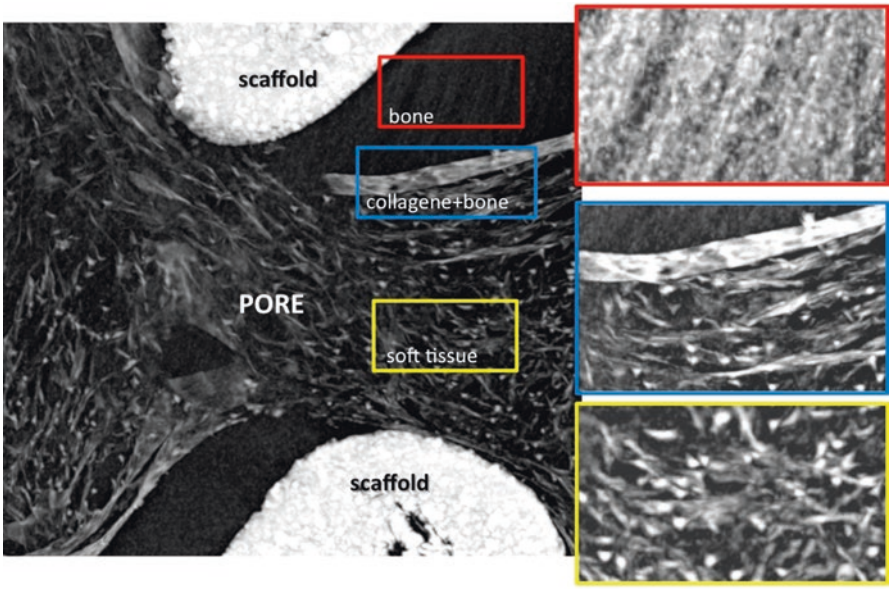

Fig. 4.6 Progressive deposition of hydroxyapatite crystals on collagen fibers matrix. The new-bone strats to form at the scaffold-pore interface and proceed toward the pore center where we can investigate the early steps of biomineralization process. The insets on the right corresponds to enlargements of the corresponding region marked with different colors in the image

cation of the different tissues participating to the bone regeneration process, in particular collagen and mineral materials. The high spatial resolution achieved by X-ray scanning techniques allows to monitor the bone formation at the first-formed mineral deposit at the organic–mineral interface within a porous scaffold. The role of collagen matrix in the organic–mineral transition is a crucial issue for this process (Fig. 4.6).

In fact the calcification process consists in the progressive deposition of hydroxyapatite crystals on collagen fibers [3]. Another XRPCT application in bone regenerative engineering is represented by the investigation of 3D distribution of both vessels and collagen matrix [4]. Thanks to the high quality of the images is possible to investigate the smallest micro-capillary structure without invasive contrast agent and without aggressive sample preparation.

6 Conclusion: Future Prospective

X-ray phase-contrast X-ray imaging (XPCI) is an innovative imaging technique that holds great promise for a wide range of nowadays advancing biomedical researches including bone regenerative engineering. When classical absorption

does not provide sufficient contrast or demonstrates limited sensitivity, it shows great potentiality. In particularly, visualization of weakly absorbing tissue of biomedical samples or/and samples with small variations in the specimen's density or composition [6].

Due to its unique ability XPCI allows to monitor the bone formation and identify the different tissues participating to the bone regeneration process, in particular collagen and mineral materials. Moreover it allows investigation of 3D distribution of both vessels and collagen matrix.

The ideal bone-graft substitute is biocompatible, biodegradable, osteoinductive and structurally similar to the bone. Within these parameters, a growing number of bone graft alternatives have been implemented. The strategic success lies on the delicate balance of native tissue properties addressed in a tissue substitute and its complete integration in vivo. In this sense, developing of advanced imaging techniques allows to monitor of bone regeneration processes in vivo is a crucial step in regenerative medicine.

References

1. Naumova AV, Modo M, Moore A, Murry CE, Frank JA (2014) Clinical imaging in regenerative medicine. Nat Biotechnol 32(8):804–818. https://doi.org/10.1038/nbt.2993
2. Oryan A, Alidadi S, Moshiri A, Maffulli N (2014) Bone regenerative medicine: classic options, novel strategies, and future directions. J Orthop Surg Res 9:18. https://doi.org/10.1186/1749-799X-9-18
3. Cedola A, Campi G, Pelliccia D, Bukreeva IN, Fratini M, Burghammer MC, Mastrogiacomo M (2014) Three dimensional visualization of engineered bone and soft tissue by combined x-ray micro-diffraction and phase contrast tomography. Phys Med Biol 59(1):189–201. https://doi.org/10.1088/0031-9155/59/1/189
4. Bukreeva I, Fratini M, Campi G, Pelliccia D, Spanò R, Tromba G, Mastrogiacomo M (2015) High-resolution x-ray techniques as new tool to investigate the 3D vascularization of engineered-bone tissue. Front Bioeng Biotechnol 3:133. https://doi.org/10.3389/fbioe.2015.00133
5. Upputuri PK, Sivasubramanian K, Mark CSK, Pramanik M (2015) Recent developments in vascular imaging techniques in tissue engineering and regenerative medicine. Biomed Res Int 2015:783983., 9 pages, 2015. https://doi.org/10.1155/2015/783983
6. Fitzgerald R (2000) Phase-sensitive x-ray imaging. Phys Today 2000(53):23
7. Lewis RA (2004) Medical phase contrast x-ray imaging: current status and future prospects. Phys Med Biol 2004(49):3573
8. Momose A (2005) Recent advances in x-ray phase imaging. Jpn J Appl Phys 44:6355
9. Betz O, Wegst U, Weide D, Heethoff M, Helfen L, Lee WK, Cloetens, P (2007) Imaging applications of synchrotron X-ray phase-contrast microtomography in biological morphology and biomaterials science. I. General aspects of the technique and its advantages in the analysis of millimetre-sized arthropod structure. J Microsc, 227:51–71. Williams I, Siu K, Runxuan G, He X, Hart S, Styles C, Lewis R (2008) Towards the clinical application of x-ray phase contrast imaging. Eur J Radiol, 68:S73–S77
10. Zhou SA, Brahme A (2008) Development of phase-contrast x-ray imaging techniques and potential medical applications. Phys Med 24:129–148
11. Bravin A, Coan P, Suortti P (2013) X-ray phase-contrast imaging: from pre-clinical applications towards clinics. Phys Med Biol 58:R1

12. Coan P, Bravin A, Tromba G (2013) Phase-contrast x-ray imaging of the breast: recent developments towards clinics. J Phys D 46:494007
13. Koehler T, Daerr H, Martens G, Kuhn N, Löscher S, van Stevendaal U, Roessl E (2015) Slit-scanning differential x-ray phase-contrast mammography: proof-of-concept experimental studies. Med Phys 42:1959–1965
14. Horn F, Hauke C, Lachner S, Ludwig V, Pelzer G, Rieger J, Schuster M, Seifert M, Wandner J, Wolf A, et al. (2016) High-energy X-ray grating-based phase-contrast radiography of human anatomy. Proc. SPIE, 9783
15. Momose A, Yashiro W, Kido K, Kiyohara J, Makifuchi C, Ito T, Nagatsuka S, Honda C, Noda D, Hattori T et al (2014) X-ray phase imaging: from synchrotron to hospital. Philos Trans Royal Soc A 372:20130023
16. Campi G, Bukreeva I, Fratini M, Mastrogiacomo M, Cedola A (2014) Imaging tissue regeneration/degeneration by combined x-ray micro-diffraction and phase contrast micro-tomography. J Tissue Eng Regen Med 8:66–67
17. Giuliani A, Mazzoni S, Mele L, Liccardo D, Tromba G, Langer M (2017) Synchrotron phase tomography: an emerging imaging method for microvessel detection in engineered bone of craniofacial districts. Front Physiol 8:769. https://doi.org/10.3389/fphys.2017.00769
18. Núñez JA, Goring A, Hesse E, Thurner PJ, Schneider P, Clarkin CE (2017) Simultaneous visualisation of calcified bone microstructure and intracortical vasculature using synchrotron x-ray phase contrast-enhanced tomography. Sci Rep 7:13289
19. Henke BL, Gullikson EM, Davis JC (1993) X-ray interactions: Photoabsorption, scattering, transmission, and reflection at e = 50–30,000 ev, z = 1–92. At Data Nucl Data Tables 54:181–342
20. Als-Nielsen, J. & McMorrow, D. (2011) Elements of Modern X-Ray Physics. Wiley, 2 edition
21. Wilkins SW, Nesterets YA, Gureyev TE, Mayo SC, Pogany A, Stevenson AW (2014) On the evolution and relative merits of hard x-ray phase-contrast imaging methods. Phil Trans R Soc A 372:20130021
22. Bilderback DH, Elleaume P, Weckert E (2005) Review of third and next generation synchrotron light sources. J Phys 38:S773–S797
23. Wu X, Liu H (2003) A general formalism for x-ray phase contrast imaging. J Xray Sci Technol 11:33–42 2003
24. Langer M, Cloetens P, Guigay JP, Peyrin F (2008) Quantitative comparison of direct phase retrieval algorithms in in-line phase tomography. Med Phys 35:4556–4566
25. Burvall A, Lundström U, Takman AC, Larsson DH, Hertz HM (2011) Phase retrieval in x-ray phase-contrast imaging suitable for tomography. Opt Express 19:10359–10376
26. Thibault P (2007) Algorithmic methods in diffraction microscopy. Cornell University, Ithaca
27. Pogany A, Gao D, Wilkins SW (1997) Contrast and resolution in imaging with a microfocus x-ray source. Rev Sci Instrum 68(7):2774–2782
28. Paganin D, Mayo SC, Gureyev TE, Wilkins PR, Wilkins SW (2002) Simultaneous phase and amplitude extraction from a single defocused image of a homogeneous object. J Microsc 206:33–40
29. Bonse U, Hart M (1965) An x-ray interferometer. Appl Phys Lett 6:155–156
30. Momose A, Takeda IY, Yoneyama A, Hirano K (1998) Phase-contrast tomographic imaging using an x-ray interferometer. J Synchrotron Radiat 5:309–314
31. Chapman D, Thomlinson W, Johnston RE, Washburn D, Pisano E, Gmür N, Zhong Z, Menk R, Arfelli F, Sayers D (1997) Diffraction enhanced x-ray imaging. Phys Med Biol 42:2015–2025
32. David C, Nöhammer B, Solak HH, Ziegler E (2002) Differential x-ray phase contrast imaging using a shearing interferometer. Appl Phys Lett 21:3287–3289
33. Snigirev A, Snigireva I, Kohn V, Kuznetsov S, Schelokov I (1995) On the possibilities of X-ray phase contrast microimaging by coherent high energy synchrotron radiation. Rev Sci Instrum 66:5486
34. Cloetens P, Pateyron-Salome M, Buffiere JY, Peix G, Baruchel J, Peyrin V, Schlenker M (1997) Observation in microstructure and damage in materials by phase sensitive radiography and tomography. J Appl Phys 81:5878–5886

35. Born M, Wolf E (1980) Principles of optics, 6th edn. Pergamon, Oxford
36. Teague MR (1983) Deterministic phase retrieval: a green's function. J Opt Soc Am 73:1434–1441
37. Cowley, J. M. (1975). Diffraction physics. Amsterdam: New York: North-Holland Pub. Co., American Elsevier
38. Groso A, Abela R, Stampanoni M (2006) Implementation of a fast method for high resolution phase contrast tomography. Opt Express 14:8103–8110
39. Bronnikov AV (1999) Reconstruction formulas for phase-contrast imaging. Opt Commun 171:239–244
40. Hehn L, Morgan K, Bidola P, Noichl W, Gradl R, Dierolf M, Noël PB, Pfeiffer F (2018) Nonlinear statistical iterative reconstruction for propagation-based phase-contrast tomography. APL Bioengineering 2:016105. https://doi.org/10.1063/1.4990387
41. Wu X, Liu H (2005) X-ray cone-beam phase tomography formulas based on phase-attenuation duality. Opt Express 13:6000–6014
42. Beltran MA, Paganin DM, Uesugi K, Kitchen MJ (2010) 2D and 3D x-ray phase retrieval of multi-material objects using a single defocus distance. Opt Express 18:6423–6436
43. Gureyev TE, Davis TJ, Pogany A, Mayo SC, Wilkins SW (2004) Optical phase retrieval by use of first born- and Rytov-type approximations. Appl Opt 43:2418–2430
44. Cloetens P, Ludwig W, Baruchel J, Van Dyck D, Van Landuyt J, Guigay JP (1999) Holotomography: quantitative phase tomography with micrometer resolution using hard synchrotron radiation x rays. Appl Phys Lett 75(19):2912–2914
45. Noh DY, Kim C, Kim Y, Song C (2016) Enhancing resolution in coherent x-ray diffraction imaging. J Phys Condens Matter 28:493001
46. Mayo SC, Davis TJ, Gureyev TE, Miller PR, Paganin D, Pogany A, Stevenson AW, Wilkins SW (2003) X-ray phase-contrast microscopy and microtomography. Opt Express 11:2289–2302
47. Paganin D, Gureyev TE, Mayo SC, Stevenson AW, Nesterets YAI, Wilkins SW (2004) X-ray omni microscopy. J Microsc 214:315–327
48. Turner D, Weber KP, Paganin D, Scholten RE (2004) Off-resonant defocus-contrast imaging of cold atoms. Opt Lett 29:232–234
49. Irvine SC, Paganin DM, Dubsky W, Lewis RA, Fouras A (2008) Phase retrieval for improved three-dimensional velocimetry of dynamic x-ray blood speckle. Appl Phys Lett 93:153901
50. Stevenson AW, Mayo SC, Hausermann D, Maksimenko A, Garrett RF, Hall CJ, Wilkins SW, Lewis RA, Myers DE (2010) First experiments on the Australian synchrotron imaging and medical beamline, including investigations of the effective source size in respect of x-ray imaging. J Synchrotron Radiat 17:75–80
51. Herman GT (1980) Image reconstruction from projections: the fundamentals of computerized tomography. Academic Press, 2 edition
52. Atala A, Allickson J (2014) Translational regenerative medicine. Academic Press, 1 edition

Chapter 5
From Projections to the 3D Analysis of the Regenerated Tissue

Francesco Brun

Abstract Computational imaging techniques such as X-ray computed tomography (CT) rely on a significant amount of computing. The acquired tomographic projections are digitally processed to reconstruct the final images of interest. This process is generically called *reconstruction*, and it includes additional steps prior to or at the end of the execution of an actual reconstruction algorithm. Most of these steps aim at improving image quality, mainly in terms of artifacts compensation and noise reduction. The reconstructed images are then digitally analyzed to derive quantitative data and to support the qualitative visual interpretation. This part involves computational approaches that fall within the generic term image *segmentation*. Pre- and post- segmentation image processing is often required to improve the final quantification and extract reliable data from a CT dataset. This chapter presents an overview of the reconstruction and segmentation fundamentals for the 3D analysis of high-resolution X-ray CT data. Better knowledge about artifacts and reconstruction issues avoid misinterpretation of the images. Similarly, more insights about the limitations of image segmentation and *quantification* help commenting the reliability of the derived numerical values. A deeper understanding of these elements is therefore beneficial to optimize the whole workflow that starts from sample preparation and leads to CT-based scientific results.

1 Introduction

Within the whole workflow that starts from the design of a CT-based experiment and leads to scientific results, several aspects need to be considered and optimized. Different steps or stages are traditionally identified, and each of these involves the choice of specific solutions as well as the fine-tuning of the related parameters.

F. Brun (✉)
Department of Engineering and Architecture, University of Trieste, Trieste, Italy

National Institute for Nuclear Physics (INFN) – Trieste Division, Trieste, Italy
e-mail: fbrun@units.it

A. Giuliani, A. Cedola (eds.), *Advanced High-Resolution Tomography in Regenerative Medicine*, Fundamental Biomedical Technologies,
https://doi.org/10.1007/978-3-030-00368-5_5

In the whole chain that goes from sample preparation to numerical quantitative results, every step gives feedback to the previous one, and, coherently, each of these steps needs to be tuned having in mind what happens next. There is therefore a strong interconnection and interrelation among the stages. Rather than optimizing independently each single step, an integrated and thorough approach to the whole problem is definitively preferable as it leads to more effective results and a more convenient use of the available resources.

Figure 5.1 reports a common workflow of an X-ray CT-based experiment with examples of the inherent choices and parameters. Common questions arise when designing the experiment, such as: How many samples are required for a robust statistical analysis? Should the acquisition protocol favor spatial resolution or contrast resolution? What amount of noise is tolerated by the segmentation approach? What is the size of a representative Volume of Interest (VOI) for the image analysis protocol? Is there a significant radiation damage that would negatively affect further analyses, such as histology? Moreover, when performing experiments at external facilities such as synchrotrons, the available machine time is also a strong constraint to consider when looking for answers to the above questions. Most of these points are interrelated, e.g., an accurate knowledge of the size of a representative VOI allows optimizing the unavoidable trade-off between small pixel size and large field of view (FOV) during projection acquisition. The need of a small pixel size (higher spatial resolution) most likely affects the detector exposure time during the acquisition with further implications for the inherent radiation damage.

A CT-based experiment typically involves a research team composed of scientists and researchers having different background and expertise. Although it might sound natural to let each member of the team solve their piece of the puzzle and produce the best results achievable, a global optimized and effective result is not granted without an integrated approach to the experiment.

This chapter focuses on the challenges required by the *reconstruction*, *segmentation*, and *quantification* stages of a CT-based experiment within tissue engineering

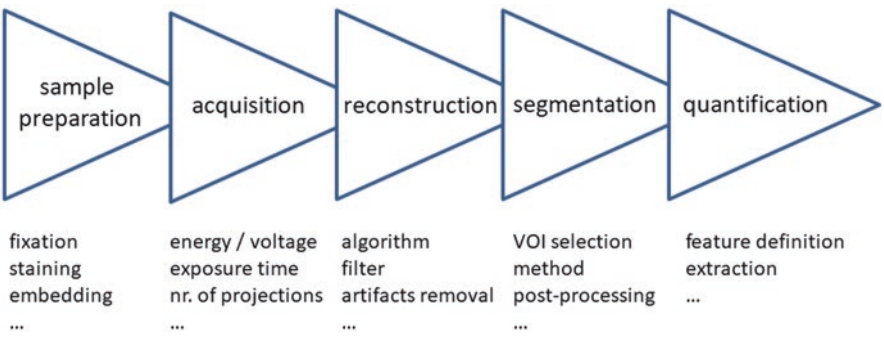

Fig. 5.1 Common workflow of an X-ray CT-based experiment with examples of some of the inherent choices and parameters for each of the involved steps

and regenerative medicine applications. Special emphasis is given to the case of very high-resolution experiments performed at synchrotron facilities where state-of-the-art imaging and image analysis protocols are investigated.

2 Reconstruction

Tomography is based on projection measurements described by equations that link the radiation source, the interaction of the radiation with matter, and the detector [1]. The reconstruction of images from these indirect measurements involves calculating maps of a characteristic parameter, such as the absorption coefficient or the refractive index (as done in phase-contrast tomography) by inverting the measurement equations. Image reconstruction is an inverse problem, in which first the direct problem, linking the measurements to the characteristic map, is formulated based on physical laws and then the characteristic map is calculated by solving the associated equations. Roughly, two main approaches are identified when trying to solve these equations, i.e., *analytical methods* and *discrete methods*.

2.1 Analytical Methods

Analytical methods rely on a description of the images and measurements by continuous functions and on a modeling of the physical laws by functional operators. They are of particular interest since the inverse operator can be expressed by an explicit inversion formula. The algorithmic implementation of these analytical methods relies simply on a discretization of this formula. The most commonly used analytical method for CT is based on the concept of Radon transform, and the filtered backprojection algorithm is the most widely adopted method for implementing a solution to the inverse problem [1]. Filtered backprojection (FBP) has proven to give a fast solution (real time in some applications) for large images even with simple hardware resources. From a practical perspective, it requires only minor decisions about the specific filtering [2] required (e.g., the so-called Ram-Lak, Shepp-Logan, Parzen) and the image interpolation (e.g., linear, bicubic) leading therefore to a "ready-to-go" effective solution for the vast majority of practical applications. An implementation of the filtered backprojection algorithm is available in popular computing environments like MATLAB(R). It is also relatively easy to replicate and include an FBP implementation in custom software tools. For these reasons, filtered backprojection is still the most widely used approach in parallel-beam CT performed at synchrotron facilities. Similarly, when considering the cone-beam geometry mainly exploited with laboratory systems based on conventional sources, the so-called FDK [3] algorithm is still the most widely used approach [4]. FDK is again a convolution-backprojection approach to solve the inverse tomographic problem.

Although speed and simplicity are definitely interesting advantages of the analytical methods, the lack of customization is however an issue when performing state-of-the-art CT experiments. When considering applications where the radiation dose is a serious concern and/or when only a few and noisy projections are acquired, the filtered backprojection approach could produce reconstructed images with inadequate quality for practical applications. In fact, analytical methods assume that projection data is available for all the angles and the data is free of noise. In many practical applications, it is either impossible or undesirable to acquire a large number of noise-free projections. Moreover, practical CT imaging involves detectors that might present miscalibrated pixels (sometimes called dead or hot pixels), and rather than correcting these pixels during the acquisition process with information coming from the single projection itself, it would be more interesting to simply exclude these pixels during the reconstruction process and let the inherent interpolation involved in the reconstruction step compensate for the exclusion of these pixels [5]. Unfortunately, the filtered backprojection approach does not offer an easy way to perform similar customizations.

2.2 Discrete Methods

Discrete methods are not based on a modeling of the tomographic problem with continuous functions, but they consider the discrete nature of digital images. These methods permit integration of prior information on the acquisition process and on the images to be reconstructed, and they allow the flexible use of diverse optimization criteria. Since an algebraic solution with iterative approaches is typically involved, these methods are also referred as *algebraic methods* or *iterative methods*. According to this approach, the acquired sinogram is represented as a singular column vector

$$\mathbf{p} = \left(p_1, \ldots, p_M \right)^T$$

and, similarly, the reconstructed image is

$$\mathbf{f} = \left(f_1, \ldots, f_N \right)^T .$$

According to the number and size of each detector column, the number of acquired projections and the desired pixel size of the reconstructed image (see Fig. 5.2), a $M \times N$ weight matrix (also called system matrix), are defined as

$$\mathbf{A} = \begin{pmatrix} a_{11} & a_{12} & \ldots & a_{1N} \\ a_{21} & . & & a_{2N} \\ \vdots & & . & \vdots \\ a_{M1} & & & a_{MN} \end{pmatrix}$$

and therefore the algebraic formulation can be modeled as the matrix product

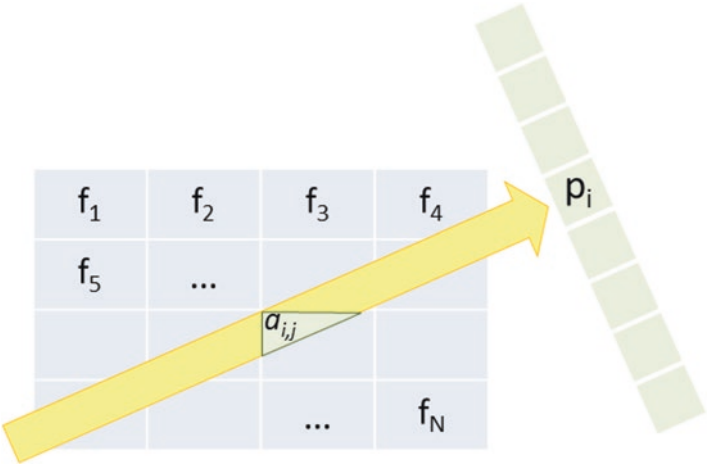

Fig. 5.2 The X-ray beam does not traverse each pixel of the image to reconstruct equally. The area of the pixel section that has actually been passed through must be included in the system of equations as a weighting

$$\mathbf{p} = \mathbf{A}\mathbf{f}$$

which means that performing a discrete tomographic reconstruction consists in finding **f** by, e.g., minimizing the ℓ_2-norm of the projection error:

$$\chi^2 = \left|\mathbf{A}\mathbf{f} - \mathbf{p}\right|^2$$

It can be easily noticed that **A** is huge even for relatively small images and of course noise affects the measurements **p**. Because of this, it is often impossible to use direct methods such as singular value decomposition to find **f**.

Instead, it is more appropriate to use methods in which the projection error is iteratively minimized. Different mathematical optimization methods can be used for this, leading to different algebraic reconstruction methods. For example, if the projection error is minimized by using gradient descent steps [6] on the projection error, the result is the simultaneous iterative reconstruction technique (SIRT). Other examples are the CGLS method where the projection error is minimized by a conjugate gradient least square method [7] and the algebraic reconstruction technique (ART) [8] where the error is minimized by the Kaczmarz method.

Iterative reconstruction methods were originally used by Hounsfield to obtain images with the first CT prototype [9]. They were rapidly abandoned when the size of the problem rapidly grew with the size of measurements and images. It simply became impractical to reconstruct images in a reasonable time with these techniques with the hardware available at the time. However, in recent years, massively parallel commodity graphics hardware (graphics processing units, GPUs) has led to a rediscovery of these methods since reasonable execution times are now feasible. Nowadays, it is safe to assume that any serious attempt at developing an advanced reconstruction algorithm for practical applications requires hardware acceleration,

often from modern GPUs. CT reconstruction packages supporting GPU operations and available with permissive or public domain licenses include OpenRTK [10], ASTRA [11], and TIGRE [12].

Despite their computational demand, algebraic approaches are interesting for their flexibility when trying to handle realistic acquisitions. For instance, it is extremely easy to exclude one or more defective pixels from the system matrix. Since algebraic methods use a model of the tomographic problem that includes only the projections that are actually acquired rather than assuming that an infinite number of projections are available, they tend to handle the problem with a limited number of acquired images better than analytical methods. Moreover, the effect of noise in the projection data can be limited in most algebraic methods by stopping the iteration process early, which is a form of implicit regularization. Algebraic approaches have proved to be useful when dealing with a reduced number of noisy projections, such as in extremely low-dose applications or ultrafast tomography.

2.3 Hybrid Approaches

It is worthy to mention that in recent years, efforts have been spent to combine the advantages of analytical methods, i.e., the computational efficiency, with the advantages of algebraic methods, i.e., a better handling of noise and a limited number of projections. Recently, a new reconstruction method called *minimum residual filtered backprojection* (MR-FBP) has been introduced [13]. MR-FBP is based on an algebraic model of the tomographic problem, resulting in a method that can reconstruct objects with limited data with higher accuracy than analytical methods. The linear system to minimize, however, is based on filtered backprojection. Therefore the system is much smaller than the ones used in algebraic methods or other approaches, leading to a computationally efficient method. Similarly, a method that approximates the algebraic SIRT by computing a special filter for the filtered backprojection called SIRT-FBP has been also proposed [14]. The resulting method can achieve a reconstruction quality similar to algebraic method using however existing computationally efficient FBP implementations.

Figure 5.3 reports a simple comparison of different reconstruction approaches when considering a test object acquired at the SYRMEP beamline of the Italian synchrotron (Elettra – Sincrotrone Trieste S.C.p.A.). The test object consists of a polyoxymethylene (CH_2OH) cylinder, 16 mm in diameter, in which six holes of 3 mm diameter have been drilled parallel to the cylinder axis. The holes were filled with water (H_2O), paraffin wax ($C_{25}H_{52}$), glycerol ($C_3H_8O_3$), glucose ($C_6H_{12}O_6$) 10 g/50 ml, and glucose 23 g/50 ml, and one of them was left empty. The object was scanned with the following experimental parameters: energy = 21 keV, sample-detector distance = 300 mm, and nominal voxel size = 9 μm. Only 180 projections were considered for reconstructing the images reported in Fig. 4.3. It can be noticed that while the most classical approach based on FBP leads to a noisy reconstructed image where some of the elements can barely be recognized, refined algorithms are

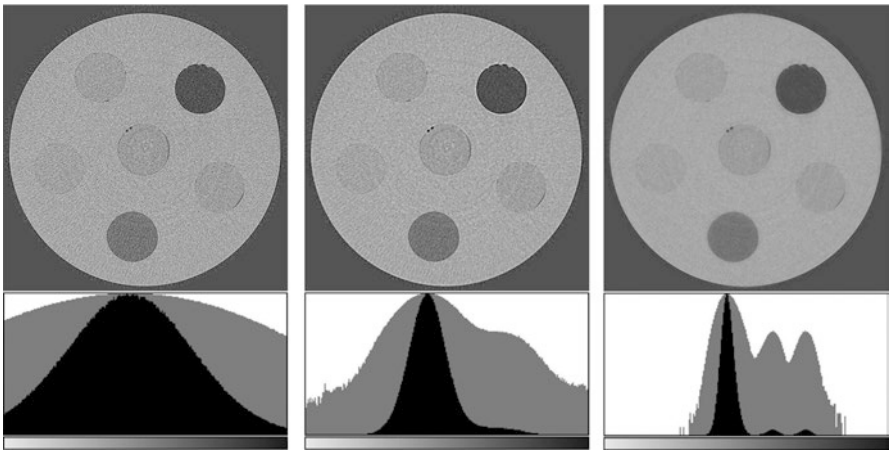

Fig. 5.3 A comparison of different reconstructions when considering a CT dataset with a reduced number of projections. From left to right: conventional analytic method (FBP); a hybrid approach (MR-FBP); algebraic method (SIRT). The corresponding gray-level histogram is reported below each image (the same gray-level window was used for all the images) [Linear scale gray-level histogram in black and logarithmic scale in gray]

able to reconstruct an image presenting a multimodal histogram where the inclusions within the test object can be more easily segmented. Several applications can greatly benefit from a reconstruction workflow where iterative algorithms can be used. CT acquisitions with a reduced number of projections can be therefore considered, thus leading to a minimization of the radiation damage, faster experiments, or, simply, more samples per experiment.

2.4 Artifacts in CT

In addition to noise, practical CT imaging is also affected by specific artifacts that might complicate the subsequent segmentation. Several artifacts can be identified and classified [15]. For instance, sample-specific artifacts are motion artifacts, photon starvation (due to strong shape irregularities of the imaged object), and metal artifacts. A physics-related artifact called beam hardening might occur with polychromatic sources. However, when imaging a regularly shaped and steady object without spurious internal metallic elements and under the assumption of monochromatic or quasi-monochromatic incident beam, the most significant and recurrent artifacts are called *ring artifacts*.

Practical CT imaging involves a step called *flat fielding* where a number of "flat" (also called open-beam or white) images are acquired and used as a reference to compensate the illumination inhomogeneities as well as camera or scintillator imperfections. To collect the flat images, the sample is removed from the field of

view, and a few images are acquired with the same source and detector settings further used to scan the object. Each projection is then normalized according to an average of these images, and this should compensate for most of the irregularities of the source/detector system. Refined flat fielding approaches have been also recently proposed to better compensate the beam fluctuations, especially for synchrotron radiation tomography where a multilayer monochromator is used [16]. Although flat fielding already reduces the effects of ring artifacts, additional image processing is commonly necessary to mitigate ring artifacts.

Ring artifacts arise from inhomogeneities in the individual pixel response of detector elements. They result from the reconstruction of stripe artifacts in the sinogram image; therefore de-striping the sinogram prior to the actual reconstruction is a classical way to face the problem. However, if a reconstructed slice is transformed into polar coordinates assuming the center of rings as the center of the Cartesian to polar conversion, the problem of ring artifacts compensation can be still brought back to a de-striping issue. Doing so, de-striping filters may be applied directly to transformed reconstructed slices. Several approaches have been proposed to both pre-reconstruction filtering and post-reconstruction filtering [17]. Interesting approaches involve also handling the ring removal issue within the reconstruction process by customizing an algebraic method [18].

Figure 5.4 shows an example of a high-resolution micro-CT slice corrupted by ring artifacts. The scanned object is an alginate/hydroxyapatite bone tissue engineering scaffold embedded in simulated body fluid [19]. CT scans were performed by means of a cone-beam CT device with a conventional X-ray source and with the following parameters: distance source-sample = 100 mm; distance source-detector = 400 mm; 1440 tomographic projections over a 360 scan angle; tube voltage = 40 kV; tube current = 200 μA; exposure time = 2.6 s; focal spot size = 5 μm;

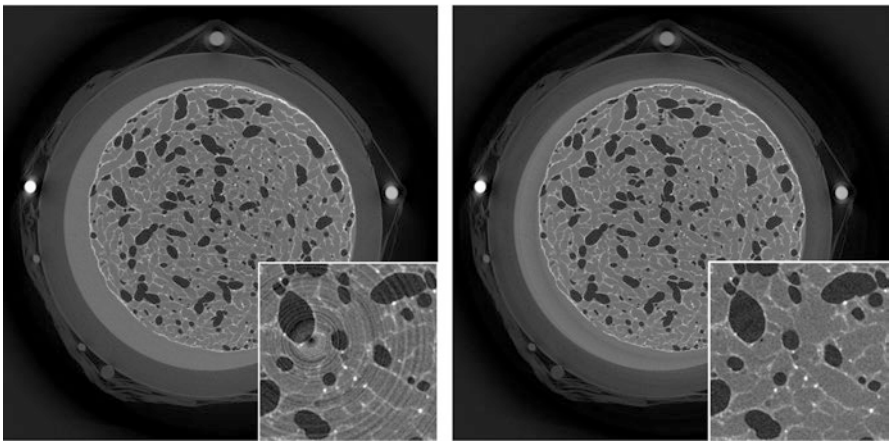

Fig. 5.4 Example of ring artifacts and compensation. On the left: reconstructed image without the introduction of an additional ring removal. On the right: reconstructed image with an additional ring removal compensation

and resulting spatial resolution = 6.25 μm. Ring artifacts were compensated after reconstruction by applying a de-striping method to the polar coordinate converted slice [20].

Ring artifacts compensation is still an open problem for several applications. When considering also propagation-based phase-contrast imaging where the projections are digitally processed with a phase retrieval algorithm, three options for ring removal can be therefore identified: ring compensation before phase retrieval, after phase retrieval (and prior to the actual reconstruction), and after reconstruction. No general strategy can be suggested. An effective solution is most likely acquisition- and sample-dependent [21]. For sure the reconstruction step in high-resolution CT imaging has to include a solution to handle the ring artifacts.

3 Segmentation

The key step for the quantitative analysis is called *segmentation*, which roughly implies a classification of the voxels aimed at identifying the interesting objects within the reconstructed volume and labels each of them with a single value. Segmentation involves reading the grayscale volume and producing an image having as many labels as the number of identified objects or phases. It is almost impossible to enumerate all the proposed approaches for segmentation. Moreover, some of them are difficult to extend to the three-dimensional case and therefore will not be taken into account in this chapter. Computational aspects have also to be considered as the memory requirement is a serious concern for volumetric image processing.

3.1 Thresholding

The simplest approach to segmentation is based on the evaluation of the gray value of each pixel against a single global threshold value: if the gray value falls below the specified threshold, the pixel is labeled as 0, otherwise it belongs to a different class, and therefore it will be assigned to value 1 (or something different from 0). For some applications, the resulting binary volume can be further refined with the application of a *connected components labeling* algorithm [22] in order to assign different labels to each separated blob. The result is sometimes represented as pseudo-colors in order to visually appreciate the identified objects.

Global thresholding is extremely simple and fast, but it requires an input grayscale volume with adequate image quality. A high amount of noise in the image might affect the segmentation leading to several misclassified voxels, i.e., “black and white” binary noise in the segmented image. To this aim, pre-segmentation filtering, e.g., edge-preserving smoothing [23, 24], or post-segmentation approaches,

e.g., morphological image processing [25], might be considered to improve the actual segmentation. Figure 5.5 reports an example of alginate/hydroxyapatite scaffold segmented with global thresholding with the addition of a post-processing "cleaning" procedure to get rid of misclassified voxels [26].

The key parameter in the thresholding process is the choice of the threshold value. The simplest way is to let users manually choose a threshold value. This value is usually chosen via visual evaluation of the results produced by a few trials with different threshold values. The starting point for this trial-and-error assessment is usually the image intensity histogram. In the case of an image intensity histogram that is clearly bimodal, with two relatively narrow peaks corresponding to the object and to the background, the threshold may be easily determined as the histogram minimum between the two peaks. However, the volume to segment may present an image histogram that does not consist of two separate peaks. In the presence of such a monomodal histogram, more efforts are required. A manual assessment of the threshold is subjective, and factors like room lighting, monitor brightness/contrast settings, operator fatigue, and limited grayscale shade perception can affect the reproducibility of this manual approach.

Automatic thresholding algorithms might be preferable. They overcome the subjectivity of manual thresholding, and they can also speed up the analysis process as the manual assessment of the threshold might be a time-consuming task for some applications, e.g., where a great number of images have to be analyzed. A few automatic thresholding methods are hereafter briefly reviewed. Kittler and Illingworth [27] proposed a method that consists in arbitrarily dividing the histogram into two parts, modeling each part with a normal distribution, comparing the model with the histogram, and assuming as optimal the threshold that minimizes a minimum error criterion function. Ridler and Calvard [28] advanced an iterative scheme in which at step n, a new threshold T_n is established using the average of the foreground and background class means. Iterations terminate when the changes $|T_n - T_{n+1}|$ become sufficiently small. Otsu [29] suggested minimizing the weighted sum of intra-class variances of the foreground and background voxels to establish

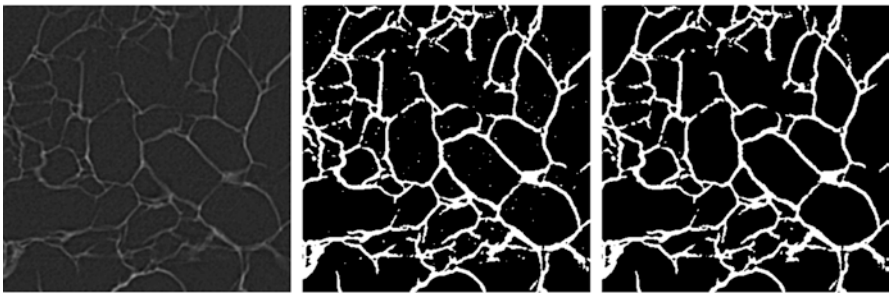

Fig. 5.5 Global thresholding with an additional "cleaning" procedure. From left to right: original crop of a micro-CT slice; global thresholding; refinement of the thresholded image after the removal of misclassified voxels. For the sake of clarity, only a 2D image is represented, but the process is performed in the 3D domain

an optimum threshold. Tsai's method [30] determines the threshold imposing that the first three moments of the input image are preserved in the output image. Pun's method [31] is based on entropic thresholding: an entropy-thresholded image is the one that preserves (as much as possible) the information contained in the original image in terms of entropy. Kapur et al. [32] improved Pun's approach considering the image foreground and background as two different classes of events. When the sum of the two class entropies reaches its maximum, the image is said to be optimally thresholded.

Adaptive (sometimes called local or dynamic) thresholding has been also proposed. Whereas the conventional thresholding operator uses a global threshold for all the voxels, adaptive thresholding changes the threshold dynamically over the image. A simple approach for adaptive thresholding is Niblack's algorithm [33]. When extended to the 3D case, the idea of this algorithm is to build a threshold based on local mean m and local standard deviation s computed in a $N \times N \times N$ neighborhood of each voxel. For each voxel, the threshold T is computed as $T = m - k * s$ where k is a constant user-defined "tuning" parameter (the other parameter being the "window" size N). Adaptive thresholding of 3D images is in general computationally intensive. Moreover, since some "tuning" parameters have to be assessed by means of a "trial-and-error" approach, the total time of the segmentation might result excessive for some applications.

3.2 Region-Based Segmentation

The thresholding methods described in the previous section are based on the intensity properties of an image. The logical extension is to consider also the spatial properties of the image for segmentation. Region growing takes into account neighboring pixels having similar intensity. However, in practice, constraints, some of which are reasonably complex, must be placed on the growth pattern to achieve acceptable results. Most of the region growing approaches have to be considered semiautomatic segmentation methods as at first user intervention is required to select seed voxels.

Two examples of region growing algorithms are here mentioned. Brice and Fenema [34] have developed a region growing method based on a set of simple growth rules. In the first stage of the process, pairs of pixels are combined together in groups called atomic regions if they are of the same amplitude and are spatially connected. Two heuristic rules are next invoked to dissolve weak boundaries between atomic regions. Adams and Bischof [35] have proposed a seeded region growing algorithm in which the user manually selects a set of seeds that placed in areas of visual homogeneity. The seeds can be single voxels for nearly noise-free images, or they can be small clusters of voxels to provide some degree of noise tolerance for noisy images. Then, conventional region growing proceeds with one new pixel added to each of the N seeded regions. The process proceeds until adjacent regions meet at a common boundary.

Most region growing techniques have an inherent dependence upon the location of seeds for each region. As a consequence, the segmented result is sensitive to the location and ordering of seeds. The region growing process is also iterative, and therefore it can be computationally intensive for high-resolution volume images as μ-CT datasets.

3.3 Clustering and Multiphase Segmentation

Classification algorithms are based on the assumption that the image to segment depicts one or more features and that each of these features belongs to one of several distinct and exclusive classes. The classes may be specified a priori by the human supervisor (as in supervised classification) or automatically clustered (i.e., as in unsupervised classification) into sets of prototype classes, where the supervisor merely specifies the number of desired categories. Image classification analyzes the numerical properties of various image features and organizes data into categories. Classification algorithms [36] typically employ two phases of processing: training and testing. In the initial training phase, characteristic properties of typical image features are isolated, and, based on these, a unique description of each classification category, i.e., training class, is created. In the subsequent testing phase, these feature-space partitions are used to classify image features. The description of training classes is an extremely important component of the classification process. In supervised classification, statistical processes (i.e., based on an a priori knowledge of probability distribution functions) or distribution-free processes can be used to extract class descriptors. Unsupervised classification relies on clustering algorithms to automatically segment the training data into prototype classes.

The most commonly used clustering method is the k-means algorithm. It is an unsupervised clustering algorithm that classifies the input data points into multiple classes based on their inherent distance from each other. The algorithm starts selecting K cluster centers. The selection can be performed manually, randomly, or by a heuristic approach. Each voxel in the image is then assigned to the cluster that minimizes the distance between the voxel and the cluster center. This difference is based on gray-level intensity, but it can combine also location measures. Cluster centers are then updated by averaging all of the voxels in the cluster. Previously steps are repeated until no voxels change clusters.

3.4 Refinement of Segmentation Results

The segmentation should be able in principle to produce a binary image having each object represented by a set of contiguous voxels (connected component). However, in some cases this could be hard to obtain due to a limited spatial and contrast resolution or due to an imperfect segmentation process. Moreover, some volumes

feature objects physically interconnected which however have to be considered as separated, or they are better characterized if they would be separated. Therefore, it is sometimes necessary to isolate each region to segment with additional image processing in order to achieve an accurate characterization.

The already-mentioned field of morphological image processing with the basic dilation and erosion operators [26] might help for the object isolation/separation issue. Dilation and erosion might be effective in some cases; however they could affect the accuracy of a more comprehensive characterization of the segmented phase that includes size and shape descriptors. A way to handle the object separation issue is by means of *watershed segmentation* [37]. Figure 5.6 shows an application of the automatic separation process performed exploiting an approach based on watershed segmentation. The alginate/hydroxyapatite scaffold was segmented with global thresholding plus an additional refinement (see Fig. 5.5). Then the single interconnected cells were separated for further measurements with watershed segmentation. Only the cells completely included into the considered sub-volume are identified and labeled with pseudo-colors.

3.5 Volume of Interest (VOI) Selection

Instead of segmenting the whole reconstructed CT volume, a Volume of Interest (VOI) is typically considered. In the final reconstructed volume, not all the voxels are equally significant for further analysis. In addition to the scanned object, the background and the sample holder could be part of the images. A VOI within the sample has to be identified. Although in principle any VOI size and shape could be considered, the representativeness of the VOI should be assessed and discussed before performing the quantification. In most cases, a regularly shaped small cube

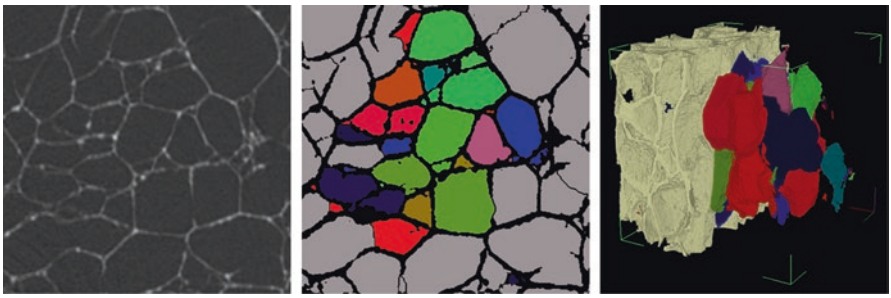

Fig. 5.6 A micro-CT sub-volume of an alginate/hydroxyapatite scaffold was segmented with global thresholding plus an additional refinement. Then the single interconnected cells were separated for further measurements with watershed segmentation. Only the cells completely included into the considered sub-volume are identified and labeled with pseudo-colors. A single 2D image is shown in the central panel, but the process is applied to the 3D domain as suggested by the volume rendering in the right panel

within the imaged object is selected. The adoption of spherical VOIs has been also proposed for some applications (e.g., a quantification of the anisotropy); however the vast majority of computing tools are designed to handle three-dimensional matrices. The size of this 3D matrix is however a critical point. The selected VOI should be representative (and therefore sometimes the acronym REV – representative elementary volume – is used); therefore it should be large enough to comprehend all the heterogeneous features of the sample. A common rule of thumb is to select a VOI having size one order of magnitude greater than the average size of the structures to analyze. However, on the other hand, the VOI should be small enough to fit the constraints imposed by the available computing hardware resources, and, of course, a smaller VOI reduces the computational time of the subsequent analysis. Moreover, the VOI size depends also on the method used for the quantification of a specific feature. While a small VOI could be adequate for the computation of, e.g., the global porosity, a bigger VOI might be required for the assessment of, e.g., the degree of connectivity. A simple method based on the consideration of variable size VOIs has been proposed, for instance, in Brun et al. [17] to assess the minimum representative size for each of the derived quantitative parameters.

3.6 Validation of the Segmentation Results

A validation of the applied segmentation is in most of the cases left to user experience. Although methods for a quantitative assessment of segmentation results might consider a cross-check with external data (such as histology), visual inspection by an expert supervisor is still the most commonly adopted method to assess the reliability of a proposed segmentation. A successful segmentation must be judged by the utility of the description that is obtained using the resulting objects. As image enhancement is generally subjectively performed, a "good" segmentation is also subjectively assessed.

The choice of the segmentation approach (e.g., the choice of the threshold value with the parameters of some additional pre- or post-segmentation filtering) is a critical step within the whole workflow of a CT-based experiment. Ideally two or more reasonable segmentation protocols should be compared in order to assess the range of reliability of the final computed values. A possible strategy is to consider a slightly under-segmented and a slightly over-segmented volume. Both the images are then used as input of the final quantification step, and a confidence interval could be defined for the derived numerical values.

3.7 Segmentation-Oriented Reconstruction

Although reconstruction and segmentation have been presented so far as consecutive separated steps, in recent years an attempt to combine the two has been introduced. In cases where a volume is composed of a few homogeneous phases and the primary intention is to distinguish these, the field of *discrete tomography* can be

considered [38]. It consists in reconstructing the volume image with the prior knowledge that only a small number of gray levels are expected. By exploiting this knowledge, the produced images typically contain fewer artifacts and do not have to be segmented, as they already contain one gray level for each composition. Although not widely adopted yet, discrete tomography is a promising field since, in general, it works effectively also with a reduced number of noisy projections. Provided that a robust discrete tomography solution is identified and applied in a reasonable amount of time, CT acquisitions with a reduced number of projections seem therefore feasible, thus leading to a minimization of the radiation damage, faster experiments, or, simply, more acquisitions per beamtime.

4 Quantification

The segmented reconstructed VOI is the starting point for the derivation of meaningful measurements of the scanned object. The parameters to quantify depend on the specific applications; however a few families of features are commonly identified and hereafter described.

4.1 Basic Structural Analysis

A set of basic morphometric indices such as relative density (or porosity) and surface density is used to characterize the segmented object [39]. The computation of these values is extremely simple as it is just based on the number of segmented voxels in the VOI. In the case of surface density, only the voxels of the surface of the identified objects are considered, i.e., the voxels at the interface between the segmented object and the background. In several applications, a simple quantification of the amount of regenerated tissue is required, and high-resolution micro-CT combined with VOI selection and segmentation allows to derive reliable values.

Figure 5.7 reports an example where porous glass-ceramic scaffolds for bone regeneration [40] were imaged with synchrotron radiation X-ray micro-CT after in vitro treatment in simulated body fluid (SBF). Different scaffolds were imaged before the treatment, after 2 weeks and after 4 weeks of embedding in SBF. The amount of newly formed apatitic phase can be quantified by simply counting the number of segmented voxels.

4.2 Thickness Measurements

In several applications the segmented regenerated tissue is composed of small structural elements, and a characterization of these might be desirable. An example is bone tissue engineering where a quantification of the size of the trabeculae is of great

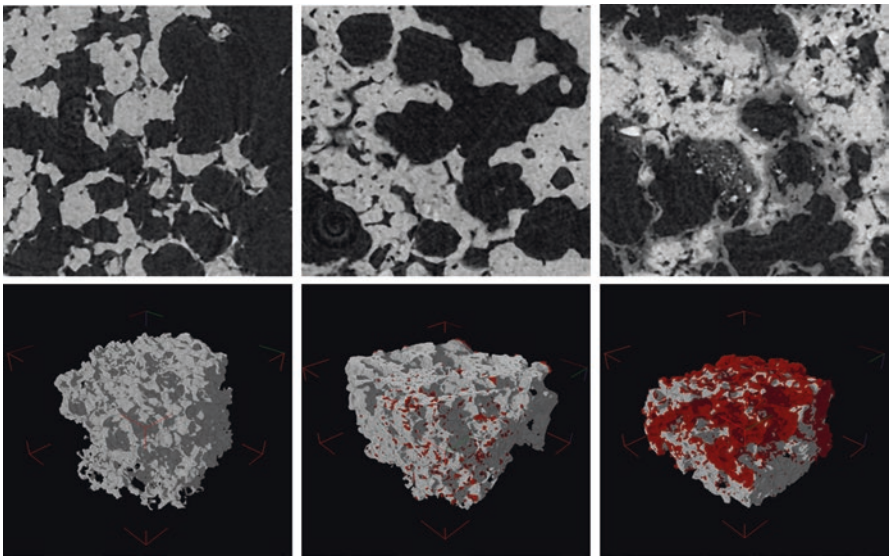

Fig. 5.7 Quantification of newly formed bone in glass-ceramic scaffolds. Measurements were carried out on the samples for each time step. From left to right: scaffolds as such; scaffolds soaked in SBF for 14 days; embedding for 28 days. A crop of the micro-CT slice is presented in the top row and a volume rendering in the bottom row. The images show the scaffold material (gray) and the newly formed apatitic phase (red). The amount of newly formed bone can be quantified by simply counting the number of voxels represented with red color

interest as it directly correlates with the biomechanical properties of the regenerated tissue. The most interesting and model-independent approach for the characterization of the local thickness in a voxel p of a segmented VOI is based on the evaluation of the largest sphere, containing the point p and which is completely inside the structure [41]. The diameter of the maximal inscribed sphere is easily derived from a binary VOI by considering the concept of *distance transform* of the segmented volume. For each voxel in a binary image, the distance transform is able to assign a number that is the distance between that voxel and the nearest background voxel. The object thickness is therefore the local maximum of the distance transform within an identified connected component. Figure 5.8 reports an example where the trabecular thickness of a newly formed bone is assessed after segmentation and computation of the distance transform. A maximal inscribed sphere can be also overlaid to the original image in order to visualize the point where the local thickness is assessed.

4.3 Anisotropy

Another parameter often used to understand the biomechanical properties of the regenerated tissue directly from the segmented images is the geometric degree of anisotropy [42]. The anisotropy corresponds to the preferential orientation(s) of the

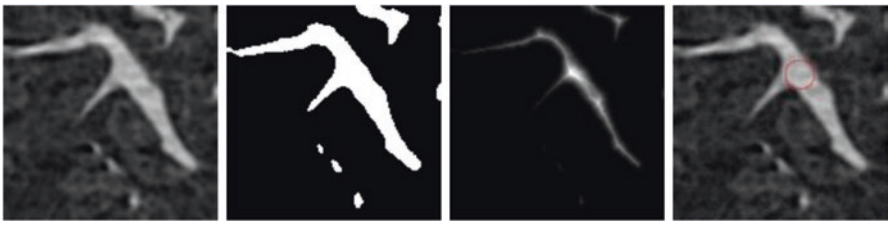

Fig. 5.8 Assessment of the trabecular thickness in a newly formed bone. From left to right: original image; segmented image; distance transform represented with gray level; overlaid maximal sphere. The local maximum of the distance transform can be considered the center of the maximal inscribed sphere, and this sphere can be also overlaid to the original image in order to visualize the point where the local thickness is assessed. For the sake of clarity, the concept is represented in 2D, but it applies to the 3D segmented domain

elements. It is constituted under the influence of strengths applied to the tissue and permits to establish resistance to these strengths in a given preferential direction. A structure is isotropic if it has no preferred orientation. Cowin and Laborde [43] introduced the term fabric as a description of the local anisotropy, and a fabric tensor was defined as any positive-definite second-rank tensor, which quantitatively describes fabric.

A method to derive anisotropic measurements, i.e., the presence of preferential orientations, is based on the concept of *mean intercept length* (MIL) reported in Fig. 5.9. The basic principle of the MIL method [44] consists of counting the number of intersections between a linear grid and the object/background interface as a function of the grid orientation ω. The mean intercept length (an intercept is the line between two intersections) is calculated as the ratio between the total length L of the line grid and the number of intersections. MIL measurements in 3D may be fitted to an ellipsoid which can be expressed as the quadratic form of a second-rank tensor M [45]. A fabric tensor H is defined as the inverse square root of M. Since the eigenvectors (u_1, u_2, u_3) of the fabric tensor H give information about the direction of the axes of the ellipsoid, and the eigenvalues (t_1, t_2, t_3) express the radii of the ellipsoid, the latter can be used to define the degree of anisotropy, which denotes the ratio between the maximal and minimal radii of the MIL. The eigenvalues are commonly summarized using the isotropy index $I = t_3/t_1$ and the elongation index $E = 1 - t_2/t_1$. The isotropy index I measures the similarity of a fabric to a uniform distribution and varies between 0 (all observation confined to a single plane or axis) and 1 (perfect isotropy). The elongation index measures the preferred orientation of a fabric in the $[u_1, u_2]$ plane and varies between 0 (no preferred orientation) and 1 (a perfect preferred orientation with only parallel observations).

4.4 Connectivity

When the imaged regenerated tissue features an interconnected pore space, one of the goals of the analysis might be a quantification of the degree of connectivity. While it was shown in the previous sections that an interconnected pore space can

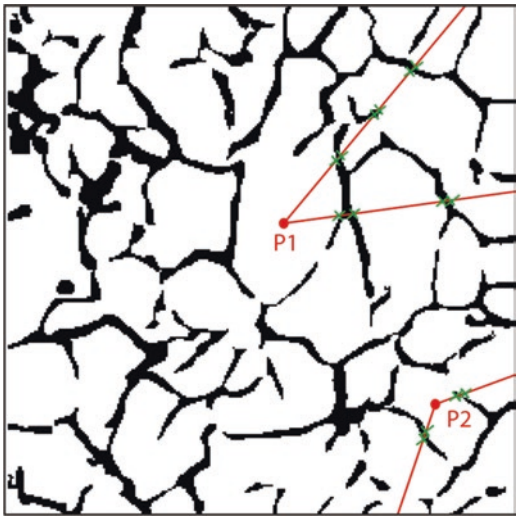

Fig. 5.9 Mean intercept length (MIL) method. The number of intersections (represented in green) along randomly generated lines (as the ones with origin in point P1 and P2, respectively) is counted in the segmented binary volume. For the sake of clarity, the concept is represented in 2D, but it can be easily extended to the 3D domain

be transformed into a "disconnected" set of blobs by means of, e.g., watershed segmentation, approaches for the characterization of the connectivity were not introduced yet. When this measure is of particular interest, skeleton analysis might be a model-independent effective approach. Skeleton analysis is based on the extraction of the curve-skeleton of a binary 3D image [46], i.e., a description of the binary object in terms of nodes and branches. The curve-skeleton (or, simply, skeleton) is a set of idealized connected thin lines that preserve the original topology and capture both boundary and region information forming what can be intuitively thought as the "spine" (or medial axis) of the object.

Several automatic methods for curve-skeleton extraction have been proposed in the literature. Practically, the skeleton is defined in terms of these desirable properties: homotopy, i.e., the skeleton is topologically equivalent to the original image (the skeleton and the original image have the same number of connected components, tunnels, and cavities); thinness, i.e., the skeleton is one voxel wide; and medialness, i.e., the skeleton is centrally located within the foreground objects (a skeleton should grant this property to be called medial axis). Different skeletonization algorithms behave differently in terms of these properties.

By scanning the skeleton, it is possible to extract the number of nodes n and branches b. The quantity $\chi_V = n - b$ provides a measure of connectivity by indicating the number of redundant connections: the breaking of a single connection will leave the network less connected, thus increasing the value of χ_V, while the addition of a redundant connection will decrease it. In order to normalize this measure with respect to the size of the considered volume V, the parameter "connectivity density" β computed as $\beta = (1 - \chi_V)/V$ is commonly adopted [47]. The connectivity density does not carry information about positions or size of connections, but it is a simple global measure of connectivity, which gives higher values for better-connected structures and lower values for poorly connected structures.

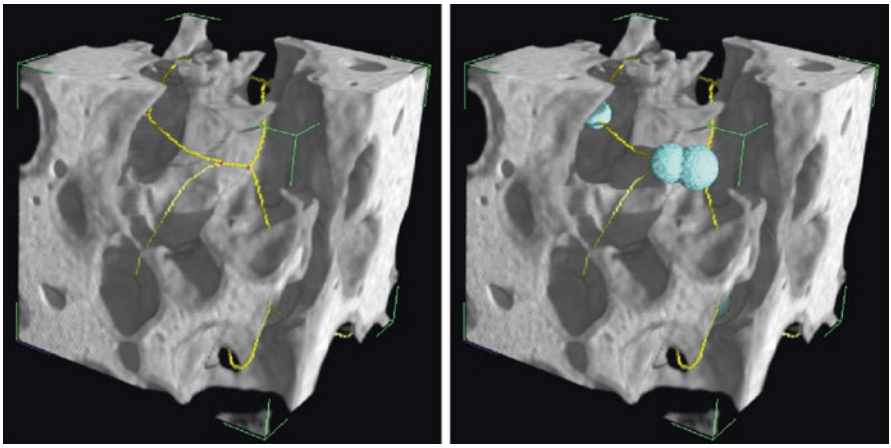

Fig. 5.10 Assessment of connectivity. The curve-skeleton of the pore space can be extracted, thus leading to a model composed of nodes (red) and branches (yellow). While two nodes having coordination number 3 each are identified without merging (on the left), a single node having coordination number 4 is considered after merging (on the right)

Similar to the concept of *coordination number* used in chemistry and crystallography (i.e., the number of atoms or ions immediately surrounding a central atom in a complex or crystal), a measure of local connectivity can be also introduced by considering the number of branches that spread out from a single node. Due to limitations of the skeletonization process, merging criteria are required to avoid the consideration of very small branches connecting two adjacent nodes and derive more reliable values for the local coordination number.

Figure 5.10 reports the extracted skeleton where nodes and branches are identified to derive connectivity density and the local coordination number. By inflating spheres (with the same principle based on distance transform used to derive thickness measurements) and looking for an overlap of these spheres, it is possible to merge two nodes separated by a very small branch in order to compute a more reliable coordination number. The principle is explained in Fig. 5.10 where a skeletonization algorithm [48] has been applied to the pore space and two nodes having coordination number 3 are identified without merging, while a single node having coordination number 4 is considered after an overlap of the inflated spheres centered onto each skeleton node.

5 Conclusion

In this chapter an overview “from projections to measurements” was presented, introducing the most significant computational aspects of high-resolution CT imaging and image analysis. The challenges of reconstruction and artifacts compensation were commented, and, most significantly, it was shown how to extract reliable quantitative parameters or descriptors directly from segmented CT images.

At the end, the crucial question of how much can one trust the computed values arises. The whole process that leads to a quantitative characterization of a sample via imaging and image analysis presents several intermediate choices and trade-offs that surely affect the reliability and reproducibility of the final results. The final results depend on several aspects, and some of them are not directly correlated to computation, such as whether the sample to image is adequate and representative for the goals of the experiment, whether the desired characteristics of the sample are actually detectable by imaging, whether the proper sub-volume of the sample is examined, and whether the correct images with adequate quality are acquired. An incorrect consideration of these aspects invalidates the results derived via imaging and image analysis.

Provided that a representative sample was adequately imaged and the acquired images are of a sufficient quality, a characterization of some properties of the sample by means of image analysis still presents crucial aspects. The most crucial ones are the segmentation of the images and the size of the Volume of Interest (VOI) as well as its location within the reconstructed volume. Again, inaccurate segmentation and inadequate VOI selection invalidate the final computed measurements. User supervision is often required in order to get accurate results. Anyway, with adequate software tools and with accurate knowledge of the challenges and limitations of the computational aspects involved in CT imaging and image analysis, carefully performed image reconstruction, segmentation, and quantification protocols are indeed attractive tools for tissue engineering and regenerative medicine applications.

References

1. Kak AC, Slaney M (1988) Principles of computerized tomographic imaging. IEEE Press, New Brunswick. (Cited on pages 10 and 11)
2. Wei Y, Wang G, Hsieh J (2005) An intuitive discussion on the ideal ramp filter in computed tomography (I). Comput Math Appl 49(5–6):731–740
3. Feldkamp LA, Davis LC, Kress JW (1984) Practical cone-beam algorithm. J Opt Soc Am 1:612–619
4. Pan X, Sidky EY, Vannier M (2009) Why do commercial CT scanners still employ traditional, filtered back-projection for image reconstruction? Inverse Probl 25(12):123009
5. Brun F, Delogu P, Longo R, Dreossi D, Rigon L (2018) Inpainting approaches to fill in detector gaps in phase contrast computed tomography. Meas Sci Technol 29(1):014001
6. Landweber L (1951) An iteration formula for Fredholm integral equations of the first kind. Am J Math 73:615–624
7. Hestenes MR, Stiefel E (1952) Methods of conjugate gradients for solving linear systems. J Res Natl Bur Stand 49(6):409–436
8. Gordon R, Bender R, Herman GT (1970) Algebraic Reconstruction Techniques (ART) for three-dimensional electron microscopy and X-ray photography. J Theor Biol 29(3):471–476 IN1-IN2,477-481
9. Hounsfield GN (1973) Computerized transverse axial scanning (tomography): I. Description of system. Br J Radiol 46(552):1016–1022
10. Rit S, Vila Oliva M, Brousmiche S, Labarbe R, Sarrut D, Sharp GC (2014) The Reconstruction Toolkit (RTK), an open-source cone-beam CT reconstruction toolkit based on the Insight Toolkit (ITK). J Phys Conf Ser 489(1):012079

11. van Aarle W, Palenstijn WJ, De Beenhouwer J, Altantzis T, Bals S, Batenburg KJ, Sijbers J (2015) The ASTRA toolbox: a platform for advanced algorithm development in electron tomography. Ultramicroscopy 157:35–47
12. Biguri A, Dosanjh M, Hancock S, Soleimani M (2016) TIGRE: a MATLAB-GPU toolbox for CBCT image reconstruction. Biomed Phys Eng Express 2:055010
13. Pelt DM, Batenburg KJ (2014) Improving filtered backprojection reconstruction by data-dependent filtering. IEEE Trans Image Process. 23(11), art. no. 2341971:4750–4762
14. Pelt DM, De Andrade V (2017) Improved tomographic reconstruction of large-scale real-world data by filter optimization. Adv Struct Chem Imaging 2:17
15. Barrett JF, Keat N (2004) Artifacts in CT: recognition and avoidance. Radiographics 24(6):1679–1691
16. Van Nieuwenhove V, De Beenhouwer J, De Carlo F, Mancini L, Marone F, Sijbers J (2015) Dynamic intensity normalization using eigen flat fields in X-ray imaging. Opt Express 23(21):27975–27989
17. Brun F, Kourousias G, Dreossi D, Mancini L, Tromba G (2011). A comparative evaluation of ring artifacts reduction filters for X-ray computed microtomography images. Proceedings of the 18th IEEE International Conference on Image Processing (ICIP). pp 405–408. Brussels, Belgium
18. Paleo P, Mirone A (2015) Ring artifacts correction in compressed sensing tomographic reconstruction. J Synchrotron Radiat 22:1268–1278
19. Brun F, Turco G, Paoletti S, Accardo A (2015) A synchrotron radiation microtomography study of wettability and swelling of nanocomposite alginate/hydroxyapatite scaffolds for bone tissue engineering. IFMBE Proc 51:288–291
20. Brun F, Kourousias G, Dreossi D, Mancini L (2009) An improved method for ring artifacts removing in reconstructed tomographic images. IFMBE Proc 25(4):926–929
21. Massimi L, Brun F, Fratini M, Bukreeva I, Cedola A (2018) An improved ring removal procedure for in-line x-ray phase contrast tomography. Phys Med Biol 63(4):045007
22. Hu Q, Qian G, Nowinski WL (2005) Fast connected-component labelling in three-dimensional binary images based on iterative recursion. Comput Vis Image Underst 99(3):414–434
23. Perona P, Malik J (1990) Scale space and edge detection using anisotropic diffusion. IEEE Trans Pattern Anal Mach Intell 12(7):629–639
24. Tomasi C, Manduchi R (1998) Bilateral filtering for gray and color images. Proceedings of the 6th IEEE International Conference on Computer Vision. pp 839–846. Bombay, India
25. Soille P (2004) Morphological image analysis: principles and applications, 2nd edn. Springer, Berlin
26. Brun F et al (2011) Automated quantitative characterization of alginate/hydroxyapatite bone tissue engineering scaffolds by means of micro-CT image analysis. J Mater Sci Mater Med 22(12):2617–2629
27. Kittler J, Illingworth J (1986) Minimum error thresholding. Pattern Recogn 19:41–47
28. Ridler TW, Calvard S (1978) Picture thresholding using an iterative selection method. IEEE Trans Syst Man Cybern 8:630–632
29. Otsu N (1979) A threshold selection method from gray-level histograms. IEEE Trans Syst Man Cybern 9(1):62–66
30. Tsai WH (1985) Moment-preserving thresholding: a new approach. Graph Models Image Process 19:377–393
31. Pun T (1981) Entropic thresholding: a new approach. Comput Graph Image Process 16:210–239
32. Kapur JN, Sahoo PK, Wong AKC (1985) A new method for gray-level picture thresholding using the entropy of the histogram. Graph Models Image Process 29:273–285
33. Niblack W (1986) An introduction to digital image processing. Prentice Hall, Englewood Cliffs
34. Brice CR, Fenema CL (1970) Scene analysis using regions. Artif Intell 1:205–226
35. Adams R, Bischof L (1994) Seeded region growing. IEEE Trans Pattern Anal Mach Intell 16(6):641–647

36. Haralick RM, Kelly GL (1969) Pattern recognition with measurement space and spatial clustering for multiple images. Proc IEEE 57(4):654–665
37. Vincent L, Soille P (1991) Watersheds in digital spaces: an efficient algorithm based on immersion simulations. IEEE Trans Image Process 16:583–598
38. Batenburg KJ, Sijbers J (2011) DART: a practical reconstruction algorithm for discrete tomography. IEEE Trans Image Process 20(9):2542–2553
39. Ohser J, Schladitz K (2009) 3D images of materials structures: processing and analysis. Wiley-VCH, Weinheim
40. Renghini C et al (2013) Microstructural characterization and in vitro bioactivity of porous glass-ceramic scaffolds for bone regeneration by synchrotron radiation X-ray microtomography. J Eur Ceram Soc 33(9):1553–1565
41. Hildebrand T, Rüegsegger P (1997) A new method for the model independent assessment of thickness in three-dimensional images. J Microsc 185(1):67–75
42. Ketcham RA, Ryan TM (2004) Quantification and visualization of anisotropy in trabecular bone. J Microsc 213(2):158–171
43. Cowin SC, Laborde AJ (1985) The relationship between the elasticity tensor and the fabric tensor. Mech Mater 4(22):137–147
44. Whitehouse WJ (1974) The quantitative morphology of anisotropic trabecular bone. J Microsc 101:153–168
45. Harrigan TP, Mann RW (1984) Characterization of microstructural anisotropy in orthotropic materials using a second rank tensor. J Mater Sci 19(3):761–767
46. Cornea ND, Silver D, Min P (2007) Curve-skeletons properties, applications and algorithms. IEEE Trans Vis Comput Graph 13(3):530–548
47. Odgaard A, Gundersen HJG (1993) Quantification of connectivity in cancellous bone, with special emphasis on 3-D reconstructions. Bone 14(2):173–182
48. Brun F, Dreossi D (2010) Efficient curve-skeleton computation for the analysis of biomedical 3D images. Biomed Sci Instrum 46:475–480

Chapter 6
In-Line X-Ray Phase Tomography of Bone and Biomaterials for Regenerative Medicine

Max Langer

The aim of this chapter is to present recent developments in X-ray tomography using in-line phase contrast and their applications to mineralised tissue, whether bone or artificial biomaterials, at micro- and nanoscale. Recently, the main efforts in reconstruction algorithms for in-line X-ray phase contrast imaging have been to push resolution towards the nanoscale and extend the possibilities for quantitative imaging to more general objects. The first is made possible by the use of X-ray optics and the second by the introduction of more advanced priors in the reconstruction. We summarise here these developments and outline recent applications of these techniques, namely, nano-tomography of the ultrastructure of bone and micro-tomography of bone formation in artificial bone grafts as well as in healthy growing mice. While still relatively little used in the field of regenerative medicine, we hope that these examples will stimulate further studies in this field.

1 Introduction

X-ray computed tomography on the micrometric scale (μCT) is nowadays a standard technique in the characterisation of biological materials such as bone [1–5]. Due to the penetrative nature of X-rays, it is ideally suited to study hard, opaque tissues. It is a 3D technique, which allows the precise study of certain structures such as trabecular bone, vessels, collagen texture and osteocyte lacunae without the need to resort to stereology. Further, if a sufficiently monochromatic beam is used, it is a quantitative technique permitting densitometric imaging [6]. This is of special

M. Langer (✉)
Creatis, CNRS UMR 5220, INSERM U1206, INSA-Lyon,
Université Claude Bernard Lyon 1, Université de Lyon, Villeurbanne, France
e-mail: max.langer@creatis.insa-lyon.fr

A. Giuliani, A. Cedola (eds.), *Advanced High-Resolution Tomography in Regenerative Medicine*, Fundamental Biomedical Technologies,
https://doi.org/10.1007/978-3-030-00368-5_6

interest in the study of regenerative medicine, since characterisation of, for example, bone healing is tantamount to evaluating the progression of mineralisation in the newly formed bone tissue.

These properties make X-ray μCT a prime candidate as a characterisation tool in biomaterial research and regenerative medicine, especially in the case of mineralised tissue. The specific challenges of imaging such samples have proven somewhat limiting, however, due to insufficient sensitivity of X-ray μCT. Often, the structures of interest are lowly contrasted, for example, small mineralisation gradients in forming bone, or vessels, fat and other soft tissues embedded in hard tissues such as bone or mineralised scaffolds. A concrete example is the imaging of 3D cultures of bone cells on a mineralised substrate, where ideally newly formed bone, pre-bone matrix, bone cells, vessels as well as mineralisation of bone and substrate should be quantified. This application will be discussed more in detail below.

While certain structures, e.g. vessels, can be enhanced by the use of contrast agents [7, 8], this often poses the risk of altering the structure to be imaged. One way to increase the sensitivity of X-ray μCT is to use phase contrast [9]. While several ways of achieving X-ray phase contrast exist [10–15], if a sufficiently coherent source, such as a synchrotron, is used, X-ray phase contrast can be achieved simply by placing the detector a small distance away from the sample [16]. The contrast thus achieved is due to Fresnel diffraction. The resulting imaging modality can be several orders of magnitude more sensitive than standard (attenuation-based) X-ray imaging depending on the material (particularly in soft tissue, the contrast is enhanced). To achieve a quantitative imaging modality, an additional reconstruction step has to be performed, however: to reconstruct the phase shift in the object from the Fresnel diffraction phase contrast images through a process known as phase retrieval [17]. The resulting phase images can then be used in conjunction with tomographic imaging to create 3D reconstructions of the refractive index and by extension the mass density distribution in the object.

Here, we will show the latest developments of X-ray phase contrast μCT relevant to imaging in regenerative medicine and recent applications. Nano-tomography of bone ultrastructure shows great promise for the analysis of cellular structure as well as collagen and mineral distribution at the ultrastructural level. So far only the proof of concept has been reported, but the technique should provide plenty of opportunity for studies, e.g. of bone healing and pathology [18–24]. In micro-tomographic imaging, newly developed reconstruction algorithms have provided unprecedented insight in bone formation in healthy growing mice [25] and in bone cell culture in mineralised 3D substrates [26].

2 Method

When an X-ray beam passes through an object, it is mainly affected in two ways: it might be absorbed in the object (through the photoelectric effect), which changes its amplitude, and it might be retarded in the object, which changes its phase. For

X-rays we can consider the object completely described by the complex refractive index. Both the attenuation and the phase shift induced by the object can be described as projections through the absorption and refractive index distributions. This means that both parts of the complex refractive index can be reconstructed by tomographic reconstruction if amplitude and phase can be measured or reconstructed for different angular settings of the sample.

For the relatively short propagation distances we are interested in here, usually up to 1 m, the effect of propagation on the exit wave field can be described in the framework of Fresnel diffraction. Such an image is referred to as a Fresnel diffraction pattern or a phase contrast image. Intensity is measurable in essentially every plane downstream of the object, but the phase shift is lost and has to be reconstructed from intensity images. There is a quantitative but non-linear relationship between the induced phase and the contrast.

We can distinguish two distinct imaging setups: one for phase contrast μCT and one for nano-CT.

In-line X-ray phase contrast μCT uses essentially the same imaging setup as μCT but with the detector mounted on a translation stage, or fixed at a position downstream of the sample stage, to permit the free space propagation necessary for the phase contrast fringes to become visible [27] (Fig. 6.1a). This setup is limited in resolution by the scintillating screen used to convert X-rays to visible light and the visible light microscope used to image the scintillating screen onto the CCD camera. This gives a diffraction-limited resolution of ~400 nm depending on the wavelength of the light emitted by the scintillator. This is the same resolution limit as in visible light microscopy-based techniques such as histology and histomorphometry.

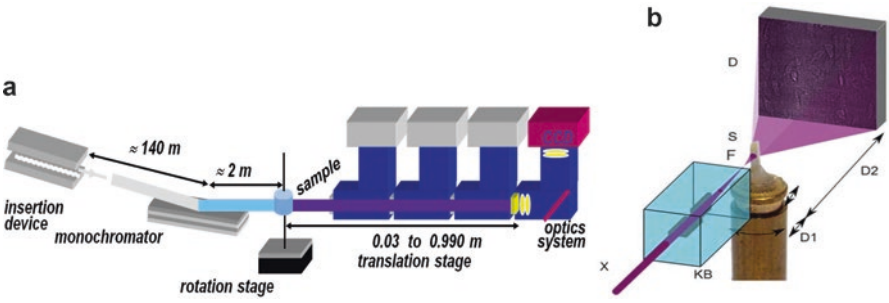

Fig. 6.1 Imaging setups in synchrotron radiation propagation-based phase contrast imaging. (**a**) In X-ray microscopy, X-rays are taken from an insertion device and then optionally monochromatised depending on the application. The long source to sample distance yields a high degree of spatial coherence necessary for good phase contrast fringe visibility. The sample is mounted on a translation-rotation stage (standard SR-μCT setup). The detector, consisting of a scintillator, light microscope optics and a CCD, is mounted on a translation stage to allow for free space propagation of the beam after the sample. (**b**) In nanoscopic imaging, the incoming (parallel) X-ray beam is first focused into a focal spot using reflective optics. The sample is placed between the focal spot and the detector in the resulting divergent beam to create geometric magnification. The sample is placed on a translation stage (with the detector position kept fixed) to vary the propagation distance and magnification [18]

X-ray in-line nano-tomography uses X-ray reflective (Kirkpatrick-Baez) optics to focus the X-ray beam [28]. The sample is then placed behind the focus in the resulting divergent beam (Fig. 6.1b). This setup achieves geometric magnification (projection microscopy) on the X-ray side. The image formed on the scintillator is thus already magnified and is then further magnified by the visible light optics. This setup is in theory diffraction limited by the wavelength of the X-rays (0.1–1 nm for hard X-rays) and in practice limited by the quality of the X-ray optics and the stability of the imaging setup.

In the microscopic case, the recorded images can be used directly as input to a tomographic reconstruction algorithm [29]. This gives rise to images that are enhanced at the interfaces between different materials in the sample. This is roughly a superposition of the standard (attenuation) tomogram and the second derivative of the real part of the 3D complex refractive index distribution and is often called edge-enhancement tomography or sometimes simply phase contrast tomography. In nano-tomography, due to the high resolution and the resulting relatively long propagation distance, the phase contrast fringes are much too delocalised to be useful in direct reconstruction [28]. Here, phase retrieval becomes a mandatory step to achieve useful images.

While edge-enhanced imaging can be an interesting technique in its own right, it is often more interesting to consider the quantitative (but non-linear) relationship between phase shift induced on the beam by the object and the resulting phase contrast. This relationship can be used to reconstruct the phase shift at the exit of the sample through a process usually called phase retrieval. Phase retrieval is a nontrivial, non-linear inverse problem and is still the subject of active research [30–38]. We focus here on two recent developments of particular interest for imaging in regenerative medicine, namely, extension of linear phase retrieval algorithms to include multi-material and heterogeneous objects [30, 39] and the use of a non-linear conjugate gradient method to improve the resolution in the reconstruction [18].

Due to the physics of the image formation, the transfer of information from phase to contrast in the low spatial frequency range is low (this can be understood, e.g. through observing that the phase contrast is approximately proportional to the second derivative of the phase shift, as mentioned above). Because of this, the reconstructed refractive index can be affected by strong low-frequency noise [40]. This can strongly inhibit the possibility to quantitatively analyse the reconstructed samples. This kind of artefact has been handled by introducing information in the low frequency range from the measured attenuation [41, 42].

By assuming that the object is homogeneous, the phase (and equivalently the attenuation, considering strict proportionality between attenuation and phase) can be estimated from a single phase contrast image [41]. This has proven to be a very successful method due to the facility of using a single phase contrast image. Great care must be taken when imaging heterogeneous objects, however, especially if quantitative (densitometric) results are required: the ratio between the real (related to phase) and imaginary (related to attenuation) part of the refractive index must vary within a narrow range, and a careful calibration must be performed to correct for the bias introduced by the homogeneity assumption [43].

A more recent development seeks to overcome the limitation of homogenous objects by using an attenuation tomogram as prior knowledge on the low spatial

frequencies of the phase [30, 39]. A tomographic scan at a short distance (depending on the resolution; short enough that phase contrast fringes are not too visible) is reconstructed and then processed in various ways to achieve an estimate of the low spatial frequencies of the real part of the refractive index. This new volume is then forward projected and used as a prior in a least square minimisation problem to retrieve the phase. This approach has some advantages, namely, it is quantitative even for non-homogeneous objects (not for all objects, however; it is somewhat dependent on the composition. Some materials, for example, bone, show a convenient quantitative, non-linear functional relationship between attenuation and phase). It also permits (somewhat paradoxically) to reduce the imaging dose by recording images at several distances, fractioning the dose between the images [44]. The disadvantages, on the other hand, are the increased complexity of using several distances. Each sample requires somewhat longer total acquisition time (due to camera displacements; the exposure time can actually be reduced for a given final image quality) and more storage space, and the images at each projection angle have to be realigned through image registration (albeit this problem has been thoroughly addressed in literature) [45]. Also, this method can clearly not be used in in situ and high frame rate imaging due to the requirement of images at several distances.

The two approaches mentioned above are based on linearised versions of the forward problem, however. In high-resolution imaging (approximately <1 μm in practice), the non-linear contributions start to be important. This presents itself mainly as a loss of resolution. Several methods to overcome this problem have been suggested [18, 33, 34, 46, 47]. The most successful so far seems to be the method based on a non-linear conjugate gradient algorithm [18]. This algorithm must be initialised with a reconstruction sufficiently close to the desired reconstruction, usually with a reconstruction using a linear algorithm, to yield good results. It has been shown to improve resolution of the reconstructions in the nano-tomography case, although there is no reason to believe it should not improve image quality in the microscopic case as well. This would be achieved at the cost of a substantially increased computation time (albeit fully acceptable using current computational resources: currently around 10 min per projection, fully parallelisable over the projections due to the independence of the projections in tomographic imaging). It should be noted that this type of algorithm does not seem to improve the low spatial frequency content of the images. Regularisation-based methods such as the ones mentioned above seem to be mandatory to resolve this problem.

3 Applications

3.1 Nano-tomography of Bone

Nano-tomography has proven to be a very interesting imaging modality for bone imaging. This is due to the ability of X-rays to image the otherwise opaque material in 3D coupled with the ability to reach resolutions below 100 nm, which is important for the imaging of the osteocyte network, which presents structures down to

approximately 100 nm [48]. While imaging of the osteocyte network was the first intended application, the first in-line nano-tomography study of bone revealed that the high sensitivity of the technique made possible to also study the collagen structure of bone, as well as mineralisation on the <100 nm length scale [20, 48].

3.1.1 Analysis of Collagen Structure

Effectively, the lacuno-canalicular network (LCN) can be imaged over a relatively large field of view (Fig. 6.2) with very good spatial resolution. The bone matrix appears strongly textured, showing an arching structure (Fig. 6.2a–c). This arching structure can be identified, by comparison to qBEI [49] and TEM [50] images, to be due to the oblique virtual cutting of the mineralised collagen fibrils. The texture due to the collagen fibrils is sufficiently contrasted to be studied directly in 3D using texture analysis [19].

Using this technique, it can be seen that the mineralised collagen fibrils in this sample are organised in a plywood structure, consisting of parallel quasi-planes, where the fibrils have the same alignment. The collagen structure in bone has been hypothesised to act as a crack arresting boundary and thus protect vessels and nerves embedded in canals within the bone [51]. A qualitative validation of the texture analysis can be performed by constructing a virtual 3D fibril model, where the local orientation is represented by cylindrical stream lines. This model compares well with the corresponding sub-volume of the original greyscale image. The arch pattern is clearly reproduced (Fig. 6.3). This illustrates the necessity of 3D analysis: the complex arrangement of the collagen fibrils cannot be retrieved from 2D sections.

3.1.2 Finite Element Modelling of Osteocytes

The porosity in bone is at least as important as the tissue matrix itself, both biologically and mechanically. In cortical bone, on the micrometric scale, the pore network is formed by the osteocyte lacunae hosting the cell bodies and the canaliculi (small tunnels connecting lacunae of neighbouring cells [52, 53]. Given the presumed importance of the osteocyte in the coordination of other bone cells and in remodelling [54, 55], the LCN has recently received increasing attention. Imaging of this pore network is an important, but not yet fully solved challenge.

An unresolved issue with the LCN was the difference in strain affecting bone in vivo (thousands microstrains) [56] and the strain required to stimulate osteocytes in vitro (tens of thousands of microstrains) [57]. One hypothesis is that there is a "strain amplification mechanism" affecting the osteocytes for them to sense deformation, for example, through the morphology of the LCN.

To test this hypothesis, in-line phase tomography was used to image human femoral cortical bone. Imaging provided volumes with 102 μm field of view and 50 nm voxel size. Rectangular volumes of interest (VOIs) were selected from the images to analyse the LCN and deformations of osteocytes. Each VOI contained a single

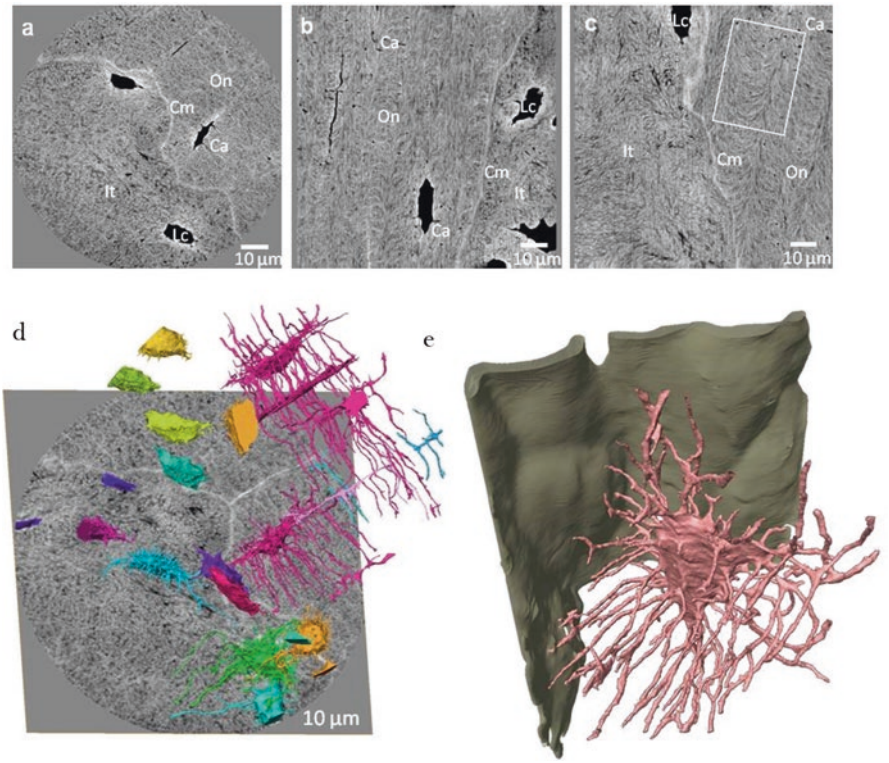

Fig. 6.2 Nano-tomography of bone. (**a**–**c**) Virtual cuts through human cortical bone. The LCN is exceptionally well contrasted. The strongly contrasted arching structure in the matrix presumably due to oblique cutting of the mineralised collagen fibres, as well as well-resolved cement lines. (**d**) Volume rendering of all LCN porosity in a tomogram showing a relatively large number of lacunae. (**e**) Zoom on one lacuna and its canaliculi (pink) and the cement line (green). The LCN is rendered in unprecedented detail. The spatial relationship to structures such as the cement line can be studied

lacuna with its canaliculi (Fig. 6.4a). The geometry of the pores was extracted using an ad hoc segmentation algorithm using thresholding, morphological operations and a connectivity enhancement algorithm [58]. In each VOI, the lacuna and canaliculi were separated into two distinct compartments, and several morphological parameters of both were quantified (Fig. 6.4b). These included volumes, surfaces, descriptors of shape as well as number, diameter and spacing of canaliculi.

Case-specific finite element models of the VOIs were created. The models included the extracellular matrix surrounding the pores, the pericellular soft tissue matrix in the lacuna and the canaliculi, as well as the cell body and processes of the osteocyte (Fig. 6.4c). The osteocytes are not directly visible in the images. Therefore, the extent of the cells was extrapolated based on observations using electron microscopy [59, 60]. Material properties were modelled as linear elastic and isotropic, with parameters assigned based on literature data [61]. A confined

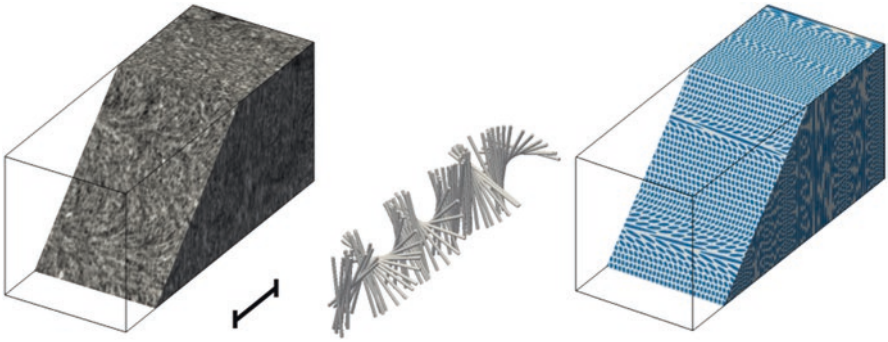

Fig. 6.3 Qualitative validation of a texture analysis approach to quantify mineralised collagen fibril orientation. Left: crop of a nano-CT image of a human femoral cortical bone. Grey values represent the inverted mass density in arbitrary units. Scale bar: 10 μm. Middle: cylinders representing the measured fibril orientation if 600 μm thick sections along one line. Right: 3D image generated based on extracted orientations with the fibrils shown in blue and the matrix in white. The arc pattern in the oblique cut corresponds well to that in the original image (left)

uniaxial compressive deformation along the direction the longest lacunar dimension was simulated in the models, with magnitude set to the physiologically relevant 1000 microstrains [56].

The finite element analysis showed that the magnitude of the strain at the dendrite/cell body junction reached up to 70 times the externally applied deformations, and further local peaks were observed in the dendrites (Fig. 6.4d). Resulting strain magnitudes are in the range reported to stimulate osteocytes in vitro [57]. This means that the shape of the osteocytes contribute to a strain amplification effect. The case-specific models predicted higher strain amplification factors compared not only to idealised ones [62–64] but also to previously reported case-specific simulations using either a different image source [61] or a less fine modelling approach [65].

3.2 In-Line Phase Micro-tomographic Imaging of Bone Formation

A very interesting application of in-line X-ray phase contrast tomography is the imaging of mineralised three-dimensional porous biomaterials used as scaffolds in bone tissue engineering and more generally for 3D bone cell culture [66, 67]. The desired properties of these biomaterials are a surface favourable for cell attachment, that they stimulate bone cell precursors to differentiate into mature bone cells and that they can contribute to bone regeneration [68]. They should also be resorbable by the receiving body and be replaced by new, living bone. While bone formation and resorption can, to a certain extent, be quantified by SR-μCT and microdiffraction [69, 70], these techniques lack the sensitivity to resolve soft and weakly mineralised tissue. Imaging of soft tissue in mineralised scaffolds is challenging due to the

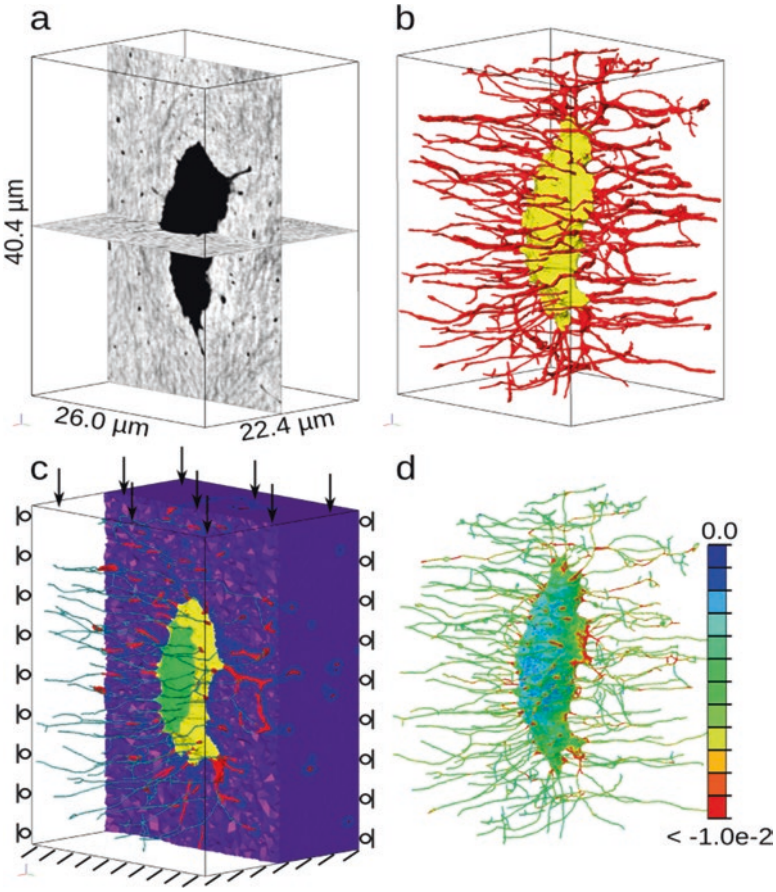

Fig. 6.4 Quantification of lacunar-canalicular morphology and simulation of strains on the osteocyte. (**a**) One lacuna and associated canaliculi cropped from the nano-CT image. (**b**) Surface rendering of the segmented lacuna (yellow) and canaliculi (red). (**c**) Finite element mesh of the mineralised extracellular matrix (purple and blue), the pericellular soft tissue (yellow) and the canaliculi (red), the cell body (light green) and processes (turquoise). The latter two were inferred based on literature data. Parts of the model are transparent to allow visualisation of all compartments. The direction of the compression of 1000 microstrains is also shown. (**d**) Minimum (compressive) principal strain on the osteocyte by FEM, showing peaks in the deformation (red: >10,000 microstrains, a strain amplification of at least 10 times) at the junctions of the dendrites and cell body as well as at certain locations of the dendrites further away from the lacuna

opacity of the structure to visible light and the necessary trade-off between sufficient penetration and attenuation of X-rays to achieve the necessary sensitivity using standard µCT. Quantification of soft tissue formation is important for the characterisation of such biomaterials, since it constitutes the sites where new bone formation is possible. The increased sensitivity of phase tomography, however, has enabled the analysis of soft issues in mineralised scaffolds [71]. Further, different soft tissues can be differentiated in the images, such as collagen, fat, vessels and cells [26].

3.2.1 Imaging of Mineralised Bone Scaffolds Cultured with Bone Cells In Vitro

As an illustration, we show the imaging of Skelite bone scaffolds seeded with human osteoblasts. Skelite is a porous biomaterial consisting of 67% silicon-stabilised tricalcium phosphate (Si-TCP) and 33% hydroxylapatite (HA). It has an open pore structure similar to human cancellous bone, with a pore size between 200 and 500 μm and a porosity level around 60% [72, 73]. Disks of Skelite measuring 9 mm in diameter and 1.2 mm in thickness were seeded with osteoblasts and cultured for 8 weeks. Samples were washed in phosphate-buffered saline, fixed in paraformaldehyde, stored in 70% ethanol and then dried before imaging. The samples were mounted three and three in a Perspex cylinder, separated by fibre tissue paper and lightly compressed with a foam material to take advantage of the 7 mm vertical field of view.

Imaging was performed using undulator radiation monochromatised to 30 keV using a single Si crystal monochromator. A 10 μm Gadox scintillating screen, standard light microscope optics and a FreLoN CCD camera were used for detection, set to yield a pixel size of 5 μm. Tomographic data sets comprising 2000 angles of view over a 180° rotation were recorded over 3 distances (0.01, 0.33 and 0.99 m), with an exposure time of 0.4 s. Phase retrieval was performed using a multi-material prior. The two δ/β-ratios were calculated using the XOP software and set to 335 for Skelite and 2000 for soft tissue.

The reconstruction is shown in (Fig. 6.5). Attenuation and phase tomograms are shown to illustrate the increased visibility of the soft tissue in the phase tomogram. This enables segmentation, visualisation (Fig. 6.5d) and quantitative analysis (such as volume, volume filling fraction and local thickness) of the soft tissue phase. Additionally, sensitivity was sufficiently high to permit segmentation of the osteoblasts. These types of measurements can be used to evaluate the osteoconductive and osteoinductive properties of different scaffold types, as well as the impact of different culture conditions, for example, different biochemical environments or microgravity.

3.2.2 Imaging of Forming Bone in Young Mice

The sensitivity of X-ray phase contrast imaging permits to reveal the main characteristics of the important tissue compartments in forming bones, including the rapidly changing soft tissue and the partially or fully mineralised bone regions, while revealing subtle density differences in 3D. Growing femur bone midshafts of healthy mice at 1, 3, 7, 10 and 14 days postpartum were imaged. It was possible to create exquisitely detailed maps of the juxtaposed soft, partially mineralised and highly mineralised bone, giving insight into the environment in which bone cells create and shape the bone matrix [25].

Growing bone exhibits a complex architecture in 3D, which undergoes extensive reorganisation and restructuring, from the initially deposited bone material to the mature bone. Consequently, these forming tissues exhibit a range of very dif-

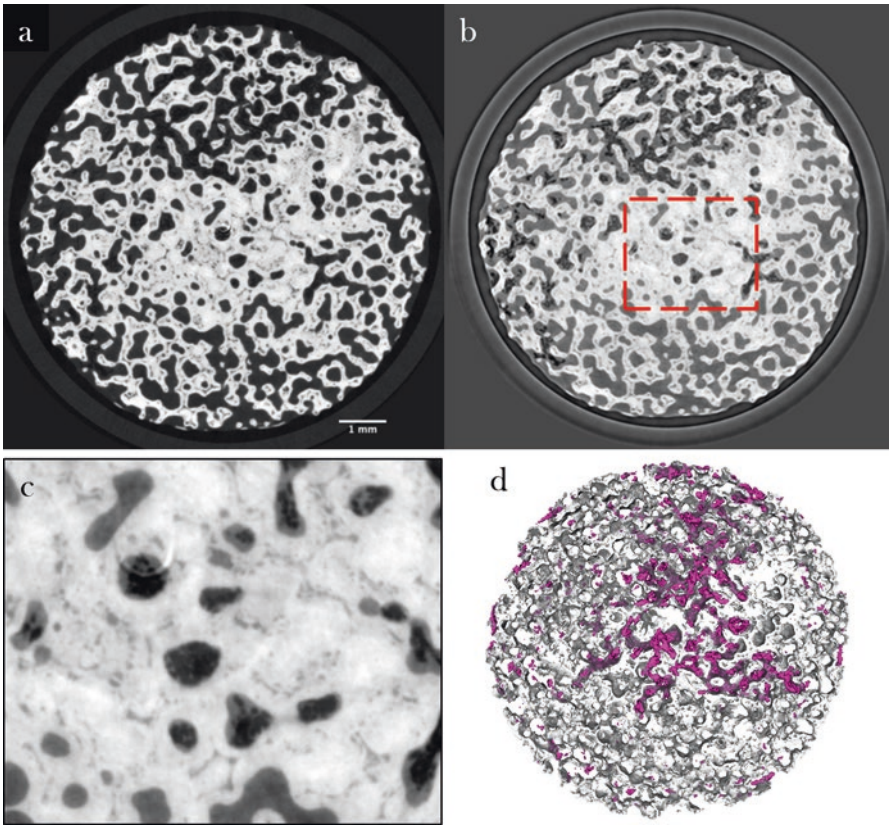

Fig. 6.5 Phase μCT imaging of mineralised scaffolds. (**a**) Standard μCT image of a Skelite disk seeded with osteoblasts. (**b**) Phase tomogram of the same disk, showing clearly the deposited soft tissue. It can be seen that soft tissue is formed mainly inside the scaffold construct and that the volume filling fraction is high. (**c**) Zoom on the marked area in (b). There is sufficient contrast to segment not only scaffold and soft tissue but the osteocytes as well. (**d**) Rendering of the scaffold and the segmented osteocytes

ferent morphologies. Different morphologies can be observed in the same skeleton during growth or healing, for example, following fracture or biomaterial implantation. When non-mineralised osteoid matrix starts to mineralise, bone material in both formation and healing conditions appears as a highly porous structure, where mineralised and soft tissues are intermixed. Such early formed bone tissues gradually transform and rearrange into solid cortical bone that eventually takes on the appearance of the mature tissue [74–81]. The initial tissue morphology is transient and contains zones of markedly different morphologies. Different degrees of mineralisation can be observed in adjacent sites at the same time. Due to the dynamically changing tissue geometry, mechanical properties are difficult to define and measure. Detailed information about both architecture and density is thus necessary for understanding and possibly predicting bone growth and tissue repair.

In-line phase tomography was used for the quantification and characterisation of the temporal evolution of morphology and mineralisation during bone genesis in healthy mice. The left femur was dissected from female wild-type C57BL/6 mice aged 1, 3, 7, 10 and 14 days after birth. Skin and muscle was partially removed, while the bones remained intact. Samples were fixed and stored in 70 wt% ethanol at 4 °C. The samples were imaged in an ethanol atmosphere, mounted within small polypropylene cylindrical vials. A filtered "pink" X-ray beam at 26 keV was used to record tomographic scans of 3999 images at five sample-to-detector distances with an exposure time of 100 ms per image. The detector was a custom-made indirect system consisting of a 10×/0.3NA Olympus objective combined with a thin-single crystal scintillator and a pco.edge sCMOS camera [82]. Phase retrieval was performed using the multi-material algorithm outlined in Sect. 2, with a delta-to-beta ratio of 429.9 in mineralised bone and 1857 elsewhere. The local mass density can be accessed through a simple scaling of the resulting phase tomograms [18].

Histogram analysis was used to calibrate slight offsets in the background (air) in the density data [20]. The images were segmented into bone and soft tissue compartments using standard thresholding [81]. 3D renderings were performed using CTVox (Bruker-microCT, Kontich, Belgium) by mapping colour and transparency in the transfer functions to tissue density.

Renderings are shown in Fig. 6.6, where blue represents soft tissue, green represents bone and red represents very high density within the bone (presumably mineralised cartilage). Cutouts are shown to reveal what would be masked by the encasing soft tissue. During development, the 3D distribution of mineralised material changes from a loosely connected foam-like structure (1–7 days) into a condensed bone cortex, sandwiched between soft tissue layers. High-density islands (possibly mineralised cartilage) seem to be encapsulated within the bone compartment.

The mineralised tissue only is shown in Fig. 6.7. The cortical bone develops from a highly porous scaffold consisting of mineralised struts into the mature solid ring seen in the samples obtained from 14-day-old animals. It can be seen in the high-resolution cutouts that the bone morphology changes extensively during maturation, through a redistribution of high-density regions located within the lower-density bone.

In addition to the qualitative morphological information, the phase tomograms permit quantification of 3D local mass density. The soft tissue was measured to have a density of 1.1–1.4 g/cm^3 at all ages. These values are slightly higher than published values for soft (skeletal) tissue (1.0–1.06 g/cm^3) [25]. The observed higher values could be due to higher concentrations of mineral precursor phases in the soft tissue. Higher density has similarly been revealed by other methods in forming bone tissue [18, 71, 76, 83] The amount of bone increases with increasing age and contains a high-density component, presumably mineralised cartilage [84–86], much of which is later replaced with less dense material (bone).

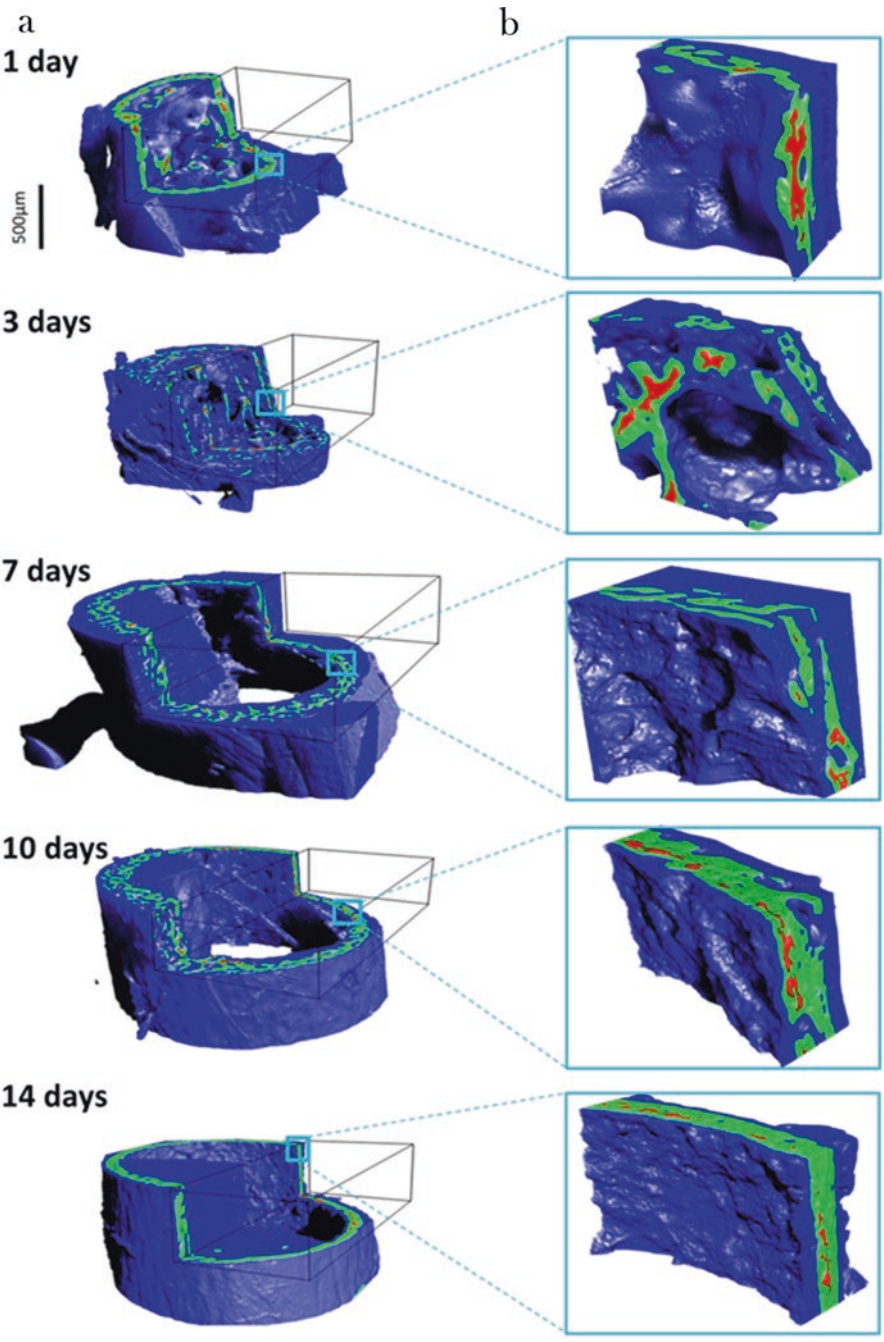

Fig. 6.6 Renderings of the mass density distribution in growing mouse femurs at different time points. (**a**) Soft tissue (blue) surrounds the mineralised bone (green). Islands of high mineral density (presumably mineralised cartilage) exceeding 1.9 g/cm^3 (red) can be seen. (**b**) The denser islands can be better observed on magnified cutouts

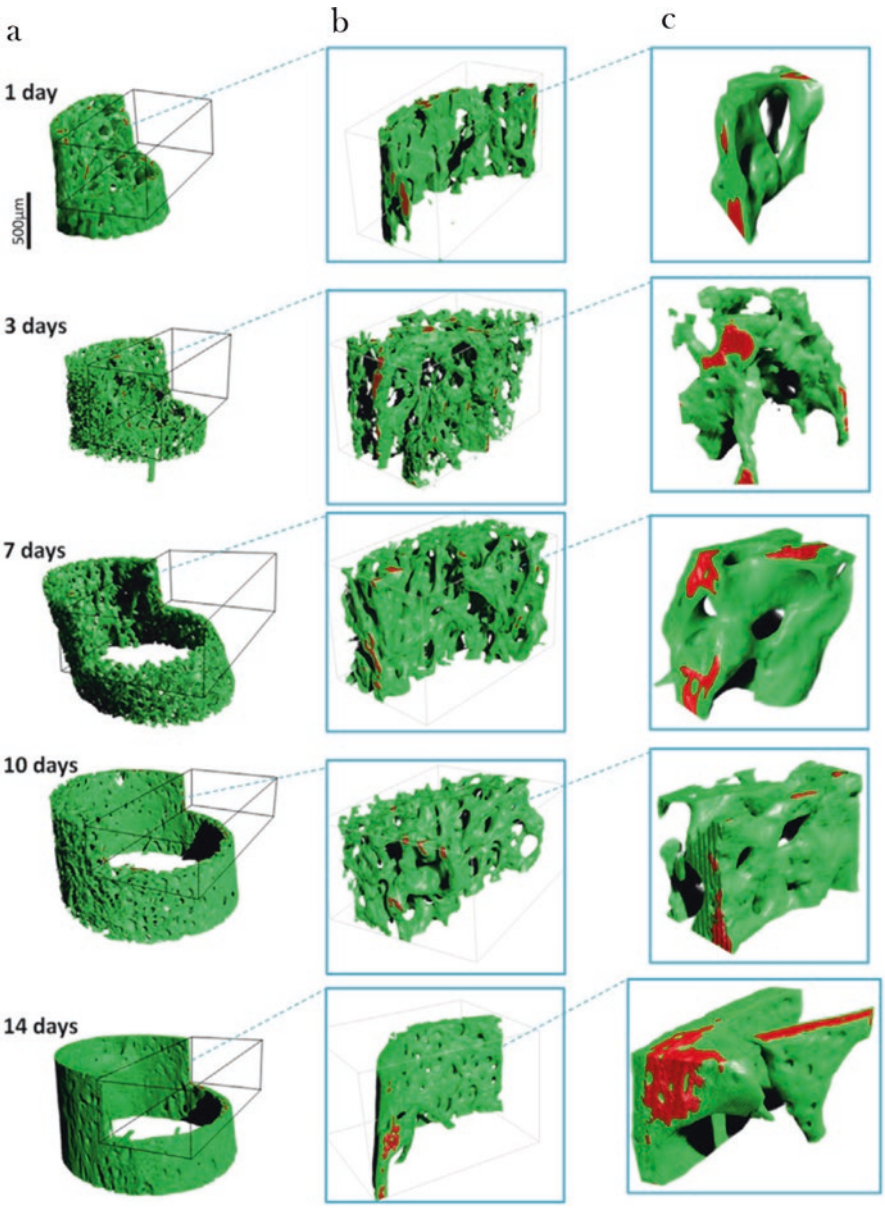

Fig. 6.7 3D renderings of the mineralised tissue only from Fig. 6.6. Bone (green) and high-density zones (red) with increasing magnifications (**a**–**c**) are shown. The high mass density (exceeding 1.9 g/cm^3) is always found within regions of lower density. Note the drastic architectural changes from 1 to 14 days, changing from a foam-like open network to a solid tube-like cortical structure

4 Perspectives

There is a growing interest in phase sensitive X-ray imaging methods in regenerative medicine. This is mainly motivated by the high resolution and sensitivity offered by the technique. We presented here examples of imaging studies using phase tomography: nano-tomography of bone and micro-tomography of growing bone in healthy growing mice and in artificial bone constructs. Similar approaches could be used to study bone tissue growth and maturation in adult animals, during healing. Indeed, much remains unknown about the similarities and differences in the 3D bone tissue dynamics when comparing bone growth/genesis and fracture and tissue healing, for example, in response to implantation of biomaterials. The ability to resolve fine density variations in different tissues might allow the elucidation of the bone formation process in the tissue engineering scenario.

References

1. Bonse U (2002) Developments in X-ray tomography II. Proc. of SPIE 4503
2. Bouxsein ML, Boyd SK, Christiansen BA, Guldberg RE, Jepsen KJ, Müller R (2010) Guidelines for assessment of bone microstructure in rodents using micro-computed tomography. J Bone Miner Res 25(7):1468–1486
3. Engelke K, Karolczak M, Lutz A, Seibert U, Schaller S, Kalender W (1999) Micro-CT. Technology and application for assessing bone structure. Radiologe 39(3):203–212
4. Hildebrand T, Laib A, Müller R, Dequeker J, Rüegsegger P (1999) Direct three-dimensional morphometric analysis of human cancellous bone: microstructural data from spine, femur, iliac crest, and calcaneus. J Bone Miner Res 14(7):1167–1174
5. Salomé M et al (1999) A synchrotron radiation microtomography system for the analysis of trabecular bone samples. Med Phys 26(10):2194
6. Nuzzo S, Peyrin F, Cloetens P, Baruchel J, Boivin G (2002) Quantification of the degree of mineralization of bone in three dimensions using synchrotron radiation microtomography. Med Phys 29:2672–2681
7. Langer M, Prisby R, Peter Z, Guignandon A, Lafage-Proust M-H, Peyrin F (2011) Simultaneous 3D imaging of bone and vessel microstructure in a rat model. IEEE Trans Nucl Sci 58(1):139–145 . PART 1
8. Prisby R et al (2011) Intermittent PTH 1-84 is osteoanabolic but not osteoangiogenic and relocates bone marrow blood vessels closer to bone forming sites. J Bone Miner Res 26(11):2583–2596
9. Momose A, Takeda T, Itai Y, Hirano K (1996) Phase–contrast X–ray computed tomography for observing biological soft tissues. Nat Med 2(4):473–475
10. Zanette I et al (2013) Holotomography versus X-ray grating interferometry: a comparative study. Appl Phys Lett 103:244105
11. Lang S et al (2014) Experimental comparison of grating- and propagation-based hard X-ray phase tomography of soft tissue. J Appl Phys 116(15):154903
12. Varga P, Weber L, Hesse B, Langer M (2016) Synchrotron X-ray phase nanotomography for bone tissue characterization. In: X-ray and neutron techniques for nanomaterials characterization. Springer Berlin Heidelberg, Berlin\Heidelberg, pp 1–42

13. Langer M, Boistel R, Pagot E, Cloetens P, Peyrin F (2010) X-ray in-line phase microtomography for biomedical applications. In: Méndez-Vilas A, Díaz J (eds) Microscopy: science, technology, applications and education, vol 1., no. 4. Formatex Research Center, Badajoz, pp 391–402
14. Hagen CK et al (2015) High contrast microstructural visualization of natural acellular matrices by means of phase-based x-ray tomography. Sci Rep 5:18156
15. Bravin A, Coan P, Suortti P (2013) X-ray phase-contrast imaging: from pre-clinical applications towards clinics. Phys Med Biol 58(1):R1–R35
16. Snigirev A, Snigireva I, Kohn V, Kuznetsov S, Schelokov I (1995) On the possibilities of x-ray phase contrast microimaging by coherent high-energy synchrotron radiation. Rev Sci Instrum 66(12):5486
17. Cloetens P et al (1999) Holotomography: quantitative phase tomography with micrometer resolution using hard synchrotron radiation x rays. Appl Phys Lett 75(19):2912
18. Langer M, Pacureanu A, Suhonen H, Grimal Q, Cloetens P, Peyrin F (2012) X-ray phase nanotomography resolves the 3D human bone ultrastructure. PLoS One 7(8):e35691
19. Varga P et al (2013) Investigation of the 3D orientation of mineralized collagen fibrils in human lamellar bone using synchrotron X-ray phase nano-tomography. Acta Biomater 9:8118–8127
20. Hesse B et al (2014) Canalicular network morphology is the major determinant of the spatial distribution of mass density in human bone tissue – evidence by means of synchrotron radiation phase-contrast nano-CT. J Bone Miner Res 30(2):346–356
21. Peyrin F, Dong P, Pacureanu A, Langer M (2014) Micro- and Nano-CT for the study of bone ultrastructure. Curr Rev Osteoporos 12:346–356
22. Hesse B et al (2014) Accessing osteocyte lacunar geometrical properties in human jaw bone on the submicron length scale using synchrotron radiation μCT. J Microsc 255(3):158–168
23. Langer M, Peyrin F (2016) 3D X-ray ultra-microscopy of bone tissue. Osteoporos Int 27(2):441–455
24. Giuliani A et al (2013) Three years after transplants in human mandibles, histological and in-line holotomography revealed that stem cells regenerated a compact rather than a spongy bone: biological and clinical implications. Stem Cells Transl. Med. 2(4):316–324
25. Bortel EL et al (2017) Combining coherent hard X-ray tomographies with phase retrieval to generate three-dimensional models of forming bone. Front Mater 4:39
26. Weber L, Langer M, Tavella S, Ruggiu A, Peyrin F (2016) Quantitative evaluation of regularized phase retrieval algorithms on bone scaffolds seeded with bone cells. Phys Med Biol 61(9):215–231
27. Cloetens P et al (1997) Observation of microstructure and damage in materials by phase sensitive radiography and tomography. J Appl Phys 81(9):5878
28. Mokso R, Cloetens P, Maire E, Ludwig W, Buffière J-Y (2007) Nanoscale zoom tomography with hard x rays using Kirkpatrick-Baez optics. Appl Phys Lett 90(14):144104
29. Cloetens P, Barrett R, Baruchel J, Guigay J-P, Schlenker M (1996) Phase objects in synchrotron radiation hard x-ray imaging. J Phys D Appl Phys 29(1):133–146
30. Langer M et al (2014) Priors for X-ray in-line phase tomography of heterogeneous objects. Philos Trans A Math Phys Eng Sci 372(2010):20130129
31. Davidoiu V, Sixou B, Langer M, Peyrin F (2013) In-line phase tomography using nonlinear phase retrieval. Ann Univ Bucharest Math Ser 4(LXII):115–122
32. Sixou B, Davidoiu V, Langer M, Peyrin F (2013) Absorption and phase retrieval with Tikhonov and joint sparsity regularizations. Inverse Probl Imaging 7(1):267–282
33. Davidoiu V, Sixou B, Langer M, Peyrin F (2014) Non-linear phase tomography based on Fréchet derivative. Adv Comput Tomogr 3(4):39–50
34. Ruhlandt A, Krenkel M, Bartels M, Salditt T (2014) Three-dimensional phase retrieval in propagation-based phase-contrast imaging. Phys Rev A 89(3):33847
35. Kostenko A, Batenburg KJ, Suhonen H, Offerman SE, van Vliet LJ (2013) Phase retrieval in in-line x-ray phase contrast imaging based on total variation minimization. Opt Express 21(1):710–723

36. Langer M, Cloetens P, Peyrin F (2009) Fourier-wavelet regularization of phase retrieval in x-ray in-line phase tomography. J Opt Soc Am A Opt Image Sci Vis 26(8):1876–1881
37. Hehn L et al (2018) Nonlinear statistical iterative reconstruction for propagation-based phase-contrast tomography. APL Bioeng 2(1):16105
38. Rositi H et al (2014) Computer vision tools to optimize reconstruction parameters in x-ray in-line phase tomography. Phys Med Biol 59(24):7767–7775
39. Langer M, Cloetens P, Pacureanu A, Peyrin F (2012) X-ray in-line phase tomography of multimaterial objects. Opt Lett 37(11):2151
40. Langer M, Cloetens P, Guigay J-P, Peyrin F (2008) Quantitative comparison of direct phase retrieval algorithms in in-line phase tomography. Med Phys 35(10):4556–4566
41. Paganin D, Mayo SC, Gureyev TE, Miller PR, Wilkins SW (2002) Simultaneous phase and amplitude extraction from a single defocused image of a homogeneous object. J Microsc 206(1):33–40
42. Langer M, Cloetens P, Peyrin F (2010) Regularization of phase retrieval with phase-attenuation duality prior for 3-D holotomography. IEEE Trans Image Process 19(9):2428–2436
43. Marinescu M et al (2013) Synchrotron radiation X-ray phase micro-computed tomography as a new method to detect Iron oxide nanoparticles in the brain. Mol Imaging Biol 15(5):552–559
44. Frachon T et al (2015) Dose fractionation in synchrotron radiation x-ray phase micro-tomography. Phys Med Biol 60(19):7543–7566
45. Weber L et al (2018) Registration of phase-contrast images in propagation-based X-ray phase tomography. J Microsc 269(1):36–47
46. Moosmann J, Hofmann R, Bronnikov A, Baumbach T (2010) Nonlinear phase retrieval from single-distance radiograph. Opt Express 18:25771–25785
47. Davidoiu V, Sixou B, Langer M, Peyrin F (2013) Nonlinear approaches for the single-distance phase retrieval problem involving regularizations with sparsity constraints. Appl Opt 52(17):3977–3986
48. Pacureanu A, Langer M, Boller E, Tafforeau P, Peyrin F (2012) Nanoscale imaging of the bone cell network with synchrotron X-ray tomography: optimization of acquisition setup. Med Phys 39(4):2229
49. Kingsmill VJ, Boyde A (1998) Mineralisation density of human mandibular bone: quantitative backscattered electron image analysis. J Anat 192(Pt 2):245–256
50. Giraud-Guille M-M, Besseau L, Martin R (2003) Liquid crystalline assemblies of collagen in bone and in vitro systems. J Biomech 36(10):1571–1579
51. Fratzl P, Weinkamer R (2007) Nature's hierarchical materials. Prog Mater Sci 52(8):1263–1334
52. Schneider P, Meier M, Wepf R, Müller R (2010) Towards quantitative 3D imaging of the osteocyte lacuno-canalicular network. Bone 47(5):848–858
53. Currey JD, Shahar R (2013) Cavities in the compact bone in tetrapods and fish and their effect on mechanical properties. J Struct Biol 183(2):107–122
54. Bonewald LF (2011) The amazing osteocyte. J Bone Miner Res 26(2):229–238
55. Qing H et al (2012) Demonstration of osteocytic perilacunar/canalicular remodeling in mice during lactation. J Bone Miner Res 27(5):1018–1029
56. Group M, Hero S, Burr DB (1996) In vivo measurement of human tibial strains during vigorous activity. Bone 18(5):405–410
57. You L, Cowin SC, Schaffler MB, Weinbaum S (2001) A model for strain amplification in the actin cytoskeleton of osteocytes due to fluid drag on pericellular matrix. J Biomech 34(11):1375–1386
58. Varga P et al (2015) Strains experienced by osteocytes in situ as predicted by case specific finite element analysis. Biomech Model Mechanobiol 14(2):267–282
59. Anderson EJ, Knothe Tate ML (2008) Idealization of pericellular fluid space geometry and dimension results in a profound underprediction of nano-microscale stresses imparted by fluid drag on osteocytes. J Biomech 41(8):1736–1746
60. McNamara LM, Majeska RJ, Weinbaum S, Friedrich V, Schaffler MB (2009) Attachment of osteocyte cell processes to the bone matrix. Anat Rec (Hoboken) 292(3):355–363

61. Verbruggen SW, Vaughan TJ, McNamara LM (2012) Strain amplification in bone mechanobiology: a computational investigation of the in vivo mechanics of osteocytes. J R Soc Interface 9(75):2735–2744
62. McCreadie BR, Hollister SJ, Schaffler MB, Goldstein SA (2004) Osteocyte lacuna size and shape in women with and without osteoporotic fracture. J Biomech 37(4):563–572
63. Bonivtch AR, Bonewald LF, Nicolella DP (2007) Tissue strain amplification at the osteocyte lacuna: a microstructural finite element analysis. J Biomech 40(10):2199–2206
64. Deligianni DD, Apostolopoulos CA (2008) Multilevel finite element modeling for the prediction of local cellular deformation in bone. Biomech Model Mechanobiol 7(2):151–159
65. Schneider P, Ruffoni D, Larsson D, Chiapparini I, Müller R (2012) Image-based finite element models for the investigation of osteocyte mechanotransduction. J Biomech 45(1):S436
66. Dorozhkin SV (2010) Calcium orthophosphates as bioceramics: state of the art. J Funct Biomater 1(1):22–107
67. Eliaz N, Metoki N (2017) Calcium phosphate bioceramics: a review of their history, structure, properties, coating technologies and biomedical applications. Materials (Basel) 10(4):334
68. Glazer PA, Spencer UM, Alkalay RN, Schwardt J (2001) In vivo evaluation of calcium sulfate as a bone graft substitute for lumbar spinal fusion. Spine J 1(6):395–401
69. Komlev VS et al (2006) Kinetics of in vivo bone deposition by bone marrow stromal cells into porous calcium phosphate scaffolds: an X-ray computed microtomography study. Tissue Eng 12(12):3449–3458
70. Cancedda R et al (2007) Bulk and interface investigations of scaffolds and tissue-engineered bones by X-ray microtomography and X-ray microdiffraction. Biomaterials 28(15):2505–2524
71. Langer M, Liu Y, Tortelli F, Cloetens P, Cancedda R, Peyrin F (2010) Regularized phase tomography enables study of mineralized and unmineralized tissue in porous bone scaffold. J Microsc 238(3):230–239
72. Sayer M et al (2003) Structure and composition of silicon-stabilized tricalcium phosphate. Biomaterials 24(3):369–382
73. Reid JW, Pietak A, Sayer M, Dunfield D, Smith TJN (2005) Phase formation and evolution in the silicon substituted tricalcium phosphate/apatite system. Biomaterials 26(16):2887–2897
74. Miller LM, Little W, Schirmer A, Sheik F, Busa B, Judex S (2007) Accretion of bone quantity and quality in the developing mouse skeleton. J Bone Miner Res 22(7):1037–1045
75. Manjubala I et al (2009) Spatial and temporal variations of mechanical properties and mineral content of the external callus during bone healing. Bone 45(2):185–192
76. Lange C et al (2011) Fetal and postnatal mouse bone tissue contains more calcium than is present in hydroxyapatite. J Struct Biol 176(2):159–167
77. Preininger B, Checa S, Molnar FL, Fratzl P, Duda GN, Raum K (2011) Spatial-temporal mapping of bone structural and elastic properties in a sheep model following osteotomy. Ultrasound Med Biol 37(3):474–483
78. Sharir A, Stern T, Rot C, Shahar R, Zelzer E (2011) Muscle force regulates bone shaping for optimal load-bearing capacity during embryogenesis. Development 138(15):3247–3259
79. Vetter A et al (2011) The mechanical heterogeneity of the hard callus influences local tissue strains during bone healing: a finite element study based on sheep experiments. J Biomech 44(3):517–523
80. Rohrbach D, Preininger B, Hesse B, Gerigk H, Perka C, Raum K (2013) The early phases of bone healing can be differentiated in a rat osteotomy model by focused transverse-transmission ultrasound. Ultrasound Med Biol 39(9):1642–1653
81. Bortel EL, Duda GN, Mundlos S, Willie BM, Fratzl P, Zaslansky P (2015) Long bone maturation is driven by pore closing: a quantitative tomography investigation of structural formation in young C57BL/6 mice. Acta Biomater 22:92–102
82. Douissard P-A et al (2012) A versatile indirect detector design for hard X-ray microimaging. J Instrum 7(9):P09016–P09016

83. Golub EE (2009) Role of matrix vesicles in biomineralization. Biochim Biophys Acta, Gen Subj 1790(12):1592–1598
84. Vanleene M, Rey C, Ho Ba Tho MC (2008) Relationships between density and Young's modulus with microporosity and physico-chemical properties of Wistar rat cortical bone from growth to senescence. Med Eng Phys 30(8):1049–1056
85. Bach-Gansmo FL, Irvine SC, Brüel A, Thomsen JS, Birkedal H (2013) Calcified cartilage islands in rat cortical bone. Calcif Tissue Int 92(4):330–338
86. Shipov A, Zaslansky P, Riesemeier H, Segev G, Atkins A, Shahar R (2013) Unremodeled endochondral bone is a major architectural component of the cortical bone of the rat (Rattus norvegicus). J Struct Biol 183(2):132–140

Chapter 7
Inside the Bone: Tissue Engineering and Regenerative Medicine Applications in Orthopedics

Marta Nardini, Maria Elisabetta Federica Palamà, Alessio Romaldini, and Milena Mastrogiacomo

Abstract One of the main problems, not fully resolved in orthopedics yet, is the regeneration of large bone defects. The intricate bone composition makes the healing process very complex when dealing with extensive lesions. Although traditional therapeutic approaches allowed significant progresses by proposing new bone substitutes and prosthetic devices, the obtained results remain questionable. To regenerate the bone tissue, tissue engineering focused on the use of mesenchymal cells derived from the bone marrow, in the attempt to restore an environment more suitable for the restitutio ad integrum of the tissue. This chapter describes and discusses the tissue engineering approach in bone repair with particular regard to the new investigative tools developed in recent years to monitor the process.

1 Bone: Micro- and Macroscopic Composition

Bone tissue represents the framework of the body of all vertebrates. It is a connective tissue with a supporting role composed of mineralized extracellular matrix, organic part, and cellular component.

The mineralized extracellular matrix consists mainly of calcium phosphate and other minerals that provide compactness. The organic part of the bone tissue is made up of type I collagen fibers, proteoglycans, and glycoproteins, mimicking the iron of reinforced concrete and giving flexibility to the skeleton.

The cellular components play an important role in the building and maintaining of the bone tissue from its origins and during life span of the organism.

The cellular portion is represented by three principal types of cells: osteoblasts, osteoclasts, and osteocytes. These three cell types have different, and almost opposite, functions. Osteoblasts are cells responsible for the production of the organic

M. Nardini · M. E. F. Palamà · A. Romaldini · M. Mastrogiacomo (✉)
Department of Experimental Medicine, University of Genoa, Genoa, Italy
e-mail: maddalena.mastrogiacomo@unige.it

A. Giuliani, A. Cedola (eds.), *Advanced High-Resolution Tomography in Regenerative Medicine*, Fundamental Biomedical Technologies,
https://doi.org/10.1007/978-3-030-00368-5_7

matrix of the bone, and preferentially they tend to work in groups on the deposition front of new bone. Osteoblasts are terminally differentiated mesenchymal stem cells (MSCs). They are capable to synthetize collagen type I and other important protein for the bone formation like osteopontin and osteocalcin that are playing a role in the formation of the matrix. Eventually this matrix undergoes a mineralization through the deposition of Ca and PO_4 salts. The osteoclasts have the opposite function compared to the osteoblasts. These cells maintain, remodel, and resorb the bone, through the acidification of the bone microenvironment and the activity of enzymes of exocytosis, like collagenase.

The osteocytes represent the quiescent cell population. They are located in the small compartments of the matrix, called *lacuna*, and are ready "to the starting point" in case there would be a trauma or a fracture, to remodel the bone. Osteocytes have cytoplasmic extensions useful for the nutrient and waste exchange.

At the macroscopic level, the bone is made of two main domains, a compact portion called *cortical* that gives strength and a portion that has cavities, like a sponge, defined as *spongiosa* or *trabecular*. This last portion gives lightness and flexibility to the bone tissue. Depending on the type of bone and the function it has to perform, this has different percentages of the two domains.

Another very important external part of the bone is represented by the *periosteum*, which has a high number of blood vessels to carry nutrients to the bone tissue and nerve endings.

The bone origins from the embryonic mesenchyme, the connective tissue of the embryo. The bone cells derive from bone marrow stromal cells (BMSC), a heterogeneous population from which originate different types of cells. To start the differentiation process to the bone lineage, several different factors are important, such as the BMP (bone morphogenetic protein) family, FGF (fibroblast growth factor), and TGF-ß1 (transforming growth factor ß1). All factors involved in the process lead to gene activation or deactivation. The main transcription factor that activates the expression of the osteoblast-specific genes is *Cbfa-1* [15, 30]. Its expression precedes the start of the osteoblast differentiation process. This transcription factor is crucial for the bone formation. Mice that are *Cbfa-1*$^{-/-}$ have a cartilaginous bone.

These processes are very important during the embryogenesis, but they continue to play a role during the life span, since the bone tissue is subjected to a continuous structural renovation.

The osteocytes, with their cytoplasmic extensions, work like mechanoreceptors. The annexes receive mechanical stimuli from the mussels inserted to the bone. Following these stimuli, specific biochemical pathways are activated, and appropriate responses are elicited, in order for the osteoblast or osteoclast to lay down or to remove the bone tissue.

2 Limits to the Bone Regeneration

Given the complexity of the entire structure of the bone, the healing of extensive bone injuries is still a difficult goal. The bone itself possesses good regenerative capacities, but these are insufficient in the case of complex lesions. In the case of complex

injuries, several negative factors intervene on an effective self-compensation. The three main factors that determine negative effects are: (i) the extended time needed to healing process because of proliferation and differentiation of osteoprogenitors and deposition of mineralized matrix, (ii) the distance between the marginal breakage of the lesion; and (iii) in many cases, the absence of an appropriate substrate on which the cells can migrate. Nowadays, the prevailing therapy is the osteotomy followed by bone distraction (Ilizarov technique) or the use of auto- or allogenic bone [3, 7].

The Ilizarov technique has a high rate of success. However, there are a lot of disadvantages including the long rehabilitation time, the high frequency of complications, and the serious discomfort for the patient, due to the presence of the fixation apparatus. The use of autologous bone also presents a lot of complications such as nonunion and infection consequent to the treatment. Moreover, this therapeutic approach requires two different interventions, the first for the bone collection and the second for its transplantation.

The allogenic bone graft has the same problems than the autologous bone transplantation, and in addition difficulties related to the donor-receiver match and strictly law regulation. The implant of bioceramics proved to be useful only for small bone defects [27, 34].

Tissue engineering and regenerative medicine could make a great contribution to the field. The first laudable results by a tissue engineering approach, i.e., the combined use of cells, biomaterial, and growth factors, were obtained in the early 2000s [21, 29]. In this study, cells expanded ex vivo were loaded on a porous ceramic scaffold, and the construct implanted in three patients with a bone loss of 4–7 cm (Fig. 7.1). However, it appears difficult that this approach could be extended, as such, to a large number of patients. The recovery from the patient and the expansion of the osteogenic cells require special lab facilities and long times of culture and entail high costs. Other only partially resolved problems are the choice of the composition for the optimal scaffold, the vascularization of the construct after its implantation, and, last but not least, the control of the immunoresponse if allogeneic cells are used.

3 New Approach in Bone Regeneration

3.1 Osteogenic Cells

According to the “classical” definition of tissue engineering based on triad of cells, biomaterials, and signalling molecules, the use of stem cells is requested to achieve a successful repair of injured tissue. A postnatal bona fide stem cell is defined as a clonogenic primitive (unspecialized) cell able to self-renew and to generate a tissue-specific terminally differentiated cell progeny (potency). Bone marrow stromal cells (BMSCs) represent an established in vitro heterogeneous population of progenitor cells isolated from patient’s bone marrow. BMSCs have been broadly used as source of osteogenic cells for bone tissue engineering procedures in preclinical and clinical studies [8, 13]. Caplan [9] termed cultured BMSCs as “mesenchymal stem cells”

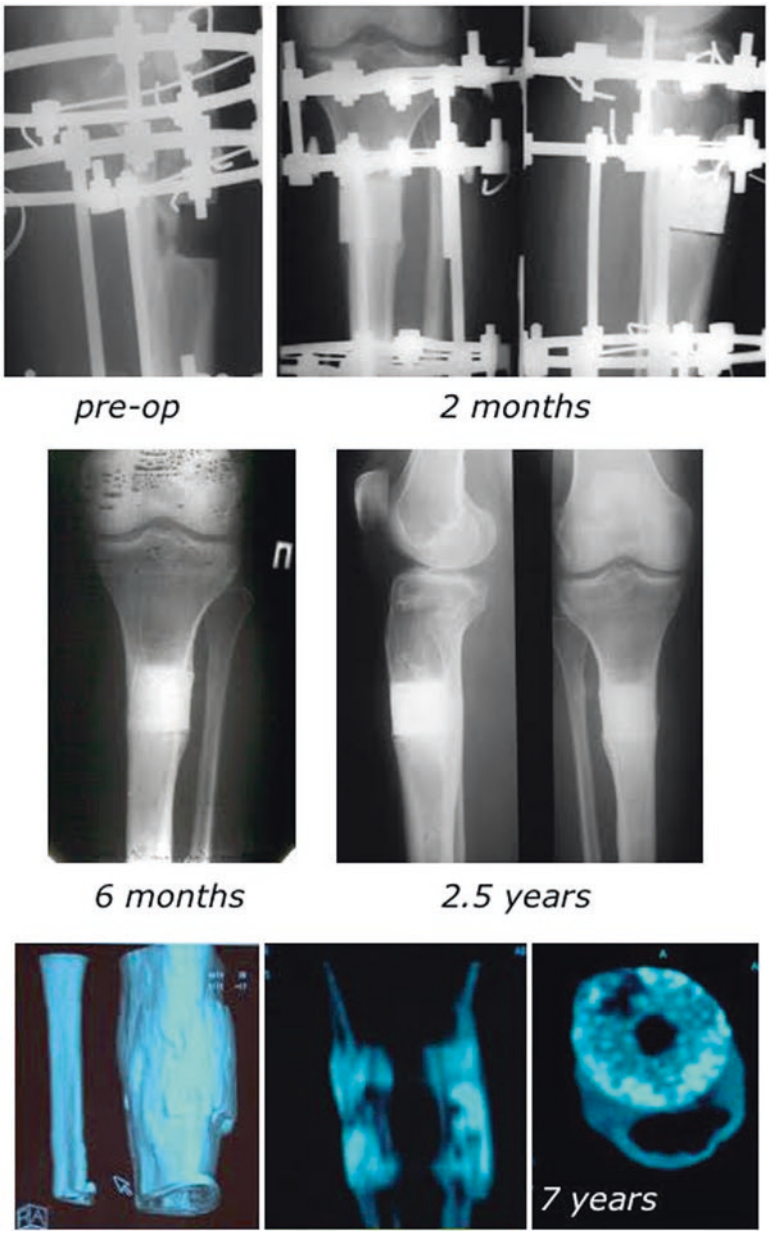

Fig. 7.1 X-rays and CT scan at different follow-up times of the first patient whose long bone defect in the proximal tibia was treated by the implantation of a porous ceramic scaffold seeded with in vitro expanded autologous BMSC. On the preoperative radiograph, a 4-cm long gap of the bone is shown. At 6 months, a good integration between the implant and the tibia was already observed. CT-scan analysis at 7 years showed a complete healing of the gap, but the non-reabsorbable HA ceramic scaffold was still present

(MSCs) since these cells were able to differentiate into osteoblasts, chondrocytes, and adipocytes. Dominici et al. [14] recommended the new designation "multipotent mesenchymal stromal cells" for MSCs and defined a standard set of criteria for identifying these cells: plastic adherence; CD105, CD73, and CD90 expression; lack of hematopoietic and endothelial marker expression; and in vitro trilineage mesenchymal – osteogenic, chondrogenic, and adipogenic differentiation. Based on this definition, cells derived from different adult and fetal tissues were described in the literature as MSCs, isolated from other than bone marrow tissues such as adipose, periosteum, placenta, or amniotic fluid [14, 25]. Moreover, it was also reported that bone marrow MSCs have a perivascular origin, and it was hypothesized the same for all types of MSCs [10, 25]. Sacchetti et al. described the existence of a subset of progenitors within BMSCs with a specific osteogenic potential [31]. In particular, these cells were defined as $CD146^+$ colony-forming unit fibroblasts (CFU-Fs) and in situ corresponded to adventitial reticular cells, which reside in bone marrow sinusoids. Upon subcutaneous transplantation into immunocompromised mice, single $CD146^+$ CFU-Fs were able to recapitulate the bone organogenesis and to generate a heterotopic ossicle (bone and bone marrow stroma) with host-derived hematopoietic tissue and blood vessels within it. From such ossicle, it was possible to harvest $CD146^+$ CFU-Fs, which could be secondarily passaged and serially transplanted. Considering these evidences concerning multipotency and self-renewal, $CD146^+$ clonogenic cells derived from bone marrow were clearly committed to skeletogenesis and were named skeletal stem cells (SSCs) [5, 31]. So far, the presence of skeletogenic stem cells within MSCs derived from other tissues has not been definitely demonstrated. The proven commitment to skeletogenesis and the easy isolation from patient's bone marrow designate BMSCs as excellent candidate for bone repair by tissue engineering. It should be also noted that the proposed use of BMSCs in clinical trials obtains faster approval by regulatory authorities because of the affinity between the cell tissue of origin and the target tissue.

3.2 Biomaterials

One of the critical issues, in the regeneration of large bone defects, concerns the need to have a support that drives the regenerative process. Therefore, the first step in the realization of an engineered tissue is the design and construction of a support structure, called biomaterial or scaffold [17]. This acts as a substrate for the growth of the cells that will give rise to the new tissue. During the 2nd Consensus Conference on Definitions in Biomaterials organized by European Society for Biomaterials, a biomaterial is described as "a material intended to interface with biological systems to evaluate, treat, augment or replace any tissue, organ or function of body" [35]. It is a sort of three-dimensional "platform," able to attract osteoprogenitors, which colonize the support and begin to generate a new tissue by proliferation, differentiation, and deposition of extracellular matrix. The scaffold structure has to allow the transport of nutrients, metabolites, and regulatory molecules to and from the cells.

The mechanical properties of the scaffold should ideally correspond to those of the tissue target, to provide mechanical integrity, resistance to pressure, and other physical parameters responding to the characteristics of the tissue in vivo.

A biomaterial must have some basic properties to be used in the field of tissue engineering [17]:

- Biocompatibility: it is the first property to consider for every type of scaffold designed for clinical application. After implantation, the construct must elicit a negligible immune reaction to avoid severe inflammatory responses, which could lead to a reduction of healing or the rejection by the organism [33].
- Biodegradation: scaffolds and constructs are not intended as permanent installations. The scaffold must therefore be reabsorbable to allow the cells to produce their own extracellular matrix. The by-products of this degradation must also be nontoxic and eliminated by the organism without interference with other organs and tissues.
- Structural organization: this characteristic affects cell migration, nutrient's diffusion within the construct, elimination of waste products outward the scaffold, and degree of vascularization [26, 28].
- Mechanical compatibility: the production of scaffolds with adequate mechanical properties is one of the major challenges in this field. The implanted scaffold must have sufficient mechanical integrity to function from the time of implantation to completion of the remodeling process.

Regarding specifically bone tissue regeneration, there are other requirements that are necessary in order to produce biomaterials suitable for the purpose:

- Osteoconductivity: the ideal material should guarantee the adhesion and proliferation of cells that generate bone tissue, as well as the formation of new vessels. In this regard, not only the composition but also the structure of the biomaterial is particularly important. For this reason, it must contain sufficient space for vascularization and cellular colonization. In the case of bone reconstruction, the penetration of the vessels is possible only in the presence of at least 100 μm pores. Therefore, the macroporosity of the material must be higher than this value. Optimization of cellular colonization is achieved with interconnected porosity and pores ranging from 50 to 300 μm [6, 24].
- Osteoinductivity: the material should stimulate osteoprogenitors in situ to differentiate into osteoblasts. This characteristic is higher if the biomaterial is similar to the extracellular matrix of the original tissue [2].

In general, biomaterials are designed on the model of the extracellular matrix of the tissue that needs the treatment, since it guarantees the interaction between the cells and the stability of the tissues through the adhesion molecules. One of the approaches, for the regeneration of bone defects, involves the use of the demineralized bone matrix, produced by cortical bone decalcified and treated with radiation and chemical agents in order to eliminate the cellular component. The result is a bone matrix consisting only of denatured proteins, an osteoconductive substrate to be used in case of structurally stable bone lesions.

Among the most common biomaterials commercially used as bone substitutes in regenerative medicine, there are those made of ceramics and polymers.

The ceramics are biomaterials composed by calcium phosphates (some examples are hydroxyapatites and tricalcium phosphate). They are widely used in the regeneration of bone tissue, for their chemical and structural similarity with the mineral component of the native bone. The ceramic materials are produced from extremely pure powders and with crystallites of dimensions <1 μm to guarantee the maximum control of the microstructure of the finished material. In biomaterials, in fact, microstructure plays a fundamental role, much greater than the chemical composition. This is the element that allows interaction with the host tissue as well as determining its mechanical strength. An optimal colonization is obtained with pores of diameter between 50 and 300 μm [16].

The optimum porosity of the material is around 50–70% in order to have a good osteoconductivity [24]. Also the reabsorbability of the biomaterial depends on the microstructure.

The microstructure also influences the mechanical properties of the material, which will be better in a dense material and worse in a porous one; materials with pores larger than 500 μm cannot be used because they are too fragile. The disadvantages associated with the use of these materials are mainly related to mechanical properties: the fragility is superior, while the elasticity is lower than the original bone.

The development of advanced surface properties (such as extension, charge, and ability to alter the absorption of chemical species) is being studied to evaluate if they can be used to promote cellular response and proliferation, to induce neoosteogenesis and osteoinduction. Since bone substitutes consisting of a single component do not reflect all the characteristics of an ideal substitute, research in recent years has been focusing on combinations of materials.

3.3 Signalling Molecules

Signalling molecules have been broadly used to achieve a complete and long-lasting repair of bone lesions by a tissue engineering/regenerative medicine approach. In general, the function of such molecules is to regulate the cell behavior and to promote a desired cell fate. In particular, signalling molecules have been used to stimulate in vitro proliferation and/or commitment of osteogenic cells before to be loaded on biomaterials or to create in situ an osteogenic microenvironment in order that locally resident osteoprogenitors could migrate to the injury site and biomaterial-loaded osteogenic cells could differentiate toward all skeletal tissues (bone, adipose tissue, fibroblasts).

As example, in accordance with the first approach, it was reported that fibroblast growth factor-2 (FGF-2) promoted in vitro proliferation of BMSCs maintaining their osteogenic potential and FGF-2-expanded BMSCs, associated with hydroxyapatite ceramic, in vivo formed bone [23]. Concerning the second approach, bone morphogenetic proteins (BMPs) were used to treat bone defects, especially nonunion fractures, in association with absorbable carriers. Physiologically, BMPs, which are members of TGFβ superfamily, are secreted and function as matrix-associated

proteins regulating developmental skeletogenesis. In preclinical studies, it was shown that BMPs were able to induce bone formation (osteoinduction) and angiogenesis [4]. BMP2 and BMP7 are currently used as FDA-approved adjunct to standard therapies for bone repair [4, 32]. However, there are some concerns regarding BMP use [8]: (i) unprotected BMPs are in situ deteriorated or chemically modified reducing used dose and their biological efficacy; (ii) BMPs have a short time of residence at the injury site; (iii) the efficiency of BMP delivery systems is poor and has to be increased; and (iv) the cost of treatment is still very high [8, 32]. Moreover, several large-scale studies confirmed the frequent occurrence of adverse events in patients treated with BMP-2, including life-threatening cervical spine swelling. Indeed, the FDA issued a warning of the potential life-threatening complications of BMP-2 [18].

4 New Technologies

To monitor the healing process, the tissue engineering approach in bone repair took a great advantage from the new investigative tools developed in recent years to monitor the process. Analyses concerning the structure of natural and engineered bone, and, in particular, the integration of the engineered bone and the ceramic scaffold highly benefited two techniques based on X-ray radiation, namely, microtomography (microCT) and microdiffraction [8].

Bulk 3D information, with micro-resolution, is mainly obtained by microCT, whereas at interfaces useful information on atomic scale can be provided by microdiffraction with sub-micrometer spatial resolution. For both techniques most of the published results were obtained using synchrotron radiation, in particular at the European Synchrotron Radiation Facility (ESRF) in Grenoble (France). Synchrotron light is the electromagnetic radiation emitted when charged particles, usually electrons or positrons, moving at velocities close to the speed of light, are forced to change direction under the action of a magnetic field. Synchrotron light is unique in its intensity and brilliance, and it can be generated across the range of the electromagnetic spectrum: from the infrared, through the ultraviolet, to the X-ray regions to investigate the structure of matter. Three successive generations of SR facilities have resulted in beam brilliances 11–12 orders of magnitude greater than the standard laboratory X-ray tube (www.esrf.it). Considering the SR contribution to the recent extraordinary revolution in biology with special reference to the field of protein structural studies in terms of crystallography and diffraction [1], the idea to use this technology in the study of bone regeneration was applied.

4.1 Synchrotron Radiation MicroCT (SR microCT)

The ESRF offers a flux, energy range, and resolution unachievable with conventional (laboratory) radiation sources. A revolutionary discovery in the field of medical imaging with X-rays occurred at the beginning of the 1970s when the first

equipment for computed tomography (CT) was developed. This method of imaging avoids several important limitations of conventional X-ray radiology and allows a three-dimensional and nondestructive reconstruction much better than that of a conventional radiograph [12].

Unlike conventional CT systems which typically have a maximum spatial resolution of about 0.5 mm, MicroCT is capable of achieving a spatial resolution up to 0.3 μm (www.esrf.fr), i.e., about three orders of magnitude lower. Use of synchrotron X-rays has several advantages compared to laboratory or industrial X-ray sources such as (i) a high photon flux which permits measurements at high spatial resolution; (ii) the X-ray source is tunable, thus allowing measurements at different energies; (iii) the X-ray radiation is monochromatic, which eliminates beam-hardening effects; and (iv) parallel beam acquisition allows the use of exact tomographic reconstruction algorithms. MicroCT allows accurate nondestructive 3D examination of samples, and it was first driven by the need for having a highly precise means of reconstructing the complex architecture of bone tissue at a high resolution.

Traditional methods for evaluating osteointegration of tissue-engineered constructs are based on 2D techniques such as histology. Martin et al. [22] described a computer-based method for the automated quantification of bone tissue in 2D histological sections of decalcified specimens, but this method didn't allow to quantify the volume of the scaffold.

More recently, taking advantage of microCT associated with SR, the kinetics of bone growth into tissue engineering constructs was investigated in an immunodeficient murine model on scaffolds seeded with cells. Newly formed bone was quantified by microCT at different times after implantation. When the preimplant scaffolds were analyzed, only one peak in the X-ray absorption histogram was observed corresponding to the biomaterial used for the manufacturing of the scaffold itself. Instead, in the implanted samples, an additional peak was observed at lower X-ray absorption values, which corresponded to the newly formed bone [19]. MicroCT investigations of scaffold microstructure provided 3D images and, when appropriate mathematical algorithms were used, also statistical, quantitative data, with a spatial resolution on the order of a few microns. This method is now a standard method for the assessment of structural and physical properties of scaffolds, particularly precious in the development of new fabrication technologies.

4.2 Synchrotron Radiation X-Ray Microdiffraction

X-ray diffraction is one of the most powerful techniques used to study the hierarchical structure of a biological material such as bone. In particular, it plays a crucial role in studying, within the nanometer scale, the distribution of organic fibers (collagen) and crystalline mineral nanoparticles (HA) that influence the mechanical optimization of bone. It has been demonstrated [11, 36] that the combination of WAXS and SAXS provides a quantitative description of the crystallographic

orientation distribution as well as the morphological orientation distribution of the plate-shaped nanoparticles of bone. On the basis of the difference in electron density between the crystals and organic phase, scattering contrast of SAXS reveals the size, shape, and orientation of the mineral crystals. Bone is a nonhomogeneous composite whose local characteristics change at the micrometer level. For these reasons, scanning SAXS and WAXS setups are developed using X-ray focusing optics, which deliver micrometer or even sub-micrometer-sized beams. In this case the sample can be locally investigated by scanning it through the small X-ray beam. Usually, acquisition of SAXS patterns requires dedicated experimental conditions, quite different from those used for WAXS experiment.

A setup has been developed [20] to perform simultaneous acquisition of WAXS and SAXS patterns for each investigated point. The scanning SAXS and WAXS techniques are combined with the rotation of the sample, so that, for each chosen position, the sample is rotated around the vertical axis, and for each rotation, 2D SAXS and 2D WAXS patterns are collected for the same volume element of the sample. At the end, the data are collected in a figure analysis.

This method, which applies the principle of the tomography to the X-ray diffraction, provides a 3D quantitative description of the crystallographic orientation distribution as well as the morphological orientation distribution of the plate-shaped nanoparticles, both with respect to the orientation of the investigated trabecula. The combination of scanning SAXS and WAXS has been applied to the investigation of newly formed bone in engineered construct of scaffold and cells in vivo. Three different regions are identified according to the results of histological analysis: the soft tissue, the newly formed bone, and the scaffold based on their microdiffraction patterns. Monitoring these regions at different times of implantation was studied the organization of the HA mineral crystals and in particular their orientation with respect to the scaffold. For tissue-engineered bone, X-ray microdiffraction provides combined microstructural information about both mineral and organic phases allowing the production of microscopic maps studying the interface between scaffold and newly formed bone. This technique provides a relevant perspective to study the growth model of bone according to the tissue engineering approach.

5 Conclusions

The intricate bone composition makes the healing process very complex when dealing with extensive lesions and in particular when traditional therapeutic approaches don't allow significant progresses. To regenerate the bone, a tissue engineering approach suggested the use of mesenchymal cells derived from the bone marrow to restore an environment more suitable for the restitutio ad integrum of the tissue. This chapter discusses this approach in bone repair demonstrating that new investigative tools developed in recent years to monitor the process are important to shed new light on bone regeneration.

References

1. Adams F, Van Vaeck L, Barrett R (2005) Advanced analytical techniques: platform for nano materials science. Spectrochim Acta B Atom Spectrosc 60:13–26. https://doi.org/10.1016/J.SAB.2004.10.003
2. Albrektsson T, Johansson C (2001) Osteoinduction, osteoconduction and osseointegration. Eur Spine J 10(Suppl 2):S96–S101. https://doi.org/10.1007/s005860100282
3. Alekberov C, Shevtsov VI, Karatosun V, Gunal I, Alici E (2003) Treatment of Tibia Vara by the Ilizarov method. Clin Orthop Relat Res 409:199–208. https://doi.org/10.1097/01.blo.0000052937.71325.a2
4. Ali IHA, Brazil DP (2014) Bone morphogenetic proteins and their antagonists: current and emerging clinical uses. Br J Pharmacol 171:3620–3632. https://doi.org/10.1111/bph.12724
5. Bianco P (2014) "Mesenchymal" stem cells. Annu Rev Cell Dev Biol 30:677–704. https://doi.org/10.1146/annurev-cellbio-100913-013132
6. Boyde A, Corsi A, Quarto R, Cancedda R, Bianco P (1999) Osteoconduction in large macroporous hydroxyapatite ceramic implants: evidence for a complementary integration and disintegration mechanism. Bone 24:579–589 Available at: http://www.ncbi.nlm.nih.gov/pubmed/10375200. Accessed 30 May 2018
7. Calif E, Stein H, Lerner A (2004) The Ilizarov external fixation frame in compression arthrodesis of large, weight bearing joints. Acta Orthop Belg 70:51–56 Available at: http://www.ncbi.nlm.nih.gov/pubmed/15055318. Accessed 31 May 2018
8. Cancedda R, Giannoni P, Mastrogiacomo M (2007) A tissue engineering approach to bone repair in large animal models and in clinical practice. Biomaterials 28:4240–4250. https://doi.org/10.1016/j.biomaterials.2007.06.023
9. Caplan A (1991) Mesenchymal stem cells. J Orthop Res 9:641–650. https://doi.org/10.1002/jor.1100090504
10. Caplan AI (2015) Adult mesenchymal stem cells: when, where, and how. Stem Cells Int 2015:1–6. https://doi.org/10.1155/2015/628767
11. Cedola A, Lagomarsino S, Komlev V, Rustichelli F, Mastrogiacomo M, Cancedda R et al (2004) High spatial resolution X-ray microdiffraction applied to biomaterial studies and archeometry. Spectrochim Acta B At Spectrosc 59:1557–1564. https://doi.org/10.1016/J.SAB.2004.05.031
12. Claesson T. A medical imaging demonstrator of computed tomography and bone mineral densitometry – semantic scholar. Available at: https://www.semanticscholar.org/paper/A-Medical-Imaging-Demonstrator-of-Computed-and-Bone-Claesson/dd30400cc9d011a7db4d1276c4860b5d4b917abd. Accessed 14 June 2018
13. Dawson JI, Kanczler J, Tare R, Kassem M, Oreffo ROC (2014) Concise review: bridging the gap: bone regeneration using skeletal stem cell-based strategies-where are we now? Stem Cells 32:35–44. https://doi.org/10.1002/stem.1559
14. Dominici M, Le Blanc K, Mueller I, Slaper-Cortenbach I, Marini F, Krause DS et al (2006) Minimal criteria for defining multipotent mesenchymal stromal cells. The international society for cellular therapy position statement. Cytotherapy 8:315–317. https://doi.org/10.1080/14653240600855905
15. Ducy P (2000) CBFA1: a molecular switch in osteoblast biology. Dev Dyn 219:461–471. https://doi.org/10.1002/1097-0177(2000)9999:9999<::AID-DVDY1074>3.0.CO;2-C
16. Heise U, Osborn JF, Duwe F (1990) Hydroxyapatite ceramic as a bone substitute. Int Orthop 14:329–338 Available at: http://www.ncbi.nlm.nih.gov/pubmed/2177732. Accessed 30 May 2018
17. Hutmacher DW, Schantz JT, Lam CXF, Tan KC, Lim TC (2007) State of the art and future directions of scaffold-based bone engineering from a biomaterials perspective. J Tissue Eng Regen Med 1:245–260. https://doi.org/10.1002/term.24
18. James AW, LaChaud G, Shen J, Asatrian G, Nguyen V, Zhang X et al (2016) A review of the clinical side effects of bone morphogenetic protein-2. Tissue Eng Part B Rev 22:284–297. https://doi.org/10.1089/ten.TEB.2015.0357

19. Komlev VS, Peyrin F, Mastrogiacomo M, Cedola A, Papadimitropoulos A, Rustichelli F et al (2006) Kinetics of in vivo bone deposition by bone marrow stromal cells into porous calcium phosphate scaffolds: an x-ray computed microtomography study. Tissue Eng 12:3449–3458. https://doi.org/10.1089/ten.2006.12.3449
20. Loidl D, Peterlik H, Paris O, Müller M, Burghammer M, Riekel C et al (2005) Structure and mechanical properties of carbon fibres: a review of recent microbeam diffraction studies with synchrotron radiation. J Synchrotron Radiat 12:758–764. https://doi.org/10.1107/S0909049505013440
21. Marcacci M, Kon E, Moukhachev V, Lavroukov A, Kutepov S, Quarto R et al (2007) Stem cells associated with macroporous bioceramics for long bone repair: 6- to 7-year outcome of a pilot clinical study. Tissue Eng 13:947–955. https://doi.org/10.1089/ten.2006.0271
22. Martin I, Mastrogiacomo M, De Leo G, Muraglia A, Beltrame F, Cancedda R et al (2002) Fluorescence microscopy imaging of bone for automated histomorphometry. Tissue Eng 8:847–852. https://doi.org/10.1089/10763270260424204
23. Martin I, Muraglia A, Campanile G, Cancedda R, Quarto R (1997) Fibroblast growth factor-2 supports ex vivo expansion and maintenance of osteogenic precursors from human bone marrow 1. Endocrinology 138:4456–4462. https://doi.org/10.1210/endo.138.10.5425
24. Murphy CM, Haugh MG, O'Brien FJ (2010) The effect of mean pore size on cell attachment, proliferation and migration in collagen–glycosaminoglycan scaffolds for bone tissue engineering. Biomaterials 31:461–466. https://doi.org/10.1016/j.biomaterials.2009.09.063
25. Murphy MB, Moncivais K, Caplan AI (2013) Mesenchymal stem cells: environmentally responsive therapeutics for regenerative medicine. Exp Mol Med 45:e54. https://doi.org/10.1038/emm.2013.94
26. Muschler GF, Nakamoto C, Griffith LG (2004) Engineering principles of clinical cell-based tissue engineering. J Bone Joint Surg Am 86–A:1541–1558 Available at: http://www.ncbi.nlm.nih.gov/pubmed/15252108. Accessed 7 Jun 2018
27. Oonishi H (1991) Orthopaedic applications of hydroxyapatite. Biomaterials 12:171–178 Available at: http://www.ncbi.nlm.nih.gov/pubmed/1652293. Accessed 31 May 2018
28. Planell JA (2009) Bone repair biomaterials. Woodhead, New Delhi
29. Quarto R, Mastrogiacomo M, Cancedda R, Kutepov SM, Mukhachev V, Lavroukov A et al (2001) Repair of large bone defects with the use of autologous bone marrow stromal cells. N Engl J Med 344:385–386. https://doi.org/10.1056/NEJM200102013440516
30. Rabie ABM, Tang GH, Hägg U (2004) Cbfa1 couples chondrocytes maturation and endochondral ossification in rat mandibular condylar cartilage. Arch Oral Biol 49:109–118 Available at: http://www.ncbi.nlm.nih.gov/pubmed/14693204. Accessed 7 June 2018
31. Sacchetti B, Funari A, Michienzi S, Di Cesare S, Piersanti S, Saggio I et al (2007) Self-renewing osteoprogenitors in bone marrow sinusoids can organize a hematopoietic microenvironment. Cell 131:324–336. https://doi.org/10.1016/j.cell.2007.08.025
32. Salazar VS, Gamer LW, Rosen V (2016) BMP signalling in skeletal development, disease and repair. Nat Rev Endocrinol 12:203–221. https://doi.org/10.1038/nrendo.2016.12
33. Stevens B, Yang Y, Mohandas A, Stucker B, Nguyen KT (2008) A review of materials, fabrication methods, and strategies used to enhance bone regeneration in engineered bone tissues. J Biomed Mater Res B Appl Biomater 85B:573–582. https://doi.org/10.1002/jbm.b.30962
34. Troczynski T (2004) Bioceramics: a concrete solution. Nat Mater 3:13–14. https://doi.org/10.1038/nmat1039
35. Williams DF (1999) The Williams Dictionary of Biomaterials. Liverpool: Liverpool University Press. Available from: http://universitypublishingonline.org/ref/id/liverpool/CBO9781846314438
36. Žižak I, Paris O, Roschger P, Bernstorff S, Amenitsch H, Klaushofer K et al (2000) Investigation of bone and cartilage by synchrotron scanning-SAXS and -WAXD with micrometer spatial resolution. J Appl Crystallogr 33:820–823. https://doi.org/10.1107/S0021889800001321

Chapter 8
Bone Regeneration: Experiences in Dentistry

Serena Mazzoni

Abstract In recent years, there has been an increasing interest in a novel approach to evaluate craniofacial bone sites by means of high-resolution X-ray microtomography (microCT). Conventional histological evaluation and corresponding histomorphometric measurements provide only bidimensional information with the consequent risk that the selected slices do not properly represent the entire bone. Three-dimensional imaging methods, like microCT, are indicated to explore the dynamic and spatial distribution of regenerative phenomena in such complex anatomic structures. However, homogeneous tissues with a low attenuation coefficient or heterogeneous materials with a narrow range of attenuation coefficients produce insufficient contrast for absorption-based imaging. For such structures, the imaging quality can be enhanced through the use of phase-contrast microtomography (PhC-microCT). In addition, whereas PhC-microCT is usually based on a single distance between the detector and the sample, holotomography (HT) involves imaging at several distances and then combining the phase shift information to generate 3D reconstructions. HT is helpful when the material of interest has very small variations in attenuation coefficients, which lead to unsatisfactory imaging results even with phase-contrast techniques.

In the present chapter, the most recent breakthroughs in regenerative dentistry will be shown, demonstrating the unique capabilities of the microCT in offering not only an advanced characterization of biomaterials that are promising scaffold candidates but also to investigate the growth kinetics of regenerated bone in different grafted sites in human jaws.

S. Mazzoni (✉)
Department of Clinical Sciences, Polytechnic University of Marche, Ancona, Italy

A. Giuliani, A. Cedola (eds.), *Advanced High-Resolution Tomography in Regenerative Medicine*, Fundamental Biomedical Technologies,
https://doi.org/10.1007/978-3-030-00368-5_8

1 Introduction

Dentistry has witnessed impressive advances in all its branches over the past three decades. In particular, large bony maxillofacial defects are nowadays a worldwide emergency.

Craniofacial tissue engineering (CFTE) has risen as a promising methodology for the repair and recovery of tissues, in particular bone, that were lost, damaged, or, as a rule, functionally traded off because of injury, damage, sickness, or aging [1, 2].

In this scenario, one of the key objectives is the enhancement and guidance of osteogenic differentiation of stem cells within three-dimensional (3D) scaffolds, in a way that would enable the in vitro engineering of clinically applicable bone constructs.

The use of a scaffold is fundamental for the fruitful building of bone tissues as it favors appropriate conditions for osteogenic cells to move, multiply, divide, and promote new bone development, giving also a solid substrate to mechanical stresses during bone recovery [3]. The ideal scaffold must be biocompatible and degrade with time in nonpoisonous substances. It ought to likewise be profoundly permeable and penetrable for cell seeding (in vitro) and invasion (in vivo), growth factor transport, tissue ingrowth, and vascularization. Moreover, the scaffold should be mechanically steady, with properties mimicking those of the local bone also in terms of osteoconductivity (attracting bone cells from the hosting sites), osteoinductivity (favoring bone cells growth), and osseointegrativity (achieving the stable connectivity of the local bone) [1, 4].

An extensive variety of commercially available and experimental materials have been examined for bone tissue designing/engineering and its repair; for the most part, they can be divided into three categories: polymers, ceramics, and composites.

Polymers, with their regular grid mimicking bone collagen, probably provide the best solution in terms of osteoinduction and osteogenesis; however, they have low mechanical modulus, preventing an adequate support to cell colonization inside [5].

In this context, maybe ceramics demonstrated the best performances [5, 6] because of their inorganic nature and ionic portion: calcium phosphates (like hydroxyapatite, tricalcium phosphate, etc.) are widely known and used for their capacity to promote and strengthen bone recovery [7, 8].

Although the stimulatory impact of ceramics on bone tissue growth has been demonstrated, new materials are actually under investigation to find ideal settings, with special reference to bone engineering in craniofacial regions.

A key option is given by the use, as scaffold, of heterologous natural bone. Collagenated bone substitute biomaterials (BSB) of porcine origin [9–11] are an interesting solution because of their composition, mainly consisting of carbonated nanocrystalline hydroxyapatite (HA) and organic material.

Another possible option is the use, as scaffold, of anorganic bovine bone (ABB). ABB is a deproteinized bovine bone, with high degree of porosity and large connectivity that, together, facilitate angiogenesis and cells migrations [11–13].

Moreover, direct transplantation of cells/stem cells is often necessary when, attempting to repair large bone defects, there are not enough endogenous cells in the surrounding sites or their migration time to the defect would take too long [14]. In these cases, cells isolated by a donor biopsy are expanded in vitro and then seeded on a scaffold that, in turn, is normally implanted into the damaged site.

However, the identification of cell location, the duration of their survival and fate, and the qualitative and quantitative evaluation of bone growth longitudinally in time require the use of nondestructive characterization techniques.

Nowadays, a crucial role is assumed by the imaging techniques, not only used for the characterization of scaffold properties and function but also increasingly involved in the investigation of conduction, induction, and cell transplantation biological processes.

Histological evaluations are often complemented with different two-dimensional (2D) imaging technologies in biological events occurring at the interface between tissues and biomaterials [14, 15]. The use of high-resolution 3D imaging technologies is required in case of opaque biological structures, which light and electron microscopic methods can only investigate at surface levels [16]. Moreover, sample slicing studied with the previously mentioned techniques commonly results in a significant alteration and destruction of the biopsy, practically inhibiting the qualitative and quantitative analysis.

The introduction of computed tomography (CT) in medical imaging has strongly improved research based on imaging methods, in particular in bone districts. CT maintains a strategic distance from possible misinterpretations due to superimposition of structures, inherent to radiographic 2D imaging. Conventional CT and high-resolution X-ray computed tomography (microCT) differ only in terms of spatial resolution: the former reaches values of maximum 500 μm, the latter easily achieves values up to 0.2–0.3 μm. Therefore, the impact of microCT has been revolutionary, enabling to investigate samples in 3D, including engineered bone, with unprecedented precision and high resolution and in a nondestructive way [17].

2 Laboratory Versus Synchrotron X-ray Sources

Laboratory-based microCT systems have become an important tool in several sectors of dental research, like in the measurement of enamel thickness, the study of root canal morphology, and the evaluation of root canal preparation and of dental implants [18]. However, their use was initially a challenge in bone engineering, as shown in Ref [19], where the authors studied by microCT the bone formation in a 15 mm defect in the rabbit radius after the implantation of a tissue-engineered construct. Three-dimensional reconstructions allowed for greater spatial resolution than radiography, but did not allow for imaging of the implanted scaffold material or the surrounding, nonmineralized tissue.

More recently, Meleo et al. [20] studied the qualitative aspects of two bone specimens, retrieved from a human jaw 4 months after grafting an ENGIpore scaffold

(first sample) and from a coagulation healing site (second sample). Laboratory-based microCT was able to detect in the first sample a high biomaterial persistence and a relevant amount of new-formed bone tissue with a few areas of high mineralization. After the same time, the second sample revealed a more important bone tissue formation with many mineralized areas, possibly indicating that the biomaterial slows down the bone neoformation process.

However, despite its capacity of efficiently computing the diverse morphometric parameters, the physical qualities of the photon beam produced by laboratory X-ray sources often prevent reliable analysis of bone mineral densities and of the bone mineralization process itself. Indeed, these microCT systems do not permit the tuning of photon energy, hampering the discrimination of the different mineralization degrees [17].

Third-generation synchrotron facilities could be extremely useful for overcoming the limits of the previously described microCT laboratory devices. Indeed, synchrotron sources produce brilliant photon beams, with spatial and temporal coherence properties, providing new opportunities for advances characterizations [17]. Thus, a reliable analysis by microCT of regenerated bone sites and of their mineralization process can be valorized when supported by synchrotron-based exploratory methods, some of which described in previous chapters.

Image quality and quantitative analysis can be sensibly improved by the use of phase-contrast (PhC) microCT. The PhC approach is different from conventional X-ray imaging where the images are exclusively based on attenuation contrast. Indeed, when X-ray beam propagates through a tissue, both its amplitude and phase are modified, also originating the phase contrast.

The effect of the X-ray beam passing through a tissue is usually described by the refractive index n:

$$n(\boldsymbol{r}) = 1 - \delta(\boldsymbol{r}) + i\beta(\mathbf{r}) \tag{8.1}$$

where δ is the refractive index decrement and β is the attenuation index.

The δ value is much larger than the imaginary part β when studying weakly absorbing substances: indeed, it can be 1000 times greater than β in the energy range appropriate for the study of soft tissues. δ is actually proportional to the mean electron density, which in turn is almost proportional to the mass density.

In particular, this method is sensitive to light elements of soft tissues (like hydrogen, carbon, nitrogen, and oxygen), and, unlike conventional attenuation-based imaging methods, it is able to discriminate tissues with similar attenuation characteristics, with a greater differentiation in the level of gray.

Decrease of the refractive index-based image contrast is less rapid with the increase of X-ray energy compared to attenuation-based setups, allowing to achieve a substantial reduction of the delivered radiation dose [21].

Moreover, the phase retrieval normally implies the reconstruction of the two different real-valued 3D distributions, $\delta(\boldsymbol{r})$ and $\beta(\boldsymbol{r})$ in Eq. (8.1). This is generally achieved performing tomographic acquisitions of (at least) two different 2D

projection series. The acquisition can be restricted to a single series, when the distributions of the real and imaginary parts of the refractive index are proportional to each other, i.e.:

$$\beta(\boldsymbol{r}) = \varepsilon \cdot \delta(\boldsymbol{r}), \tag{8.2}$$

where the constant value ε does not depend on $\boldsymbol{r}$. This simplification is possible only in two experimental cases: when investigating very weakly absorbing pure-phase objects or for samples consisting predominantly of a single material but with spatially varying density [22, 23]. One case is represented by the engineered bone of craniofacial districts, being at the early stages of bone formation, with a slow variation of the mass density ("monomorphous" sample).

3 Synchrotron Radiation-Based Analysis of Engineered Bone

Several interesting microCT studies have been performed on different biomaterials that have previously been indicated as optimal candidates for bone substitutes in dental districts.

Successful maxillary sinus elevation was recently reported using biphasic calcium phosphate materials [24, 25], with morphologies of the scaffolds in shape of granules or structured blocks, used either in an acellular strategy (colonization of the scaffold by endogenous cells) [24] or seeding the biomaterial with cells [26].

Previous studies have usually been based on single time points; long-term kinetics on the same biomaterials were recently fully investigated in a clinical study [27], quantifying the regenerative kinetics of blocks versus granules in biphasic calcium phosphate scaffolds by synchrotron radiation-based microCT. Twenty-four bilateral sinus augmentations, previously grafted with (nr.12) granules and (nr.12) blocks of β-TCP/HA (70/30%), were retrieved after 3, 5/6, and 9 months from grafting. Synchrotron-based microCT was performed to quantitatively evaluate bone regeneration, graft resorption, and neovascularization. Significant quantities of regenerated bone, together with a good rate of biomaterial resorption and neovascularization, were found in the retrieved biopsies. Similar results were obtained before 5/6 months from grafting but, 9 months after grafting, microCT revealed that the sites grafted with blocks (Fig. 8.1, panels a–c) mimicked the healthy native bone of the maxillary site slightly better than those grafted with granules (Fig. 8.1, panels d–f).

The previous study contributed to confirm that not only the chemical composition of the scaffold but also its morphology and morphometry influence long-term kinetics of bone regeneration.

A promising alternative to biphasic calcium phosphate materials is the naturally produced bioceramics. Their interconnected porous morphology, the resistance to compressive forces, and the good biocompatibility and resorbability make corals a promising candidate as a scaffold for bone engineering in dental sites [11, 28].

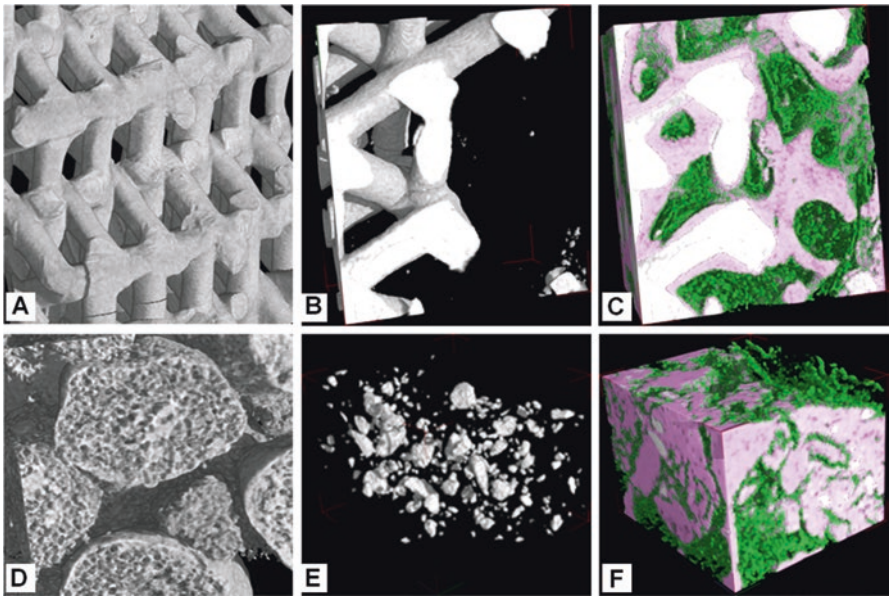

Fig. 8.1 MicroCT 3D reconstruction of (**a**) block-based TCP/HA scaffold before grafting, (**b**, **c**) block-based TCP/HA scaffold 9 months after grafting, (**d**) granule-based TCP/HA scaffold before grafting, and (**e**, **f**) granule-based TCP/HA scaffold 9 months after grafting. (**b**, **e**) Residual scaffold after 9 months from grafting. White phase: scaffold; pink phase: regenerated bone; green phase: regenerated vessels (From Ref. [27])

Biocoral® is a relevant example of ceramic biomaterial, made of coral-derived calcium carbonate. Synchrotron radiation microCT was recently used within a comparative study with β-tricalcium phosphate and biphasic calcium phosphate scaffold grafts in human maxillary defects. By microCT, 6 months after grafting, a huge amount of newly formed bone was found in the retrieved Biocoral-based biopsies, together with a good rate of the scaffold resorption and the formation of a homogeneous vascularization. The morphometric parameters were comparable to those obtained in the biphasic calcium phosphate grafts at the same time point, confirming the good in vivo performance of the biocorals but also demonstrating that graft success is strictly dependent on scaffold morphology [29].

Successful bone regeneration was also obtained using collagenated porcine-derived biomaterials. Special morphologies of 3D scaffolds, preserving both the cancellous and cortical bone structure, achieved very efficient systems to be used in combination with stem cells. Two studies [30, 32] quantitatively demonstrated, by synchrotron radiation PhC-microCT and other comparative methods, the osteoinductive properties of a cortico-cancellous porcine-derived scaffold cultured with human periodontal ligament stem cells (hPDLSCs). In particular, hPDLSCs demonstrated in vitro a good capacity of bone regeneration, with high proliferation rates and immunomodulatory properties, especially in xeno-free media [32]. Briefly, populations of hPDLSCs, obtained from the alveolar crest and the horizontal fibers of the periodontal ligament, were seeded onto demineralized cortico-cancellous

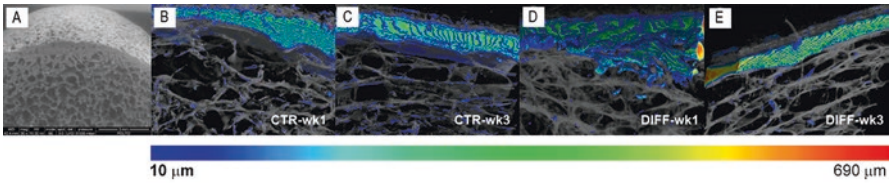

Fig. 8.2 (**a**) Scanning electron microscopy image of the porcine-derived cortico-cancellous biomaterial before cell seeding. (**b**–**e**) Synchrotron radiation PhC-microCT 3D images of the same biomaterial cultured with hPDLSCs in xeno-free media in (**b**, **c**) basal (CTR) and (**d**, **e**) osteogenic (DIFF) conditions. The scaffold interacted with cells and media producing 3D microCT images with two different phases, having different δ (refractive index decrement) values: the demineralized porcine-derived scaffold (shown in translucent gray) and the newly formed mineralized bone (color map of bone thickness distribution at the bottom of the figure); (**b**, **d**) at week 1 and (**c**, **e**) at week 3 (From Ref. [31])

scaffolds and cultured in vitro for 3 weeks. Three-dimensional images were obtained by PhC-microCT at several time points during the culture process, using a phase-retrieval algorithm based on the transport of intensity equation (TIE), fully described in the previous chapters. This experimental method was first demonstratively applied for the 3D characterization of the constructs in not xeno-free media [30], quantitatively monitoring the early stages of bone formation in basal and differentiating conditions; subsequently, the same experimental protocol was used for studying xeno-free cultures [31]. Interestingly, it quantitatively showed a significant acceleration of the mineralization process in the xeno-free environment, regardless of basal or differentiating conditions. Indeed, PhC-microCT easily discriminated the newly formed mineralized bone from the demineralized biomaterial. Figure 8.2a shows a scanning electron microscopy image of the cortico-cancellous scaffold before cell seeding. Its interactions with the hPDLSCs and the media produced, over 3 weeks of time from culture starting, microCT images in which, because of their different refractive indexes, two phases appeared, the demineralized scaffold and the newly mineralized bone.

Figure 8.2, panels b–e show the samples cultured in basal (CTR) or differentiating (DIFF) media for 1 and 3 weeks. A significant quantity of newly mineralized bone, in shape of spots or fibrils, was already visible after the first week of culture both in CTR and in DIFF media. This finding seems better than results previously obtained in the non-xeno-free media where the newly mineralized bone was detectable only after the second week of culture. All the investigated morphometric parameters, within the spongy volume of the samples, showed that no significant differences were present between CTR and DIFF cultures at identical time points but that a significant increase of the mineralized volume was detected between the first and third week of culture in both the culture media.

Interestingly, PhC-microCT studies revealed an overall significant increase in trabecular thickness in both media, from the first to the third week of culture, but only a slight increase (not significant) of the mean thickness in the mineralized portion. This seems to indicate that the porcine-derived biomaterial resorption is well compensated by cell growth.

Porcine-derived heterologous bone was also recently used to fill human post-extraction sockets, supporting the healing process. Indeed, the management of extraction sockets is nowadays a challenge because bone dimensional changes normally occur after tooth extraction [32]. Horizontal and vertical bone loss have been observed, with the greatest bone volume decrease in the period between 3 and 6 months after extraction [33, 34]. Thus, the regenerative potential of this biomaterial was recently investigated by synchrotron radiation microCT and histology in order to quantitatively evaluate the kinetics of healing and compare that with control post-extraction sockets, spontaneously healed after 12 months [35]. MicroCT morphometric analysis performed on the retrieved biopsies showed an overall increase of bone volume for the grafted sites with the healing period. In agreement with the literature [33, 34] and with histology performed on the same samples, the more significant bone growth was found between 3 and 6 months from grafting, when a marked dimensional growth of the bone and a consequent decrease of marrow spaces were observed (Fig. 8.3). The microCT quantitative analysis clarified that this growth was not strictly due to the increase in trabecular thickness but to a significant growth of the number of trabeculae. Indeed, both microCT and histology revealed that the newly formed bone progressively surrounded residual biomaterial granules, originating new trabeculae. Moreover, they also showed that the bone continues to grow, even if at slower rate, after 6 months from the biomaterial grafting, with the same dynamics of the previous period. After 12 months from grafting, the socket filled with the biomaterial showed the presence of more trabeculae (although slightly reduced in thickness) than the control post-extraction socket, spontaneously healed after 12 months. As the strength of a bone depends also on the microscopic

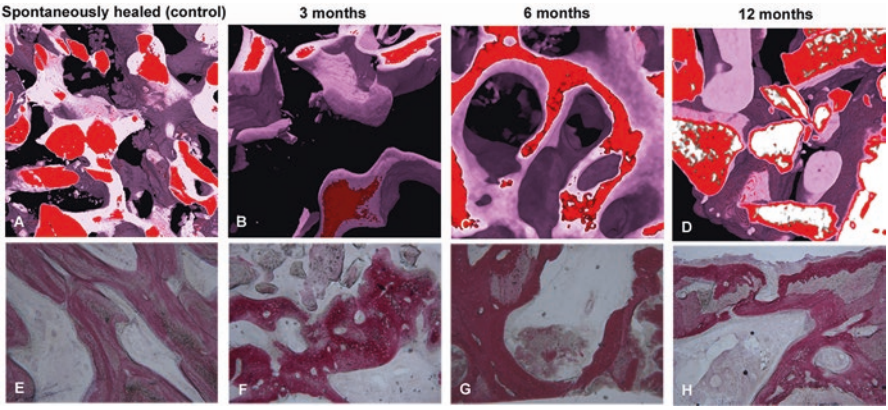

Fig. 8.3 (**a**–**d**) Subvolumes of the microCT 3D reconstructions. Legend: white tissue →residual scaffold; pink tissue → bone under remodeling; red tissue → fully mineralized bone. (**e**–**h**) Selected histologic sections. Toluidine blue and acid fuchsin. Original magnification ×100. (**a**–**e**) Spontaneously healed socket retrieved after 12 months from extraction; (**b**–**f**) porcine-derived bone retrieved 3 months after socket preservation procedure; (**c**–**g**) porcine-derived bone retrieved 6 months after socket preservation procedure; (**d**–**h**) porcine-derived bone retrieved 12 months after socket preservation procedure (From Ref. [35])

pattern of the trabecular network [36], the increased number of trabeculae resulting from the interactions between the biomaterial and the surrounding native bone tissue is expected to increase the structure's connectivity, improving also its biomechanical performances under loading.

In the last few years, it has been demonstrated that PhC-microCT presents a better soft tissue contrast than conventional absorption-based microCT, allowing to study in 3D several tissues and organs: lung [37], esophagus [37], brain [38–40], liver [37, 41], kidney [42], breast tissues [43, 44], cartilage [45–47], and vessels [48].

These findings led some authors to investigate the 3D vascularization of the engineered bone in dental sites. Indeed, 3D imaging and quantitative description of the complete vascular network in such districts is crucial for monitoring the relationship between bone formation and vascularization. Very recently, the osteogenic potential of the woven bone (WB) formed by human dental pulp stem cells (hDPSCs) after 40 days of culture in standard medium was tested using synchrotron-based PhC-microCT [49].

PhC-microCT, using a polychromatic beam and a single-distance setup, easily distinguished in 3D the newly formed bone phase from the hDPSC culture, producing images in which two different phases, with different refractive indices, appeared: the WB tissue and small clusters of mineralized bone that were also quantified, as shown in Fig. 8.4. However, it was not possible to detect any vascularization using the PhC-microCT technique based on a single sample-detector distance.

In this regard, another phase-contrast technique that provides additional information is holotomography (HT). HT, unlike PhC-microCT based on a single sample-detector distance, is based on tomographic scans at multiple propagation distances (Fig. 8.5a), followed by a method of phase retrieval that has recently been fully described in [50].

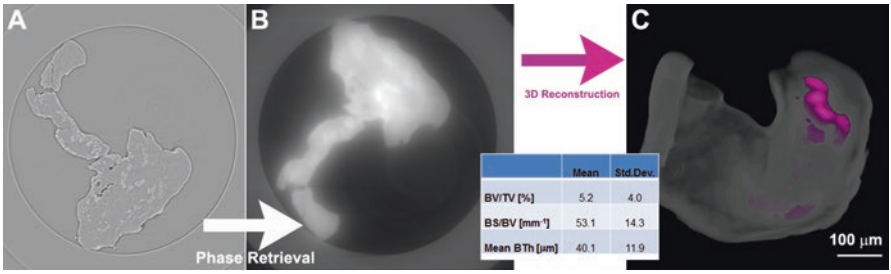

Fig. 8.4 (**a**) 2D slice non-processed with phase-retrieval algorithms: the edge-enhancement signal prevents the quantification of the woven and newly mineralized bone phases. (**b**) The same 2D slice after phase-retrieval processing; (**c**) 3D reconstruction of the human dental pulp stem cells culture in standard medium (40 days) after processing by phase retrieval. Woven bone → translucent white; newly formed mineralized bone → magenta. Bottom inset: morphometric analysis of the mineralized bone: BV/TV (%)→ volume ratio of the newly formed mineralized bone (BV) to the total woven bone volume (TV); BS/BV (mm^{-1}) → newly formed bone specific surface; BTh (μm) → mean thickness of the bone clusters. Data are expressed as *mean* ± *standard deviation* (From Ref. [49])

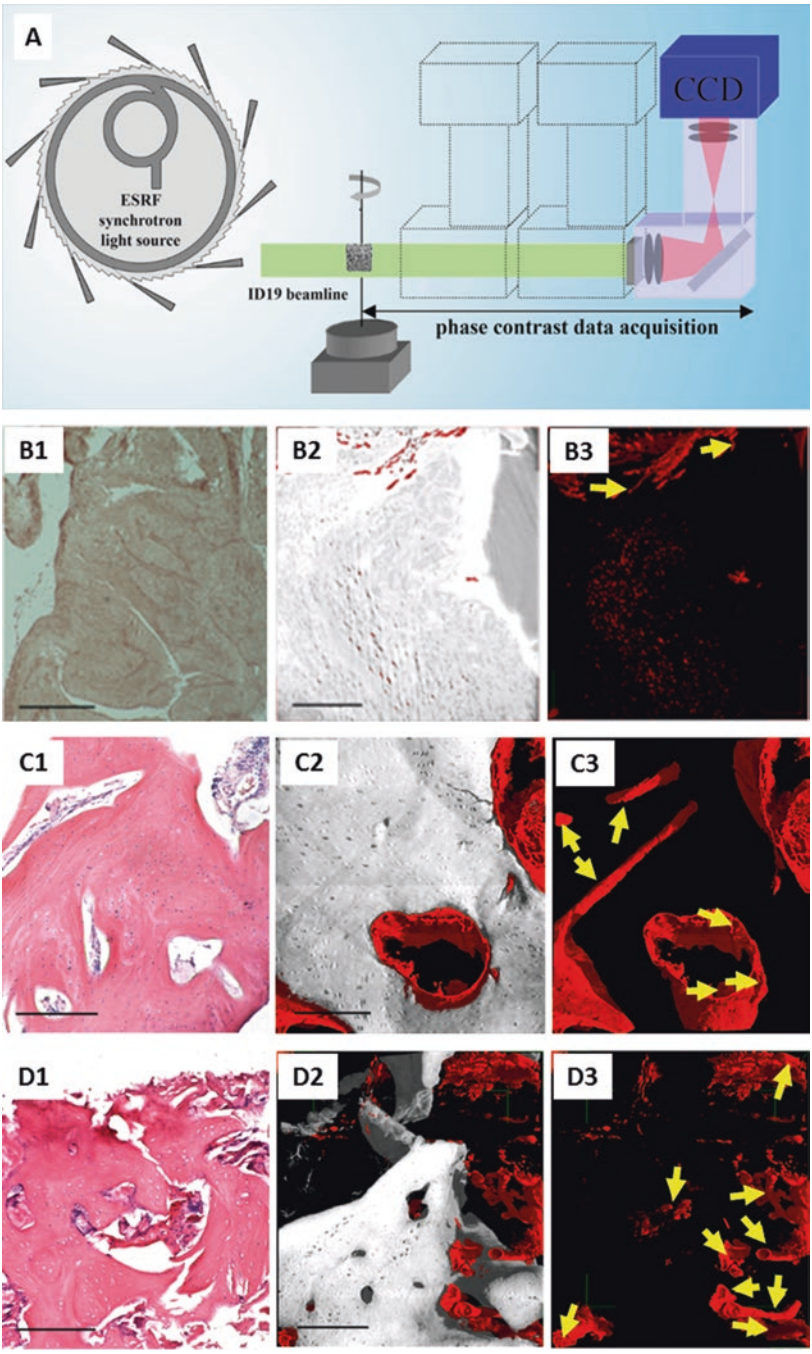

Fig. 8.5 Synchrotron radiation-based phase-contrast holotomography (HT) [48]. (**a**) HT setup at the ID19 beamline of the European synchrotron radiation facility (Grenoble, France).

HT analysis allowed to achieve a nanometric 3D reconstruction of the WB (Fig. 8.5b1, b2), also assessing the presence of new vessels (Fig. 8.5b3). This last finding confirmed deductions derived from the evidence that hDPSCs strongly expressed high levels of VEGF and PDGF-A which correlates with vessel formation in the WB [49].

Another recent study performed by synchrotron radiation HT has confirmed hDPSCs properties of differentiating into osteoblasts when seeded on collagen I scaffolds [51]. The stability and the quality of the regenerated bone and vessel network were assessed, with conventional procedures and in-line HT, 3 years after the grafting intervention.

A representative histological slice is shown, as a reference, in Fig. 8.5c1, while a sampling subvolume of the 3D reconstruction deriving from the HT scan is reported in Fig. 8.5c2 ,c3, where the unminiralized tissues were virtually suppressed for a better visualization of bone (rendered in gray) and its neovascularization (rendered in red). The same representation is used to show a sampling subvolume of the mandible control (Fig. 8.5d1–d3). As clearly appears from these figures, it was found that the hDPSCs generated a compact rather than a spongy bone; thus, a type of bone completely different from normal alveolar bone. Therefore, grafted DPSCs seemed to not pursue the local environmental signals produced by the alveolar hosting site, demonstrating that the HT technique could be an important method with which to investigate the still unknown cellular events involved in bone regeneration.

4 Conclusions

MicroCT, in conventional absorption or in several phase-contrast setups, was found to be very useful in delivering reliable 3D quantitative information in dentistry and in particular in craniofacial bone engineering. It was extensively used to investigate the growth kinetics of regenerated bone in different environments: in vitro, onto scaffolds cultured with stem cells, and in vivo, onto constructs, composed of the same cells and scaffold, retrieved from animal models or humans.

Furthermore, it must be highlighted that these studies, making use of the microCT, produced significant results on statistical samples, often narrower than those involved in the histologic evaluation, practically making the calculation of the statistical power no longer necessary [35, 52]. In the studies previously reported, microCT often allowed to achieve significant results in spite of the limited number of samples (in vitro constructs, animals or patients) that, perhaps, would not have been sufficient in other experimental protocols, exclusively based on histology.

Fig. 8.5 (continued) (**b**) Histological (**b1**) and HT (**b2, b3**) analysis of the woven bone (WB) formed by hDPSCs after 40 days of culture in standard medium. (**c**) Histological (**c1**) and HT (**c2, c3**) analysis of a human hDPSC-treated mandible. (**d**) Histological (**d1**) and HT (**d2, d3**) analysis of a human mandible control. Histological sections (panel 1): H&E staining, as reference; HT reconstructions: all phases were virtually deleted except for bone and vessels (panel 2), or exclusively except for vessels (panel 3). Yellow arrows: neovascularization. Scale bars = 250 μm

The reason for this is linked to the 3D nature of microCT acquisition, based on the stacking of at least 1000 successive 2D sections (each with the same thickness of a histologic slice). This is of fundamental significance, as it allows to perform clinical trials on a reduced number of patients and, in animal model studies, makes it possible to restrict the number of sacrifices to a minimum, in accordance with the most recent ethical regulations.

Acknowledgments The majority of the research here reported is the result of collaborations created within the Action COST MP1005 "From nano to macro biomaterials (design, processing, characterization, modeling) and applications to stem cells regenerative orthopedic and dental medicine (NAMABIO)" and the PRIN Project – Prot. 20102ZLNJ5 funded by the Italian Ministry of Education and Research.

The author acknowledges Dr. Alessandra Giuliani, Principal Research Scientist at Polytechnic University of Marche, Department of Clinical Sciences, for her fundamental suggestions during the chapter drafting.

References

1. Laurencin C, Khan Y, El-Amin SF (2006) Bone graft substitutes. Expert Rev Med Devices 3:49–57
2. Giannoudis PV, Dinopoulos H, Tsiridis E (2005) Bone substitutes: an update. Injury 36(Suppl 3):S20–S27
3. Fröhlich M, Grayson L, Wan L, Marolt D, Drobnic M, Vun-jak-Novakovic G (2008) Tissue engineered bone grafts: biological requirements, tissue culture and clinical relevance. Curr Stem Cell Res Ther 3(4):254–264
4. Wang M (2003) Developing bioactive composite materials for tissue replacement. Biomaterials 24:2133e51
5. Liu X, Ma PX (2004) Polymeric scaffolds for bone tissue engineering. Ann Biomed Eng 32:477–486
6. Hench LL (1998) Bioactive materials: the potential for tissue regeneration. J Biomed Mater Res 41:511e8
7. Klein C, de Groot K, Chen W, Li Y, Zhang X (1994) Osseous substance formation induced in porous calcium phosphate ceramics in soft tissue. Biomaterials 15:31e4
8. Ripamonti U (1996) Osteoinduction in porous hydroxyapatite implanted in heterotopic sites of different animal models. Biomaterials 17:31e5
9. Barone A, Aldini NN, Fini M, Giardino R, Calvo Guirado JL, Covani U (2008) Xenograft versus ex-traction alone for ridge preservation after tooth removal: a clinical and histomorphometric study. J Periodontol 79(8):1370e7
10. Orsini G, Scarano A, Piattelli M, Piccirilli M, Caputi S, Piattelli A (2006) Histologic and ultra-structural analysis of regenerated bone in maxillary sinus augmentation using a porcine bone-derived biomaterial. J Periodontol 77(12):1984e90
11. Iezzi G, Piattelli A, Giuliani A, Mangano C, Barone A, Manzon L, Degidi M, Scarano A, Filippone A, Perrotti V (2017) Molecular, cellular and pharmaceutical aspects of bone grafting materials and membranes during maxillary sinus-lift procedures. Part 2: detailed characteristics of the materials. Curr Pharm Biotechnol 18(1):33–44. https://doi.org/10.2174/1389201017666161202104002
12. Haas R, Mailath G, Dörtbudak O, Watzek G (1998) Bovine hydroxyapatite for maxillary sinus augmentation: analysis of interfacial bond strength of dental implants using pull-out tests. Clin Oral Implants Res 9(2):117–122

13. Hing KA, Best SM, Tanner KE, Bonfield W, Revell PA (2004) Mediation of bone ingrowth in porous hydroxyapatite bone graft substitutes. J Biomed Mater Res A 68(1):187–200
14. Alsberg E, Hill EE, Mooney DJ (2001) Craniofacial tissue engineering. Crit Rev Oral Biol Med 12(1):64–75
15. Nam SY, Ricles LM, Suggs LJ, Emelianov SY (2015) Imaging strategies for tissue engineering applications. Tissue Eng Part B 21(1):88–102
16. Zehbe R, Haibel A, Schmidt F, Riesemeier H, Kirkpatrick CJ, Schubert H, Brochhausen C (2010) High resolution x-ray tomography – 3D imaging for tissue engineering applications. In: Eberli D (ed) Tissue engineering. InTech, Rijeka. https://doi.org/10.5772/8577 Available from: http://www.intechopen.com/books/tissue-engineering/high-resolution-x-ray-tomography-3d-imaging-for-tissue-engineering-applications
17. Cancedda R, Cedola A, Giuliani A, Komlev V, Lagomarsino S, Mastrogiacomo M, Peyrin F, Rustichelli F (2007) Bulk and interface investigations of scaffolds and tissue-engineered bones by x-ray microtomography and x-ray microdiffraction. Biomaterials 28:2505e24
18. Swain MV, Xue J (2009) State of the art of micro-CT applications in dental research. Int J Oral Sci 1(4):177–188
19. Hedberg EL, Kroese-Deutman HC, Shih CK, Lemoine JJ, Liebschner MA, Miller MJ, Yasko AW, Crowther RS, Carney DH, Mikos AG, Jansen JA (2005) Methods: a comparative analysis of radiography, microcomputed tomography, and histology for bone tissue engineering. Tissue Eng 11(9–10):1356–1367
20. Meleo D, Bedini R, Pecci R, Mangione F, Pacifici L (2012) Microtomographic and morphometric characterization of a bioceramic bone substitute in dental implantology. Ann Ist Super Sanita 48(1):59–64. https://doi.org/10.4415/ANN_12_01_10
21. Arfelli F, Assante M, Bonvicini V, Bravin A, Cantatore G, Castelli E, Dalla Palma L, Di Michiel M, Longo R, Olivo A, Pani S, Pontoni D, Poropat P, Prest M, Rashevsky A, Tromba G, Vacchi A, Vallazza E, Zanconati F (1998) Low-dose phase contrast x-ray medical imaging. Phys Med Biol 43(10):2845–2852
22. Gureyev TE, Pogany A, Paganin DM, Wilkins SW (2004) Linear algorithms for phase retrieval in the Fresnel region. Opt Commun 231(1–6):53–70
23. Gureyev TE, Paganin DM, Myers GR (2006) Phase-and-amplitude computer tomography. Appl Phys Lett 89(3):034102
24. Mangano C, Perrotti V, Shibli JA, Mangano F, Ricci L, Piattelli A, Iezzi G (2013) Maxillary sinus grafting with biphasic calcium phosphate ceramics: clinical and histologic evaluation in man. Int J Oral Maxillofac Implants 28:51–56
25. Ohayon L (2014) Maxillary sinus floor augmentation using biphasic calcium phosphate: a histologic and histomorphometric study. Int J Oral Maxillofac Implants 29:1143–1148
26. Barboni B, Mangano C, Valbonetti CL, Marruchella G, Berardinelli P, Martelli A, Muttini A, Mauro A, Bedini R, Turriani M, Pecci R, Nardinocchi D, Zizzari VL, Tetè S, Piattelli A, Mattioli M (2013) Synthetic bone substitute engineered with amniotic epithelial cells enhances bone regeneration after maxillary sinus augmentation. PLoS One 8(5):e63256
27. Giuliani A, Manescu A, Mohammadi S, Mazzoni S, Piattelli A, Mangano F, Iezzi G, Mangano C (2016) Quantitative kinetics evaluation of blocks versus granules of biphasic calcium phosphate scaffolds (HA/β-TCP 30/70) by synchrotron radiation x-ray microtomography: a human study. Implant Dent 25(1):6–15
28. Iezzi G, Piattelli A, Giuliani A, Mangano C, Manzon L, Degidi M, Iaculli F, Scarano A, Filippone A, Perrotti V (2017) Molecular, cellular and pharmaceutical aspects of bone grafting materials and membranes during maxillary sinus-lift procedures. Part 1: a general overview. Curr Pharm Biotechnol 18(1):19–32. https://doi.org/10.2174/138920-1017666161221155237
29. Giuliani A, Manescu A, Larsson E, Tromba G, Luongo G, Piattelli A, Mangano F, Iezzi G, Mangano C (2014) In vivo regenerative properties of coralline-derived (biocoral) scaffold grafts in human maxillary defects: demonstrative and comparative study with Beta-tricalcium phosphate and biphasic calcium phosphate by synchrotron radiation x-ray microtomography. Clin Implant Dent Relat Res 16(5):736–750. https://doi.org/10.1111/cid.12039

30. Manescu A, Giuliani A, Mohammadi S, Tromba G, Mazzoni S, Diomede F, Zini N, Piattelli A, Trubiani O (2016) Osteogenic potential of dualblocks cultured with human periodontal ligament stem cells: in vitro and synchrotron microtomography study. J Periodontal Res 51(1):112–124. https://doi.org/10.1111/jre.12289
31. Mazzoni S, Mohammadi S, Tromba G, Diomede F, Piattelli A, Trubiani O, Giuliani A (2017) Role of cortico-cancellous heterologous bone in human periodontal ligament stem cell xeno-free culture studied by synchrotron radiation phase-contrast microtomography. Int J Mol Sci 18(2):E364. https://doi.org/10.3390/ijms18020364
32. Barone A, Aldini NN, Fini M, Giardino R, Calvo Guirado JL, Covani U (2008) Xenograft versus extraction alone for ridge preservation after tooth removal: a clinical and histomorphometric study. J Periodontol 79(8):1370–1377
33. Iasella JM, Greenwell H, Miller RL, Hill M, Drisko C, Bohra AA, Scheetz JP (2003) Ridge preservation with freeze-dried bone allograft and a collagen membrane compared to extraction alone for implant site development: a clinical and histologic study in humans. J Periodontol 74(7):990–999
34. Tan WL, Wong TL, Wong MC, Lang NP (2012) A systematic review of post-extractional alveolar hard and soft tissue dimensional changes in humans. Clin Oral Implants Res 23(5):1–21
35. Giuliani A, Iezzi G, Mazzoni S, Piattelli A, Perrotti V, Barone A (2018) Regenerative properties of collagenated porcine bone grafts in human maxilla: demonstrative study of the kinetics by synchrotron radiation microtomography and light microscopy. Clin Oral Investig 22(1):505–513. https://doi.org/10.1007/s00784-017-2139-6
36. Benhamou CL, Lespessailles E, Royant V (1996) Bone structure and mechanical resistance of the bone tissue. Presse Med 25(6):249–254
37. Lewis RA, Hall CJ, Hufton AP, Evans S, Menk RH, Arfelli F, Rigon L, Tromba G, Dance DR, Ellis IO, Evans A, Jacobs E, Pinder SE, Rogers KD (2003) X-ray refraction effects: application to the imaging of biological tissues. Brit J Radiol 76(905):301–308
38. Connor DM, Benveniste H, Dilmanian FA, Kritzer MF, Miller LM, Zhong Z (2009) Computed tomography of amyloid plaques in a mouse model of Alzheimer's disease using diffraction enhanced imaging. NeuroImage 46(4):908–914. https://doi.org/10.1016/j.neuroimage.2009.03.019
39. Marinescu M, Langer M, Durand A, Olivier C, Chabrol A, Rositi H, Chauveau F, Cho TH, Nighoghossian N, Berthezène Y, Peyrin F, Wiart M (2013) Synchrotron radiation x-ray phase micro-computed tomography as a new method to detect iron oxide nanoparticles in the brain. Mol Imaging Biol 15(5):552–559. https://doi.org/10.1007/s11307-013-0639-6
40. Pinzer BR, Cacquevel M, Modregger P, McDonald SA, Bensadoun JC, Thuering T, Aebischer P, Stampanoni M (2012) Imaging brain amyloid deposition using grating-based differential phase contrast tomography. NeuroImage 61(4):1336–1346
41. Herzen J, Willner MS, Fingerle AA, Noël PB, Köhler T, Drecoll E, Rummeny EJ, Pfeiffer F (2014) Imaging liver lesions using grating-based phase-contrast computed tomography with bi-lateral filter post-processing. PLoS One 9(1):e83369. https://doi.org/10.1371/journal.pone.0083369
42. Velroyen A, Bech M, Zanette I, Schwarz J, Rack A, Tympner C, Herrler T, Staab-Weijnitz C, Braunagel M, Reiser M, Bamberg F, Pfeiffer F, Notohamiprodjo M (2014) X-ray phase-contrast tomography of renal ischemia-reperfusion damage. PLoS One 9(10):e109562. https://doi.org/10.1371/journal.pone.0109562
43. Arfelli F, Bonvicini V, Bravin A, Cantatore G, Castelli E, Palma LD, Michiel MD, Fabrizioli M, Longo R, Menk RH, Olivo A, Pani S, Pontoni D, Poropat P, Prest M, Rashevsky A, Ratti M, Rigon L, Tromba G, Vacchi A, Vallazza E, Zanconati F (2000) Mammography with synchrotron radiation: phase-detection techniques. Radiology 215(1):286–293
44. Stampanoni M, Wang Z, Thuring T, David C, Roessl E, Trippel M, Kubik-Huch RA, Singer G, Hohl MK, Hauser N (2011) The first analysis and clinical evaluation of native breast tissue using differential phase-contrast mammography. Investig Radiol 46(12):801–806
45. Coan P, Bamberg F, Diemoz PC, Bravin A, Timpert K, Mützel E, Raya JG, Adam-Neumair S, Reiser MF, Glaser C (2010) Characterization of osteoarthritic and normal human patella

cartilage by computed tomography x-ray phase-contrast imaging: a feasibility study. Investig Radiol 45(7):437–444. https://doi.org/10.1097/RLI.0b013e3181e193bd
46. Marenzana M, Hagen CK, Das Neves Borges P, Endrizzi M, Szafraniec MB, Ignatyev K, Olivo A (2012) Visualization of small lesions in rat cartilage by means of laboratory-based x-ray phase contrast imaging. Phys Med Biol 57(24):8173–8184
47. Horng A, Brun E, Mittone A, Gasilov S, Weber L, Geith T, Adam-Neumair S, Auweter SD, Bravin A, Reiser MF, Coan P (2014) Cartilage and soft tissue imaging using x-rays: propagation-based phase contrast computed tomography of the human knee in comparison with clinical imaging techniques and histology. Investig Radiol 49(9):627–634
48. Giuliani A, Mazzoni S, Mele L, Liccardo D, Tromba G, Langer M (2017) Synchrotron phase tomography: an emerging imaging method for microvessel detection in engineered bone of craniofacial districts. Front Physiol 8:769. https://doi.org/10.3389/fphys.2017.00769
49. Paino F, La Noce M, Giuliani G, De Rosa A, Mazzoni S, Laino L, Amler E, Papaccio G, Desiderio V, Tirino V (2017) Human DPSCs fabricate vascularized woven bone tissue: a new tool in bone tissue engineering. Clin Sci 131:699–713
50. Langer M, Cloetens P, Peyrin F (2010) Regularization of phase retrieval with phase-attenuation duality prior for 3D holotomography. IEEE Trans Image Process 19:2428–2436
51. Giuliani A, Manescu A, Langer M, Rustichelli F, Desiderio V, Paino F, De Rosa A, Laino L, d'Aquino R, Tirino V, Papaccio G (2013) Three years after transplants in human mandibles, histological and inline HT revealed that stem cells regenerated a com-pact rather than a spongy bone: biological and clinical implications. Stem Cells Transl Med 2:316–324
52. Suresh KP, Chandrashekara S (2012) Sample size estimation and power analysis for clinical research studies. J Hum Reprod Sci 5(1):7–13

Chapter 9
The Challenge of the Vascularization of Regenerated Tissues

Michela Fratini

Abstract Tissue engineering (TE) technology combines different aspects of medicine, biology, and engineering to generate, repair, or replace human tissues. In particular, the bone TE approach may be used to induce new functional bone regeneration via the synergistic combination of implanted porous ceramic scaffold with bone marrow stromal cells (BMSC) in vivo. The efficiency of an *artificially implanted construct* depends on the timely delivery and exchange of nutrients from blood vessels to the BMSC and the contemporary removal of the metabolism waste products. Therefore, the control of the angiogenesis of the microvascular network with proper spatial organization is a key step to obtain tissue regeneration and repair (Carano and Filvaroff, Drug Discov Today 8:980–989, 2003). In this review, we discuss the fundamentals of bone tissue engineering, highlighting the most recent advances in the understanding of the relation between bone formation and vascularization.

1 Introduction

Biomineralization (BM) is the widespread and fascinating process by which living organisms form mineral materials, in organized crystals. In the BM process, ions in solution are converted in solid composites (biominerals) thanks to chemical-physical transformations performed by the cellular activity. The process creates sophisticated composite materials, composed of organic and inorganic compounds, with a wide range of properties depending on the many different functions they have to carry out. These include the mechanical functions of exo- and endoskeletons and free-ion regulation or sensing. The research goals in BM are to understand the underlying mechanisms that organisms use to control mineral formation. Only the full comprehension of the morphology and functionality of the biomineralized

M. Fratini (✉)
Institute of Nanotechnology, CNR, Rome, Italy

Santa Lucia Foundation, Rome, Italy

A. Giuliani, A. Cedola (eds.), *Advanced High-Resolution Tomography in Regenerative Medicine*, Fundamental Biomedical Technologies,
https://doi.org/10.1007/978-3-030-00368-5_9

tissue (i.e., shell, bone, and teeth) will provide the opportunity to mimic nature for the development of bio-inspired materials. Bone provides an important and intriguing model system to investigate the mechanisms involved in BM.

In particular, a deeper comprehension of the BM process is at the basis of tissue engineering (TE) and regenerative medicine developments. Several in vivo and in vitro studies were dedicated to this purpose via the application of 2D and 3D diagnostic techniques. However, due to the complexity of the process, a complete and exhaustive explanation, still far to be reached, requires the synergy of different advanced experimental techniques.

The scaffold plays a crucial role in tissue regeneration since it acts as a guide and it stimulates the bone growth creating living biocomposites [2, 3]. The physical characteristics of the scaffold are represented by a high porosity, maximal surface area for bone growth, and an interconnected pore space, with pores having a sufficiently large size to allow the penetration and diffusion of the blood vessels [4]. In addition, the efficiency of an artificially implanted construct (scaffold) depends on several factors, such as the rate of exchange and removal of substances (as nutrients and metabolism waste, respectively) from the surrounding blood vessels to the bone marrow stromal cell (BMSC, see Fig. 9.1) loaded in the scaffold. The control of the angiogenesis of the vascular network by providing an appropriate template for its spatial organization is a key step to obtain tissue regeneration and repair [1]. In this framework, the formation of vascular networks with tissue-appropriate structure is crucial to tissue engineering (TE) [5, 6]. Thus, a quantitative analysis of the 3D vasculature arrangements in TE is essential to the evaluation of the success of a given strategy. However, to image blood vessels using conventional high-resolution techniques based on X-ray absorption is challenging and often requires the introduction of contrast agents or corrosion casts that generate absorption contrast. In turn, this can result in a nonuniform filling of the vessels and possibly in the need to destroy the rest of the tissue. Complete reliance on absorption contrast thus leads to significant challenges when attempting to simultaneously identify multiple tissue features in a single sample (e.g., microvascular and soft tissue structure).

Recent works [7, 8] demonstrated the capability of synchrotron X-ray phase-contrast micro-tomography (SXPCmT) to visualize the 3D neuronal network architecture and vascular network in the central nervous system at scales spanning

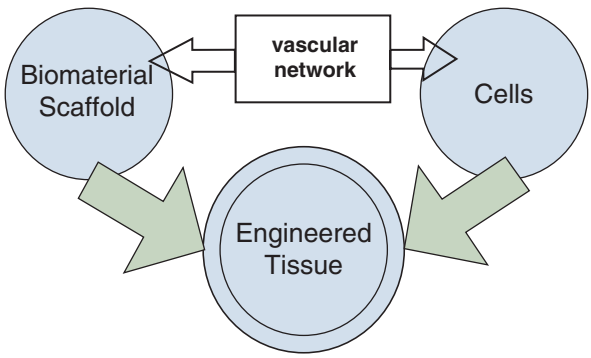

Fig. 9.1 Pictorial view of the relation between bone formation and vascularization

from millimeters to hundreds of nanometers, without contrast agent and without a destructive sample preparation, which could lead to data misinterpretation.

The potential of SXPCmT was also confirmed in recent works [9], where it was applied to the visualization and analysis of the 3D microvascular networks in bone-engineered constructs, made of porous ceramic scaffolds loaded with BMSC, in an ectopic bone formation mouse model. Samples seeded and not seeded with BMSC were compared, with or without the use of contrast agents. Thanks to the high quality of the images, it was possible to simultaneously investigate the 3D distribution of both vessels and organic collagen matrix. This approach represents a valuable tool for quantitative studies of angiogenesis in TE and for any other preclinical investigations wherein a quantitative analysis of the vascular network has an important role. In this framework, in the following paragraph, we present the most recent advances in the understanding of the relation between bone formation and vascularization using high-resolution imaging techniques.

2 Vascularization

An active blood vessel network is an essential prerequisite for the development of TE bone and for its integration with the existing host tissue. Various scaffold constructs have thus been developed with the specific goal of promoting angiogenesis, in turn stimulating bone regeneration [10, 11].

Indeed, the greatest amount of new bone formation occurs in the most vascularized areas, whereas an inadequate vascularization at bone defect sites is associated with decreased bone tissue repair and regeneration and has been identified as the main hindrance to successful bone TE (BTE) [11]. Specifically, until the timely onset of construct vascularization (typically on the order of hours to days), seeded cells in an implanted bone TE construct rely on diffusion for the uptake of nutrients (i.e., oxygen, glucose, etc.) and the clearing of metabolic by-products. However this transport mechanism is only efficient over short distances (i.e., less than 200 μm) [12]. These diffusional constraints result in viable cells being located only superficially (i.e., at the periphery of the constructs) and thus limit the success of BTE throughout the entire thickness of the defect. To remedy this obstacle, scientists have proposed several methods to accelerate the onset of neovascularization for survival and integration of BTE with host tissue including (1) scaffold design, (2) inclusion of angiogenic growth factors, (3) in vitro pre-vascularization (i.e., co-culture of endothelial and osteogenic cells), and (4) in vivo pre-vascularization. Although it is still unclear which method is the best for successful in vivo application, a combination of these methods may prove to be most effective.

The achievement of a full understanding of the processes of angiogenesis, osteogenesis, and tissue engineering strategies would offer exciting future therapeutic opportunities for skeletal repair and regeneration in orthopedics.

In this framework, the ability to quantitatively analyze, in three dimensions, the vascular structure in TE is essential for the evaluation of the success of a given strategy. In the following, we will present the imaging techniques most used to evaluate the vascularization in the scaffold.

3 Assessment of BTE Microvessel Detection by Imaging Approaches

Different imaging methods are available to monitor the vascularization. In particular, it is possible to classify the vascular imaging approaches into three main groups: nonoptical techniques (X-ray, magnetic resonance, ultrasound, and positron emission imaging), optical techniques (optical coherence, fluorescence, multiphoton, and laser speckle imaging), and hybrid techniques (photoacoustic imaging) [13]. In the first group, great interest is focused on X-ray imaging methods, which are based on X-ray attenuation by the different tissues and have been successfully used to visualize large blood vessels.

In addition, micro-tomography [14] is able to provide higher-resolution imaging (about 1 μm) than ultrasound (about 30 μm) and MRI (about 100 μm), enabling the visualization and quantification of microvasculature. However, this level of performance can normally be obtained only with the use of contrast agents [15]. A recently emerging method, synchrotron phase-contrast micro-tomography, could help overcome this limitation. This method permits to combine 3D imaging with the analysis of microvascularization and bone microstructure [16], enabling the simultaneous identification of multiple tissue features without using contrast agents. This is due to the increased sensitivity of phase-sensitive X-ray imaging techniques. Indeed, this technique also overcomes the intrinsic limitations of conventional tomographic approaches, often unable to reliably reconstruct the full vascularization network in case of an incomplete filling of microvessels by contrast agents [17]. In addition, conventional characterization techniques have other limitations: 2D imaging, such as histology, yields incomplete spatial coverage with possible data misinterpretation, whereas conventional micro-CT does not achieve sufficient resolution and contrast.

4 X-Ray Phase-Contrast Tomography

The advent of synchrotron radiation supported the development of advanced 3D imaging techniques, such as X-ray phase-contrast tomography. Classical radiography and tomography are based on absorption, and they are well-known tools for imaging objects with hard X-rays. For studies of weakly absorbing materials, such as biological samples, the attenuation in the sample becomes often too small to give detectable contrast. In these cases, a better contrast can be achieved by imaging the *phase modulation* induced by an object in a coherent beam, which makes phase-based methods attractive for studies of weakly absorbing samples, both in materials and life sciences.

Various techniques have been developed to exploit phase contrast in the X-ray range. They can be classified into five main categories: propagation-based imaging (PBI) methods, analyzer-based imaging (ABI) methods, interferometric methods based on the use of crystals, and grating interferometric and grating non-interferometric methods [18]. These methods differ not only for their experimental

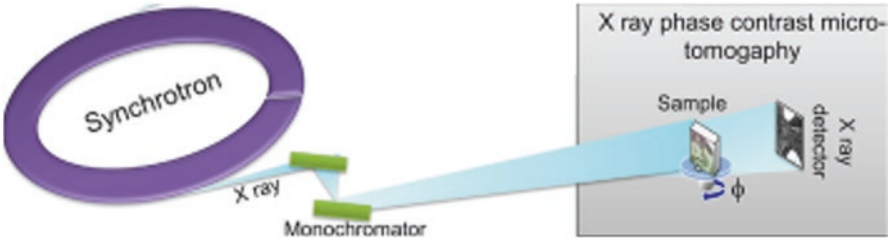

Fig. 9.2 Pictorial view of the X-ray phase-contrast micro-tomography experimental approach

setup and for their requirements in terms of the X-ray beam spatial and temporal coherence but also for the nature and amplitude of the provided image signal and for the amount of radiation dose that is delivered to the sample.

A simple yet effective phase-contrast method for hard X-rays is based upon in-line imaging after free-space propagation. When synchrotron X-rays illuminate the sample, variations in the optical path length produce slight local deviations (refraction) of the X-ray beam from its original path (Fig. 9.2).

In absorption radiography, the detector is generally placed close enough to the sample that these variations are unnoticed. On the contrary, when a larger free-space propagation distance is allowed between the sample and detector, the recorded image contains the refraction information in the form of interference fringes appearing at the interfaces between different materials within the sample (edge-enhancement effect) [19]. The fringes thus enhance the visibility of low-absorbing features. Nevertheless, the image captured by in-line propagation always contains mixed absorption and phase effects. Therefore, specific algorithms have to be used to recover the morphological distribution of absorption and phase within the object [20, 21]. Strictly speaking, the quantitative estimation of the object-projected thickness is possible only for mono-elemental samples under monochromatic illumination [20]. On the other hand, although the refractive indices of different soft tissues are very similar for hard X-rays, a semiquantitative phase imaging is still possible taking into account the specific interfaces between tissues [21].

The phase retrieval algorithm is applied to all projections of the tomographic measurements, using the code ANKAphase [20], based on Paganin algorithm (see Chap. 5). The algorithm produces the projected thickness of the object which is proportional to the refractive index decrement if the object is homogeneous. When applied to all tomographic projections, the retrieved phase maps can be fed to a standard filtered back-projection algorithm to obtain phase tomograms.

5 Experience in Bone Tissue Using X-Ray Phase-Contrast Tomography

Conventional X-ray micro-CT is a technique that enables a good visualization of the structure of mineralized bone and of biomaterials, but it fails when attempting to discern soft tissues at high resolutions. On the contrary, SXPCmT, based on

propagation-based settings, presents a better soft tissue contrast than conventional CT, clearly discriminating neural and vascular structures [7]. These results enable the investigation of the 3D vascularization of BTE. Detailed imaging and a quantitative description of the complete vascular network in such constructs are indeed crucial for monitoring the relation between bone formation and vascularization, and phase tomography was shown to efficiently discriminate between tissues with similar absorption coefficients (like collagen fibrils and blood vessels) [22–25]. In addition, the high quality achieved for the 3D images obtained by SXPCmT enabled the extraction of quantitative pieces of information (number, section, and distribution of the vessels crossing each section) for all the different sample preparations. In this framework, we have investigated by SXPCmT the 3D imaging of a vascular network in samples that underwent different preparations. Details on the sample preparation and animal treatment can be found in [9]. In particular, samples seeded with BMSC and perfused by the radiopaque medium MICROFIL were compared with samples seeded with BMSC and unstained, thus obtaining evidence that a high-resolution imaging of the vascular network is also possible without any previous staining treatment (Fig. 9.3a, b).

In addition, we also investigated samples not seeded with BMSC to study how such seeding affects vascularization process (Fig. 9.3c).

In particular, we have explored a central cube volume of 1.4 mm side, for all the samples. The precision of the selected volume was assured by the precision of the experimental setup, which allowed to illuminate equal portions of the samples. Exploiting the 3D character of the tomographic approach, we systematically analyzed the virtually selected sections (each 640 nm thick) of the samples, perpendicular to any chosen direction, studying the number, diameter, and distribution of the vessels crossing each section. To get insights on the structure of the vascular trees in the recovered implants, we first plotted the number of vessels of the vascular network reaching the system at different depths, and then we investigated the depth distribution of vessels with different sizes.

We observed that the major difference lies in the average number of branches forming the vascular trees. The sample not seeded with BMSC was poorly ramified, while the other three samples displayed thriving trees with many branches. It is important to emphasize that the histological studies performed on samples unseeded with cells also show a poor vascularization (Fig. 9.4).

Even though SXPCmT was able to visualize the 3D vascularization network inside the scaffold without any sample sectioning and preparation, the use of a coherent, highly brilliant X-ray synchrotron source was mandatory in order to achieve a high image quality with sub-micrometer spatial resolution.

This could certainly limit a possible future use of this technique in the clinical routine; however, this remains a highly valuable experimental approach in preclinical researches such as those involving the investigation of the vascularization process in different scaffolds.

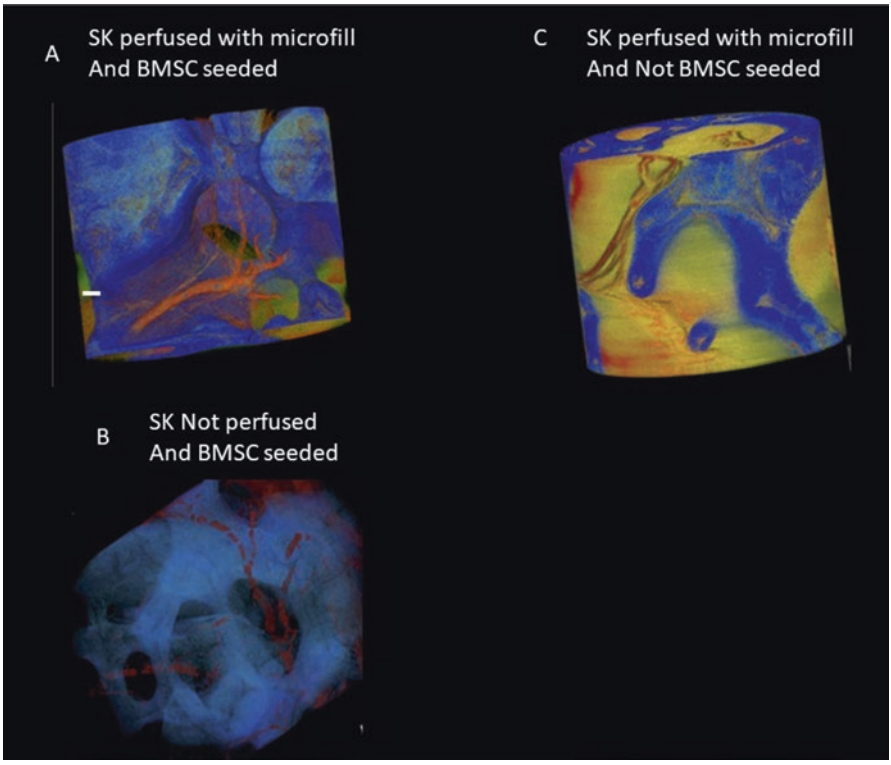

Fig. 9.3 The scale bar corresponds to 30 μm. (**a**) Sample A was prepared with MICROFIL®, and it was pre-seeded with BMSCs. The vessels in sample A are rendered in red, the scaffold in blue, and the soft tissue in yellow and green. (**b**) The 3D volume of sample B is reported. The segmentation renders the vessels in red and the scaffold in blue. The soft tissues were computationally removed from the 3D rendering to highlight the vessel distribution inside the scaffold. Sample B was also pre-seeded with BMSCs, but it was left unstained after the recovery of the scaffold from the animal. (**c**) Sample C was not BMSC seeded, but it was perfused with MICROFIL. The vessels are rendered in red and the soft tissue in yellow and green (Figure adapted from Bukrreva et al. [9])

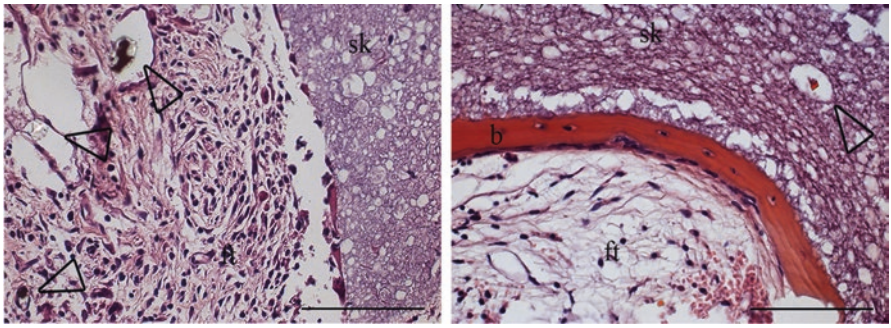

Fig. 9.4 Histological studies of (right side) scaffold skelite without cells; (left side) scaffold with cells. The arrows indicate vessels marked by MICROFIL. Acquisition by Zeiss Axiovert 200 M. sk skelite, ft fibrous tissue, b bone tissue, m MICROFIL; 40×, scale bar 100 μ micron. (Figure adapted from Bukrreva et al. [9])

6 Imaging Vascular Segmentation Method

SXPCmT provides an excellent investigation tool for soft tissues, in particular the mapping of the cellular and vascular distribution in biological samples without any casting preparation and with resolution in the 1–10 μm range [7]. Moreover, the capability to distinguish the vascular network without contrast agents has already been demonstrated [7, 26, 27], for example, in the case of the liver or for tumors and for the central nervous system [7, 27, 28]. Even in the visual inspection of tomography data, image segmentation is a crucial step for obtaining quantitative information. In particular, the purpose of any segmentation method is to classify the voxels of a particular feature in order to further assess significant parameters, thus providing a better visualization of the region of interest. Several approaches exist in order to reach this goal, including intensity- and model-based algorithms [29–31].

A simple intensity-based segmentation method, which can be employed, for example, to detect the vascular network, is based on the gray levels of the image, by considering the result of different threshold values in the image histogram. In intensity-based segmentation, indeed, the extraction of the voxels to be assigned to the different features (e.g., to the vessels) is based on the analysis of the image histogram. In particular, the image histogram is characterized by a multimodal distribution with slightly asymmetric tails on both sides of the modal value. It is easy to recognize that the main peak is to be assigned to the scaffold, so that it should not to be included in the segmented volume if we want to isolate only the vessels. On the other hand, voxels compatible with vessel lumen or walls and connective tissues have to be included and are located on gray levels identified by two small peaks at both sides of the main one, respectively. The result of the threshold application to the whole tomographic volume is shown in Fig. 9.5. Segmentation is able to reproduce the spatial arrangement of the different features in the vascular network, and it is possible to skeletonize and quantify the different features.

Unfortunately, the usage of a simple intensity approach presents several drawbacks.

Since no assumption on the continuity of the detected structure is considered, voxels with a local contrast decrease will not be included even though they represent part of the vessel.

In order to overcome this limitation, “undecided” voxels can be attached to segmented ones using different approaches [32]. Overall, intensity-based segmentation provides a good starting point to obtain fast and quantitative results.

7 Conclusions

SXPCmT is able to visualize the 3D vascularization network inside the scaffold without any sample sectioning and preparation. However, in order to achieve a higher image quality with sub-micrometer spatial resolution, the use of a coherent,

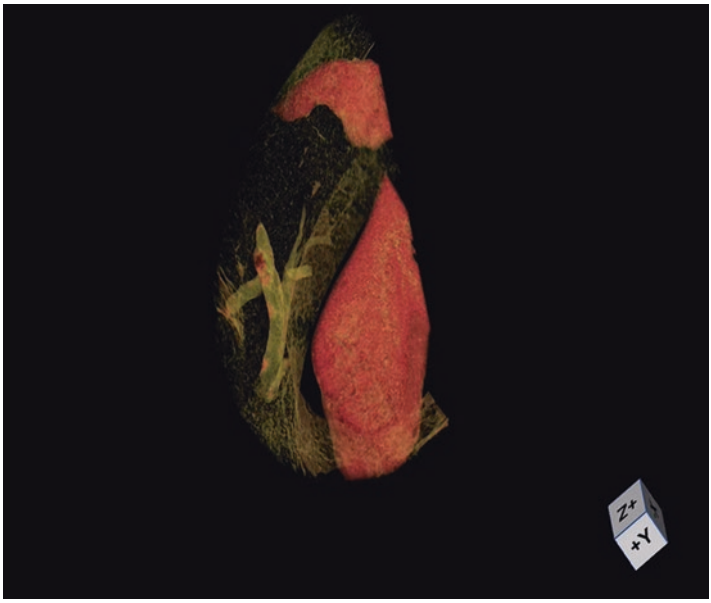

Fig. 9.5 3D rendering of soft tissue in the scaffold. In red the scaffold and in green the soft tissue and vessels

highly brilliant X-ray synchrotron source was mandatory. While this could certainly limit a possible future use of this technique in the clinical routine, PCmT remains a highly valuable experimental approach in preclinical researches such as those involving the investigation of different scaffold vascularizations. We therefore propose our approach as a tool for angiogenesis studies in TE and for any other preclinical investigations where the quantitative analysis of the vascular network is required.

References

1. Carano RA, Filvaroff EH (2003) Angiogenesis and bone repair. Drug Discov Today 8:980–989
2. Hench LL, Polak JM (2002) Third-generation biomedical materials. Science 295:1014–1017
3. Cancedda R, Dozin B, Giannoni P, Quarto R (2003) Tissue engineering and cell therapy of cartilage and bone. Matrix Biol 22:81–91
4. Quarto R et al (2001) Repair of large bone defects with the use of autologous bone marrow stromal cells. NEJM 344:385–386
5. Francis ME, Uriel S, Brey EM (2008) Endothelial cell–matrix interactions in neovascularization. Tissue Eng Part B Rev 14(1):19–32
6. Francis-Sedlak ME, Moya ML, Huang JJ, Lucas SA, Chandrasekharan N, Larson JC, Cheng MH, Brey EM (2010) Collagen glycation alters neovascularization in vitro and in vivo. Microvasc Res 80(1):3–9

7. Fratini M, Bukreeva I, Campi G, Brun F, Tromba G, Modregger P et al (2015) Simultaneous submicrometric 3D imaging of the micro-vascular network and the neuronal system in a mouse spinal cord. Sci Rep 5:8514
8. Cedola A, Bravin A, Bukreeva I, Fratini M, Pacureanu A, Mittone A, Massimi L, Cloetens P, Coan P, Campi G, Spanò R, Brun F, Grigoryev V, Petrosino V, Venturi C, Mastrogiacomo M, Kerlero De Rosbo N, Uccelli A (2017) X-ray phase contrast tomography reveals early vascular alterations and neuronal loss in a multiple sclerosis model. Sci Rep 7:5890
9. Bukrreva I et al (2015) High-resolution X-ray techniques as new tool to investigate the 3D vascularization of engineered-bone tissue. Front Bioeng Biotechnol 3:133
10. Kanczler JM, Oreffo RO (2008) Osteogenesis and angiogenesis: the potential for engineering bone. Eur Cell Mater 15:100–114
11. Das A, Botchwey E (2011) Evaluation of angiogenesis and osteogenesis. Tissue Eng Part B Rev 17(6):403–414
12. Muschler GF, Nakamoto C, Griffith LG (2004) Engineering principles of clinical cell-based tissue engineering. J Bone Joint Surg Am 86-A(7):1541–1558
13. Upputuri PK et al (2015) Recent developments in vascular imaging techniques in tissue engineering and regenerative medicine. Biomed Res Int 2015:783983
14. Barbetta A, Bedini R, Pecci R, Dentini M (2012) Role of X-ray microtomography in tissue engineering. Ann Ist Super Sanita 48:10–18
15. Langer M, Prisby R, Peter Z, Guignandon A, Lafage-Proust MH, Peyrin F (2011) Simultaneous 3D imaging of bone and microstructure in a rat model. IEEE Trans Nucl Sci 58:139–145
16. Giuliani A, Mazzoni S, Mele L, Liccardo D, Tromba G, Langer M (2017) Synchrotron phase tomography: an emerging imaging method for microvessel detection in engineered bone of craniofacial districts. Front Physiol 8:769
17. Fei J, Peyrin F, Malaval L, Vico L, Lafage-Proust MH (2010) Imaging and quantitative assessment of long bone vascularization in the adult rat using microcomputed tomography. Anat Rec 293:215–224
18. Bravin A, Coan P, Suortti P (2013) X-ray phase-contrast imaging: from pre clinical applications towards clinics. Phys Med Biol 58:R1–R35
19. Wilkins SW, Gureyev TE, Gao D, Pogany A, Stevenson AW (1996) Phase-contrast imaging using polychromatic hard X-rays. Nature 384(6607):335
20. Paganin D, Mayo SC, Gureyev TE, Miller PR, Wilkins SW (2002) Simultaneous phase and amplitude extraction from a single defocused image of a homogeneous object. J Microsc 206(1):33–40
21. Beltran MA, Paganin DM, Uesugi K, Kitchen MJ (2010) 2D and 3D X-ray phase retrieval of multi-material objects using a single defocus distance. Opt Express 18(7):6423–6436
22. Campi G, Fratini M, Bukreeva I, Ciasca G, Burghammer M, Brun F, Tromba G, Mastrogiacomo M, Cedola A (2015) Imaging collagen packing dynamics during mineralization of engineered bone tissue. Acta Biomater 23:309–316
23. Albertini G, Giuliani A, Komlev V, Moroncini F, Pugnaloni A, Pennesi G et al (2009) Organization of extracellular matrix fibers within polyglycolic acid-polylactic acid scaffolds analyzed using X-ray synchrotron-radiation phase-contrast micro computed tomography. Tissue Eng C Methods 15:403–411
24. Giuliani A, Manescu A, Langer M, Rustichelli F, Desiderio V, Paino F et al (2013) Three years after transplants in human mandibles, histological and in-line HT revealed that stem cells regenerated a compact rather than a spongy bone: biological and clinical implications. Stem Cells Trans Med 2:316–324
25. Cedola A, Campi G, Pelliccia D, Bukreeva I, Fratini M, Burghammer M, ... & Sodini N (2013). Three dimensional visualization of engineered bone and soft tissue by combined x-ray micro-diffraction and phase contrast tomography. Phys Med Biol 59(1):189
26. Mittone A, Ivanishko Y, Kovalev S, Lisutina P, Lotoshnikov M, Tkachev S, Tkacheva M, Crippa L, Dmitriev V, Bravin A (2018) High resolution hard X-ray 3D mapping of a *Macaca fascicularis* eye: a feasibility study without contrast agents. Phys Med 51:7–12

27. Lang S, Müller B, Dominietto MD, Cattin PC, Zanette I, Weitkamp T et al (2012) Three-dimensional quantification of capillary networks in healthy and cancerous tissues of two mice. Microvasc Res 84(3):314–322
28. Ciasca G, Sassun TE, Minelli E, Antonelli M, Papi M, Santoro A, Giangaspero F, Delfini R, De Spirito M (2016) Nano-mechanical signature of brain tumours. Nanoscale 8(47):19629–19643
29. Müller B, Beckmann F, Huser M, Maspero F, Szekely G, Ruffieux K et al (2002) Nondestructive three-dimensional evaluation of a polymer sponge by microtomography using synchrotron radiation. Biomol Eng 19(2):73–78
30. Pham DL, Xu C, Prince JL (2000) Current methods in medical image segmentation. Annu Rev Biomol Eng 2(1):315–337
31. Massimi L et al (2016) Characterization of mouse spinal cord vascular network by means of synchrotron radiation X-ray phase contrast tomography. Phys Med 32:1779–1784
32. Atwood RC, Lee PD, Konerding MA, Rockett P, Mitchell CA (2010) Quantitation of micro-computed tomography-imaged ocular microvasculature. Microcirculation 17(1):59–68

Chapter 10
Synchrotron X-Ray-Based Functional and Anatomical Lung Imaging Techniques

Sam Bayat, Christian Dullin, Marcus J. Kitchen, and Goran Lovric

Abstract Lung diseases are a major burden of public health especially in developed countries and therefore continue to be an active interest in preclinical and clinical research. Due to the complex structure and motion of the lung, an in vivo or in situ analysis would be very beneficial. However, this is very challenging for virtually all imaging technologies in small animal models of lung disease due to the small size of the organ and its rapid breathing motion. To study lung disease in detail, the interaction of molecular events, anatomical alterations, and changes in the lung function need to be assessed in parallel. The use of synchrotron light sources has enabled the development of several lung imaging techniques such as phase-contrast CT, 4D lung imaging, virtual histology of lung tissue, k-edge subtraction imaging for measuring regional lung ventilation and perfusion, as well as speckle-based airflow measurements. The application of these techniques has allowed to gain more insight into anatomical alterations as well as functional parameters in small animal lung disease models, which will be demonstrated in this chapter.

S. Bayat
Department of Clinical Physiology, Sleep and Exercise,
Université de Grenoble Alpes & Grenoble University Hospital, Grenoble, France

Department of Anaesthesia, Pharmacology and Intensive Care, Geneva University Hospital, Geneva, Switzerland

C. Dullin (✉)
Institute for Diagnostic and Interventional Radiology, University Hospital Goettingen, Goettingen, Germany

Italian synchrotron light source "Elettra", Trieste, Italy

Translational Molecular Imaging, Max-Plank-Institute for Experimental Medicine, Goettingen, Germany
e-mail: christian.dullin@med.uni-goettingen.de

M. J. Kitchen
School of Physics and Astronomy, Monash University, Clayton, VIC, Australia

G. Lovric
Swiss Light Source, WBBA/217, Paul Scherrer Institut, Villigen, Switzerland

A. Giuliani, A. Cedola (eds.), *Advanced High-Resolution Tomography in Regenerative Medicine*, Fundamental Biomedical Technologies,
https://doi.org/10.1007/978-3-030-00368-5_10

1 Introduction

The lung is an anatomically and functionally complex organ composed of a branching airway tree leading to terminal airspaces where gas exchange occurs. Lung diseases are one of the major health burdens worldwide [15]. Many lung diseases are induced or exacerbated by exposure to airborne environmental microorganisms and pollutants. Better understanding of lung structure and function remains therefore highly important for developing new therapies and diagnostic approaches. However, the deep location of the lung within the body, its constant motion with breathing and cardiovascular pulsation, and its high porosity pose extreme challenges for imaging especially in preclinical lung disease models in small animals such as mice, rats, or rabbits.

To date virtually only X-ray-based imaging methods provide the necessary spatial and/or temporal resolution. Here we will present different synchrotron radiation-based imaging methods: (i) free propagation phase-contrast zoom tomography [10], (ii) high-speed lung imaging [34], (iii) k-edge subtraction imaging [2], and (iv) speckle-based lung imaging [27]. Those techniques can be used to address morphological alterations [14], study ventilation and perfusion patterns [56], perform 2D and 4D elastography [24, 35], or track the migration of immune cells [13]. Due to the adverse effects of ionizing radiation such as X-rays onto biological tissue, not all these methods have potential applications in patients or living laboratory animals; thus the chapter is structured as follows: (i) in situ/ex vivo techniques and (ii) in vivo application of phase-contrast lung imaging.

2 Applications of Phase-Contrast Imaging for In Situ/Ex Vivo Analysis of Lungs in Small Animal Lung Disease Models

The use of a synchrotron as X-ray source with a comparable small source size, a very high photon flux, and a large source-to-sample distance allows to exploit the wave nature of the X-ray beam rather than only focusing on its attenuation as source of image contrast like in classical CT [42]. One way of doing this is to place the detector at a larger distance behind the object allowing the X-ray wave fronts that have passed through the object and have been deformed by its internal structure to interfere and cause strong edge enhancements on the recorded radiographs [55]. If this imaging scheme is combined with the application of "phase retrieval" algorithms, images with a strongly increased contrast-to-noise ratio can be obtained [44] which inherit the potential for significant reduction in X-ray dose [22]. This so-called propagation-based imaging (PBI) technique has proven to be especially suited for lung imaging due to the strong (sharp) interference fringes caused by the air-to-tissue surfaces in the lung microstructures [14, 29, 35, 45].

2.1 *In Situ Phase-Contrast Imaging of Entire Mouse Lungs*

The application of PBI enables quantification of subtle morphological alterations in small animal lung disease models. Moreover, the gain in image quality can be exploited to study, for instance, the fate of contrast agent-labeled macrophages in situ [13] as shown in Fig. 10.1. Alveolar macrophages clear the airways from inhaled pathogens and are one of the main effector cells in asthma [39]. Using PBI we demonstrated that macrophages can migrate from the airspace back into the bronchial walls, a previously unknown effect that may aid to a better understanding of the underlying pathomechanisms of asthma.

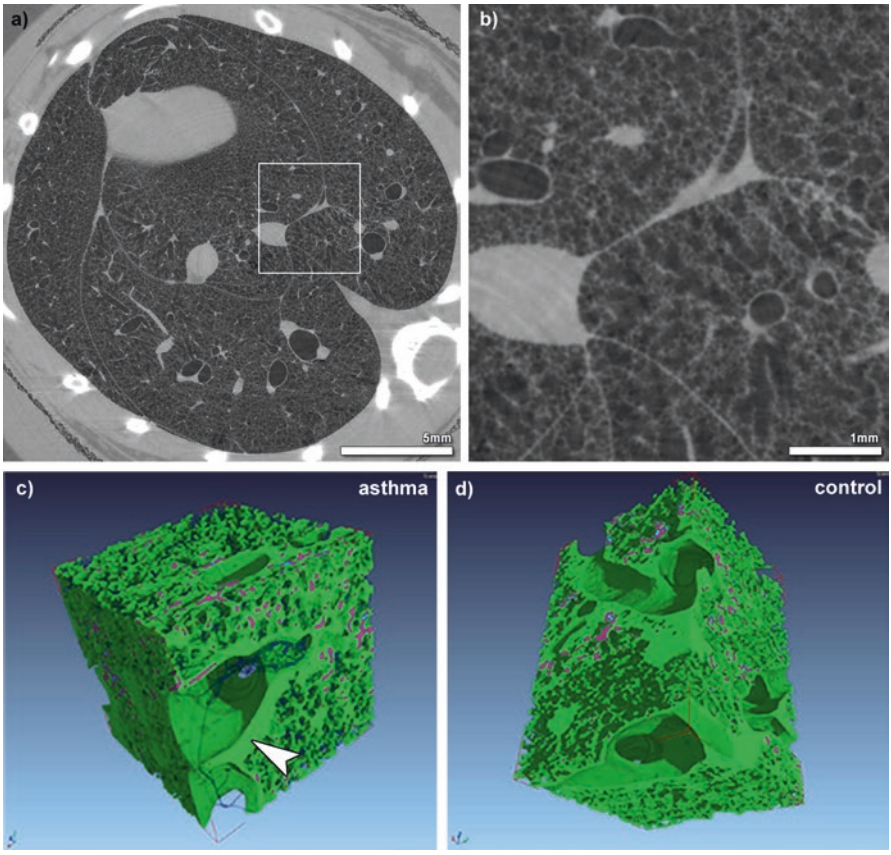

Fig. 10.1 (**a**) PBI image (9 µm pixel size) of an in situ mouse lung inflated with air at a constant pressure of 30 cm water column. (**b**) shows the level of detail that can be achieved with that approach. (**c**, **d**) displays the 3D rendering of volumes of interest from (**c**) and asthmatic and (**d**) a healthy mouse. Both mice were injected with 6×10^6 barium sulfate-labeled alveolar macrophages (violet). It can be seen that both morphological alterations like the symptomatic bronchial wall thickening in asthma (white arrow head) and migration sites of the macrophages can be analyzed simultaneously

2.2 Zoom-In Tomography for Localized High-Resolution Analysis Within the Lung

In contrast to lung disease like asthma that usually displays homogenously distributed morphological alterations within the lung, other lung diseases like idiopathic pulmonary fibrosis (IPF) [11] or especially lung cancer are characterized by a patchy appearance or only a few local foci. Despite the importance of an early diagnosis which could also benefit from the application of PBI, to study the local environment around a lung nodule, for instance, would be of great interest. Such an approach obviously requires a high spatial resolution. Thus, a zoom-tomography approach can be applied that uses a low-resolution scan to localize sites of interest and places a local area high-resolution scan at that position as demonstrated by [28].

2.3 Virtual Histology of Lung Tissue

Another important aspect in which synchrotron phase-contrast CT can be beneficial for lung research is to improve histological analysis. Histology can be considered the gold standard in tissue analysis especially in combination with immunohistochemistry. It allows to specifically highlight certain tissues or cell types and therefore study a pathology in detail. The main disadvantage of histology is that the specimen needs to be sectioned and is therefore destroyed within the process. Moreover, the sectioning is done in a blind manner and can only hardly be targeted to sites of interests. Phase- contrast CT allows to study embedded lung tissue prior to sectioning without the need of additional staining protocols and with strongly reduced radiation dose [49]. This so-called virtual histology technique even though it doesn't allow for specific highlighting of cells can aid classical histology by providing 3D analysis and can be used to guide the sectioning process to sites of interest [1]. Moreover, stored paraffin-embedded tissue samples that have been processed with the standard workflow for histological analysis and are associated with a verified clinical diagnosis could be analyzed, paving the way for setting up computer-aided decision systems in clinical pathology.

3 In Vivo Applications of Synchrotron X-Ray Imaging

3.1 K-Edge Subtraction Imaging

One of the most challenging goals of X-ray imaging is to quantitatively map the distribution of contrast agents within living tissues and organs with enough sensitivity, temporal and spatial resolution, and to enable the assessment of dynamic phenomena such as blood perfusion, microvascular permeability, or regional lung

ventilation. The ability to image the underlying morphology simultaneously is valuable for studying regional organ function, disease mechanisms, or the distribution of theranostic or toxic nanoparticles.

K-edge subtraction (KES) imaging is based on the sharp increase in the attenuation coefficient of an element, when the energy of incident X-rays exceeds the K-edge. Because synchrotron radiation flux is several orders of magnitude higher than a standard X-ray source, virtually monochromatic X-ray beams can be separated from the full spectrum while maintaining enough flux so that images can be acquired with short acquisition times on the order of ~1 ms. Separate maps of density distribution due to tissue and inhaled Xe gas or iodine injected in the blood can be obtained [2, 56]. The method can be extended to multi-K-edge and spectral K-edge imaging, where either multiple discrete energies or a range of energies spanning across multiple elemental K-edges is used [60]. A comprehensive review of K-edge and multispectral X-ray imaging techniques can be found in Thomlinson et al. [57].

3.1.1 Applications to the Investigation of Regional Lung Structure and Function

The distribution of regional ventilation is inhomogeneous in normal lung, and this inhomogeneity increases dramatically under pathologic conditions. Although classically attributed to the effect of gravity on lung expansion, the causes of this ventilation inhomogeneity both in normal lung and in pathologic conditions still remain a matter of debate. Experiments performed in microgravity [47] and using positron emission tomography [12] and hyperpolarized helium magnetic resonance imaging [43] have shown that in normal lung, a large share of ventilation heterogeneity arises independently of gravity and beyond the spatial resolution of these imaging modalities. A unique feature of KES imaging is that it allows quantitative measurements of ventilation distribution, down to sub-acinar spatial resolutions which enables the study of mechanisms leading to ventilation inhomogeneity at length scales that other imaging modalities cannot investigate.

The uneven distribution of ventilation has major fundamental and clinical implications. Ventilation heterogeneity affects the matching of regional ventilation and perfusion leading to less efficient gas exchange and can significantly affect the apparent degree of mechanical obstruction. Moreover, ventilation distribution importantly determines the distribution of inhaled medications and inhaled environmental pollutants.

One of the lung diseases where ventilation distribution inhomogeneity is enhanced is asthma. Asthma is characterized by the exaggerated contractile response of airways to various stimuli. For asthma diagnosis, airway responsiveness is often investigated using pharmacological substances that directly stimulate the airway smooth muscle. In asthmatic individuals however, airway constriction is indirectly induced by stimulation of inflammatory cells such as mast cells and eosinophils that release constricting mediators. Using KES imaging, it was demonstrated in

anesthetized rabbits that when airway constriction is induced by the inhalation of histamine mimicking an asthma attack, regional ventilation becomes very heterogeneous with development of patchy areas of reduced ventilation [5, 6, 48]. It was further shown that the kinetics of airway response to histamine is very different in central versus small peripheral airways, with faster constriction and recovery in the lung periphery, while central airways were slower to reach their maximal constriction [5], occasionally showing paradoxical dilatations [6]. This phenomenon may be due to the dynamic tidal expansion of proximal bronchi when distal airways constrict downstream [5] or serial airway interdependence [59].

The mechanism through which airway smooth muscle constriction is induced results in radically different patterns of airway constriction [7]. In rabbits sensitized to ovalbumin, airway constriction was induced either non-specifically by methacholine, which acts directly on the airway smooth muscle, or specifically through an allergen such as ovalbumin following allergic sensitization, which constricts the airways indirectly by triggering the activation of mast cells and eosinophils. While methacholine induced mainly central airway constriction, the allergen caused a much more heterogeneous pattern of ventilation distribution in the lung periphery (Fig. 10.2). The inhomogeneous airway reaction in allergic animals may have been due to the local heterogeneity of the distribution of immune cells involved in the allergic reaction itself [30]. Moreover, the inhomogeneous distribution of an inhaled aerosol containing environmental antigens or constricting agonists can result in an inhomogeneous peripheral airway response. Recently, the regional deposition of aerosol particles containing iodine was quantitatively mapped in rabbit lungs [47]. Ventilation distribution using KES imaging during Xe wash-in and the lung airway branching morphology, both critical parameters in determining aerosol transport and deposition, were also imaged. This study showed that the deposition of aerosol particles of a median aerodynamic diameter of ~3 μm was strongly heterogeneous (Fig. 10.3), decreased following methacholine-induced airway constriction, and

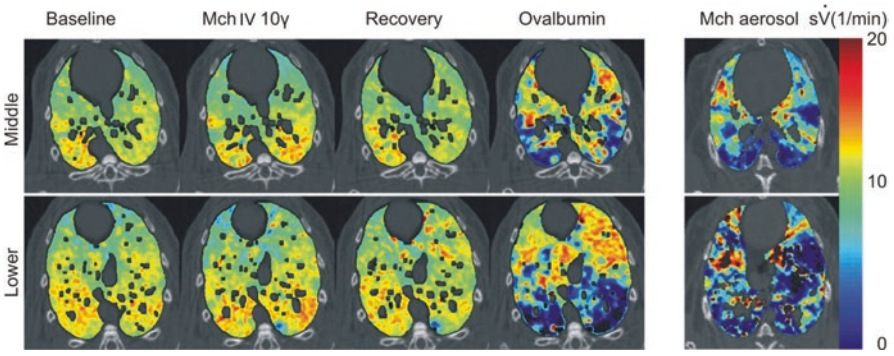

Fig. 10.2 Left panel: images of specific ventilation in one representative sensitized rabbit at baseline, during methacholine (Mch) infusion, on recovery, and after ovalbumin provocation. Right panel: images of regional ventilation in one representative control rabbit after Mch aerosol inhalation. Black color indicates zero specific ventilation (From Bayat et al. [6])

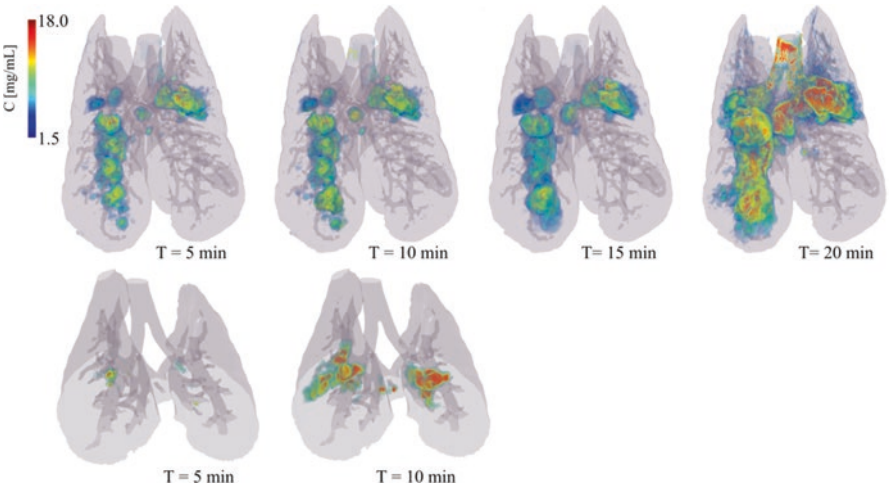

Fig. 10.3 Three-dimensional rendering of the regional deposition of iodine expressed as concentration (mg/ml) versus the duration of inhalation in a representative control (top row, whole lung) and an MCH animal (bottom row, 35 mm vertical height). Gray color: surface rendering of lung and conducting airway morphology; dark gray shows the projection of segmented conducting airways. Values below 1.5 mg/ml were not represented in order to better reveal focal areas of strong iodine deposition. Note the strongly inhomogeneous pattern and increasing amount of deposition with time in the control animal and a similarly inhomogeneous pattern but less overall deposition in the MCH animal

that deposition distribution could be imaged repeatedly with KES to obtain data on the kinetics of regional deposition or to determine how interventions can change the deposition pattern of aerosol particles.

Patients with acute respiratory distress syndrome (ARDS) invariably require mechanical ventilation in order to manage the work of breathing and improve gas exchange. In this condition, inflammation leads to high microvascular permeability edema and widespread patchy regions of alveolar flooding and collapse interspersed with normally aerated lung regions, which reduces the volume of aerated lung and leads to significant mechanical heterogeneity. Positive pressure ventilation in this condition imposes mechanical stresses on the parenchyma that can worsen lung injury, a condition known as ventilator-induced lung injury (VILI) [12, 43, 54]. Both excessive mechanical strain on the pulmonary alveoli due to large volume excursions in alveoli that remain aerated and tidal recruitment and decruitment of peripheral airspaces, referred to as “atelectrauma” [53], are thought to contribute to this process. Overall measurements of lung function do not allow assessing the functional behavior of the lung periphery under mechanical ventilation. Using KES imaging, positive end-expiratory pressure (PEEP) was shown to improve aeration in collapsed lung regions but not to eliminate overventilation of normal lung units in a model of experimental lung injury in rabbit [3]. Combined measurements of lung aeration based on tissue-density images, and regional ventilation based on Xe wash-in, allow distinguishing regions of alveolar collapse that are tidally ventilated,

exposing them to concentration of mechanical stresses [38], or regions with full or partial gas trapping, while static CT images do not allow this distinction [3]. Moreover, the administration of exogenous surfactant [4] or the impact of different modes of mechanical ventilation such as volume control or pressure-regulated modes on regional lung function can be assessed by KES imaging [46].

3.2 Time-Resolved Tomographic Microscopy (4D Imaging)

3.2.1 General Aspects About Microscopic 4D-CT

Time-resolved synchrotron-based tomographic microscopy (4D-SRμCT) allows for the study of rapid evolving processes that occur at microscopic resolutions (micrometer and below) and in all three spatial dimensions. To describe dynamic processes, tomograms are then taken at consecutive time points to create 4D type of movies. With the steady improvements of both acquisition protocols and X-ray instrumentation, it is nowadays possible to acquire single tomograms at a micrometer-sized spatial resolution in just a fraction of a second. Due to fast data streaming, the total acquisition time and hence the number of subsequent tomograms can be increased almost to an arbitrary extent [41]. This makes the technique available to a wide range of scientific disciplines (materials and geoscience, soft matter physics, functional biology, etc.) [40]. A further increase in temporal resolution is possible by the utilization of gating, i.e., by imaging different time points within the phase of an essentially periodic process. In that case, the tomographic projection images are then prospectively or retrospectively re-sorted in order to derive full tomographic datasets. Applied to the study of dynamic microscopic features under living conditions, and in particular microscopic aspects of pulmonary inflation, we have to consider several typical physiological aspects, which both determine the acquisition protocol in use and define the ultimate limitation of the technique.

3.2.2 Biological Aspects

The transition from standard μCT (with typical pixel sizes of 10–100 μm) toward high-speed tomographic microscopy is mostly characterized by the time scale required to capture the motion. We typically refer to “fast” tomographic acquisitions when they take less than a second at the micrometer scale. The smaller the microscopic feature of interest, the shorter the exposure time to capture its motion has to be. This not only requires a highly brilliant source like a synchrotron (high flux and coherence) but, in addition, a flexible imaging endstation that offers advanced signaling and precise triggering of all components that are part of the image acquisition process [37]. In the case of lungs, even small pressure oscillations of up to $\Delta p = \pm 0.1$ cmH_2O (caused by heart motion) lead to motion blurring in the CT-reconstructed images and render the distinction of individual alveolar septa

impossible. Although the breathing motion of the lung can be externally "adjusted," both in amplitude and frequency, by means of mechanical ventilation (MV) and deep anesthesia, the heartbeat frequency is determined by the instantaneous physiological condition of the living animal and is subject to strong variability. This is manifested in the variation of each beat-to-beat interval (R-R interval), the so-called heart rate variability (HRV), and alters the condition of strict motion periodicity, which on the other hand represents a prerequisite for standard gating techniques. Against this background, however, any attempt to image the lung in vivo with alveolar and septal spatial resolution in 3D must ensure the precise capturing of the lung motion at identical heartbeat and respiratory phases. While this problem is theoretically solvable by acquiring abundant tomographic data, the approach is further complicated by the fact that the X-ray exposure can easily exceed the tolerizeable radiation dose. Immediate effects from radiation on the investigated sample are then possible, being particularly the case when investigating biological materials with pixel sizes close to a few microns [8].

3.2.3 Technical Aspects

To overcome the aforementioned physiological aspects, a range of experimental conditions have to be met. For addressing the heartbeat aperiodicity, ultrashort single-projection exposures in the order of a few milliseconds (ms) as well as a precise adjustment of the time point within the cardiac cycle (R-R interval), at which the imaging takes place, are essential for obtaining artifact-free images. Subsequently, the imaging and X-ray exposure on the detector's side have to be adequately synchronized with all bio-signals that are monitored in the animal (e.g., respiration, ECG, anesthesia, and/or contrast agent administration), hence requiring an accurate (in the order of microseconds) signaling of all involved components. As an example of a typical case, we consider a prospectively heartbeat-gated technique, where each heartbeat triggers the image acquisition of one single tomographic projection. The interplaying components as well as the resulting tomographic slices at three different pressures are depicted in Fig. 10.4. First, after detecting the QRS complex, a trigger is fired that initiates the opening sequence of the X-ray shutter; consider the shutter's opening time to be very small (in the order of milliseconds or even microseconds), the detector should start the image acquisition only after the shutter is fully opened; likewise, once the detector's chip has been exposed (and detector's readout is en route), the shutter has to be closed instantaneously; taken that this process is conducted under a continuous rotation (in contrast to a snap and step technique, where each tomographic exposure is followed by an angular motion of the high-precision rotation axis), additionally, the explicit angle of the tomographic projection angle has to be recorded as well, being necessary for attributing the non-equidistant angular sampling during the CT-reconstruction phase; finally, the process is repeated until the desired number of tomographic projections has been recorded.

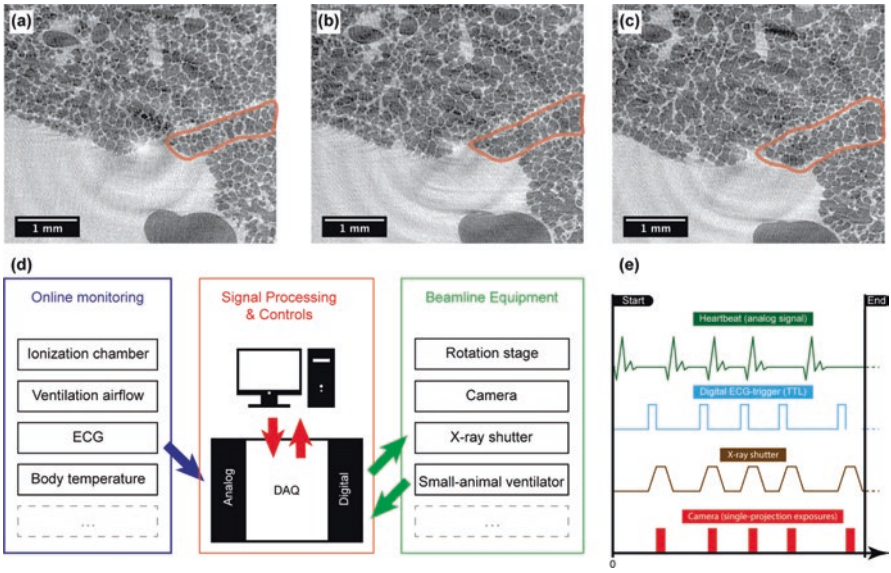

Fig. 10.4 Tomographic slices of rat lung at three different pressures: (**a**) 5 cmH_2O, (**b**) 10 cmH_2O, and (**c**) 15 cmH_2O. A schematic of all interacting beamline components is shown in (**d**), where DAQ stands for the data acquisition module, and in (**e**) the order (from top to bottom) of all triggering signals is shown during a full 180° rotation. (The images are adapted from Lovric et al. [36])

Following from that example, the total acquisition time and hence the total number of tomographic projections are both determined by the heartbeat rate of the investigated animal. The whole process can be conducted prospectively or retrospectively, but due to the stochastic nature of varying HR beat-to-beat intervals, the "prospective" approach is more dose-efficient. With the latter, pixel sizes of 1–3 μm have been reached in a murine and rat animal model [36]. The application of a more advanced anesthesiologic protocol might also appear favorable to stabilize the HRV and selectively increase or decrease HR. Under these conditions it has been possible to study different grades of pulmonary inflation, e.g., under pathologic states and/or other disease conditions. Up to date, however, the accumulated dose rates necessary to acquire multiple tomographic datasets at different time points or intrapulmonary pressures go beyond the scale of grays and thus are compatible only with acute (terminal) experiments. A number of studies conducted in the field of radiation therapy [16, 50, 51] have shown that acute radiation doses in the range of 20–90 gray (Gy) allow for a time window of at least a week before immediate effects from the radiation on the investigated biological samples will be present. Due to the very small fields of view (FOV), the dose is typically centered in a small part of the lung volume. As such, the technique does not only allow to study the functional effects of certain conditions on the alveolar scale but also different routes of intervention on shorter time scales. Taken that future developments of highly sensitive optical systems and detectors are on the way, it cannot be excluded that at a latter point in the

future, longitudinal experiments might be at reach, allowing for more complex lung disease models to be studied in vivo.

3.3 *Measurement of Lung Structure and Function from Phase- Contrast Speckle*

The air/tissue interfaces within the lung produce stronger phase gradients than any other pair of materials that naturally occur within mammalian tissues. In this way the air serves as a natural contrast agent when employing phase contrast and provides orders of magnitude greater image contrast than is possible with conventional X-ray imaging [25, 34]. Figure 10.5 shows an example of a propagation-based phase-contrast projection image of the thorax of a rabbit kitten. It has been shown that this type of imaging can readily reveal individual alveoli at the periphery of

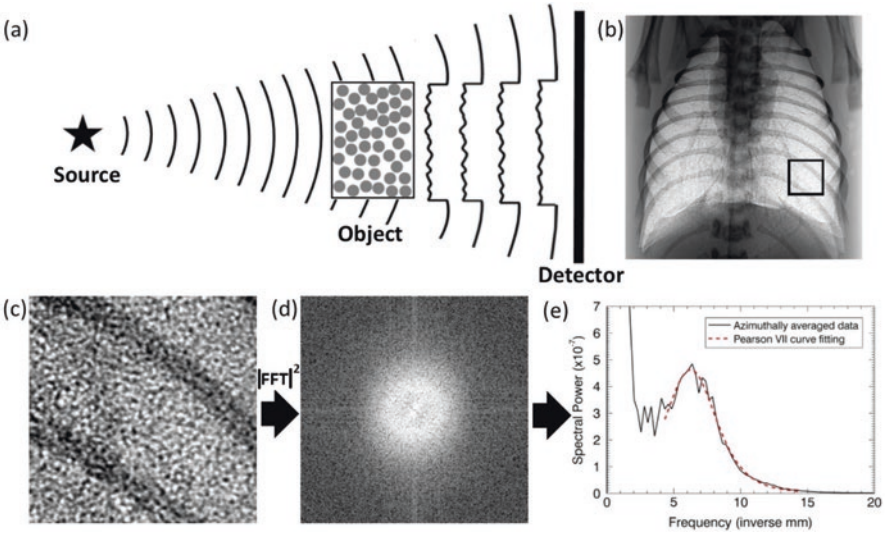

Fig. 10.5 (**a**) Illumination of a random phase object by partially coherent radiation creates a chaotic speckled intensity pattern upon propagation through space to the detector as a result of interference effects. The many airways in lung tissue can serve as a random phase screen for X-rays, resulting in a speckled pattern such as that shown in (**b**). This phase-contrast image of the lungs of a newborn rabbit kitten was acquired at beamline 20B2 of the SPring-8 synchrotron. Beam energy, 24 keV. Object-to-detector propagation distance, 1 m. Image size, 22.9×23.7 mm^2. A 256×256 pixel region of interest indicated by the black square is shown magnified in (**c**), which reveals the speckle detail. (**d**) The two-dimensional (2D) power spectrum of (**c**) (log scale). (**e**) Azimuthal average of (**d**) showing the raw data fit with a Pearson type VII function for measuring the position of the peak in the power spectrum caused by the speckle. The peak centroid at 6.2 ± 0.4 mm^{-1} reveals that the dominant length scale of this region of lung speckle is 159 ± 10 μm. (From Kitchen et al. [23], © Institute of Physics and Engineering in Medicine. Reproduced by permission of IOP Publishing. All rights reserved)

the lung [19]. In Fig. 10.5 we see that where there are many alveoli overlapping in projection, a seemingly random pattern of bright and dark spots (speckles) arises. These speckle patterns are not random noise, but instead encode information about the underlying structure of the lung tissue. Simulations have revealed that the speckles arise due to local focusing effects, whereby the multiple overlapping alveoli act as aberrated compound refractive lenses [27]. The knowledge that these complex patterns can be explained in simple terms of geometrical optics (i.e., focusing of X-rays) has enabled techniques to be developed to extract information about the structure of the lungs from single-projection images without the need for tomographic reconstruction and the associated increase in radiation exposure and data acquisition time.

3.3.1 In Vivo Measurements of Regional Lung Air Volume

Unlike the three-dimensional (3D) images of CT shown in section ("Applications of Phase-Contrast Imaging for In Situ/Ex Vivo Analysis of Lungs in Small Animal Lung Disease Models" – (Sect. 1 in this chapter)), which provide volumetric information, two-dimensional (2D) projection images are generally considered to have no depth information.

However, imaging objects comprised a single (monomorphous) material imaged with X-rays using phase or absorption contrast; it is possible to digitally recover the quantitative projected thickness of the material using a single-projection image [44]. Such calculations require a priori knowledge of the energy-dependent complex refractive index of the material. However, any voids within the material will be lost (collapsed) in the recovered projected thickness maps. Hence when imaging the isolated lung with phase contrast, it is possible to accurately determine local variations in projected lung tissue thickness, but the information on lung air volume is lost [26]. However, recent studies have shown it is possible to recover this information by addition of a single extra source of information.

Kitchen et al. [24] showed that by simply placing a small animal in a tube of water during imaging, it is possible to accurately measure changes in regional lung air volume at least as small as 25 μL. This technique measures volume change via fluid displacement by measuring changes in X-ray attenuation through the sample. As the lungs aerate, water is displaced out of the tube and away from the chest, which increases the intensity of the X-ray beam through the lungs. The Beer-Lambert attenuation law then enables the regional changes in projected water volume to be calculated, and the volume change of air inferred, under the assumption that the whole object has the same complex refractive index of water. While the soft tissues are effectively comprised of water, the complex refractive index of the overlapping bones is clearly very different to the surrounding tissues. However, if the volume of bone tissue does not move within a chosen region of interest (ROI), then the relative change in lung air volume can be accurately measured within that ROI [24]. Motion of the lungs and bones during breathing restricts the ROIs to relatively large areas, typically into four lung segments, for quantitative measurement.

To enable volume measurement down to the pixel level, Leong et al. developed a temporal subtraction algorithm that isolated the lung tissue from the bones using a calibration image recorded of a thorax with unaerated lungs [32]. An alternative approach for absorption contrast imaging is to simultaneously acquire two images at dual energies and mathematically segment the ribcage via logarithmic subtraction [9].

More recently, Leong et al. [33] exploited the information within the lung speckle patterns to enable quantitative absolute measures of lung volumes within small ROIs that also negates the strong influence of the bones. They exploited the fact that lung speckles are all of similar size and hence produce a strong peak when displayed in Fourier space as a power spectrum (Fig. 10.5). Leong et al. [33] showed that the area under this peak is related to the volume of the objects that cause the speckle. Since the bones are much larger than speckles, the peak is only minimally affected by the absorption contrast of the bones. The relationship between the peak area and the lung volume is not simple, but it was shown that absolute regional lung air volume can be calculated by first calibrating the speckle against known regional lung air volumes using the water displacement technique described above [24]. Since the speckles are present without immersing the animal in water, this calibrated technique removes the need for a water bath.

3.3.2 In Vivo Measurements of Regional Alveolar Dimensions

Leong et al. [33] showed that if the alveoli are considered as isolated spherical cavities, the power spectrum of lung speckle is directly proportional to the size of the alveoli. In a subsequent paper, they showed that the alveolar dimensions can be measured if the lung volume is known first [31]. This enabled the alveoli to be measured as they expand and contract throughout the respiratory cycle. Moreover, this technique enabled their size distribution to be measured regionally across the lungs in real time. Later, Kitchen et al. [23] showed that the position of the power spectrum peak gives a direct measure of the dominant length scale of the airway dimensions within the ROI. Thus, when the lungs are well aerated, and the bulk of the air volume is within the alveoli, then the peak position gives a simple and direct measure of alveolar dimensions. Likewise, if the alveoli collapse, the peak position indicates the average size of the remaining patent airways. This study revealed that immature alveoli of prematurely born animals will more readily collapse at birth than more mature lungs and that speckle analysis provides a sensitive measure of this maturity.

The techniques developed for quantifying lung structure and function from the phase-contrast speckle have been used to quantify real-time changes of lung liquid clearance and aeration at birth in a rabbit model. These studies have completely changed our understanding of the complexities underpinning the transition of the cardiopulmonary system to life after birth. They subsequently enabled clinical researchers to develop safer methods of resuscitating premature infants at birth who fail to breathe without medical intervention (see [17, 18, 20, 21, 52] and references therein).

4 Conclusion

Lung imaging remains challenging due to the deep location of the organ and its breathing motion. Nevertheless, the application of X-ray-based imaging strategies especially while using synchrotron light sources can provide insights in anatomical alterations on a cellular level, perfusion, and ventilation of the lung in vivo, can analyze elastic properties, and can be used to measure regional air volumes and alveolar dimensions. The latter techniques required only little X-ray dose and might therefore allow for clinical lung analysis as well. This strongly reduced X-ray dose is related to the exploitation of the wave nature of the X-rays using novel contrast regimes such as phase-contrast imaging, speckle formation imaging, dark-field imaging, etc.; it can therefore be expected that following phase-contrast breast imaging in patients [58], lung imaging will be the next application of these techniques in patients.

References

1. Albers J, Markus MA, Alves F, Dullin C (2018) X-ray based virtual histology allows guided sectioning of heavy ion stained murine lungs for histological analysis. Sci Rep 8:7712
2. Bayat S, Le Duc G, Porra L, Berruyer G, Nemoz C, Monfraix S, Fiedler S, Thomlinson W, Suortti P, Standertskjöld-Nordenstam C-G (2001) Quantitative functional lung imaging with synchrotron radiation using inhaled xenon as contrast agent. Phys Med Biol 46:3287
3. Bayat S, Porra L, Albu G, Suhonen H, Strengell S, Suortti P, Sovijärvi A, Peták F, Habre W (2013) Effect of positive end-expiratory pressure on regional ventilation distribution during mechanical ventilation after surfactant depletion. Anesthesiol J Am Soc Anesthesiol 119:89–100
4. Bayat S, Porra L, Broche L, Albu G, Malaspinas I, Doras C, Strengell S, Peták F, Habre W (2015) Effect of surfactant on regional lung function in an experimental model of respiratory distress syndrome in rabbit. J Appl Physiol 119:290–298. https://doi.org/10.1152/japplphysiol.00047.2015
5. Bayat S, Porra L, Suhonen H, Nemoz C, Suortti P, Sovijärvi ARA (2006) Differences in the time course of proximal and distal airway response to inhaled histamine studied by synchrotron radiation CT. J Appl Physiol Bethesda Md 1985 100:1964–1973. https://doi.org/10.1152/japplphysiol.00594.2005
6. Bayat S, Porra L, Suhonen H, Suortti P, Sovijärvi ARA (2009) Paradoxical conducting airway responses and heterogeneous regional ventilation after histamine inhalation in rabbit studied by synchrotron radiation CT. J Appl Physiol 106:1949–1958. https://doi.org/10.1152/japplphysiol.90550.2008
7. Bayat S, Strengell S, Porra L, Janosi TZ, Petak F, Suhonen H, Suortti P, Hantos Z, Sovijärvi ARA, Habre W (2009) Methacholine and ovalbumin challenges assessed by forced oscillations and synchrotron lung imaging. Am J Respir Crit Care Med 180:296–303. https://doi.org/10.1164/rccm.200808-1211OC
8. Boistel R, Pollet N, Tinevez J-Y, Cloetens P, Schlenker M (2009) Irradiation damage to frog inner ear during synchrotron radiation tomographic investigation. J Electron Spectrosc Relat Phenom 170:37–41
9. Carnibella R, Fouras A, Kitchen M (2012) Single-exposure dual-energy-subtraction X-ray imaging using a synchrotron source. J Synchrotron Radiat 19:954–959

10. Cloetens P, Barrett R, Baruchel J, Guigay J-P, Schlenker M (1996) Phase objects in synchrotron radiation hard x-ray imaging. J Phys Appl Phys 29:133
11. Crystal RG, Fulmer JD, Roberts WC, Moss ML, Line BR, Reynolds HY (1976) Idiopathic pulmonary fibrosis: clinical, histologic, radiographic, physiologic, scintigraphic, cytologic, and biochemical aspects. Ann Intern Med 85:769–788
12. Dreyfuss D, Soler P, Basset G, Saumon G (1988) High inflation pressure pulmonary edema. Respective effects of high airway pressure, high tidal volume, and positive end-expiratory pressure. Am Rev Respir Dis 137:1159–1164. https://doi.org/10.1164/ajrccm/137.5.1159
13. Dullin C, dal Monego S, Larsson E, Mohammadi S, Krenkel M, Garrovo C, Biffi S, Lorenzon A, Markus A, Napp J, Salditt T, Accardo A, Alves F, Tromba G (2015) Functionalized synchrotron in-line phase-contrast computed tomography: a novel approach for simultaneous quantification of structural alterations and localization of barium-labelled alveolar macrophages within mouse lung samples. J Synchrotron Radiat 22:143–155. https://doi.org/10.1107/S1600577514021730
14. Dullin C, Larsson E, Tromba G, Markus AM, Alves F (2015) Phase-contrast computed tomography for quantification of structural changes in lungs of asthma mouse models of different severity. J Synchrotron Radiat 22:1106–1111. https://doi.org/10.1107/S1600577515006177
15. Ferkol T, Schraufnagel D (2014) The global burden of respiratory disease. Ann Am Thorac Soc 11:404–406. https://doi.org/10.1513/AnnalsATS.201311-405PS
16. Hong Z-Y, Eun SH, Park K, Choi WH, Lee JI, Lee E-J, Lee JM, Story MD, Cho J (2014) Development of a small animal model to simulate clinical stereotactic body radiotherapy-induced central and peripheral lung injuries. J Radiat Res (Tokyo) 55:648–657
17. Hooper SB, Kitchen MJ, Polglase GR, Roehr CC, te Pas AB (2018) The physiology of neonatal resuscitation. Curr Opin Pediatr 30:187–191. https://doi.org/10.1097/MOP.0000000000000590
18. Hooper SB, Kitchen MJ, Siew ML, Lewis RA, Fouras A, te Pas AB, Siu KK, Yagi N, Uesugi K, Wallace MJ (2009) Imaging lung aeration and lung liquid clearance at birth using phase contrast X-ray imaging. Clin Exp Pharmacol Physiol 36:117–125. https://doi.org/10.1111/j.1440-1681.2008.05109.x
19. Hooper SB, Kitchen MJ, Wallace MJ, Yagi N, Uesugi K, Morgan MJ, Hall C, Siu KK, Williams IM, Siew M (2007) Imaging lung aeration and lung liquid clearance at birth. FASEB J 21:3329–3337
20. Hooper SB, Siew ML, Kitchen MJ, te Pas AB (2013) Establishing functional residual capacity in the non-breathing infant. Semin Fetal Neonatal Med 18:336–343. https://doi.org/10.1016/j.siny.2013.08.011
21. Hooper SB, te Pas AB, Kitchen MJ (2016) Respiratory transition in the newborn: a three-phase process. Arch Dis Child Fetal Neonatal Ed 101:F266–F271. https://doi.org/10.1136/archdischild-2013-305704
22. Kitchen MJ, Buckley GA, Gureyev TE, Wallace MJ, Andres-Thio N, Uesugi K, Yagi N, Hooper SB (2017) CT dose reduction factors in the thousands using X-ray phase contrast. Sci Rep 7:15953
23. Kitchen MJ, Buckley GA, Leong AFT, Carnibella RP, Fouras A, Wallace MJ, Hooper SB (2015) X-ray specks: low dose in vivo imaging of lung structure and function. Phys Med Biol 60:7259–7276. https://doi.org/10.1088/0031-9155/60/18/7259
24. Kitchen MJ, Lewis RA, Morgan MJ, Wallace MJ, Siew ML, Siu KKW, Habib A, Fouras A, Yagi N, Uesugi K, Hooper SB (2008) Dynamic measures of regional lung air volume using phase contrast x-ray imaging. Phys Med Biol 53:6065–6077. https://doi.org/10.1088/0031-9155/53/21/012
25. Kitchen MJ, Lewis RA, Yagi N, Uesugi K, Paganin D, Hooper SB, Adams G, Jureczek S, Singh J, Christensen CR, Hufton AP, Hall CJ, Cheung KC, PAvlov KM (2005) Phase contrast X-ray imaging of mice and rabbit lungs: a comparative study. Br J Radiol 78:1018–1027. https://doi.org/10.1259/bjr/13024611
26. Kitchen MJ, Paganin D, Lewis RA, Yagi N, Uesugi K (2005) Analysis of speckle patterns in phase-contrast images of lung tissue. Nucl Instrum Methods Phys Res Sect Accel Spectrometers Detect Assoc Equip 548:240–246. https://doi.org/10.1016/j.nima.2005.03.096

27. Kitchen MJ, Paganin D, Lewis RA, Yagi N, Uesugi K, Mudie ST (2004) On the origin of speckle in x-ray phase contrast images of lung tissue. Phys Med Biol 49:4335–4348. https://doi.org/10.1088/0031-9155/49/18/010
28. Krenkel M, Markus A, Bartels M, Dullin C, Alves F, Salditt T (2015) Phase-contrast zoom tomography reveals precise locations of macrophages in mouse lungs. Sci Rep 5:09973
29. Krenkel M, Töpperwien M, Dullin C, Alves F, Salditt T (2016) Propagation-based phase-contrast tomography for high-resolution lung imaging with laboratory sources. AIP Adv 6:035007. https://doi.org/10.1063/1.4943898
30. Layachi S, Porra L, Albu G, Trouillet N, Suhonen H, Peták F, Sevestre H, Suortti P, Sovijärvi A, Habre W, Bayat S (2013) Role of cellular effectors in the emergence of ventilation defects during allergic bronchoconstriction. J Appl Physiol Bethesda Md 1985 115:1057–1064. https://doi.org/10.1152/japplphysiol.00844.2012
31. Leong AF, Buckley GA, Paganin DM, Hooper SB, Wallace MJ, Kitchen MJ (2014) Real-time measurement of alveolar size and population using phase contrast x-ray imaging. Biomed Opt Express 5:4024–4038
32. Leong AF, Fouras A, Islam MS, Wallace MJ, Hooper SB, Kitchen MJ (2013) High spatio-temporal resolution measurement of regional lung air volumes from 2D phase contrast x-ray images. Med Phys 40:041909
33. Leong AFT, Paganin DM, Hooper SB, Siew ML, Kitchen MJ (2013) Measurement of absolute regional lung air volumes from near-field x-ray speckles. Opt Express 21:27905. https://doi.org/10.1364/OE.21.027905
34. Lewis RA, Yagi N, Kitchen MJ, Morgan MJ, Paganin D, Siu KKW, Pavlov K, Williams I, Uesugi K, Wallace MJ, Hall CJ, Whitley J, Hooper SB (2005) Dynamic imaging of the lungs using x-ray phase contrast. Phys Med Biol 50:5031–5040. https://doi.org/10.1088/0031-9155/50/21/006
35. Lovric G, Barré SF, Schittny JC, Roth-Kleiner M, Stampanoni M, Mokso R (2013) Dose optimization approach to fast X-ray microtomography of the lung alveoli. J Appl Crystallogr 46:856–860
36. Lovric G, Mokso R, Arcadu F, Oikonomidis IV, Schittny JC, Roth-Kleiner M, Stampanoni M (2017) Tomographic in vivo microscopy for the study of lung physiology at the alveolar level. Sci Rep 7:12545
37. Lovric G, Mokso R, Schlepütz CM, Stampanoni M (2016) A multi-purpose imaging endstation for high-resolution micrometer-scaled sub-second tomography. Phys Med Eur J Med Phys 32:1771–1778
38. Mead J, Takishima T, Leith D (1970) Stress distribution in lungs: a model of pulmonary elasticity. J Appl Physiol 28:596–608
39. Mizue Y, Ghani S, Leng L, McDonald C, Kong P, Baugh J, Lane S, Craft J, Nishihira J, Donnelly S (2005) Role for macrophage migration inhibitory factor in asthma. Proc Natl Acad Sci U S A 102:14410–14415
40. Mokso R, Marone F, Irvine S, Nyvlt M, Schwyn D, Mader K, Taylor G, Krapp H, Skeren M, Stampanoni M (2013) Advantages of phase retrieval for fast x-ray tomographic microscopy. J Phys Appl Phys 46:494–504
41. Mokso R, Schlepütz CM, Theidel G, Billich H, Schmid E, Celcer T, Mikuljan G, Sala L, Marone F, Schlumpf N (2017) GigaFRoST: the gigabit fast readout system for tomography. J Synchrotron Radiat 24:1250–1259
42. Momose A, Takeda T, Itai Y, Hirano K (1996) Phase–contrast X–ray computed tomography for observing biological soft tissues. Nat Med 2:473–475
43. Muscedere JG, Mullen JB, Gan K, Slutsky AS (1994) Tidal ventilation at low airway pressures can augment lung injury. Am J Respir Crit Care Med 149:1327–1334. https://doi.org/10.1164/ajrccm.149.5.8173774
44. Paganin D, Mayo SC, Gureyev TE, Miller PR, Wilkins SW (2002) Simultaneous phase and amplitude extraction from a single defocused image of a homogeneous object. J Microsc 206:33–40. https://doi.org/10.1046/j.1365-2818.2002.01010.x
45. Parsons DW, Morgan K, Donnelley M, Fouras A, Crosbie J, Williams I, Boucher RC, Uesugi K, Yagi N, Siu KK (2008) High-resolution visualization of airspace structures in intact mice via synchrotron phase-contrast X-ray imaging (PCXI). J Anat 213:217–227

46. Porra L, Bayat S, Malaspinas I, Albu G, Doras C, Broche L, Strengell S, Peták F, Habre W (2016) Pressure-regulated volume control vs. volume control ventilation in healthy and injured rabbit lung: an experimental study. Eur J Anaesthesiol 33:767–775. https://doi.org/10.1097/EJA.0000000000000485
47. Porra L, Dégrugilliers L, Broche L, Albu G, Strengell S, Suhonen H, Fodor GH, Peták F, Suortti P, Habre W, Sovijärvi ARA, Bayat S (2018) Quantitative imaging of regional aerosol deposition, lung ventilation and morphology by synchrotron radiation CT. Sci Rep 8:3519. https://doi.org/10.1038/s41598-018-20986-x
48. Porra L, Peták F, Strengell S, Neitola K, Janosi TZ, Suhonen H, Suortti P, Sovijärvi AR, Habre W, Bayat S (2010) Acute cigarette smoke inhalation blunts lung responsiveness to methacholine and allergen in rabbit: differentiation of central and peripheral effects. Am J Physiol Lung Cell Mol Physiol 299:L242–L251
49. Saccomano M, Albers J, Tromba G, Dobrivojević M, Gajović S, Alves F, Dullin C (in press) Synchrotron inline phase contrast μCT enables detailed virtual histology of embedded soft-tissue samples with and without staining. J Synchrotron Radiat
50. Semenenko VA, Molthen RC, Li C, Morrow NV, Li R, Ghosh SN, Medhora MM, Li XA (2008) Irradiation of varying volumes of rat lung to same mean lung dose: a little to a lot or a lot to a little? Int J Radiat Oncol Biol Phys 71:838–847
51. Seppenwoolde Y, Lebesque JV (2001) Partial irradiation of the lung. Elsevier. pp 247–258
52. Siew ML, Kitchen MJ, te Pas AB, Hooper SB (2015) Pulmonary transition at birth. In: The lung: development, aging and the environment. Academic, Oxford, pp 251–264
53. Slutsky AS (1999) Lung injury caused by mechanical ventilation. Chest 116:S9
54. Slutsky AS, Ranieri VM (2013) Ventilator-induced lung injury. N Engl J Med 369:2126–2136. https://doi.org/10.1056/NEJMra1208707
55. Snigirev A, Snigireva I, Kohn V, Kuznetsov S, Schelokov I (1995) On the possibilities of x-ray phase contrast microimaging by coherent high-energy synchrotron radiation. Rev Sci Instrum 66:5486–5492. https://doi.org/10.1063/1.1146073
56. Suhonen H, Porra L, Bayat S, Sovijärvi A, Suortti P (2008) Simultaneous in vivo synchrotron radiation computed tomography of regional ventilation and blood volume in rabbit lung using combined K-edge and temporal subtraction. Phys Med Biol 53:775
57. Thomlinson W, Elleaume H, Porra L, Suortti P (2018) K-edge subtraction synchrotron X-ray imaging in bio-medical research. Phys Med 49:58–76
58. Tromba G, Longo R, Abrami A, Arfelli F, Astolfo A, Bregant P, Brun F, Casarin K, Chenda V, Dreossi D (2010) The SYRMEP beamline of elettra: clinical mammography and bio-medical applications. AIP. pp 18–23
59. Winkler T, Venegas JG (2007) Complex airway behavior and paradoxical responses to bronchoprovocation. J Appl Physiol 103:655–663. https://doi.org/10.1152/japplphysiol.00041.2007
60. Zhu Y, Samadi N, Martinson M, Bassey B, Wei Z, Belev G, Chapman D (2014) Spectral K-edge subtraction imaging. Phys Med Biol 59:2485

Chapter 11
Better Cartilage Imaging at Synchrotron Facilities

Annie Horng

Abstract Phase-contrast imaging is a novel x-ray-based technique which provides previously unprecedented radiation-based soft tissue depiction. Radiography and CT are both possible on intact joints as well as small samples, showing detailed cartilage structure depiction from a macroscopic to microscopic level and therefore opening a wide range of possibilities for detecting cartilage lesions, analyzing cartilage anatomy, and understanding natural aging, which is important to develop future treatment options for preserving or repairing cartilage and slow the course of osteoarthritis. Given its high resolution of cartilage matrix depiction, it might also provide a promising tool for studying engineered cartilage cultures and their evolution, which might aid in development of better cartilage transplantation specimen.

Establishment and optimization of PCI in suited animal models might provide a useful tool for preclinical research for facilitating longitudinal follow-up of osteoarthritic changes or efficiency of therapeutical treatments/repairs.

1 From Overview to Microscopic Scale

1.1 Introduction

Osteoarthritis (OA) is a growing public health problem representing the most common cause of disability giving the aging demographics but also change in lifestyle of the younger population nowadays with consecutive annual costs up to $128 billion for the health system in the USA [1, 2].

OA is the advanced form of joint degeneration, which occurs over the lifespan based on everyday wear but might be accelerated by overuse, trauma, overweight, and other risk factors [3].

A. Horng (✉)
RZM – Radiologisches Zentrum München-Pasing, München, Germany
e-mail: horng@rzm.de

A. Giuliani, A. Cedola (eds.), *Advanced High-Resolution Tomography in Regenerative Medicine*, Fundamental Biomedical Technologies,
https://doi.org/10.1007/978-3-030-00368-5_11

Cartilage degradation is regarded as a precursor for OA, and as cartilage is known to possess only limited healing properties, the optimal procedure to prevent or decelerate OA would be early prevention of cartilage damage or endorsement of cartilage regeneration.

But to enable early intervention and therapy, an appropriate imaging technique is needed as a tool, which optimally noninvasively can both depict early cartilage changes sufficiently and allow for reliable follow-up examinations to support and evaluate beginning, choice, and efficiency of the chosen therapy.

2 Cartilage Composition

Understanding anatomy and natural aging of cartilage tissue has therefore become important in understanding the development of OA.

Articular cartilage is a multiphasic tissue with fluid and solid components. Chondrocytes and the extracellular matrix (proteoglycans and collagen) form about 30–50% (solid phase), water and dissolved electrolytes/minor glycoproteins/lipids about 50–70% (fluid phase) of the wet weight of normal cartilage. Articular cartilage can be divided into four distinct zones with differing collagen orientations: the superficial zone (collagen fibrils arranged parallel to the surface), the transitional zone (fibril orientation is less organized), the deep zone (fibrils are perpendicular to the surface of the joint), and the calcified cartilage zone (Fig. 11.1) [4–8].

The chondrocytes synthesize molecular matrix components and incorporate those into the extracellular matrix with the purpose of preserving its structural integrity and biomechanical properties such as tensile strength and elasticity, which are both necessary for the capability of absorbing and distributing loading forces.

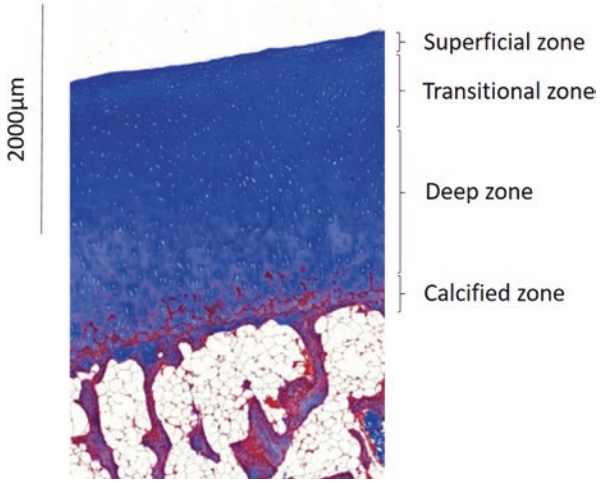

Fig. 11.1 Histological section of the human patellar articular cartilage (Azan staining) showing the anatomical layers

Disturbance of this well-coordinated process may lead to deterioration of the matrix. The collagen fibril arrangement in the extracellular matrix, especially their orientation, influences the tensile behavior. Initial degenerative changes assumedly result from an impaired ability of the solid matrix to support loads, which causes a breakdown of the matrix, further reducing its load-bearing capacity [9, 10]. Fatigue micro-cracks may develop within the cartilage or on its surface, which may grow with the diminishing load-carrying capacity of the matrix. In the natural development of OA, initially, the most superficial collagen fibers are weakened, which leads to surface fibrillation with subsequent disturbance of the whole network of fibrils down to the boundary with the subchondral bone. The weakening of the collagen network in turn results in tissue swelling and loss of its ability to sustain loading [5].

Unfortunately, the biomechanical properties as well as the aging process in cartilage are still not well understood given the lack of a suitable imaging method to evaluate and visualize that process.

3 Current State of Cartilage Imaging

Direct cartilage imaging is possible by computer tomography (CT) and magnetic resonance imaging (MRI). However, clinical CT only plays a minor role, as it does depict the cartilage layer as well as cartilage height but only with restricted resolution and also lacking the visibility of structural cartilage changes due to insufficient soft tissue contrast within the tissue itself. Therefore, MRI is currently the method of choice for the clinical evaluation of cartilage status, which depending on the choice of sequences provides superior structural information about the matrix, volume, and height and even quantitative information regarding biochemical content such as collagen or proteoglycan changes [11]. However, morphological MRI techniques for cartilage imaging still suffer limitations in achievable resolution, while quantitative MRI techniques still require complex time-consuming post-processing.

So, clinically rough structural depiction of cartilage is possible to some extent, while a more detailed structural analysis still lacks a suitable imaging method.

4 Feasibility Cartilage Imaging with Phase-Contrast Imaging

The novel x-ray-based phase-contrast imaging (PCI) is a technique, which utilizes the dual property of x-rays when they are passing through tissue. It provides contrast information about tissue architecture by using the proportional larger refraction signal by phase shifts, which occur at tissue borders, even when its absorption contrast differences are imperceptible [12].

This ability is promising for imaging tissues with low absorption contrast differences, such as cartilage. For over a decade, PCI has been applied on complete or partial joints and cartilage samples using different techniques, such as propagation-based imaging, analyzer-based imaging, and grating interferometry [13].

5 Planar Synchrotron X-Ray Radiography

Early application of PCI as planar synchrotron x-ray radiography (analyzer-based technique) applied on ex-articulated rabbit femoral head samples confirms the visibility of a thin cartilage layer as compared to conventional synchrotron x-ray radiography [14].

Given the feasibility of cartilage depiction, the next step was to evaluate whether the technique can depict cartilage matrix changes.

An experiment with larger ex vivo human ex-articulated human ankle joints using the same technique examined several samples of the talar dome comprising normal healthy and samples of different degenerated cartilage stages based on macroscopic inspection. PCI radiography was able to both depict the surface and underlying cartilage tissue inhomogeneity and defects in the different samples and to discriminate mild to severe degeneration [15]. However, those visible changes are considered already as gross anatomical changes, which already represent irreparable changes. While impressing that cartilage defects of different stages are depictable using an x-ray technique, it still would be desirable to capture even earlier matrix changes to facilitate early treatment.

MRI has been deemed able to depict a lamellar structure of the cartilage which resembles the currently understood anatomy of the cartilage structure [16–18]. Knowing that PCI provides images with markedly improved gains in soft tissue contrast as compared to the conventional radiography technique warrants further application with higher resolution and evaluation whether it could compete with MRI or provide even more information about tissue structure. Phase-contrast radiography performed on human femoral head slices with a thickness of 1 cm was able to resolve vertical structures with an arcade formation in the superficial zone which resemble the assumed collagen fiber arrangement [19], similar as described in electron microscopy [20], and was hypothesized to present density jumps between the major collagen bundles.

Phase-contrast radiography has also been performed on an unaltered intact human cadaveric knee joint, which is an important step in evaluating the performance of the technique in depicting cartilage in their natural environment. The cartilage is still depictable and the surface even assessable; however, given the complex three-dimensional anatomy of the joint, parts of the cartilage layer cannot be seen freely because of cartilage-cartilage or cartilage-bone overlap [21].

6 Computer Tomography Synchrotron Imaging in Clinically Relevant Samples

So, planar phase-contrast imaging with high resolution has been shown to visualize collagen fiber orientation, cartilage fibrillation, and defects. But unfortunately this is only possible in small samples or thin slices of tissue. In thicker samples or whole

specimen, structures are superimposed on one image, and therefore structural information is either lost or masked. In the case of cartilage changes, disruptions of the tissue might still be visible, but the local information about the extent or orientation might still be lost and presumably resulting in underestimation of lesions.

A possibility to overcome overlap problems is the acquisition of an image volume. Phase-contrast imaging computed tomography (PCI-CT) has been performed on intact complete human cadaveric knee joints using both the analyzer-based and the propagation-based techniques. It presented soft tissue contrast surpassing conventional CT with clear delineation of ligamentous, tendinous, muscular, vascular, and fatty structures (Fig. 11.2) [22, 23].

It provided visualization of altered cartilage regions invisible in absorption and conventional CT. Delineation of surface changes was approximating alterations seen on high-resolution 3T MRI using cartilage-dedicated sequences, though being less conspicuous in PCI (Fig. 11.3).

Examination of the performance of PCI-CT of grading cartilage lesions resulted in a sensitivity, specificity, and accuracy of 50%, 70.8%, and 55.2%, respectively – similar as using a 3T MRI (54.2%, 66.7%, and 57.3%) [24]. However those numbers need to be taken with caution because of several factors. First visual assessment,

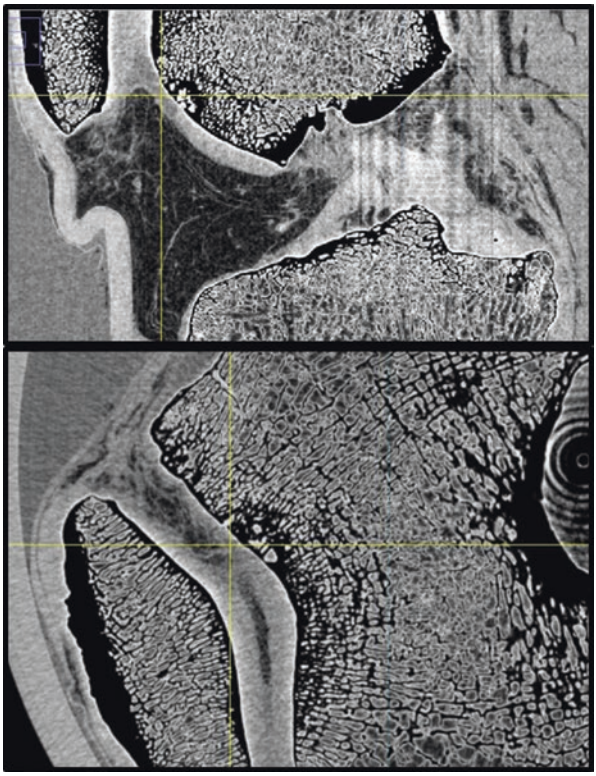

Fig. 11.2 Sagittal (top image) and axial (lower image) section from a 3D phase-contrast imaging computer tomography dataset of an intact human knee joint showing clear delineation of soft tissue structures including the cartilage layer. Also visible, in situ challenge of depicting the cartilage border in contact areas

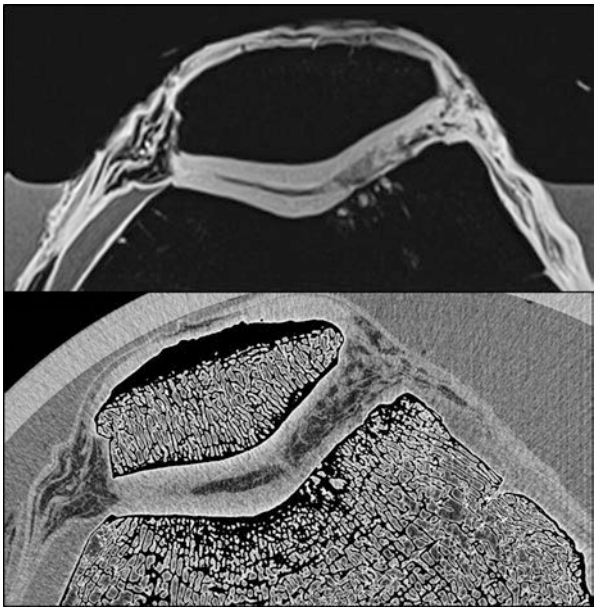

Fig. 11.3 Axial slices of a cartilage-dedicated sequence (3Tesla, FLASH – fast low-angle shot sequence, top image) and a phase-contrast imaging computed tomography dataset (lower image) taken from an intact human cadaveric knee joint depicting cartilage thinning with subchondral cystic changes in the lateral trochlea. The lesion is well visible in the PCI image though less conspicuous as compared to the MRI

which only reveals through eye sight visible lesions, was used simulating arthroscopy, which is the common gold standard for assessing cartilage lesions and for evaluating the performance of imaging techniques. Even for the current cartilage imaging gold standard MRI, there is an ongoing non-resolved controversy about its correlation with arthroscopy regarding detection and grading of cartilage lesions. The grading of cartilage lesions itself also is applied quite diversely depending on the utilized grading scale and personal training of the observer. Another point needed to be taken into account is that PCI-CT provides a new kind of image contrast for cartilage tissue and the lesions to which the observer still needs to get accustomed to and which eventually need to be validated, e.g., histologically to learn what is really depicted.

Simultaneously, underlying bony changes were depicted in high detail, which correlated well with conventional CT [24]. Additionally, cartilage and meniscal calcifications were visible on PCI which were neither perceptible on conventional CT nor MRI [22].

7 High-Resolution Computer Tomography Synchrotron Imaging

Application of PCI-CT (propagation-based technique) on cylindrical small cartilage-bone samples (7 mm), drilled from human patellar specimen with a resolution of 8 μm^2, provided a high-resolution image of the cartilage layer showing thickness,

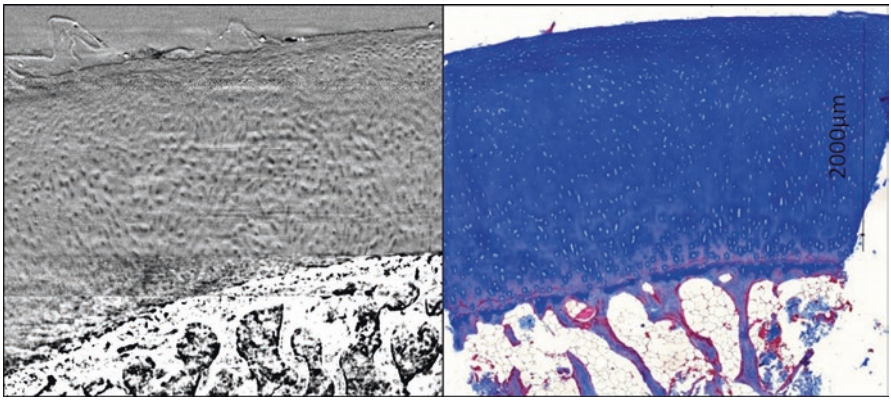

Fig. 11.4 Sagittal reformation of a 3D PCI-CT dataset vs. histologic section (Azan staining). The high-resolution PCI-CT sections depict numerous chondrocytes as well as their distribution. Observation of the chondrocyte arrangement might suggest an underlying structural organization. The depicted anatomical structures in the PCI-CT are concordant to the histologic section

surface, and even chondrocytes and their distribution within the cartilage depth, which has been unprecedented with current imaging techniques. The phase-contrast image reflected similar tissue information as compared to histology (Fig. 11.4) [25]. Another study with a similar setup using a cylindrical bovine cartilage-bone sample showed similar results [26].

The possibility of detailed delineation of the cartilage structures offers interesting new possibilities. Detailed depiction of chondrocytes in a certain tissue volume enables us for the first time to quantitatively analyze spatial cell distribution and density, which might be a first step in learning to understand the three-dimensional composition of cartilage, its biomechanical function, as well as evolution of degeneration.

8 Animal Model

Besides the effort to adapt phase-contrast imaging for future clinical appliances in humans to enhance cartilage diagnostics, establishment of animal models is also of interest. As the PCI has been proven to provide both possible cartilage visualization in small samples and intact joint specimen, evaluation and validation of an animal model might be useful for preclinical research.

Phase-contrast radiographic evaluation of intact canine knee joints with different grades of cartilage degeneration was possible to some extent as lesions were partially visible [27] but partially altered or masked due to technical artifacts and anatomical structural overlay as already described also for human specimen.

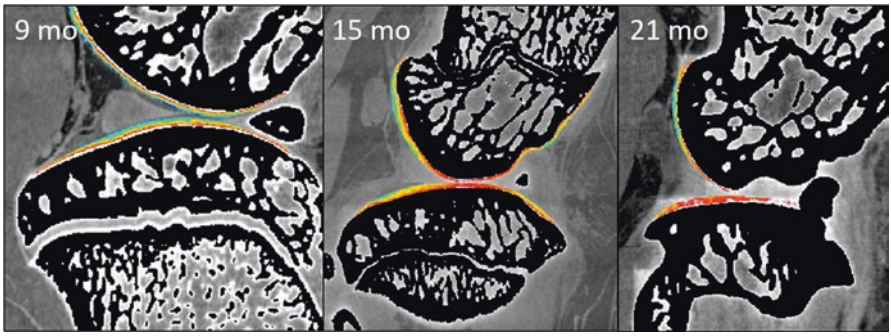

Fig. 11.5 Colormapping on sagittal reformations of 3D PCI-CT datasets of fast-aging guinea pigs of three different ages reveals changes in electron density with increasing age of the animal

For animal models micro-CT are already utilized, which achieve higher resolution with respect to the smaller specimen size as compared to convention clinically used CT machines.

PCI-CT on the intact knee joint of guinea pigs of three different ages from the Hartley strain, which naturally age fast and develop OA, reveal improved cartilage depiction as compared to micro-CT images. Colormapping was attempted on the PCI datasets to evaluate whether structural changes of the thin cartilage layer could be enhanced, revealing that the cartilage of the different age groups indeed show differences with increasing values in electron density with increasing age (Fig. 11.5) [28]. The anatomical substrate of those changes however remains to be determined.

Given the very thin cartilage of guinea pigs and the consecutively challenging interpretation of cartilage change, PCI-CT was also tested on an intact rabbit knee joint model. In the rabbit model, OA was induced by lateral meniscectomy. The rabbit cartilage proved to be thicker and better visible as in the guinea pig model and reveal initial cartilage thinning and electron density changes after colormapping 6 weeks after the surgery [29].

PCI-CT therefore proves feasible for cartilage imaging in intact joints of different animal models. With further optimization of this technique, establishment of an animal model for osteoarthritis research would very desirable, especially for longitudinal in vivo assessment of the efficacy of novel therapeutic strategies.

9 Limitation of PCI in Cartilage Imaging

Given the rather young application of PCI in cartilage imaging, technical optimization as well as understanding and removing imaging artifacts in imaging cartilage in different environments is still necessary.

Another relevant point is the work on reduction of radiation dose and imaging time. The radiation dose of an intact human knee joint reaches up to 145 mGy, with the use of an improved reconstruction algorithm and reduced projections still up to 50 mGy, which are clearly above the permitted radiation threshold for in vivo imaging.

Specifically PCI-CT data size is also an issue not to be neglected. Even datasets from small samples can easily reach a size of several gigabytes because of the high-resolution images, datasets from intact joints even considerably more. This restricts data handling and viewing as both sufficient computer hardware and software are needed for proper analysis of the collected data.

10 Outlook and Prospects

PCI radiography and especially PCI-CT offer excellent soft tissue delineation and enable cartilage visualization both in clinically relevant large samples such as a whole human knee specimen with superior depiction of cartilaginous changes previously undetectable by the conventional x-ray techniques as well as high-resolution imaging resembling histological resolution. Analyzing the cartilage on a (sub) micron level will help to better understand its function and degradation, possibly opening prospects for developing methods to preserve or repair cartilage, improve cartilage engineering, and slow OA formation.

Application of PCI on animal models might have potential in becoming a valuable method in preclinical imaging providing 3D investigations of whole specimens for longitudinal follow-up of osteoarthritic changes or therapeutical effects.

References

1. Cheng YJ, Hootman JM, Murphy LB, Langmaid GA, Helmick CG (2010) Prevalence of doctor-diagnosed arthritis and arthritis-attributable activity limitation – United States, 2007–2009. MMWR 59(39):1261–1265
2. CDC (2007) National and state medical expenditures and lost earnings attributable to arthritis and other rheumatic conditions-United States, 2003. MMWR 56:4–7
3. Johnson VL, Hunter DJ (2014) The epidemiology of osteoarthritis. Best Pract Res Clin Rheumatol 28(1):5–15
4. Mow VC, Proctor CS, Ma K (1989) Biomechanics of articular cartilage. Lea & Febiger, Philadelphia
5. Walker JM (1998) Pathomechanics and classification of cartilage lesions, facilitation of repair. J Orthop Sports Phys Ther 28(4):216–231
6. Weiss C, Rosenberg L, Helfet AJ (1968) An ultrastructural study of normal young adult human articular cartilage. J Bone Joint Surg Am 50(4):663–674
7. Huber M, Trattnig S, Lintner F (2000) Anatomy, biochemistry, and physiology of articular cartilage. Investig Radiol 35(10):573–580
8. Benninghoff A (1925) Form und Bau der Gelenkknorpel in ihren Beziehungen zur Funktion. Z Zellforsch Mikrosk Anat 2(5):783–862

9. Guilak F, Ratcliffe A, Lane N, Rosenwasser MP, Mow VC (1994) Mechanical and biochemical changes in the superficial zone of articular cartilage in canine experimental osteoarthritis. J Orthop Res 12(4):474–484
10. Pathria MN, Chung CB, Resnick DL (2016) Acute and stress-related injuries of bone and cartilage: pertinent anatomy, basic biomechanics, and imaging perspective. Radiology 280(1):21–38
11. Eckstein F, Guermazi A, Gold G, Duryea J, Hellio Le Graverand MP, Wirth W et al (2014) Imaging of cartilage and bone: promises and pitfalls in clinical trials of osteoarthritis. Osteoarthr Cartil 22(10):1516–1532
12. Born M, Wolf E (1999) Principles of optics: electromagnetic theory of propagation, interference and diffraction of light. Cambridge University Press, Cambridge, UK
13. Diemoz PC, Bravin A, Coan P (2012) Theoretical comparison of three X-ray phase-contrast imaging techniques: propagation-based imaging, analyzer-based imaging and grating interferometry. Opt Express 20(3):2789–2805
14. Muehleman C, Chapman LD, Kuettner KE, Rieff J, Mollenhauer JA, Massuda K et al (2003) Radiography of rabbit articular cartilage with diffraction-enhanced imaging. Anat Rec A Discov Mol Cell Evol Biol 272(1):392–397
15. Mollenhauer J, Aurich ME, Zhong Z, Muehleman C, Cole AA, Hasnah M et al (2002) Diffraction-enhanced X-ray imaging of articular cartilage. Osteoarthr Cartil 10(3):163–171
16. Rubenstein J, Recht M, Disler DG, Kim J, Henkelman RM (1997) Laminar structures on MR images of articular cartilage. Radiology 204(1):15–16 author reply 7-8
17. Olivier P, Loeuille D, Watrin A, Walter F, Etienne S, Netter P et al (2001) Structural evaluation of articular cartilage: potential contribution of magnetic resonance techniques used in clinical practice. Arthritis Rheum 44(10):2285–2295
18. Yoshioka H, Haishi T, Uematsu T, Matsuda Y, Anno I, Echigo J et al (2002) MR microscopy of articular cartilage at 1.5 T: orientation and site dependence of laminar structures. Skelet Radiol 31(9):505–510
19. Muehleman C, Majumdar S, Issever AS, Arfelli F, Menk RH, Rigon L et al (2004) X-ray detection of structural orientation in human articular cartilage. Osteoarthr Cartil 12(2):97–105
20. Clark JM (1985) The organization of collagen in cryofractured rabbit articular cartilage: a scanning electron microscopic study. J Orthop Res 3(1):17–29
21. Li J, Wilson N, Zelazny A, Meyer J, Zhong Z, Muehleman C (2012) Assessment of diffraction-enhanced synchrotron imaging for cartilage degeneration of the human knee joint. Clin Anat. 2013 Jul;26(5):621–9
22. Horng A, Brun E, Mittone A, Gasilov S, Weber L, Geith T et al (2014) Cartilage and soft tissue imaging using X-rays: propagation-based phase-contrast computed tomography of the human knee in comparison with clinical imaging techniques and histology. Investig Radiol 49(9):627–634
23. Li J, Zhong Z, Connor D, Mollenhauer J, Muehleman C (2009) Phase-sensitive X-ray imaging of synovial joints. Osteoarthr Cartil 17(9):1193–1196
24. Geith T, Brun E, Mittone A, Gasilov S, Weber L, Adam-Neumair S et al (2018) Quantitative assessment of degenerative cartilage and subchondral bony lesions in a preserved cadaveric knee: propagation-based phase-contrast CT versus conventional MRI and CT. AJR Am J Roentgenol 210(6):1317–1322
25. Coan P, Bamberg F, Diemoz PC, Bravin A, Timpert K, Mutzel E et al (2010) Characterization of osteoarthritic and normal human patella cartilage by computed tomography X-ray phase-contrast imaging: a feasibility study. Investig Radiol 45(7):437–444
26. Zehbe R, Haibel A, Riesemeier H, Gross U, Kirkpatrick CJ, Schubert H et al (2010) Going beyond histology. Synchrotron micro-computed tomography as a methodology for biological tissue characterization: from tissue morphology to individual cells. J R Soc Interface 7(42):49–59
27. Muehleman C, Li J, Zhong Z (2006) Preliminary study on diffraction enhanced radiographic imaging for a canine model of cartilage damage. Osteoarthr Cartil 14(9):882–888

28. Horng A, Geith T, Brun E, Mittone A, Gasilov S, Adam-Neumair S et al (2014) Cartilage imaging in a guinea pig knee joint model of different ages using high resolution propagation-based phase-contrast CT ESSR; Riga, Latvia
29. Geith T, Brun E, Mittone A, Gasilov S, Weber L, Adam-Neumair S et al (2015) Phase contrast imaging for osteoarthritis diagnosis: a suitable animal model for longitudinal preclinical studies. IMXP; Garmisch-Partenkirchen, Germany

Chapter 12
Into the Heart: What Contributions to Cardiac Regeneration?

Alessandra Giuliani and Mara Mencarelli

Abstract One of the leading causes of death in the western world is undoubtedly cardiovascular diseases, with special reference to myocardial infarction and consequent heart failure. The therapeutic strategies adopted nowadays are based on drug therapy, coronary artery angioplasty, pacemakers and implantable defibrillator, coronary artery bypass grafts, ventricular remodeling, dynamic cardiomyoplasty, organ transplantation, and mechanical circulatory assistance devices. However, all these procedures are often ineffective and invasive. Moreover, myocardial heart engineering has experienced significant progress over the last 10 years, with fundamental advances in stem cell biology and knowledge of biomaterials. However, one of the limiting factors in the overall interpretation of clinical results obtained by cell therapy is represented by the lack of in vivo visualization of the injected cells and of their fate within the myocardium. This chapter shows that X-ray microtomography (microCT) and in particular phase-contrast imaging may offer the unique possibility to detect with high definition and resolution the three-dimensional spatial distribution of stem cells, once injected inside an infarcted heart in small animal models. It was shown, through microCT, the migration of these cells within the damaged cardiac tissue, achieving an appropriate identification and localization of the injected cells. Thus, phase-contrast microCT appears to be an innovative and exclusive way to investigate the cellular events involved in cardiac regeneration and represents a promising tool for future clinical translations.

1 Introduction

One of the leading causes of death in the western world is undoubtedly cardiovascular diseases (CVDs), with special reference to myocardial infarction (MI) and consequent heart failure (HF) [1–3], caused by irreparable loss or dysfunction of

A. Giuliani (✉) · M. Mencarelli
Department of Clinical Sciences, Polytechnic University of Marche, Ancona, Italy
e-mail: a.giuliani@univpm.it

A. Giuliani, A. Cedola (eds.), *Advanced High-Resolution Tomography in Regenerative Medicine*, Fundamental Biomedical Technologies,
https://doi.org/10.1007/978-3-030-00368-5_12

cardiomyocytes due to the abrupt deprivation of oxygen supply. In this context, with only small fractions of myocytes retaining the capacity to replicate, the heart has a very limited self-regeneration capacity.

Thus, the therapeutic strategies adopted nowadays for HF are based on drug therapy, coronary artery angioplasty (using balloons and stents), pacemakers and implantable defibrillator, coronary artery bypass grafts, ventricular remodeling, dynamic cardiomyoplasty, organ transplantation, and mechanical circulatory assistance devices. However, all these procedures are often ineffective and invasive.

On the other hand, considerable progress has been made in myocardial heart engineering over the last 10 years, with fundamental advances in stem cell biology and knowledge of biomaterials.

Unfortunately, despite these advantages, clinical trials applying myocardial heart engineering have shown contradictory results, with moderate or no evident benefits for patients.

These approaches were mainly based on cellular therapy with the objective to generate new myocardium by transcoronary and intramyocardial cell injection, mainly of bone marrow [4] and skeletal muscle [5] origin. However, despite the limited positive impact on cardiac repair [6], these studies demonstrated a positive impact on patients with chronic MI and HF, with negligible adverse effects and without significant increase of arrhythmias [7].

Resident cardiac progenitor cells (CPCs) are an alternative cell source with which to treat ischemic cardiomyopathies. Indeed, progenitor cells living in the heart are programmed to generate the myocardium, i.e., the tissue lost with MI [8–13]. Cardiac mesenchymal stem cells (MSCs) [14] are a special type of resident cells, recently found in the cardiac stroma [15], referred to in the literature as cardiac mesenchymal stemlike cells [16] or cardiac mesenchymal-like stromal cells [17, 18].

However, detection of these injected cells within the myocardium is still a challenge, independently of their origin, because a reliable reconstruction of their fate is hampered by the lack of an efficient method for their 3D imaging and quantification within the heart.

Light, fluorescence, scanning, and transmission electron microscopy techniques efficiently image and quantify the tissue-rebuilding process but have the limitation of delivering only 2D local information, thus hampering their applicability for cell tracking, as shown by Terrovitis et al. [19]. Indeed, as only a few sections per sample are typically analyzed, the quantitative evaluation is often subjected to variability and sampling errors.

Moreover, 3D imaging methods, like MRI, PET, and conventional CT, despite having been shown to provide reliable quantification of the rebuilding process (including longitudinal cell tracking), introduce different limitations in the localization of the injected cells within the heart, mainly due to the need to use contrast agents [19, 20].

2 Synchrotron Radiation-Based Imaging of Stem Cell Homing in Infarcted Hearts

Third-generation synchrotron structures, producing brilliant photon beams, with spatial and temporal coherence properties [21, 22], have proved extremely useful for studying ex vivo the myocardium in animal models [23–25] and humans [26].

These studies demonstrated that image quality and quantitative information are sensibly improved by the use of phase-contrast microtomography (PhC-microCT). As fully described in the previous chapters, while in conventional microCT the signal is exclusively based on attenuation contrast, in the PhC approach both the amplitude and the phase of the X-ray wave are modified when passing through a tissue. This effect is described by the refractive index n:

$$n(\boldsymbol{r}) = 1 - \delta(\boldsymbol{r}) + i\beta(\boldsymbol{r}) \tag{12.1}$$

The δ value, the refractive index decrement, is actually proportional to the mean electron density, which in turn is almost proportional to the mass density. It is much larger than β, the attenuation index, at the energies used to study soft tissues, with the δ/β ratio close to 10^3.

The novelty that differentiates the phase-contrast method from the conventional absorption-based one is the capacity of the first in discriminating tissues with similar attenuation [27], like myocardial structure, coronary vessels, and conduction bundle.

Kaneko et al. [26] imaged all these structures on five non-pretreated whole infantile and fetal heart specimens obtained by autopsy. The study was carried out at the SPring-8 synchrotron radiation facility using the Talbot grating interferometer at the bending magnet beamline BL20B2 and demonstrated that PhC-microCT could be a powerful tool for elucidating unanswered questions concerning congenital heart diseases.

Dullin et al. [23] depicted the same conclusion on animal models: they attempted a phosphotungstic acid (PTA) ex vivo staining approach with the objective to efficiently enhance the X-ray attenuation of soft tissues for a better visualization of mouse hearts by microCT. This study demonstrated that the technique allowed the ex vivo imaging of several structures (atrium, ventricles, fiber structure of the myocardium, vessel walls) of PTA-stained mouse hearts, not requiring monochromatic and/or coherent X-ray sources. Moreover, by volumetric measurements, they were able to assess the plaque volumes in the aortic valve region of mice from ApoE−/− mouse models.

Some authors [24] recently showed that microCT offers the possibility of visualizing in 3D and in ex vivo conditions, with high definition and resolution, rat cardiac progenitor cells (CPCs) after injection in infarcted rat hearts. Myocardial infarction was induced by coronary binding of the left anterior descending coronary artery in the male Wistar rats (*Rattus norvegicus*). Three weeks later, 5×10^5 rat clonogenic

CPCs, previously labeled with iron oxide (Feridex) nanoparticles, were injected intramyocardially in the rat hearts. Sham-operated rats were treated similarly, but without tying a ligature around the artery. One week later, the animals were sacrificed and the hearts were fixed for the microCT analysis.

The microCT acquisitions were performed at the beamline BM05 of the European Synchrotron Radiation Facility (ESRF), using a 15 keV monochromatic X-ray beam, at two different sample-to-detector distances: 25 mm and 500 mm to achieve both the absorption- and the phase-contrast signal.

A full fusion automatic algorithm described elsewhere [28] was used to superimpose the two sets of data, merging them in a single image dataset for further 3D visualization.

The injected cells were observed in 3D, after migration to the damaged cardiac tissue, with structural information not previously imaged by conventional 2D imaging techniques.

The X-ray absorption of cells labeled with iron oxide was higher than for the surrounding hosting tissues, allowing their discrimination as bright spots in the reconstructed volumes (Fig. 12.1). One week after the injection, the labeled cells were mostly found in the infarcted area (Fig. 12.1c, d, f), indicating their migration from the injection site, close to the coronary binding, toward the damaged tissue. The fingerlike cell structures detected in the left ventricular wall (Fig. 12.1d, f) constitute another morphological finding that was never observed by histological methods. Moreover, single smaller units were also found in the atria, in large vessels (Fig. 12.1c, e), and in the right ventricle (Fig. 12.1c).

This study first showed that microCT offers the possibility of obtaining 3D visualization of the cell spatial distribution and a quantification of the number of cells that are able to migrate from the site of injection to different areas of the rat heart tissue, with special reference to the infarcted myocardium. Notably, this microCT approach was validated by two independent methodologies of cell tracking based on quantum dots labeling and genetically engineered EGFP cells.

However, imaging by microCT of soft structures, like those present in an engineered heart, remains challenging, and often phase-contrast settings are preferred to conventional attenuation contrast because of their superior sensitivity. Thus, being unclear which phase tomography method could produce more significant results, some authors [29] recently imaged a rat heart, comparing the performances of three phase tomography methods implemented at the beamline ID19 of the ESRF. They tested the X-ray grating interferometry (XGI) and two propagation-based settings, i.e., the one based on a single sample-detector distance (SD-PhC) and the holotomography (HT), described in detail in the previous chapters. They found that, even if the XGI data generally exhibit much better contrast-to-noise ratios, the spatial resolution available to detect the morphological features was about a factor of two better for HT and SD-PhC compared to XGI.

In this direction, Izadifar [30] recently explored synchrotron radiation phase-contrast methods to image and quantify the efficiency of 3D-printed cardiac patches implanted in a rat myocardial infarction model. Indeed, another objective of cardiac tissue engineering is the development of implantable constructs and of cardiac patches, which provide physical and biochemical cues for myocardium regeneration.

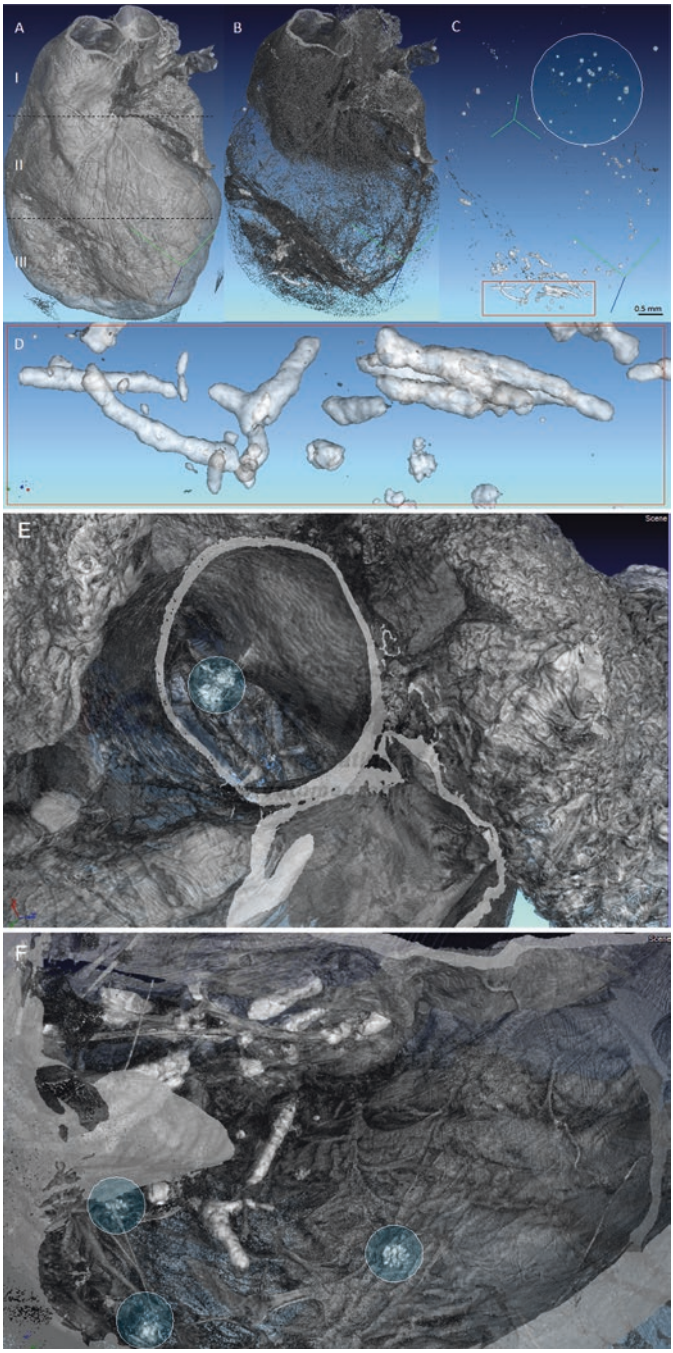

Fig. 12.1 MicroCT reconstruction of an infarcted rat heart injected with 5×10^5 rat CPCs [24]. (**a**) 3D image as produced using the full fusion algorithm. By segmentation, it is possible to achieve information on the internal structure of the heart (**b**) and the distribution of labeled cells (**c, d**). 3D reconstructions of two different regions of interest: (**e**) atria and large vessels; (**f**) infarcted ventricle. Lighted circles facilitate the recognition of the CPCs

In this study [30], innovative nanoparticles expected to modulate the temporal control of growth-factor (GF) release in cardiac patches were successfully developed. Propagation-based PhC-microCT was performed at BMIT-BM beamline of the Canadian Light Source (CLS), using a 25 keV beam energy and three distinct phase propagation distances of 22 cm, 76 cm, and 147 cm. Images obtained by phase retrieval showed and quantified the microstructural features of fibrin and alginate, which were low-density (>97% water) constituents of the patch. Moreover, several anatomical details, including the microvessels surrounding the implanted patch, were observed.

Remarkably, the morphometric information on patch and heart was achieved without using any contrast agent, suggesting that the PhC-microCT could play a key role in quantitative monitoring, in a nondestructive way, of these engineered bio-constructs.

3 Phase-Contrast Imaging to Evaluate Stem Cell Therapy: An Intriguing Hypothesis

The available imaging methodologies, including microCT, still present problems to be solved before translating myocardial regeneration on clinical grounds [19, 20]. In stem cell therapy, when cells injected in the ischemic tissue are preventively labeled with contrast agents, these techniques often proved to be unable to quantify cell engraftment, because of the injected cells' proliferation and the consequent underestimation caused by the hyper-dilution below the detection limit or by unequal distribution of the tracer on dividing cells. Moreover, Gianella et al. [31] evidenced the activation of macrophages when injecting endothelial progenitors, previously loaded with iron oxide nanoparticles, into ischemic tissues. Indeed, dying cells release these tracers, afterward taken up by macrophages.

A few years ago, Albertini et al. [32] used the PhC-microCT for the first time to visualize in 3D the extracellular matrix (ECM) organization after in vitro seeding of bone marrow-derived human and murine mesenchymal stem cells, induced to myogenic differentiation and labeled with iron oxide nanoparticles, onto polyglycolic acid-polylactic acid scaffolds (PGA-PLLA).

Another study performed by Zehbe et al. [33] first observed microCT efficiency in tracking unlabeled stem cells when seeded onto a scaffold. Their study, performed by synchrotron radiation-based microCT, had the purpose of testing a method for the control of neuronal cell growth through the application of an electrical potential. The authors expected to observe only strongly absorbing deposited gold structures and weekly absorbing polymer substrates, but, unexpectedly, also the unlabeled cells were well imaged and with a distribution in agreement with the fluorescence microscopic images acquired previously.

More recently, Giuliani et al. [34] adopted the same PhC-microCT protocol used in [32] to study in vitro cultures of endothelial colony-forming cells (ECFCs) from healthy controls and patients with Kaposi sarcoma and human CD133+

muscle-derived stem cells seeded onto PGA-PLLA. In this case, the structural organization of cells on the bioscaffold was imaged and the rate at which cells modified the construct at different time points from seeding was quantified.

The three previously reported studies inspired a fourth study [20], a demonstrative investigation in which the appropriateness of the X-ray PhC-microCT approach to track unlabeled cells within the myocardium was discussed.

When studying, by microCT, tissues predominantly made of atoms with low atomic number Z (like the myocardium), phase-contrast approaches are often preferred to conventional absorption-based ones because of their greater sensitivity, as discussed in detail in some of the previous chapters. Moreover, mismatches in shape and integration between the regular pattern of a tissue and embedded different structures also lead to PhC-microCT reconstructions with highly improved contrast between these different phases: this is the case of stem cells injected in an infarcted heart that migrate in the damaged myocardium.

Figure 12.2 shows how it is possible to visualize and track unlabeled cells within the myocardium by X-ray PhC-microCT. The cardiac progenitor cells (CPCs), at early stages after the injection, are still undifferentiated and not integrated with the hosting tissue, as shown in Fig. 12.2a-I. In propagation-based PhC-microCT, the detector is placed at a suitable distance from the sample in order to allow the detection of the typical edge-enhanced profile of the CPCs (Fig. 12.2a-II). Thus, as shown in the 3D reconstruction of a rat heart subvolume of Fig. 12.2a-III (inner wall of the infarcted left ventricle), the unlabeled CPCs are clearly visible inside the damaged ventricle, as indicated by the red arrows [20]. Several tests showed that this finding, unexpected and new, was attributable to phase-contrast phenomenon. Indeed, propagation-based PhC-microCT enabled to track the CPCs at different time points, allowing to obtain the same information on the kinetics, previously exclusively supported in the literature by 2D microscopy analysis [20].

Briefly, ten Wistar male rats were submitted to a ligature around the left descending coronary vessel in order to induce a myocardial infarction in the left ventricle. After 3 weeks, 5×10^5 stem cells were directly injected in the ligature site: five rats were injected with rat cardiac progenitor cells (rCPCs), the remaining five with the analogue quantity of human cardiac stromal cells (hCStCs). The rCPCs and the hCStCs were obtained from atrial auricle of Wistar rats and donor patients undergoing cardiac surgery (i.e., aortic valve replacement, coronary artery bypass), respectively [17, 20]; in some animals, cells labeled with iron oxide nanoparticles (Feridex) were injected; in others, prior to injection, the cells were cultured with the growth factor of insulin-transferrin-sodium selenite (ITS) or in total absence or with combined use of Feridex and ITS. Times to sacrifice after injection were the following ones: 24–48 h, 12–13 days, 21 days, and 30 days. The microCT experiments were carried out at the ID19 beamline of the ESRF using a 15 keV X-ray energy and a distance between sample and detector of 25 mm.

The sections obtained at 25 mm for an infarcted rat heart injected with unlabeled CPCs showed the presence of very contrasted structures (white spots), mainly concentrated in the infarcted area (Fig.12.2b). This contrast is not justified by physical phenomena due to X-ray absorption since the injected cells had not been marked

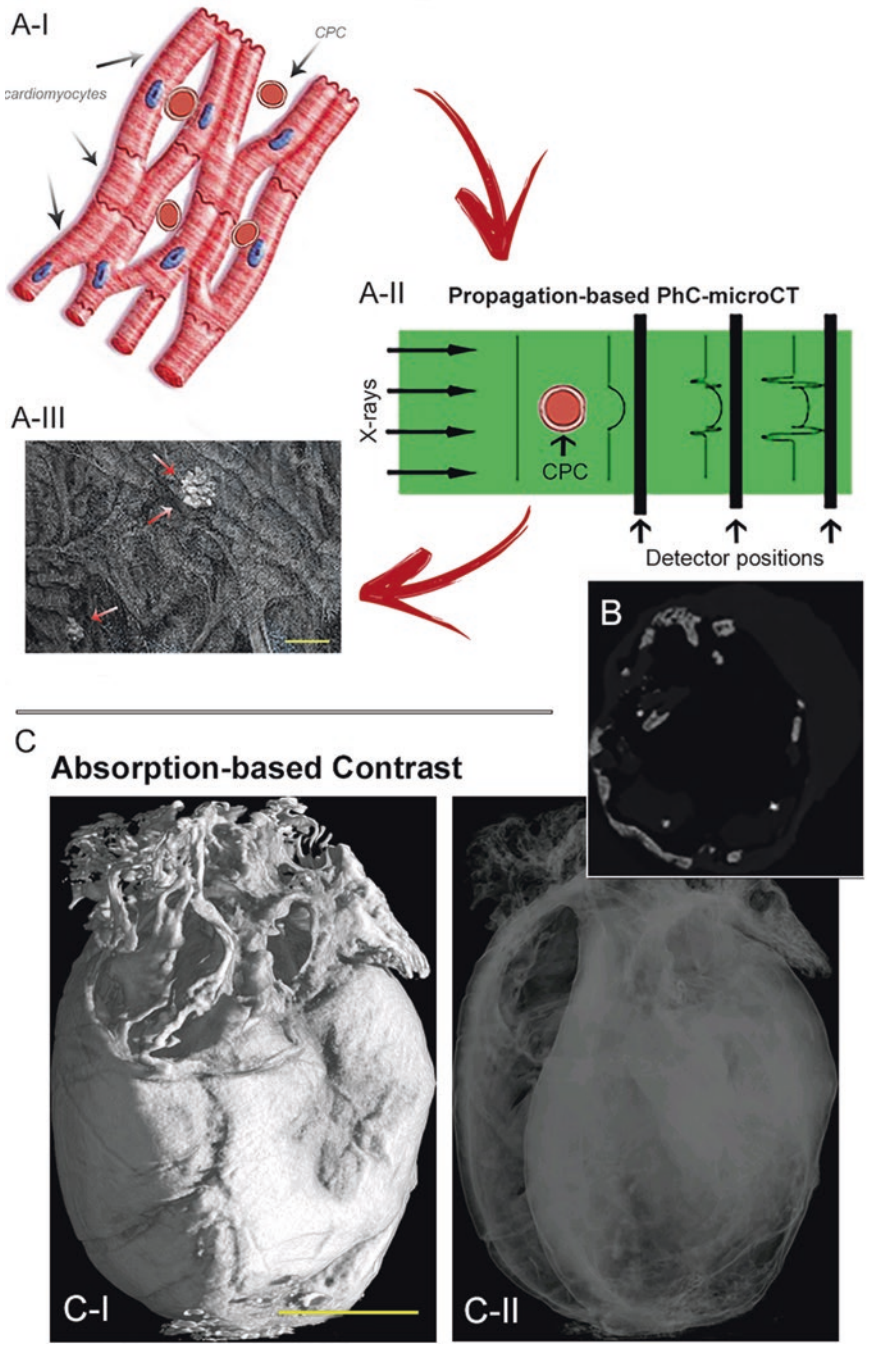

Fig. 12.2 Phase-contrast ability of visualizing the injected cardiac progenitor cells (CPCs) into the rat myocardium [20]. (**a**–I) The cells, early after their injection, are still undifferentiated and not integrated in the hosting myocardium; (**a**–II) edge-enhanced profile of the CPCs when the

with any contrast agent and the sample preparation procedure was not affected by the presence of contaminants with high atomic number Z. Indeed, a not-infarcted rat heart, injected with only vehicle saline solution (but without cells) and sacrificed using an identical protocol, did not present any contrast signal [25]. Another study involving differential imaging [35] of sequential axial slices further confirmed that the observed signal is due to phase contrast (data not shown). Moreover, conventional microCT, based on the mapping of the absorption contrast, furtherly confirmed that the white spots were due to phase contrast. Indeed, an infarcted rat heart injected with 5×10^5 unlabeled rCPCs was studied by means of a SkyScan 1174 (Bruker, Kontich, Belgium): as shown in Fig.12.2, panel c–II, the strong contrast is no longer present in the 3D reconstruction, when the myocardium has been virtually rendered translucent to visualize the internal structures.

Some microCT images of rat hearts injected with unlabeled CPCs are shown in Fig. 12.3a–c: the signal depicted in magenta was attributed to the injected cells for many reasons. Firstly, the analysis of a noninfarcted rat heart injected with the same amount of CPCs revealed an analogue signal, even if more homogeneous and diluted (data not shown). Moreover, the quantitative results obtained in the study on the ten rats (Fig. 12.3d) further confirmed this evidence [20].

Based on these observations and the deriving quantitative analysis, Giuliani et al. [20] formulated the following hypothesis:

1. PhC-microCT is capable of discriminating the injected cells from the myocardium: the reason can lie in the electron density difference between undifferentiated (injected) and differentiated cells (the myocardium) and/or to mismatches in integration between the regular pattern of the myocardium and the injected cells before their engraftment.
2. The aggregate cell volume increases up to 21 days from cell injection, possibly due to injected cell proliferation and/or the activation of the endogenous stem cells.
3. The aggregate cell volume decreases from 21 to 30 days after cell injection, possibly indicating the beginning of differentiation/cell engraftment of the injected cells. This hypothesis is supported by Rossini et al. [17] who found in the same rat model of chronic MI, after 21 days from hCStC injection, a portion of them showing sarcomere striation and volume compatible with that of adult cardiomyocytes.
4. Feridex labeling was confirmed to interfere with the regeneration process activated by the CPCs, possibly because of macrophage action previously described [31].
5. ITS seems to favor tissue regeneration by supporting cell engraftment [19] and CPC proliferation.

Fig. 12.2 (continued) detector is placed at a suitable distance from the sample in a propagation-based PhC-microCT setting; (**a**–III) 3D reconstruction of the inner wall of the infarcted left ventricle of a rat: the injected (unlabeled) CPCs are clearly visible and indicated by the red arrows. Bar, 50 μm. (**b**) An axial slice of the infarcted rat heart treated with unlabeled rCPCs. It was reconstructed without the application of the Paganin filter to evaluate the edge enhancement. (**c**) Infarcted rat heart injected with unlabeled rCPCs: conventional (absorption-based) microCT analysis. Solid (**c**–I) and semitransparent (**c**–II) 3D reconstructions. The unlabeled CPCs are not visible anymore. Yellow bar, 300 μm

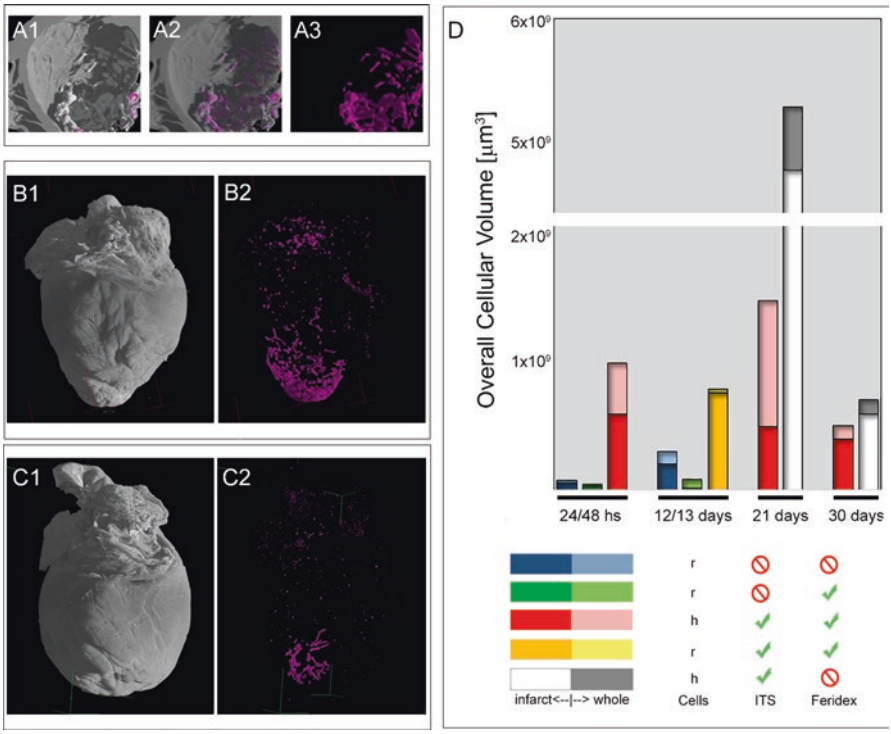

Fig. 12.3 MicroCT 3D reconstructions of the infarct in a rat heart injected with unlabeled hCStCs (**a1**–**a3**) and of the entire hearts when injected with hCStCs, previously cultured with ITS and without Feridex (**b1**–**b2** at 21 days, **c1**–**c2** at 30 days from cell injection) [20]. *Gray* myocardium, *magenta* hCStCs. (**d**) Quantitative results. *h* human-derived CStCs, *r* rat-derived CPCs

4 From Stem Cell Therapy to Heart Engineering: The New Frontiers

Myocardium engineering by cell therapy still requires further research, mainly focused on the objective to improve cell delivery methods, before its introduction for drug screening and patient-specific disease modeling [36]. Indeed, it was found that transplanted cells are not able to survive for long periods because of pathologically modified extracellular matrix (ECM), proapoptotic factors, and inflammatory response. Thus, testing of antioxidant, anti-inflammatory, angiogenic, and antiapoptotic products should be performed in order to favor the survival of transplanted cells.

In this direction, porous biomaterials should offer a suitable microenvironment for cell survival and function, mimicking the natural extracellular environment. Natural and innovative synthetic biomimetic scaffolds are under investigation with the main objective to allow cell attachment and their colonization and, by their

grafting to the damaged myocardium, to achieve a modulated delivery of such cells, releasing biochemical factors and nutrients. For instance, a polyglycerol sebacate (PGS) matrix was recently developed for cardiac patch application with the objective of supporting the adhesion and growth of rat and human cardiac progenitor cells [37].

Synchrotron radiation-based PhC-microCT techniques are expected to give an invaluable support in this direction, elucidating unanswered questions concerning the kinetics of tissue repairing.

However, preclinical application of PhC-microCT for the vivo imaging of small animal hearts is nonetheless challenging because scan times are still longer than a single respiratory or cardiac cycle. To overcome this problem on rodent models, Holbrook et al. [38] recently proposed two strategies for cardiac gating in dual-source, preclinical microCT: fast prospective gating (PG) and uncorrelated retrospective gating (RG). These methods combined with a sophisticated iterative image reconstruction algorithm provided faster acquisitions and high image quality in low-dose 4D (i.e., 3D + Time) cardiac microCT.

Clinical application of PhC-microCT is also gaining traction [39], even if the in vivo imaging of the heart remains challenging also in this case. Indeed, as the heart is surrounded by the air-filled alveoli of the lungs, artifacts caused by X-ray refraction could emerge [26], and the strong X-ray absorption of the ribs could reduce the detection of phase-shift values inside compared to an isolated heart.

Thus, future development of the PhC-microCT systems and methods for in vivo human heart imaging are expected in the coming few years.

References

1. Roger VL (2013) Epidemiology of heart failure. Circ Res 113:646–659
2. Mozaffarian D, Benjamin EJ, Go AS, Arnett DK, Blaha MJ, Cushman M, de Ferranti S, Després JP, Fullerton HJ, Howard VJ, Huffman MD, Judd SE, Kissela BM, Lackland DT, Lichtman JH, Lisabeth LD, Liu S, Mackey RH, Matchar DB, McGuire DK, Mohler ER 3rd, Moy CS, Muntner P, Mussolino ME, Nasir K, Neumar RW, Nichol G, Palaniappan L, Pandey DK, Reeves MJ, Rodriguez CJ, Sorlie PD, Stein J, Towfighi A, Turan TN, Virani SS, Willey JZ, Woo D, Yeh RW, Turner MB (2015) Heart disease and stroke statistics – 2015 update: a report from the American Heart Association. Circulation 131(4):e29–e322 Corrigendum: (2015). Circulation, 131, e98; Circulation, 131, e117; Circulation, 131, e163; Circulation, 131, e319
3. Benjamin EJ, Blaha MJ, Chiuve SE, Cushman M, Das SR, Deo R, de Ferranti SD, Floyd J, Fornage M, Gillespie C, Isasi CR, Jiménez MC, Jordan LC, Judd SE, Lackland D, Lichtman JH, Lisabeth L, Liu S, Longenecker CT, Mackey RH, Matsushita K, Mozaffarian D, Mussolino ME, Nasir K, Neumar RW, Palaniappan L, Pandey DK, Thiagarajan RR, Reeves MJ, Ritchey M, Rodriguez CJ, Roth GA, Rosamond WD, Sasson C, Towfighi A, Tsao CW, Turner MB, Virani SS, Voeks JH, Willey JZ, Wilkins JT, Wu JH, Alger HM, Wong SS, Muntner P, American Heart Association Statistics Committee, Stroke Statistics Subcommittee (2017) Heart disease and stroke statistics-2017 update: a report from the American Heart Association. Circulation 135(10):e146–e603. https://doi.org/10.1161/CIR.0000000000000485

4. Strauer BE, Steinhoff G (2011) 10 years of intracoronary and intramyocardial bone marrow stem cell therapy of the heart: from the methodological origin to clinical practice. J Am Coll Cardiol 58:1095–1104
5. Menasché P, Alfieri O, Janssens S, McKenna W, Reichenspurner H, Trinquart L, Vilquin JT, Marolleau JP, Seymour B, Larghero J, Lake S, Chatellier G, Solomon S, Desnos M, Hagège AA (2008) The myoblast autologous grafting in ischemic cardiomyopathy (MAGIC) trial: first randomized placebo-controlled study of myoblast transplantation. Circulation 117:1189–1200
6. Sanganalmath SK, Bolli R (2013) Cell therapy for heart failure: a comprehensive overview of experimental and clinical studies, current challenges, and future directions. Circ Res 113:810–834
7. Fisher SA, Doree C, Mathur A, Martin-Rendon E (2015) Meta-analysis of cell therapy trials for patients with heart failure. Circ Res 116:1361–1377
8. Chamuleau SA, Vrijsen KR, Rokosh DG, Tang XL, Piek JJ, Bolli R (2009) Cell therapy for ischaemic heart disease: focus on the role of resident cardiac stem cells. Neth Heart J 17:199–207
9. Frati C, Savi M, Graiani G, Lagrasta C, Cavalli S, Prezioso L, Rossetti P, Mangiaracina C, Ferraro F, Madeddu D, Musso E, Stilli D, Rossini A, Falco A, Angelis AD, Rossi F, Urbanek K, Leri A, Kajstura J, Anversa P, Quaini E, Quaini F (2011) Resident cardiac stem cells. Curr Pharm Des 17:2074–2099
10. Leri A, Kajstura J, Anversa P (2011) Role of cardiac stem cells in cardiac pathophysiology: a paradigm shift in human myocardial biology. Circ Res 109:941–961
11. Li TS, Cheng K, Malliaras K, Smith RR, Zhang Y, Sun B, Matsushita N, Blusztajn A, Terrovitis J, Kusuoka H, Marbán L, Marbán E (2012) Direct comparison of different stem cell types and subpopulations reveals superior paracrine potency and myocardial repair efficacy with cardiosphere-derived cells. J Am Coll Cardiol 59:942–953
12. Nadal-Ginard B, Ellison GM, Torella D (2014) The cardiac stem cell compartment is indispensable for myocardial cell homeostasis, repair and regeneration in the adult. Stem Cell Res 13:615–630
13. Savi M, Bocchi L, Rossi S, Frati C, Graiani G, Lagrasta C, Miragoli M, Di Pasquale E, Stirparo GG, Mastrototaro G, Urbanek K, De Angelis A, Macchi E, Stilli D, Quaini F, Musso E (2016) Antiarrhythmic effect of growth factor-supplemented cardiac progenitor cells in chronic infarcted heart. Am J Physiol Heart Circ Physiol 310(11):H1622–H1648. https://doi.org/10.1152/ajpheart.00035.2015
14. Leite CF, Almeida TR, Lopes CS, Dias da Silva VJ (2015) Multipotent stem cells of the heart—do they have therapeutic promise? Front Physiol 6:123. https://doi.org/10.3389/fphys.2015.00123
15. Chong JJ, Chandrakanthan V, Xaymardan M, Asli NS, Li J, Ahmed I, Heffernan C, Menon MK, Scarlett CJ, Rashidianfar A, Biben C, Zoellner H, Colvin EK, Pimanda JE, Biankin AV, Zhou B, Pu WT, Prall OW, Harvey RP (2011) Adult cardiac-resident MSC-like stem cells with a proepicardial origin. Cell Stem Cell 9:527–540. https://doi.org/10.1016/j.stem.2011.10.002
16. Ryzhov S, Sung BH, Zhang Q, Weaver A, Gumina RJ, Biaggioni I, Feoktistov I (2014) Role of adenosine A2B receptor signaling in contribution of cardiac mesenchymal stem-like cells to myocardial scar formation. Purinergic Signal 10:477–486. https://doi.org/10.1007/s11302-014-9410-y
17. Rossini A, Frati C, Lagrasta C, Graiani G, Scopece A, Cavalli S, Musso E, Baccarin M, Di Segni M, Fagnoni F, Germani A, Quaini E, Mayr M, Xu Q, Barbuti A, Di Francesco D, Pompilio G, Quaini F, Gaetano C, Capogrossi MC (2011) Human cardiac and bone marrow stromal cells exhibit distinctive properties related to their origin. Cardiovasc Res 89(3):650–660. https://doi.org/10.1093/cvr/cvq290
18. Vecellio M, Meraviglia V, Nanni S, Barbuti A, Scavone A, DiFrancesco D, Farsetti A, Pompilio G, Colombo GI, Capogrossi MC, Gaetano C, Rossini A (2012) In vitro epigenetic reprogramming of human cardiac mesenchymal stromal cells into functionally competent cardiovascular precursors. PLoS One 7:e51694. https://doi.org/10.1371/journal.pone.0051694

19. Terrovitis JV, Ruckdeschel Smith R, Marbàn E (2010) Assessment and optimization of cell engraftment after transplantation into the heart. Circ Res 106:479–494
20. Giuliani A, Mencarelli M, Frati C, Savi M, Lagrasta C, Pompilio G, Rossini A, Quani F (2018) Phase-contrast microtomography: are the tracers necessary for stem cell tracking in infarcted hearts? Biomed. Phys Eng Express 4 055008
21. Cancedda R, Cedola A, Giuliani A, Komlev V, Lagomarsino S, Mastrogiacomo M, Peyrin F, Rustichelli F (2007) Bulk and interface investigations of scaffolds and tissue-engineered bones by X-ray microtomography and X-ray micro-diffraction. Biomaterials 28:2505e24
22. Rominu M, Manescu A, Sinescu C, Negrutiu ML, Topala F, Rominu RO, Bradu A, Jackson DA, Giuliani A, Podoleanu AG (2014) Zirconia enriched dental adhesive: a solution for OCT contrast enhancement. Demonstrative study by synchrotron radiation microtomography. Dent Mater 30(4):417–423. https://doi.org/10.1016/j.dental.2014.01.004
23. Dullin C, Ufartes R, Larsson E, Martin S, Lazzarini M, Tromba G, Missbach-Guentner J, Pinkert-Leetsch D, Katschinski DM, Alves F (2017) μCT of ex-vivo stained mouse hearts and embryos enables a precise match between 3D virtual histology, classical histology and immunochemistry. PLoS One 12(2):e0170597. https://doi.org/10.1371/journal.pone.0170597
24. Giuliani A, Frati C, Rossini A, Komlev VS, Lagrasta C, Savi M, Cavalli S, Gaetano C, Quaini F, Manescu A, Rustichelli F (2011) High-resolution X-ray microtomography for three-dimensional imaging of cardiac progenitor cell homing in infarcted rat hearts. J Tissue Eng Regen Med 5(8):e168–e178. https://doi.org/10.1002/term.409
25. Giuliani A (2012) 3D visualization of transplanted stem cells in infarcted rat hearts by high-resolution X-ray microtomography. IL NUOVO CIMENTO C 35(5):157–167. https://doi.org/10.1393/ncc/i2012-11318-2
26. Kaneko Y, Shinohara G, Hoshino M, Morishita H, Morita K, Oshima Y, Takahashi M, Yagi N, Okita Y, Tsukube T (2017) Intact imaging of human heart structure using X-ray phase-contrast tomography. Pediatr Cardiol 38(2):390–393. https://doi.org/10.1007/s00246-016-1527-z
27. Arfelli F, Assante M, Bonvicini V, Bravin A, Cantatore G, Castelli E, Dalla Palma L, Di Michiel M, Longo R, Olivo A, Pani S, Pontoni D, Poropat P, Prest M, Rashevsky A, Tromba G, Vacchi A, Vallazza E, Zanconati F (1998) Low-dose phase contrast X-ray medical imaging. Phys Med Biol 43(10):2845–2852
28. Stokking R, Zubal IG, Viergever MA (2003) Display of fused images: methods, interpretation, and diagnostic improvements. Semin Nucl Med 33:219–227
29. Lang S, Zanette I, Dominietto M, Langer M, Rack A, Schulz G, Le Duc G, David C, Mohr J, Pfeiffer F, Müller B, Weitkamp T (2014) Experimental comparison of grating- and propagation-based x-ray phase tomography of soft tissue. J Appl Phys 116:154903. https://doi.org/10.1063/1.4897225
30. Izadifar M (2016) Development of nanoparticle rate-modulating and synchrotron phase contrast-based assessment techniques for cardiac tissue engineering. PhD thesis. University of Saskatchewan Saskatoon, Division of Biomedical Engineering, Saskatchewan
31. Gianella A, Guerrini U, Tilenni M, Sironi L, Milano G, Nobili E, Vaga S, Capogrossi MC, Tremoli E, Pesce M (2010) Magnetic resonance imaging of human endothelial progenitors reveals opposite effects on vascular and muscle regeneration into ischaemic tissues. Cardiovasc Res 85(3):503–513
32. Albertini G, Giuliani A, Komlev V, Moroncini F, Pugnaloni A, Pennesi G, Belicchi M, Rubini C, Rustichelli F, Tasso R, Torrente Y (2009) Organization of extracellular matrix fibers within polyglycolic acid-polylactic acid scaffolds analyzed using X-ray synchrotron-radiation phase-contrast micro computed tomography. Tissue Eng C Methods 15:403–411
33. Zehbe R, Haibel A, Schmidt F, Riesemeier H, Kirkpatrick CJ, Schubert H, Brochhausen C (2010) High resolution X-ray tomography – 3D imaging for tissue engineering applications. In: Eberli D (ed) Tissue engineering. InTech, Rijeka, pp 337–358
34. Giuliani A, Moroncini F, Mazzoni S, Belicchi ML, Villa C, Erratico S, Colombo E, Calcaterra F, Brambilla L, Torrente Y, Albertini G, Della Bella S (2014) Polyglycolic acid-polylactic acid scaffold response to different progenitor cell in vitro cultures: a demonstrative and compara-

tive X-ray synchrotron radiation phase-contrast microtomography study. Tissue Eng Part C Methods 20:308–316
35. İlsever M., Ünsalan C (2012) Pixel-Based Change Detection Methods. In: Two-Dimensional Change Detection Methods. SpringerBriefs in Computer Science. Springer, London, p 7–21
36. Hirt MN, Hansen A, Eschenhagen T (2014) Cardiac tissue engineering. State of the art. Circ Res 114:354–367
37. Rai R, Tallawi M, Barbani N, Frati C, Madeddu D, Cavalli S, Graiani G, Quaini F, Roether JA, Schubert DW, Rosellini E, Boccaccini AR (2013) Biomimetic poly(glycerol sebacate) (PGS) membranes for cardiac patch application. Mater Sci Eng C Mater Biol Appl 33(7):3677–3687. https://doi.org/10.1016/j.msec.2013.04.058
38. Holbrook M, Clark DP, Badea CT (2018) Low-dose 4D cardiac imaging in small animals using dual source micro-CT. Phys Med Biol 63(2):025009
39. Donath T, Pfeiffer F, Bunk O, Grünzweig C, Hempel E, Popescu S, Vock P, David C (2010) Toward clinical X-ray phase-contrast CT: demonstration of enhanced soft-tissue contrast in human specimen. Investig Radiol 45:445–452

Chapter 13
Frontiers in Muscle Diseases: The X-ray Microtomography Support to Latest Researches

Fabrizio Fiori

Abstract Muscle diseases occur in all age groups, but their impact is particularly severe when children and young adults are affected. There are many different forms of muscular diseases, with different causes and outcomes, which require different treatments.

In particular, with regard to the various forms of muscular dystrophy, no treatment is currently available to stop or reverse the disease. In fact, the present therapies are mainly aimed at treating the various problems arising from this pathology and improving the quality of life of the patients.

However, the new frontiers of research, in particular regarding gene therapy and stem cell perfusion, have recently led to promising results. In this context, the use of three-dimensional imaging methods to visualize tissues and evaluate the efficiency of treatments is crucial.

This chapter presents some examples in which high-resolution X-ray tomography (micro-CT) techniques are applied to the investigation of neuromuscular diseases and their possible treatments.

1 Introduction

Muscle diseases occur in all age groups and can cause serious physical disability. Their impact is especially severe when children and young adults are affected. The needs of these patients are numerous and complicated, and frequently not adequately met. Some muscle diseases respond well to medical treatment, and many of the deriving physical disabilities can be improved or prevented. Hence, although muscle diseases are not as common as neurological disorders (such as stroke or epilepsy), they deserve full attention.

F. Fiori (✉)
Department of Clinical Science, Polytechnic University of Marche, Ancona, Italy
e-mail: f.fiori@univpm.it

A. Giuliani, A. Cedola (eds.), *Advanced High-Resolution Tomography in Regenerative Medicine*, Fundamental Biomedical Technologies,
https://doi.org/10.1007/978-3-030-00368-5_13

There are many different forms of muscle diseases, with different causes and outcomes, which require different treatments [1]. They can be divided into two main categories, genetic and not genetic. Genetic muscle diseases are related to a genetic disorder and include a wide range of diseases, the most well-known of which are the muscular dystrophies (MD) [2]. One of the most serious of these is the Duchenne muscular dystrophy (DMD) [3–5], characterized by a rapid progression of muscle degeneration leading to loss of deambulation and death, often in late adolescence and rarely when the patient is older than 30. DMD affects almost exclusively male individuals (about 1 in 3500 worldwide), during the 1st years of life (the first symptoms appear at the age of 3–5 years); females can be carriers and can be afflicted if the father is afflicted and the mother is a carrier. DMD is due to an alteration of the X chromosome, causing the nonproduction of the dystrophin protein. The absence of dystrophin allows an excessive penetration of calcium into the sarcolemma (the cell membrane); consequently, in a complex and not completely understood cascade process involving different paths, serious damages are caused in the sarcolemma, which lead to cell death. The muscle fibers lacerate during contraction, undergo necrosis, and are then replaced by adipose and connective tissue.

Other genetic muscle diseases include congenital myopathies, storage myopathies, mitochondrial diseases, and periodic paralyses. Among the nongenetic muscle diseases (i.e., acquired), the most important ones are the inflammatory muscle diseases, such as myasthenia gravis, in which the body's own immune system inappropriately injures its muscles [6]. Other nongenetic muscle diseases may be due to drugs or hormonal disorders.

Concerning in particular the various forms of MD, no treatment is currently available to stop or reverse it. Present therapies and medications aim mainly to treat the various problems resulting from MD and improve the quality of life for patients.

Nevertheless, new frontiers of research, particularly concerning gene therapy and stem cell perfusion, have recently led to promising results. For example, the efficacy of an innovative gene therapy in the treatment of DMD was recently demonstrated [7]: after injecting microdystrophin (a "shortened" version of the dystrophin gene) via a drug vector, restoration of the muscle strength and stabilization of the clinical symptoms were achieved in dogs naturally affected by DMD. Other promising improvements of gene therapy have been recently obtained for the correction of myotubular myopathy [8] and other kinds of inherited and inflammatory muscle diseases [9, 10].

In this framework, the use of three-dimensional (3D) methods to visualize the tissues and evaluate the effects of treatments is fundamental. In particular, few examples are presented in this chapter in which high-resolution X-ray tomography (micro-CT) techniques are applied to the investigation of neuromuscular diseases and their possible treatments.

2 Stem Cells for the Treatment of Duchenne Muscular Dystrophy (DMD)

Recent reports support the idea that stem cells can reach the site of muscle regeneration though systemic routes and thus contribute to muscle repair more efficiently than canonical myogenic progenitors [11, 12]. In particular, several studies are focused on a subpopulation of human circulating stem cells, expressing the CD133 antigen, that can participate in muscle regeneration and replenish the satellite cell compartment in the dystrophic muscles. CD133 cells were shown to produce a significant regeneration of skeletal muscle structure and function when delivered, by the femoral artery, to skeletal muscle tissues of scid-mdx mice [11].

In order to evaluate the detection and fate of CD133 stem cells in dystrophic mice, synchrotron radiation-based micro-CT experiments were performed at the European Synchrotron Radiation Facility (ESRF) in Grenoble (France). A first series of measurements was performed under ex vivo conditions, on cubic biopsies of 2 mm side, removed from the hind limb of animals previously injected with 50,000, 100,000, and 500,000 stem cells [13]. In order to improve the contrast of absorption, the stem cells were labeled with iron oxide nanoparticles (Endorem), as described in [13]. Biopsies were excised 2, 12, and 24 h after the injection of the stem cells. The experimental dimension of the voxel was that of a cube of about 1.6 μm of side.

Figure 13.1 shows the distribution of stem cells in a biopsy, 24 h after the intra-arterial injection.

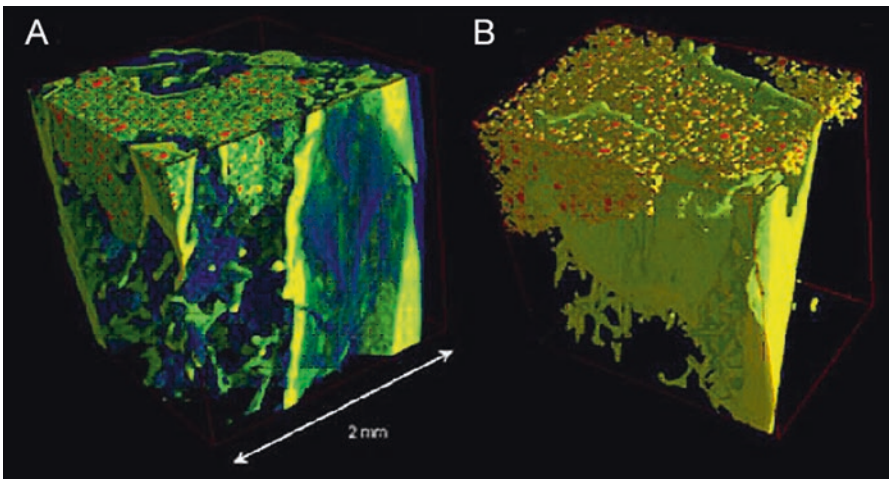

Fig. 13.1 Two views (**a**, **b**) of the 3D micro-CT reconstruction of a sample. The biopsy was retrieved from a dystrophic mouse, 24 h after the intra-arterial injection of stem cells labeled with iron oxide nanoparticles. The labeled injected cells, red; vessels, green; fibrosis, blue. (From Ref. [13])

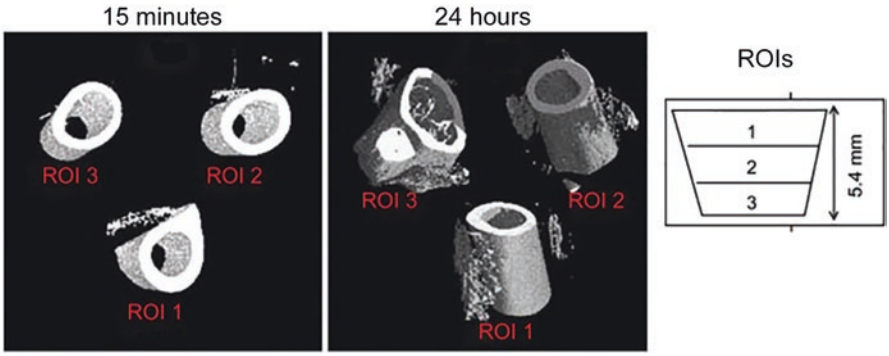

Fig. 13.2 Micro-CT analysis protocol. Tomograms of the tight region 15 min and 24 h after injection. The femur volume has been subtracted to the overall signal to calculate the volume fraction of the Endorem-labeled cells. (Figure adapted from Ref. [14])

This experiment showed the ability of micro-CT to detect stem cells and to determine their distribution in the mouse muscular tissue.

On this basis, a further in vivo experiment was carried out at ESRF [14]. An ad hoc sample holder was built in order to keep the leg of an anesthetized mouse fixed inside the X-ray beam, after the injection of 500,000 iron oxide-labeled stem cells into the femoral arteria. The mouse was analyzed at different times after cell injection (15 min, 2 h, 13 h, and 24 h). The voxel size was about $7 \times 7 \times 7$ μm^3, with a total field of view of $14.5 \times 14.5 \times 7$ mm^3.

Three different consecutive regions of interest (ROIs), in the direction parallel to the femur, were investigated. Figure 13.2 shows, in these ROIs, the distribution of the labeled stem cells around the femur of the mouse, 15 min and 24 h after their injection. From these images, a quantification of the relative "apparent" volume fraction of the stem cells (i.e., the volume fraction seen by the X-ray beam during the scan, taking into account oscillations of the tissue due to heartbeat) was carried out.

Moreover, the kinetics of the cellular homing in the muscular tissue was evaluated. As shown in Fig. 13.3, after 2 h, the injected cells completely moved from the vessels to the tissues. These results were shown to be in good agreement with Q-PCR measurements [14].

3 Muscle Regeneration After Ischemia

Leroux et al. [15] recently investigated the ability of bone marrow mesenchymal stem cells (MSCs), exposed to short-term hypoxic conditions, to participate in vascular and muscular regeneration in an in vivo model of hind limb ischemia.

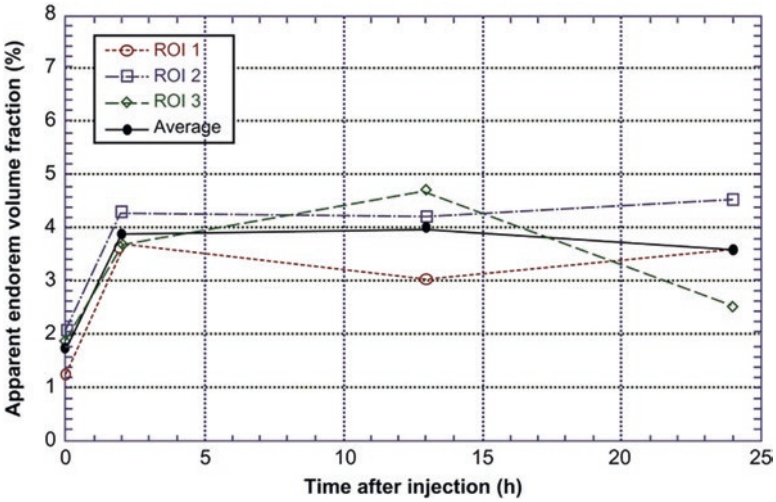

Fig. 13.3 Endorem signal in the investigated ROIs of the leg muscles: its apparent volume fraction increased up to 2 h, reaching a plateau and remaining constant in the following hours. (From Ref. [14])

The experimental strategy consisted in low-oxygen (O_2) preconditioning of MSCs before their seeding into ischemic tissues, mimicking the stem cell niche microenvironment.

The 1% O_2 concentration was assumed as the level found in vivo, in bone marrow stem cell niche areas.

The role of hypoxic gradients in stem cell trafficking in ischemic tissue is also known; indeed, at molecular level, temporary oxygen deprivation is known to regulate gene transcription and differentiation of stem cells.

The ability of hypoxic preconditioned murine MSCs (HypMSC), compared to non-preconditioned MSCs (NormMSC), to engraft into ischemic tissue and to participate at muscular and vascular regeneration was assessed. A subacute murine limb ischemia model was used to mimic the clinical setting of critical limb ischemia in patients.

Three groups were studied: a control (Cont) group receiving saline injection, a NormMSC group receiving intramuscular injection of 500,000 MSCs in normal oxygen concentration, and an HypMSC group injected with the same amount of MSCs in reduced oxygen concentration.

A high-resolution micro-CT imaging system, in combination with other techniques, was used to prove muscular and vascular regeneration, as shown in Fig. 13.4.

Repaired muscles after ischemia were characterized by the smaller size of the fibers and the presence of centrally located nuclei defined by the presence of skeletal fibers with a central nucleus. They are typically found in the middle of muscle area in repair.

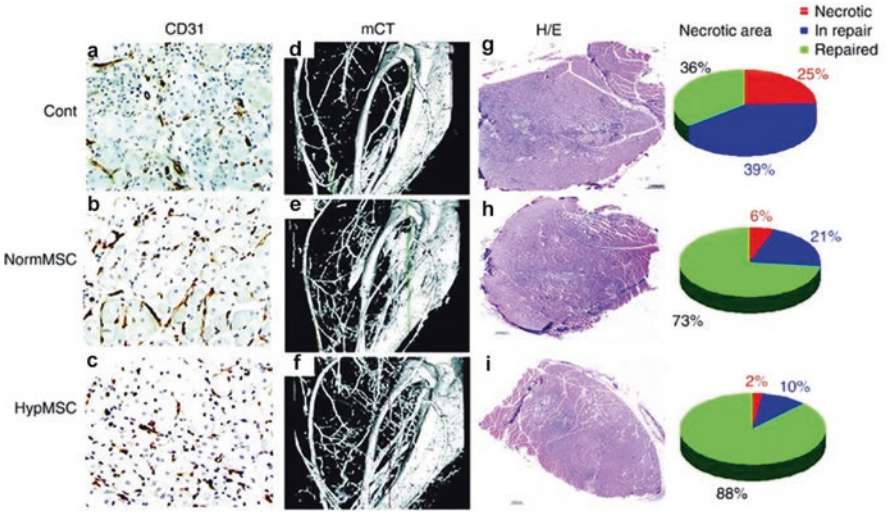

Fig. 13.4 (**a**–**c**) Vessels after CD31 immunolabeling in the control (**a**), NormMSC (**b**), and HypMSC (**c**) groups. (**d**–**f**) Reconstructed 3D micro-CT images of control- (**d**), NormMSC- (**e**), and HypMSC (**f**)-injected hind limb, 7 days after ischemia. (**g**–**i**) Representative histologic (H/E) sections of repaired muscle surface in control- (**g**), NormMSC- (**h**), and HypMSC (**i**)-injected hind limb. Pie charts (right side): ratio of necrotic, in repair and repaired tissue with respect to the total muscular area. (From Ref. [15])

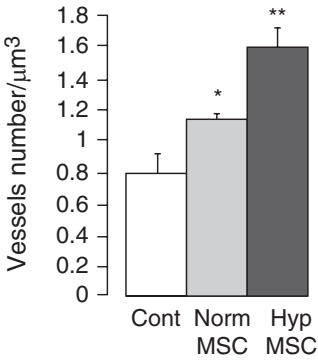

Fig. 13.5 Vessel concentration in control mice (Cont) and mice injected with MSCs under normal oxygenation (NormMSC) and under hypo-oxygenation (HypMSC) conditions. (From Ref. [15])

In particular, the quantification of vessel number, as measured by micro-CT, is shown in Fig. 13.5, demonstrating that hypo-oxygenation conditions increase the neoangiogenesis.

These results showed that HypMSC have a greater capacity for engraftment in ischemic tissue than NormMSC, improving skeletal muscle regeneration and inducing more neoangiogenesis.

4 Gene Therapy in Myopathy and Muscular Dystrophy

Current treatments of congenital muscular dystrophies are limited and aim to prolong deambulation and survival. Since most of the genes responsible for congenital muscular dystrophies are still unknown, researches on these genes may provide new insights that can lead to innovative treatments.

Fibrillins are large structural macromolecules that are important constituents of all connective tissues. There are three fibrillin genes in humans, whereas the gene for fibrillin-3 was lost in mouse because of chromosomal rearrangement.

Fibrillin-2 (FBN2) null mice are known to be born with myopathy and contractures, exhibiting accumulation of white fat during the early postnatal period. The histological features of both myopathy and fat accumulation are rescued by inhibiting bone morphogenetic protein (BMP) signaling.

Recently, the influence of BMP signaling in FBN2 null mice was investigated by Sengle et al. [16]. Skinned forelimbs were fixed and treated with OsO_4. Micro-CT was used, combined with other experimental techniques, to visualize fat and bone.

Figure 13.6 shows the increased depositions of fat throughout most of the forearm muscle, from the wrist to the elbow. In wild-type forearms, fat was located at the periphery of muscles, while, in FBN2 null forearms, fat was observed between the bone and muscle or infiltrating the muscle bundles.

The hind limb muscle analysis by micro-CT showed, in addition to an abnormal fat deposition, a reduced muscle mass, as shown in Fig. 13.7.

Moreover, the hypothesis that lowering the expression level of Bmp7 should have beneficial effects on the FBN2 null myopathy was verified by micro-CT. FBN2 +/− mice were crossed with BMP7+/− mice, generating FBN2 +/−; BMP7 +/− double heterozygous mice. Afterward, FBN2 +/−; BMP7 +/− mice were crossed with each other, generating FBN2 −/−; BMP7 +/− mice. Forelimb muscle and fat were investigated by micro-CT, after fixation and labeling with OsO_4.

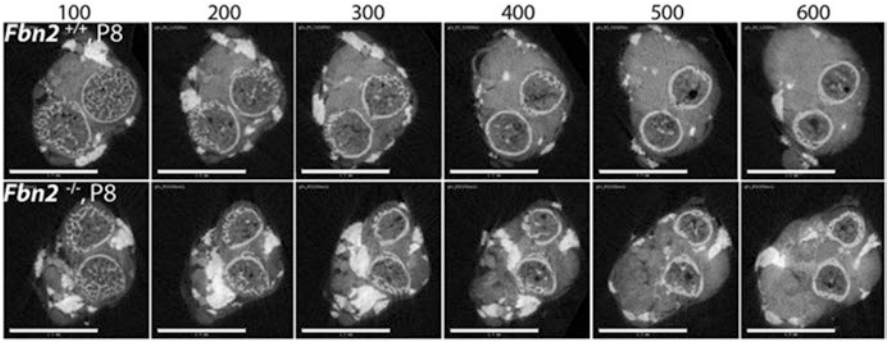

Fig. 13.6 Selection of axial (3 μm thick) slices (numbers above each panel), as generated by micro-CT. A comparable series of sections of wild-type (top) and FBN2 null (bottom) forearms. Fat, solid white; bone, light gray space within the circular bone collar. Bars = 1 mm. *P8* progeny nr.8. (From Ref. [16])

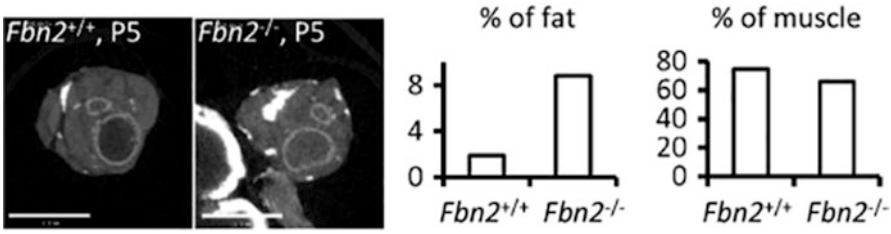

Fig. 13.7 Muscle and fat in hind limb of wild-type and FBN2 null mice. Micro-CT (3 μm thick) slices of comparable hind limb regions of Fbn2 +/+ (wild type) and FBN2 −/− mice are shown (left). Bars = 1 mm. Percentages of fat and muscle (right) in Fbn2 +/+ (wild type) and FBN2 −/− mice. An increase of fat and a reduction of muscle were found also in FBN2 null hind limbs. *P5* progeny nr.5. (From Ref. [16])

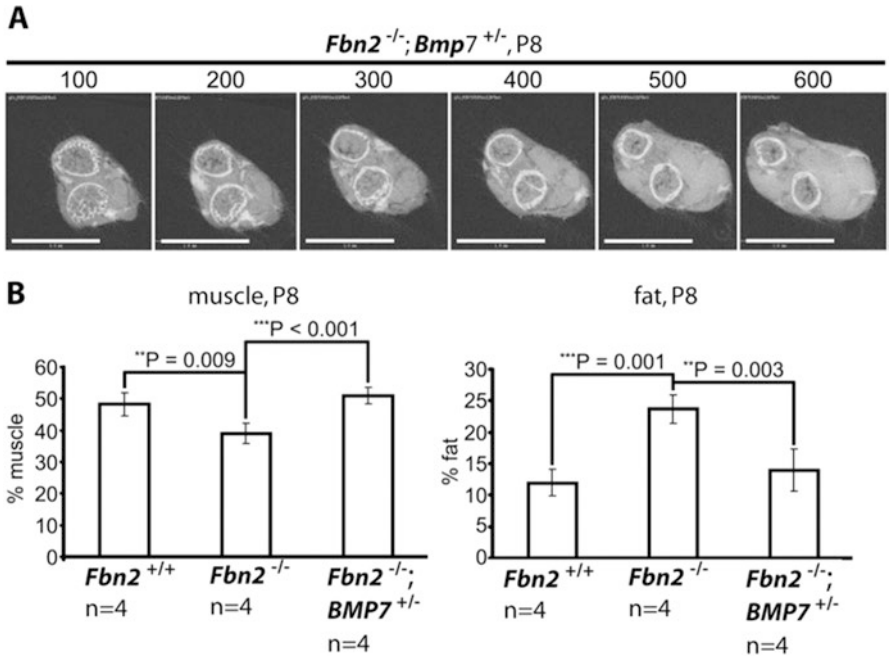

Fig. 13.8 (**a**) Series of axial slices (numbered at the top) of FBN2−/−; BMP7+/− forearms. (**b**) Quantification of muscle and fat across the genotypes. Bars = 1 mm

A series of axial slices deriving from FBN2 −/−; BMP7 +/− forelimb is shown in Fig. 13.8a. Fat and muscle percentages were compared to those found in comparable micro-CT slices of wild-type (FBN2 +/+) and FBN2 null forearms. The analysis of FBN2 −/−; Bmp7 +/− forelimbs indicated that the amounts of muscle and fat on serial slices are comparable to those found in wild-type (FBN2 +/+) mice (Fig. 13.8b). These micro-CT data provided evidence that activated BMP signaling is responsible for the FBN2 null myopathy, consisting in the reduction of muscle mass and in the increase of fat infiltrating the muscle.

5 Conclusions

In conclusion, we showed some preclinical trials in which X-ray micro-CT, combined to other investigation methods, was implemented to monitor muscle mass but also, in proof of principle, studies to identify the onset of new muscle engineering. A better knowledge of muscle pathophysiology imaging will allow to plan more accurately the schedule for drug administration to mice affected by various muscle diseases. We believe this procedure could be widely applied to other disease models, including aging animals, as well as to other species, as rats, to assist drug development and search for efficient treatments of muscle diseases.

References

1. https://medlineplus.gov/neuromusculardisorders.html
2. Askanas V, Engel K (eds) (2015) Neuromuscular diseases: pathology and molecular pathogenesis. Biochim Biophys Acta (BBA) Mol Basis Dis (special issue) 1852(4):561–692
3. Birnkrant DJ et al (2018) Diagnosis and management of Duchenne muscular dystrophy, part 1: diagnosis, and neuromuscular, rehabilitation, endocrine, and gastrointestinal and nutritional management. Lancet Neurol 17(3):251–267
4. Birnkrant DJ et al (2018) Diagnosis and management of Duchenne muscular dystrophy, part 2: respiratory, cardiac, bone health, and orthopaedic management. Lancet Neurol 17(4):347–361
5. Birnkrant DJ et al (2018) Diagnosis and management of Duchenne muscular dystrophy, part 3: primary care, emergency management, psychosocial care, and transitions of care across the lifespan. Lancet Neurol 17(5):445–455
6. Dalakas MC (2015) Inflammatory muscle diseases. N Engl J Med 372:1734–1747
7. Le Guiner C, Servais L, Dickson G (2017) Long-term microdystrophin gene therapy is effective in a canine model of Duchenne muscular dystrophy. Nat Comm 8:16105. https://www.nature.com/articles/ncomms16105
8. Mack DL et al (2017) Systemic AAV8-mediated gene therapy drives whole-body correction of myotubular myopathy in dogs. Mol Ther 25(4):839–854
9. Han S-o et al (2017) Low-dose liver-targeted gene therapy for Pompe disease enhances therapeutic efficacy of ERT via immune tolerance induction. Mol Ther Methods Clin Dev 4:126–136
10. Mendell JR et al (2017) Follistatin gene therapy for sporadic inclusion body myositis improves functional outcomes. Mol Ther 25(4):870–879
11. Torrente Y et al (2004) Human circulating AC133+ stem cells replenish the satellite cell pool, restore dystrophin expression and ameliorate function upon transplantation in murine dystrophic skeletal muscle. J Clin Invest 114:182–195
12. Sampaolesi M et al (2003) Cell therapy of alpha-sarcoglycan null dystrophic mice through intra-arterial delivery of mesoangioblasts. Science 301 (2003):487–492
13. Torrente Y, Gavina M, Belicchi M, Fiori F, Komlev V, Bresolin N, Rustichelli F (2006) High-resolution X-ray microtomography for three-dimensional visualization of human stem cell muscle homing. FEBS Lett 580:5759–5764
14. Farini A et al (2012) Novel insight into stem cell trafficking in dystrophic muscles. Int J Nanomed 7:3059–3067
15. Leroux L et al (2010) Hypoxia preconditioned mesenchymal stem cells improve vascular and skeletal muscle Fiber regeneration after ischemia through Wnt4-dependent pathway. Mol Ther 18(8):1545–1552
16. Sengle G et al (2015) Abnormal activation of BMP signaling causes myopathy in Fbn2 null mice. PLoS Genet 11(6):e1005340

Chapter 14
Nervous Tissue and Neuronal Cells: Patterning by Electrophoresis for Highly Resolved 3D Images in Tissue Engineering

Rolf Zehbe and Kerstin Zehbe

Abstract Restoring peripheral nerve damage can be considered being an important research topic in regenerative medicine. Consequently, neuronal tissue engineering science investigates the so-called nerve conduits as promising approach to re-establish neuronal function, serving as guidance for axonal growth in vivo and possibly bridging damaged or severed nerves. In this regard, significant research has been conducted using certain biomolecules like the nerve growth factor (NGF) protein to stimulate intrinsic regenerative processes. Nevertheless, the damaged nerve tissue lacks the organotypic arrangement of cells and extracellular matrix. Here, a common approach in tissue engineering uses oriented biomaterial structures as nerve conduits with prearranged autologous neuronal cells or other cells supporting axonal growth to allow for better control of tissue-specific regeneration.
In this context, it is well known that biological cells are especially susceptible to electrical potentials, allowing for porating the cell membranes, fusing cells or depositing cells on surfaces of biomaterials as possible means for initial and beneficial patterning.

One research focus of our work was the investigation of the three-dimensional structure of an approximately 800 μm (diameter) rat sciatic nerve using synchrotron-generated X-rays in a tomography setup at the BAMline of BESSY, Berlin. Furthermore, the tissue microstructure was examined using scanning transmission electron microscopy (STEM) imaging. These results served as basis for a tissue engineering approach using cell deposition by electrophoresis. The established patterned electrodes were investigated via light microscopy and X-ray tomography, comparing it to data from a previous study on the three-dimensional structure of electrophoretically deposited cells using serial sectioning by utilizing a focussed ion beam in a cross-beam setup.

R. Zehbe (✉)
University of Potsdam, Institute of Physics and Astronomy, Potsdam, Germany
e-mail: zehbe@uni-potsdam.de

K. Zehbe
University of Potsdam, Department of Chemistry, Potsdam, Germany

A. Giuliani, A. Cedola (eds.), *Advanced High-Resolution Tomography in Regenerative Medicine*, Fundamental Biomedical Technologies,
https://doi.org/10.1007/978-3-030-00368-5_14

1 Introduction

1.1 Neuronal Tissue Engineering

Damaged neuronal tissue generally undergoes unspecific repair mechanisms, inhibiting fully functional tissue regeneration. Therefore, understanding these mechanisms is one key research topic and necessary to develop both therapeutic methods and appropriate models in tissue engineering.

A literature survey has been presented by Battiston et al. [1], reviewing current approaches in sensory nerve regeneration from a clinical viewpoint while comparing biological and synthetic nerve conduits. Historically, the initial approach was based on suturing techniques, attempting to suture two nerve ends, but leading to poor clinical results. Better results were obtained by utilizing an autologous nerve graft to bridge the defect site [2, 3]. The main disadvantage has been ascribed to the fact that another surgical intervention is required to obtain the autograft, often leading to sensory deficits at the removal site while suitable autograft tissue is scarce, especially so for bridging lengthy defects. Nevertheless, tissue autografts are generally considered being the gold standard in neuronal tissue engineering, and novel biomaterial-based approaches are one possible alternative to overcome the limitations presented by the autograft availability [4, 5]. Biomaterial-based nerve conduits are usually limited to (bio)polymeric, nontoxic and degradable materials. Here, degradable polyesters like poly-lactides, poly-glycolides, poly-ε-caprolactone and similar biopolymers are of interest as these polymers are commercially available in pharmaceutical quality and the degradation in vivo is well known [6–8]. To further optimize the biological performance of biomaterials, tissue-specific substances can be incorporated therein, stimulating or inhibiting repair mechanisms and regeneration. Well-known examples for biologically active molecules in neuronal development are the neurotrophic factors [9] like the nerve growth factor (NGF) [10]. Another potential target molecule in neuronal regeneration is fibrin, which is abundant after traumata due to the coagulation cascade; the reader is referred to Akassoglou and Strickland reviewing the role of fibrin in neuronal tissue [11]. In this context, we have shown that fibrin can be electrically co-deposited with cells on the anode part of structured gold electrode systems in vitro via a methodology we called inverse inkjet printing [12, 13]. In-depth analyses of this setup demonstrated that a voltage of 1.2 V should not be exceeded to prevent excessive cell membrane poration or breakdown [14].

1.2 Three-Dimensional Imaging

Three-dimensional imaging has become a powerful tool in almost all scientific disciplines, ranging from the application in materials sciences to medical diagnostics. For X-ray tomography, the mathematical fundamentals date back to 1917,

when Johann Radon [15] developed a methodology to calculate cross-sectional views from rotational projection images, utilizing the high penetration of X-rays in matter, thus establishing the projection-slice theorem.

While X-rays can be produced either in tube-based experimental setups or in synchrotrons, the later offer superior beam properties including high photon flux over a large range of energies, high brilliance and high level of polarization and coherency. This combined range of properties allows for exceptional image quality for many scientific disciplines including the life sciences. An in-depth literature survey is presented in [16].

Nevertheless, a resolution on the cellular level, allowing differentiating between subcellular structures currently, is only partially possible in even advanced synchrotron radiation facilities due to experimental limitations, including rotational stability and other parameters. In this regard, we have investigated the potential of cross-beam electron microscopes, utilizing the possibility to cut into a specimen in situ via a focussed ion beam while imaging with an electron beam. This setup enables highly resolved serial imaging, including possible element contrast as in X-ray tomography via specific heavy metal stains like osmium tetroxide (OsO_4), according to [14].

2 Sciatic Nerve Imaging via X-ray Synchrotron Tomography and Scanning Transmission Electron Microscopy

The sciatic nerve is one of the larger nerves in both humans and animals connecting the lumbar and sacral plexus to the leg and foot, innervating several muscles from the lateral rotator group. Due to its size it is relatively easy to remove undamaged from the surrounding tissue and to prepare it as specimen for further analytical investigations via X-ray tomography and scanning transmission electron microscopy (STEM). Figure 14.1 depicts the site of removal of the investigated rat sciatic nerve, which has been obtained from a female Wistar rat (approximately 11 weeks

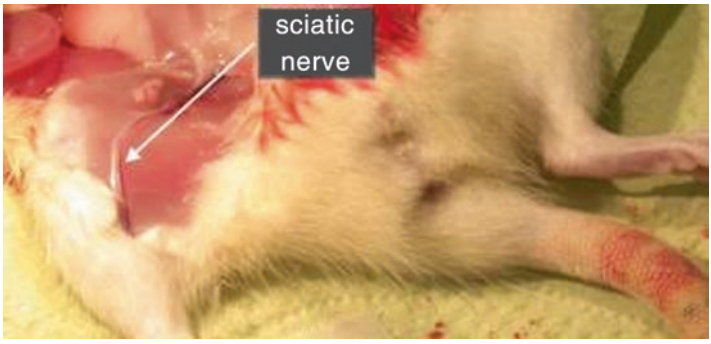

Fig. 14.1 Rat sciatic nerve from a female Wistar rat

old, weight approximately 200 g) and which was terminated at the planned endpoint of another animal study [17] (with ethical approval granted under registration number G 0445-08, according to the Animal Welfare Act as of May 1998).

After removal, the sciatic nerve was immediately rinsed thoroughly with phosphate-buffered saline (PBS) followed by contrasting in solution of 1.0% glutaraldehyde, sodium cacodylate (0.1 M) and 1.0% OsO_4 solution for 60 min at room temperature in the dark followed again by repeated rinsing in PBS adapting a protocol as published by Johnson et al. [18]. Next, the sample was rinsed in deionized water and dehydrated in series of graded ethanol. Finally, the sample was treated with methyl benzoate as intermedium for several minutes before embedding in methyl methacrylate monomer and subsequent polymerization over several days at 37 °C in the dark. The cured sample was sectioned with the diamond blade of an ultramicrotome obtaining several ultra-thin sections for later transmission electron microscopy. The remaining sample was glued on top of a brass rod according to Fig. 14.2 and was used in the depicted synchrotron tomography setup at the BAMline of BESSY, Berlin, according to the protocols as already described elsewhere [16, 19]. The general beamline layout is shown in the bottom inset of Fig. 14.2. Specifically, the sample was rotated in steps of 180°/1200 using a monochromatic X-ray energy of 20 keV. The recorded data was pixel-binned, resulting in a voxel size of the tomographic data of 6.7 µm. ImageJ was used to convert the data into a set of sequential 16-bit TIF images which were flat-field corrected and reconstructed into sliced data using the software NRecon (Bruker) on an Apple iMac Quad-Core i7. Voreen (University of Münster, Germany) was used for three-dimensional rendering and visualization of the data using a green colour look-up table (CLUT) instead of grey values.

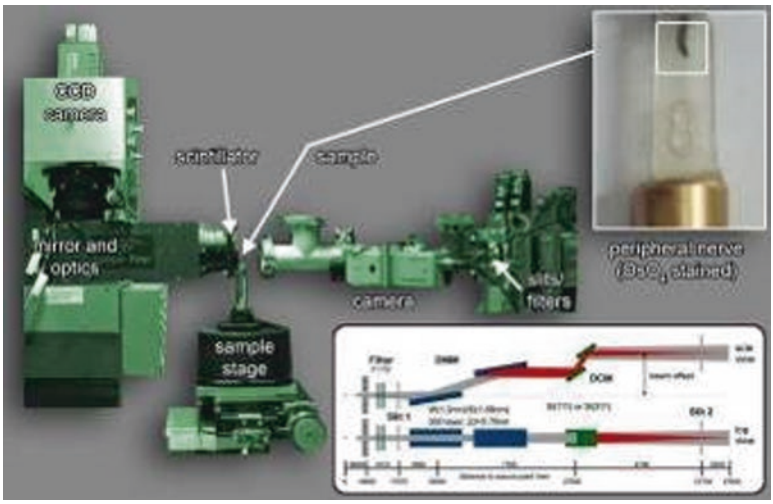

Fig. 14.2 Synchrotron tomography setup. The top inset shows the sciatic nerve sample, while the bottom inset shows the beamline layout according to [16]

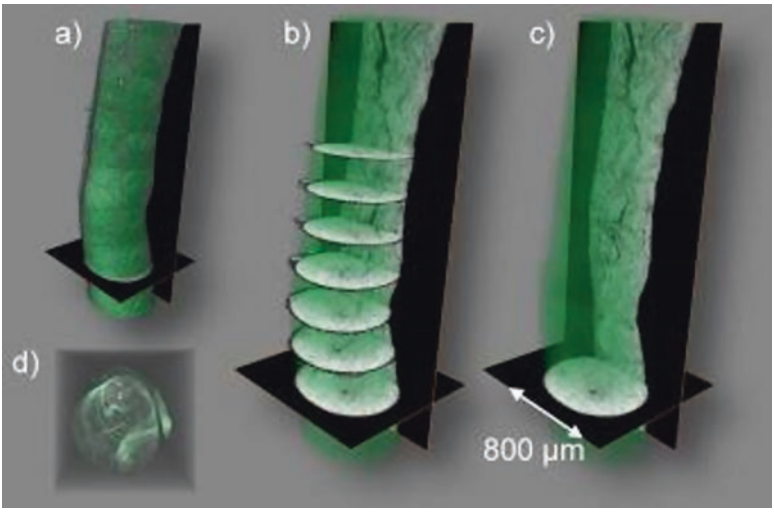

Fig. 14.3 Tomography data renderings of the sciatic nerve sample in different views (**a**–**e**)

The sciatic nerve tomography data is displayed in Fig. 14.3 showing the tissue surface (Fig. 14.3a); it's inside using several superimposed slices (Fig. 14.3b) and without the superimposed slices (Fig. 14.3c). In addition, the nerve is shown in axial view from top to bottom (Fig. 14.3d). The tissue shows the typical zigzag or wavy inner structure, which can be generally observed in peripheral nervous tissue [20] and results from the myelinated fibres which are bundled and appear highly stained by the used contrasting agent OsO_4. Due to the resolution limitation of the recorded tomography data, further investigations were conducted using a Zeiss Crossbeam EsB 1540 (Carl Zeiss AG, Germany) with scanning transmission electron microscopy (STEM) detector.

Here, the individual nerve fibres and the myelinated axons are clearly visible as shown in Fig. 14.4. Figure 14.4a shows an overview image corresponding nicely with the tomography data. Higher resolved STEM images are shown in Fig. 14.4b–d, with Fig. 14.4d displaying the myelinated axons with the approximately 2 µm-thick myelin sheath. This highly ordered and mostly parallel aligned tissue structure serves as basis and template for almost all tissue engineering strategies in neuronal repair. Our approach in this direction is presented in the following section.

3 Neuronal Tissue Engineering by Electrophoretic Cell Patterning

In previous research, we were successful in utilizing an inkjet printer to achieve electrode designs by combining the inkjet printing process with following sputter-coating and ultrasonic ink removal. These electrodes were used for cell patterning

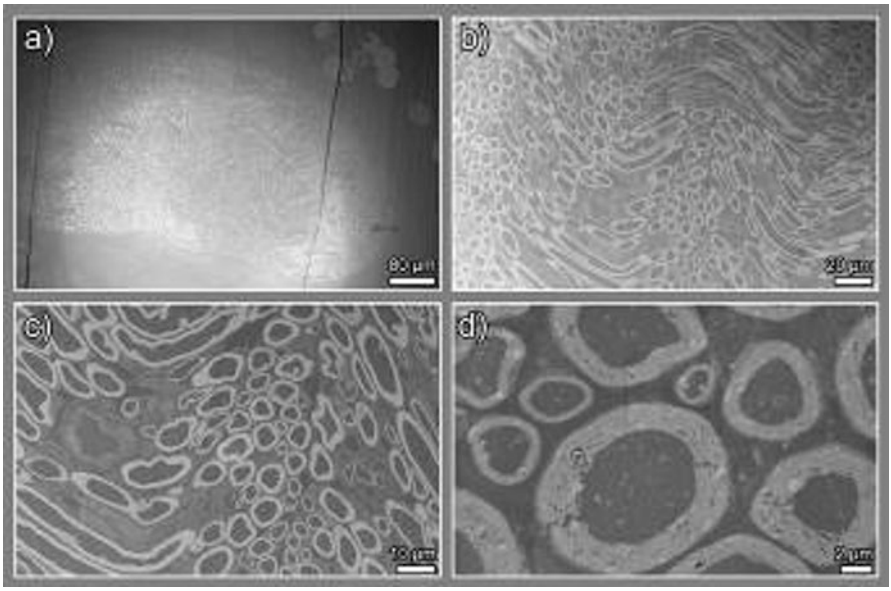

Fig. 14.4 Ultrastructural views of the sciatic nerve using STEM with increasing magnification from (**a**–**d**)

and protein deposition [12, 13]. For our preliminary approach in neuronal tissue engineering, a parallel aligned row structure of thin gold was chosen, co-depositing a hippocampal cell line (HT-22, a subclone of HT-4 [21, 22]) with fibrin at 1.2 V according to [16] and as depicted in Fig. 14.5a. Vital cell patterning was demonstrated in a 12-well plate for cell cultivation purposes applying voltage via lead outs. After cell deposition, the lead outs were removed to ensure sterile handling. Following this, cell vitality has been demonstrated to be near 100% vitality using a combined assay using fluorescein diacetate/ethidium bromide (FDA/EB) as seen in Fig. 14.5b.

Several of these pre-cultivated parallel aligned electrode structures were stacked and cultivated for another day followed by cross-linking in glutaraldehyde, rinsing in distilled water and freeze-drying for the later synchrotron micro-tomography investigations. The resulting multilayered electrode appeared stable and did not delaminate, possibly due to the co-deposited fibrin layer [16].

Similar to the native sciatic nerve, the multilayer stack was glued on a brass rod and subjected to the monochromatic X-ray beam at the synchrotron beamline. The sample was rotated in steps of 180°/1200 using a monochromatic X-ray energy of 10 keV. The resulting voxel size of the tomography data was estimated to be 3.6 µm. Reconstruction and visualization of the data were performed according to the above description and the same software tools. Unfortunately, the data suffered from several ring artefacts, which could not entirely be removed via sinogram correction. Nevertheless, the full tomography data clearly depicts a nice and orderly array of

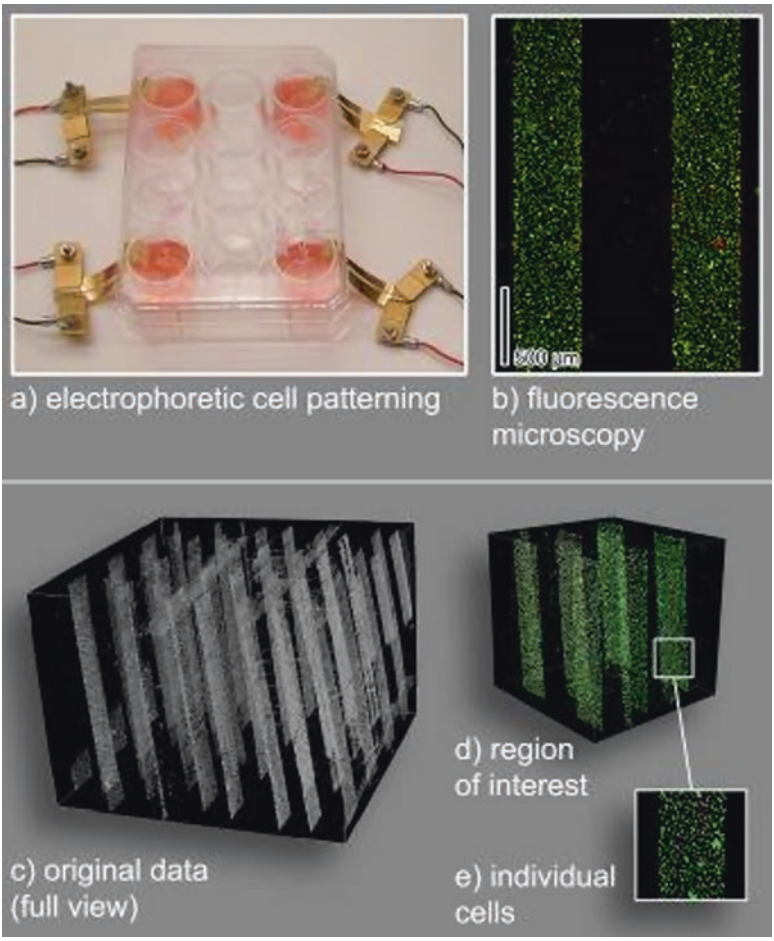

Fig. 14.5 (**a**) Setup for cocultivating neuronal cells and fibrin on parallel aligned electrodes in a 12-well plate setup. (**b**) Fluorescence microscopy showing near 100% vitality in FDA/EB staining. (**c**) Rendered tomography data of a multilayered electrode stack, (**b**, **c**) magnified data showing individual cells

parallel aligned electrodes (Fig. 14.5c). In higher magnification, individual cells (Fig. 14.5d, e) can be seen, having similar density and shape as observed in fluorescence microscopy; therefore, the tomography data was recoloured using a green CLUT to better visualize this correspondence.

Although X-ray tomography can yield highly resolved data, a true cellular resolution with the possibility to discriminate intracellular structures was not possible at the time of measurement. For a true cellular resolution advancing the results of the beamline as referenced in [19], the rotational stage needs higher precision over the time of the measurement. Moreover, optical limitations of the used scintillator and its thickness define the quality of the recorded data. In this regard, current dual beam

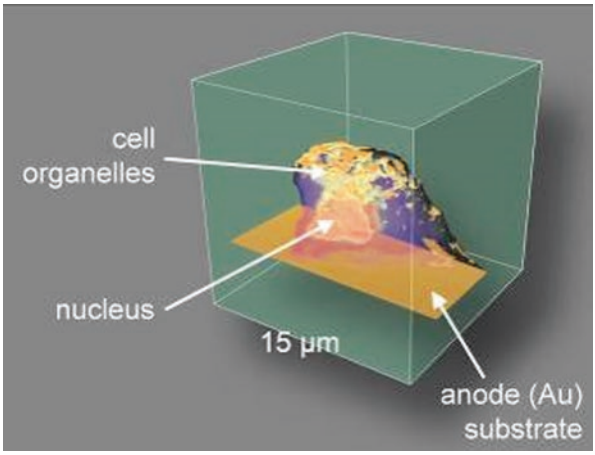

Fig. 14.6 Focussed ion beam sectioned and reconstructed cell on top of a gold on polymer electrode, showing intracellular organelles and structures

electron microscopy technology as available, for example, in the Zeiss Crossbeam devices, can yield sequential slicing and imaging capabilities and therefore the possibility of a tomography approach by utilizing a focussed ion beam for the slicing operation. This methodology was used to reconstruct the complete three-dimensional representations of the electrophoretically deposited HT-22 cells as described in [14]. A vital task in this process is the compensation of the image shift in the recorded sliced data, which has been achieved using automated ImageJ scripts. One reconstructed HT-22 cell is shown in Fig. 14.6 on top of the thin gold on polymer electrode. Well visible and distinguishable are the nucleus and several other cell organelles, which have been recoloured in the graphical depiction.

According to our previous work and without co-deposited fibrin, cells on the anode part were possibly subject to membrane hyperpolarization or poration resulting in intracellular morphological changes which we identified as condensed chromatin which can be a sign for impending cell death. On the contrary, cells co-deposited with fibrin on the anode of the electrodes apparently did not suffer from the above-described effects and appeared vital even after prolonged cultivation in vitro [12, 13].

4 Outlook and Discussion

Neuronal regeneration is a still relevant and open research topic. This chapter might hint at a new methodology to bridge the gap between functional and unspecific repair of nerve tissue, while demonstrating current technological possibilities in three-dimensional imaging. A similar scientific approach has been outlined by Watling et al. [23], explaining how microcomputed tomography can be a useful tool

both for studying the location and the extent of nerve ingrowth into a polymeric scaffold. Nevertheless, such polymeric scaffolds have only limited flexibility controlling the location of neuronal cells, the axonal growth and consequently the quality of the regenerated tissue.

Here, our approach describes a preliminary methodology and should be seen regardless of the presented channel structure and the electrode design.

As an outlook, we want to draft the further direction of this work according to the schematic in Fig. 14.7. Currently, we are able to deposit vital cells and even proteins on top of gold microstructures (Fig. 14.7a). In a next step, we plan to cover this deposit with a castable biopolymer system like gelatin (Fig. 14.7b) and remove these biopolymer sheets together with the adherent cells afterwards (Fig. 14.7c). In this regard, Shimizu et al. [24] have presented a cell cultivation technique, termed cell sheet engineering, which should be seen in the context of this work. A thermoresponsive polymer (poly(N-isopropylacrylamide), PIPAAm) can be switched from a hydrophilic state to a hydrophobic state by decreasing the temperature under 32 °C. A thin layer of PIPAAm between the gold electrodes of this work and the deposited cells might be a useful addition that would allow an easier removal of the gelatin-cell sheets.

In a final step, these sheets might be rolled giving a predefined channel structure with predeposited cells serving as viable nerve conduit and functional repair (Fig. 14.7d).

Concerning the presented three-dimensional imaging methodologies, we have showed two very different approaches. The first approach is based on X-ray tomography, utilizing the projection-slice theorem according to the fundamental works of Johann Radon to image a sciatic nerve sample. The second approach exploits three-dimensional reconstruction from sequential sliced images derived from focussed ion beam slicing and SEM imaging.

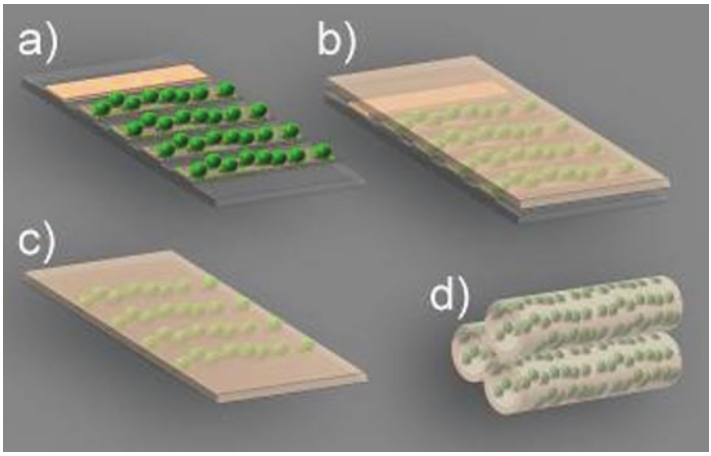

Fig. 14.7 Future direction of cell patterning to achieve pre-cultivated and prestructured nerve conduits

Acknowledgements This chapter is dedicated to our children Hanna and Emma.

The authors would like to thank the following persons for technical assistance: M. Dilger for sample preparation and staining, C. Große-Siestrup for supervision of the animal study under registration number G0445-08, F. Schmidt for STEM imaging and H. Riesemeier for supervision of the BAMline at BESSY.

References

1. Battiston B, Geuna S, Ferrero M, Tos P (2005) Nerve repair by means of tubulization: literature review and personal clinical experience comparing biological and synthetic conduits for sensory nerve repair. Microsurgery 25(4):258–267
2. Millesi H, Meissl G, Berger A (1972) The interfascicular nerve-grafting of the median and ulnar nerves. JBJS 54(4):727–750
3. Seddon H (1963) Nerve grafting: Watson-Jones lecture delivered at the Royal College of Surgeons of England on 10th January 1963. Ann R Coll Surg Engl 32(5):269
4. Evans GR (2001) Peripheral nerve injury: a review and approach to tissue engineered constructs. Anat Rec 263(4):396–404
5. Schmidt CE, Leach JB (2003) Neural tissue engineering: strategies for repair and regeneration. Annu Rev Biomed Eng 5(1):293–347
6. De Ruiter GC, Onyeneho IA, Liang ET, Moore MJ, Knight AM, Malessy MJ et al (2008) Methods for in vitro characterization of multichannel nerve tubes. J Biomed Mater Res A 84(3):643–651
7. Luis AL, Rodrigues JM, Lobato JV, Lopes MA, Amado S, Veloso AP et al (2007) Evaluation of two biodegradable nerve guides for the reconstruction of the rat sciatic nerve. Biomed Mater Eng 17(1):39–52
8. Oh SH, Lee JH (2007) Fabrication and characterization of hydrophilized porous PLGA nerve guide conduits by a modified immersion precipitation method. J Biomed Mater Res A 80(3):530–538
9. Henderson CE (1996) Role of neurotrophic factors in neuronal development. Curr Opin Neurobiol 6(1):64–70
10. Sun W, Lin H, Chen B, Zhao W, Zhao Y, Dai J (2007) Promotion of peripheral nerve growth by collagen scaffolds loaded with collagen-targeting human nerve growth factor-β. J Biomed Mater Res A 83(4):1054–1061
11. Akassoglou K, Strickland S (2002) Nervous system pathology: the fibrin perspective. Biol Chem 383(1):37–45
12. Zehbe R, Gross U, Knabe C, Radlanski R, Schubert H (2007) Anodic cell-protein deposition on inverse inkjet printed micro structured gold surfaces. Biosens Bioelectron 22(7):1493–1500
13. Zehbe R, Gross U, Schubert H (2007) Inverse inkjet printed gold micro electrodes for the structured deposition of epithelial cells and fibrin. Biomol Eng 24(5):537–542
14. Schmidt F, Kühbacher M, Gross U, Kyriakopoulos A, Schubert H, Zehbe R (2011) From 2D slices to 3D volumes: image based reconstruction and morphological characterization of hippocampal cells on charged and uncharged surfaces using FIB/SEM serial sectioning. Ultramicroscopy 111(4):259–266
15. Radon J (1917) Uber die Bestimmung von Funktionen durch ihre Integralwerte langs gewissez Mannigfaltigheiten, Ber. Verh Sachs Akad Wiss Leipzig, Math Phys Klass. p 69
16. Zehbe R, Haibel A, Schmidt F, Riesemeier H, Kirkpatrick CJ, Schubert H et al (2010) High resolution X-ray tomography-3D imaging for tissue engineering applications. Tissue Engineering: InTech
17. Thiem A, Bagheri M, Grosse-Siestrup C, Zehbe R (2016) Gelatin-poly (lactic-co-glycolic acid) scaffolds with oriented pore channel architecture—from in vitro to in vivo testing. Mater Sci Eng C 62:585–595

18. Johnson JT, Hansen MS, Wu I, Healy LJ, Johnson CR, Jones GM et al (2006) Virtual histology of transgenic mouse embryos for high-throughput phenotyping. PLoS Genet 2(4):e61
19. Zehbe R, Riesemeier H, Kirkpatrick CJ, Brochhausen C (2012) Imaging of articular cartilage–data matching using X-ray tomography, SEM, FIB slicing and conventional histology. Micron 43(10):1060–1067
20. Stolinski C (1995) Structure and composition of the outer connective tissue sheaths of peripheral nerve. J Anat 186(Pt 1):123
21. Maher P, Davis JB (1996) The role of monoamine metabolism in oxidative glutamate toxicity. J Neurosci 16(20):6394–6401
22. Morimoto BH, Koshland DE (1990) Excitatory amino acid uptake and N-methyl-D-aspartate-mediated secretion in a neural cell line. Proc Natl Acad Sci 87(9):3518–3521
23. Watling CP, Lago N, Benmerah S, FitzGerald JJ, Tarte E, McMahon S et al (2010 2010/04/30/) Novel use of X-ray micro computed tomography to image rat sciatic nerve and integration into scaffold. J Neurosci Methods 188(1):39–44
24. Shimizu T, Yamato M, Kikuchi A, Okano T (2003) Cell sheet engineering for myocardial tissue reconstruction. Biomaterials 24(13):2309–2316

Chapter 15
X-Ray Phase Contrast Tomography in Tissue Engineering: Focus on Laboratory Implementations

Charlotte K. Hagen

Abstract Tissue engineering, which is aimed at producing "lab-grown" organs and tissues, could revolutionise modern medicine by overcoming the shortage of donor organs. Imaging is key to virtually every aspect of this research; however, the gold standard methods (e.g. histology and electron microscopy) have significant shortcomings, preventing important investigations from being done. Most prominently, they rely upon a destructive sample preparation, making them incompatible with small animal imaging, which is however indispensable for preclinical studies. X-ray phase contrast computed tomography, which is sensitive to phase shifts induced by a sample, has the potential to solve this issue. This chapter provides an overview of laboratory implementations of x-ray phase contrast tomography (as opposed to synchrotron implementations, which are discussed elsewhere in this book) and their application to tissue engineering and related areas.

1 Introduction

Tissue engineering is a subdiscipline of regenerative medicine that combines the fields of cell biology and materials science. In highly simplified terms, the challenge of tissue engineering is to employ and combine appropriate scaffolds, cells and bioreactors with the aim of creating "lab-grown" organs and tissues. Suitable scaffolds must allow and promote cell growth, requiring biocompatibility, an appropriate biodegradation profile, and mechanical properties, components and microarchitecture that mimic the environment of the organ/tissue to be engineered. Scaffolds have traditionally been divided into natural ones, e.g. derived through decellularization of native (cadaveric) tissue, and synthetic ones, e.g. based on hydrogels or other biomaterials or those fabricated via the 3D printing of biopolymers.

C. K. Hagen (✉)
Department of Medical Physics and Biomedical Engineering, University College London, London, UK
e-mail: charlotte.hagen.10@ucl.ac.uk

A. Giuliani, A. Cedola (eds.), *Advanced High-Resolution Tomography in Regenerative Medicine*, Fundamental Biomedical Technologies,
https://doi.org/10.1007/978-3-030-00368-5_15

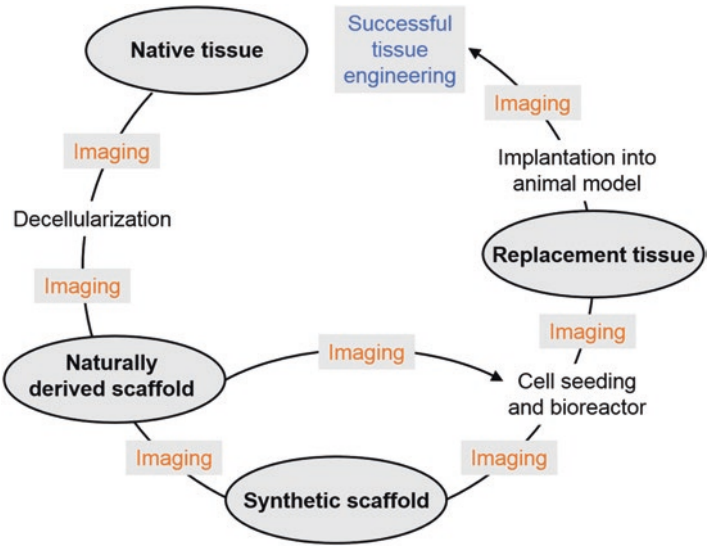

Fig. 15.1 Schematic illustrating the role of imaging in tissue engineering research

Imaging plays a vital role in virtually every aspect of tissue engineering research, as outlined in the (admittedly highly simplified) schematic in Fig. 15.1. First, the structure and functionality of native tissue must be thoroughly studied to gain a "gold standard" understanding of what tissue engineering is supposed to achieve. When natural scaffolds are derived via the decellularisation (e.g. application of detergents) of native tissue, their microstructure must be examined to evaluate the decellularization process, which is considered effective if all cellular material is removed while the native architecture and vascular network are kept intact. The analysis of naturally derived scaffolds is also important to drive the development of synthetic ones aimed at replicating native tissue micro-environments. Synthetic scaffolds, e.g. 3D-printed ones, must be inspected after fabrication to evaluate the reliability of the manufacturing process. In general, any type of scaffold must be imaged following cell seeding and maturation in a bioreactor to understand their ability to promote cell adhesion, proliferation and differentiation. Finally, any engineered implant must be monitored after transplantation into a small animal model to understand the ultimate performance and long-term outcome through pre-clinical studies.

These imaging tasks require an imaging modality that:

- Achieves sufficiently high spatial resolutions (tens of μm to a few μm or below) to resolve the scaffolds' structural features of interest.
- Generates sufficiently high image contrast to visualise cells growing on the scaffolds.
- Provides 3D images to inspect entire specimens and understand cell growth in a volumetric setting.

- Does not require a destructive preparation of the sample, to enable in vivo imaging and longitudinal studies.
- Can accommodate fields of view large enough (a couple of cm) to fit small-scale specimens as well as small animals, e.g. mice, so it can be used for both in vitro and in vivo studies.
- Allows for fast scanning to cope with the high number of specimens often encountered in biomedical research.
- Is easily accessible; ideally, the imaging modality should be installed directly inside tissue engineering labs or in nearby a site, e.g. within a local hospital or research institute.

As it stands, none of the imaging techniques used routinely in biomedical research or clinical practice fulfils all these requirements at once. A comprehensive evaluation and discussion of several routine techniques in the context of tissue engineering has been published a few years ago [1], but we would also like to list a few examples here to elucidate the point. Electron microscopy and histology rely on either sectioning or staining of the sample, hence they involve a destructive sample preparation and are not suited to longitudinal studies or in vivo monitoring. In general, optical imaging methods, to which histology belongs, are limited in depth penetration, thus are only suited for relatively superficial analysis. Magnetic resonance imaging fails to achieve the required spatial resolutions within short scan times, making the method unsuited to high-resolution investigations. Also, scanners might be difficult to access as they are costly and often already used to capacity for medical diagnostics. Standard (attenuation-based) x-ray tomography and micro-tomography provide insufficient soft tissue contrast for visualising cell growth on scaffolds unless cell labelling techniques or contrast agents are used. On the contrary, x-ray phase contrast tomography has the potential to solve many of these issues. For example, as an advantage over standard x-ray tomography, image contrast is generated from phase shifts that occur within the sample rather than from attenuation, which can lead to significantly increased image contrast for soft biological samples that exhibit weak attenuation properties.

The aim of this chapter is to provide an overview of the benefits that x-ray phase contrast tomography could bring about for tissue engineering research. The focus is on high-resolution laboratory implementations of the method as opposed to synchrotron implementations, which are discussed elsewhere in this book. The relatively small number of synchrotrons worldwide and competitive application procedures for beam time limit accessibility and barely allow for longitudinal studies. On the contrary, laboratory implementations usually involve relatively small-scale experimental setups (comparable in size to standard x-ray tomography or micro-tomography scanners) and could ultimately be installed directly on the site where the tissue engineering research is taking place, thus being much easier to access. However, implementing x-ray phase contrast tomography outside synchrotrons comes with its own challenges as beams with a relatively weak spatial and temporal coherence (resulting from extended focal spot sizes and broad energy spectra, respectively) produced by standard, commercially available x-ray tubes

must be tolerated, and nonideal experimental conditions such as source drifts or environmental vibrations must be withstood. Moreover, it can be difficult to achieve sufficiently fast scan times given the relatively low flux emitted by x-ray tubes.

Several different x-ray phase contrast tomography methods have been developed over the years. Broadly speaking, these can be categorised as crystal-based methods (e.g. analyser-based imaging, Bonse-Hart interferometry), grating-based interferometric methods (e.g. Talbot interferometry), grating-based non-interferometric methods and propagation-based methods. Most of them originate from synchrotrons and were later adapted for use with standard x-ray tubes. However, not all methods are naturally suited to use outside synchrotrons and under nonideal experimental conditions; for example, crystal-based methods require a monochromatic beam and a highly stable setup to ensure a perfect alignment of the crystal at all times.

In Sect. 2, we provide a brief overview of those x-ray phase contrast tomography methods most commonly used outside synchrotrons. In Sect. 3, we describe four case studies in which these methods have been used in tissue engineering or other applications with relevance to the field. It should be noted that we do not attempt to provide a complete review of the literature, but rather to draw attention to a few striking examples of what x-ray phase contrast tomography can achieve. Finally, in Sect. 4, we reflect on the remaining challenges that need to be addressed before laboratory-based x-ray phase contrast tomography can become an established imaging modality in tissue engineering research, and discuss the perspectives for the future.

2 Laboratory Implementations of X-Ray Phase Contrast Tomography

Below we provide a brief overview of the different x-ray phase contrast tomography methods most suited for use in non-synchrotron, laboratory settings, and comment on their requirements in terms of spatial and temporal coherence. For a more detailed overview of all existing phase contrast imaging methods, we would like to refer to some excellent review papers [2–4].

Propagation-Based Imaging A propagation-based imaging setup resembles a conventional radiographic setup in that it only comprises an x-ray beam and a detector. The key difference is, however, that the detector is placed at some distance from the sample. In this configuration, an interference pattern, resulting from the phase shifts that are introduced by the sample, emerges as the beam propagates. This results in an edge enhancement effect in the images, where sharp features within the sample are surrounded by black and white fringes. It is often desirable to convert this fringe contrast into area contrast as this can simplify the interpretation of the images. This requires performing phase retrieval, i.e. quantitatively extracting the phase

shift from the data, in addition to tomographic image reconstruction. In propagation-based imaging, phase retrieval typically involves measuring interference patterns at several propagation distances and combining them according to a dedicated algorithm [5]. Provided that simplifying conditions apply, e.g. the sample is quasi-homogeneous, it can be sufficient to use only one propagation distance [6]. Propagation-based imaging tolerates the broad spectra emitted from standard x-ray tubes as each polychromatic interference pattern is effectively a weighted sum of individual monochromatic components [7]. However, the method requires a relatively high degree of spatial coherence as otherwise the interference pattern suffers from blurring, leading to a reduction of contrast [7].

Grating Interferometry Grating interferometry, also known as Talbot or Talbot/Lau interferometry, is based on the Talbot self-imaging effect. A typical experimental setup contains a phase grating that generates an interference pattern and an absorption grating placed at a Talbot distance from the phase grating (where the interference pattern is a replica of the latter). The detector is positioned immediately behind the absorption grating. By transversally step-scanning one of the gratings (a process known as phase stepping), a sinusoidal pattern is recorded. Phase shifts that occur within the sample lead to a transverse shift of this pattern; phase retrieval can thus be performed by quantitatively comparing the sinusoidal patterns recorded in the absence and presence of the sample [8]. Instead of the absolute phase shift, phase retrieval in grating interferometry yields its first derivative, thus requiring its integration before tomographic image reconstruction, or the use of a dedicated filter function during the reconstruction process (the Hilbert filter). This makes grating interferometry belong to the group of differential phase contrast imaging techniques. As the formation of a Talbot self-image is an intrinsically coherent effect, grating interferometry relies on the use of a spatially coherent beam. However, the method can be adapted to beams with weak spatial coherence by introducing a third grating into the setup, placed in front of the x-ray source, generating mutually incoherent but individually coherent sub-sources [8]. Weak temporal coherence can be tolerated to a limited extent; as the gratings have a specific design energy, the use of very broad spectra leads to a reduction in visibility (the separation of minima and maxima of the sinusoidal phase stepping pattern), compromising the method's sensitivity [9].

Edge Illumination This method employs a narrow x-ray beam which is aligned with an edge in front of the detector. Phase shifts that occur within the sample lead to a slight deviation of the beam from its original path, either causing a larger portion of it to be absorbed by the edge and decreasing the measured intensity or to fall onto the active area of the detector and increasing the measured intensity. In the laboratory adaptation, this concept is expanded to two-dimensional fields of view by means of two opportunely designed x-ray masks [10]. The first mask (sample mask) creates an array of narrow beamlets, and the second mask (detector mask) creates a series of edges immediately in front of the detector. The mask periods match the pixel size, considering magnification. Phase

retrieval in edge illumination requires that two images are acquired, taken with the beamlets illuminating the opposing edges of the apertures in the detector mask and processed according to a dedicated algorithm [11, 12]. Like in grating interferometry, phase retrieval yields the first derivative of the phase shift, also making edge illumination a differential phase contrast technique. In edge illumination, temporal coherence is not required as the measured signal is a weighted average of individual monochromatic components; hence the method makes use of the full x-ray spectra generated by standard x-ray tubes [13]. Weak spatial coherence is tolerated so long as the blur induced by the source is sufficiently small to keep the individual beamlets physically separated [14].

Zernike Phase Contrast In this method, the x-ray beam is focused onto the sample by means of a condenser ring. After passing through the sample where diffraction occurs, the beam is focused again using a zone plate. Next, a phase ring introduces an amplitude reduction and a known phase shift to the portion of the beam that has not been diffracted. The latter now has a similar intensity (but a different phase shift) to the diffracted beam portion, and the interference of both leads to intensity variations on the detector plane, manifesting as edge enhancement in the images. By means of phase retrieval, performed by applying a dedicated filter function to the images, the edge contrast can be converted into area contrast [26]. Zernike phase contrast relies on a monochromatic beam as the optical elements involved are designed for a specific energy. A relatively high degree of spatial coherence is needed as otherwise the spatial separation of directly incident and diffracted beam portions would be reduced, which in turn would lead to a reduction in contrast (Fig. 15.2).

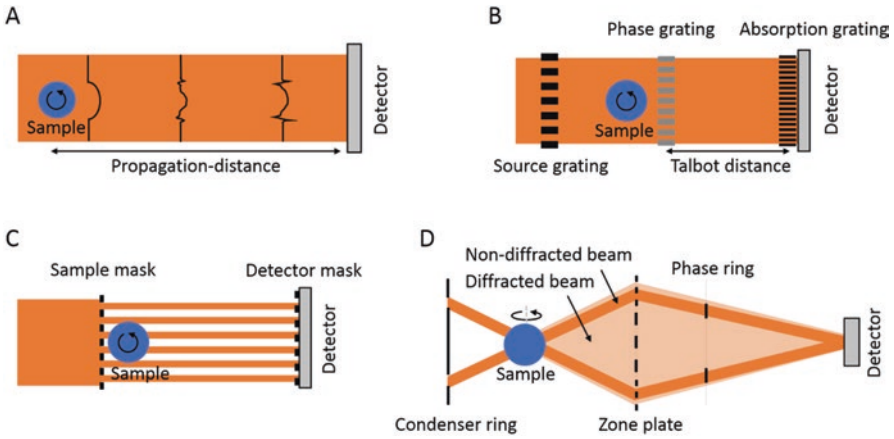

Fig. 15.2 Schematic of the x-ray phase contrast tomography methods most commonly used outside synchrotrons: propagation-based imaging (**a**), grating interferometry (**b**), edge illumination (**c**) and Zernike phase contrast (**d**). These drawings are not to scale, and the beam is typically conical rather than planar

3 Application in Tissue Engineering and Related Areas

The following case studies are supposed to illustrate a range of recent applications of x-ray phase contrast tomography in tissue engineering and related fields. In addition, we would like to point to other important publications [15–19] and to an earlier review paper on the topic [20].

Visualising the Mouse Brain on a Cellular Level A team of scientists from the University of Goettingen (Germany) have developed a protocol for performing "3D virtual histology" of soft biological specimens using high-resolution x-ray phase contrast tomography based on propagation-based imaging [21]. This was demonstrated on a mouse brain, which was dehydrated in ethanol before being placed in xylene until this eventually evaporated. This sample preparation process was demonstrated to effectively remove water and lipids from the specimen. The results are shown in Fig. 15.3. To obtain a spatial coherence sufficiently high for propagation-based imaging, the experimental setup comprised a liquid-metal jet micro-focal x-ray source (Excillum, Sweden). The source was operated at 40 kVp and 1.43 mA, and the focal spot was 10 µm. However, since in a standard propagation-based imaging geometry (the sample placed close to the source and far from the detector) the spatial resolution is largely determined by the source size, this focal spot was too

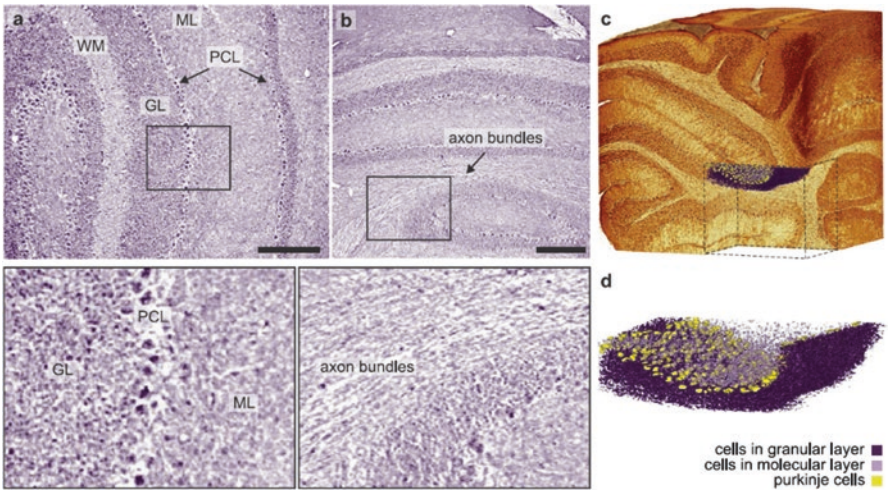

Fig. 15.3 X-ray phase contrast tomograms (scale bars: 200 µm) of a mouse brain acquired with propagation-based imaging. The high spatial resolution and the strong contrast between the tissue protein matrix and surrounding air allowed for a volumetric analysis of cellular structures within the sample. (**a**) Transverse slice showing the molecular layer (ML), granular layer (GL), white matter (WM) and Purkinje cell layer (PCL) of the cerebellar vermis. (**b**) Longitudinal slice showing axon bundles within the white matter. (**c**) Volume rendering of the sample, indicating the cellular segmentation shown in (**d**). (**d**) Cellular segmentation. Due to the high level of detail in the images, the described sample preparation and scanning protocol could be used to study cell migration on tissue engineering scaffolds. (Figure and caption adapted from Toepperwien et al. [21])

large to achieve spatial resolutions on a cellular level. Therefore, a setup with an "inverse geometry" was used, in which the sample is placed relatively far from the source (at 158.75 mm) and closer to the detector (at 18.3 mm), still maintaining a propagation distance sufficiently large for interference patterns to develop. In this configuration, the spatial resolution is largely driven by the point spread function of the detector. In the Goettingen setup, the detector was a lens-coupled scintillator-based camera (XSight, Rigaku, Japan) with an effective pixel size of 0.54 μm (0.48 μm on the sample plane). The tomographic scan involved the acquisition of 1000 projections over a total sample rotation range of 180°. The exposure time per projection was 50 s, leading to a total exposure time of approximately 14 h. The protocol further consisted of phase retrieval using a method called "Bronnikov-aided correction" [22] based on data acquired at one propagation distance only and tomographic reconstruction using a commercial software (Bronnikov Algorithms, Netherlands). The spatial resolution in the final images was measured to be 3.53 μm.

Towards Small Animal Imaging Researchers from the Technical University of Munich (Germany) have used x-ray phase contrast tomography based on grating interferometry to demonstrate the feasibility of imaging mouse models for pre-clinical research [23]. The results are shown in Fig. 15.4. The imaged animal, a deceased 19-month-old mouse, had been fixed in formaldehyde using a perfusion fixation protocol. The experimental setup comprised an Enraf Nonius FR 591 x-ray tube with a rotating molybdenum target. The tube was operated at 35 kVp and 70 mA, and the focal spot was 300 μm. The detector was a Pilatus II silicon-based photon-counter with an effective pixel size of 120 μm on the sample plane. The setup employed three gratings with periods of 10 μm (source grating), 3.51 μm (phase grating) and 5.40 μm (absorption grating), each having a fill factor of two. The distance between the phase and absorption gratings was 5.27 cm, corresponding to the third Talbot order. The design energy of the gratings was 23 keV, corresponding to the centre of the

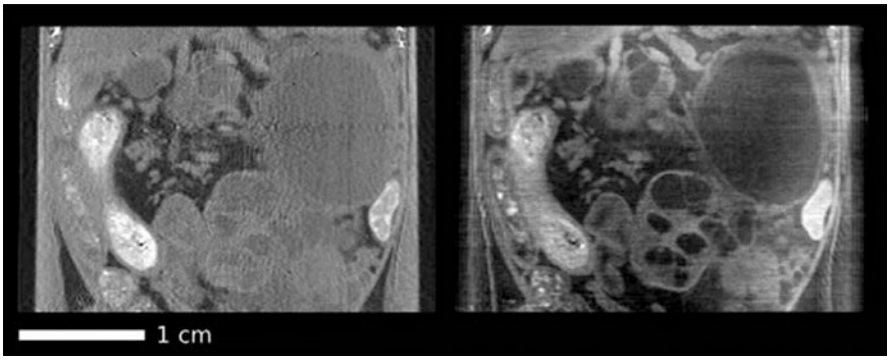

Fig. 15.4 Coronal slices extracted from an attenuation tomogram (left) and a phase contrast tomogram (right) acquired with a grating interferometer showing the abdominal area of a deceased, formalin-fixed mouse. The latter features higher image contrast for most organs and soft tissue types. (Figure adapted from Tapfer et al. [23])

polychromatic x-ray spectrum produced by the x-ray tube. The tomographic scan involved acquiring data for 301 rotational views of the sample, and at each view 10 images were recorded during the phase stepping procedure. The exposure time per phase step image was 12 s, leading to a total exposure time of approximately 10 h. Following phase retrieval, tomographic images were reconstructed using the filtered back-projection algorithm. The spatial resolution in the final images was not measured.

Revealing the Microarchitecture of a Decellularized Rabbit Oesophagus A study conducted at University College London (United Kingdom) focused on using x-ray phase contrast tomography based on edge illumination to image a natural tissue engineering scaffold derived from a rabbit oesophagus via decellularization [24]. The work was motivated by the development of a new decellularization method known as detergent enzymatic treatment during which the native tissue is flushed with a combination of enzymes and detergents, with the aim of being gentler to the collagen microarchitecture while being as effective in removing cellular material as previous methods. Imaging the decellularised tissue was required to understand the performance of the new method and to inform potential improvements should these be necessary. The results are shown in Fig. 15.5. The imaging setup comprised a Rigaku MicroMax-007 HF x-ray tube with a rotating Mo target, operated at 40 kVp and 25 mA, corresponding to a source size of approximately 70 μm. The sample was positioned at 1.6 m from the source. The detector, a Hamamatsu C9732DK flat panel with

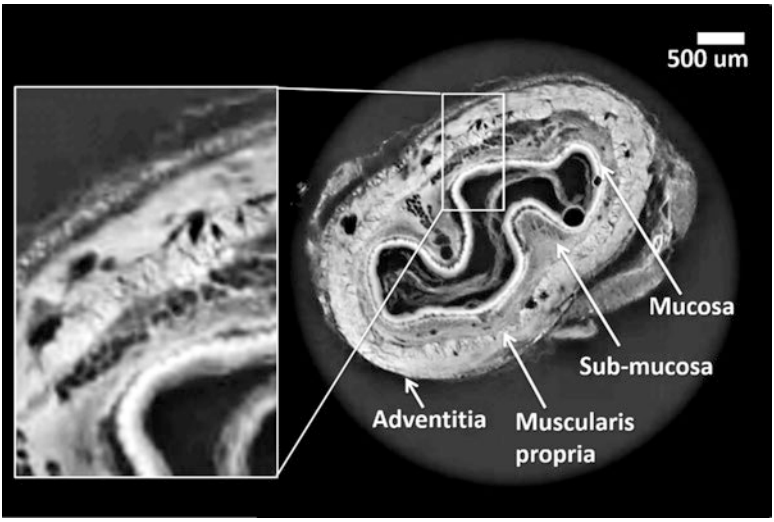

Fig. 15.5 X-ray phase contrast tomogram (scale bar, 500 μm) acquired with edge illumination, showing a transverse cross section of a rabbit oesophagus scaffold derived via decellularization using detergent enzymatic treatment. The image reveals an intact microstructure of the specimen, confirming the presence and integrity of all native anatomical layers, thus providing valuable feedback on the used decellularisation technique. (Figure and caption adapted from Hagen et al. [24])

a pixel size of 50 μm, was placed at 0.4 cm from the sample. The sample and detector mask periods were 79 μm and 98 μm, respectively, and their pitches were 23 μm and 29 μm, respectively. These dimensions correspond to a "line-skipping" configuration which is often used when a detector has high levels of cross-talk between adjacent pixels; neglecting every other detector column effectively reduces the cross-talk [25]. The tomographic scan involved taking data at 720 view angles, equally spaced over 360°. In preparation for phase retrieval, two projections, taken with the beamlets illuminating opposing detector mask edges, were acquired at each angle. Moreover, at each angle, the sample was displaced ten times by 7.9 um (a tenth of the sample mask period), a projection was taken at each displacement, and these projections were eventually combined. This procedure known as "dithering" is used to increase the spatial resolution. Each projection was acquired with 1.2 s exposure time, leading to a total exposure time of 4.8 h. Following phase retrieval, phase contrast tomograms were reconstructed using the filtered back-projection algorithm. The pixel size in the final images was 7.9 μm; however, the actual spatial resolution was not measured.

Quantifying Cell Growth on Polymer Scaffolds A team of researchers from the Henry Mosely X-ray Imaging Facility in Manchester (United Kingdom) have demonstrated that x-ray phase contrast nano-tomography based on Zernike phase contrast can enable the three-dimensional analysis of cells growing on polymer scaffolds fabricated by means of electrospinning [26]. The results are shown in Fig. 15.6.

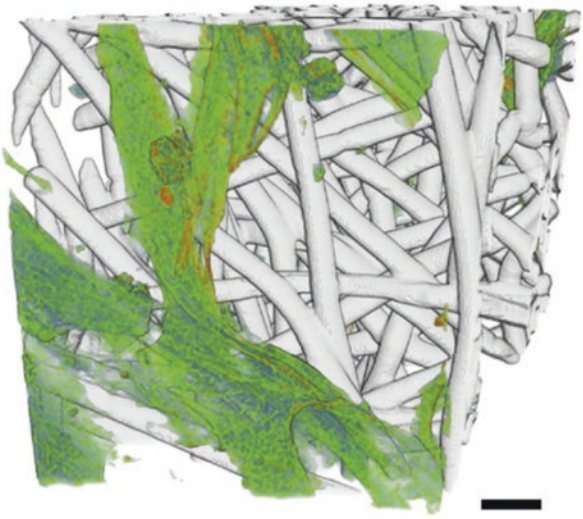

Fig. 15.6 Volume rendering (scale bar: 10 μm) of an x-ray phase contrast tomogram acquired with Zernike phase contrast, showing cells distributed on and within an electrospun scaffold. Segmentation of the scaffold and of the cellular material has enabled quantifying scaffold porosity, pore size and fibre diameter and cell length and diameter. Moreover, the distance of the cells from the upper scaffold surface could be measured, providing an indicator for the extent of cell migration. (Figure adapted from Bradley et al. [26], © 2016 Bradley RS, Robinson IK, Yusuf M. Published by WILEY-VCH Verlag GmbH & Co. KGaA, Weinheim)

The imaging system was a commercial Zeiss Xradia 810 Ultra machine, featuring a field of view of 65 μm. The x-ray beam was quasi-monochromatic with an energy of 5.4 keV. The tomographic dataset comprised 541 projections acquired over a sample rotation range of 180°. Each projection was taken with an exposure time of 10 s, leading to a total exposure time of approximately 1.5 h. Tomographic image reconstruction was performed using the filtered back-projection algorithm, which was followed by phase retrieval to convert the phase-based edge enhancement contrast into area contrast. The pixel size in the final images was 127 nm, and the spatial resolution has been estimated to be approximately 320 nm. To image a larger sample section than permitted by the very small field of view, two adjacent sections of the scaffold were imaged in consecutive scans, the results stitched together and analysed as a single dataset.

4 Remaining Challenges and Future Perspectives

The above case studies show that there is much versatility in terms of how x-ray phase contrast tomography can be implemented outside synchrotrons, and how it can be used for tissue engineering and related applications, and that each of the presented methods comes with its own pros and cons. Propagation-based imaging features a relatively simple experimental setup but has rather stringent requirements on spatial coherence. This necessitates the use of micro-focal x-ray sources which are often limited in flux. On the other hand, since the method does not employ any optical elements that attenuate the beam, the available flux is used in an optimal way. Grating interferometry has been shown to be highly sensitive to phase shifts due to the small periods of the used gratings (a few μm) [27]. On the flipside, these small periods require a precise alignment of the experimental setup, which is not always possible to maintain [28]. Likewise, edge illumination employs two sets of masks that must be kept well aligned at all times, although this requirement is somewhat relaxed by the fact that the mask periods are generally about one order of magnitude larger (tens of μm) than the grating periods in grating interferometry, which has been shown not to lead to reduced sensitivity [29]. Edge illumination has the advantage that the spatial resolution is to some extent decoupled from the source blur and the detectors point spread function as it is effectively driven by the aperture width of the sample mask [30]. Zernike phase contrast readily achieves spatial resolutions on the lower micrometre scale and below; however, this comes at the cost of small fields of view, often limited to tens of micrometres.

Considering the presented methods in the context of the imaging challenges of tissue engineering outlined in Sect. 1, it becomes apparent that several of the required criteria are already met by laboratory based x-ray phase contrast tomography. Spatial resolution sufficiently high to resolve features of interest of tissue engineering specimens, such as the scaffolds' microarchitecture, has been demonstrated to be feasible. Some methods even allow tailoring the spatial resolution to the imaging application at hand, for example, propagation-based imaging can be used in

different geometries (standard and "inverse"). This provides options for "zoom-in" tomography, where a scout scan, taken with a relatively coarse spatial resolution, is used to identify a region of interest within a sample, and followed by a high-resolution scan of that area [21]. Such approaches could prove especially valuable to the study of 3D-printed scaffolds which are often engineered to have specific hierarchical features, like pores with diameters on the macro- and microscale. Image contrast has been demonstrated to be sufficiently high for a range of tissue engineering applications, most notably monitoring cell growth and imaging of a mouse model. By default, being tomographic techniques, all methods provide 3D images, facilitating, amongst others, the understanding of cell migration in a volumetric setting. In terms of setup size, the methods which have been commercialised (e.g. Zernike phase contrast in the Zeiss XRadia x-ray microscopes, grating interferometry in the Bruker SkyScan machines) take up about as much space as clinical x-ray tomography scanners or less, fitting inside tissue engineering labs or a site nearby. Those methods that only exist as custom-made experimental setups built by individual research groups are of similar dimensions.

However, it is also apparent that x-ray phase contrast tomography still falls short in terms of some important requirements. In those methods providing the higher end of achievable spatial resolutions, e.g. propagation-based imaging in "inverse" geometry or Zernike phase contrast, the fields of view are not currently large enough to scan samples with sizes comparable to a small animal or an entire scaffold. In propagation-based imaging, this is because an effective pixel size of a few μm or below is needed, but detectors generally contain a limited number of pixels (typically around 2000 in one direction), restricting the field of view to a few mm. In Zernike phase contrast, this is also due to the difficulty of fabricating large zone plates. While in general no destructive sample preparation is required in x-ray phase contrast tomography, making it an attractive choice for longitudinal studies and in vivo applications, some sample damage due to the use of ionising radiation might occur [26]. Finally, x-ray phase contrast tomography still fails to meet one of the most important criteria for routine use in tissue engineering research to achieve fast acquisitions. Total exposure times in the presented case studies have ranged from 1.5 h to approximately 19 h due to three reasons: (i) relatively long exposure times were applied per tomographic view angle, (ii) in some cases multiple projections were taken at each angle in preparation for phase retrieval and/or for increasing the spatial resolution (e.g. "dithering" in edge illumination) and (iii) in some studies the number of tomographic view angles was large. These scan times are clearly at odds with the need to cope with the high number of specimens potentially encountered, as well as with the requirements of in vivo imaging.

Yet, significant research effort is currently dedicated to solving these problems, and solutions are beginning to emerge. The biggest issue, scan time, is being tackled through several approaches at once. First, the development of new x-ray sources based on liquid-metal jet targets [31], which support higher electron-beam power than standard fixed or rotational targets, has significantly increased the available flux, potentially reducing exposure time in those methods relying on micro-focal x-ray sources due to their requirement for a relatively high degree of spatial coherence.

Although one such source has been used in one of the case studies discussed here where the exposure time was rather long, it should be noted that this was in part due to the small effective detector pixel size, making such a long exposure time necessary to achieve appropriate x-ray statistics. Another option for potentially reducing exposure time is through novel detector technology with increased sensitivity, e.g. via the elimination of electronic noise from the images (photon-counting detectors). In addition to those technological advances, several new phase retrieval methods have been developed that reduce the number of required input images. These are typically based on simplifying assumptions. For example, as already mentioned in Sect. 2, in propagation-based imaging, if the sample is quasi-homogeneous, i.e. it is made from a single material or the ratio of phase shift and attenuation is constant throughout, it is sufficient to use only one propagation distance and to apply Paganin's algorithm [6]. Although in general tissue engineering specimens do not strictly fulfil this condition apart from synthetic scaffolds made from a single biomaterial, it is often a good approximation so long as samples can be described as "soft biological tissue", i.e. they do not contain any strongly phase shifting or attenuating components like bone or calcifications. The same assumption has been used to derive a single-image phase retrieval method for edge illumination, allowing to acquire only one sample projection at each tomographic view angle [32]. A single-image phase retrieval method not relying on any simplifying assumptions based on Moire analysis has been developed for grating interferometry [33]. While it still needs to be understood if these new methods ultimately require the same total x-ray statistics as their multiple image-based counterparts, and thus the same exposure time, they are certainly more practical as they do not rely on mechanical alterations of the experimental setup during an acquisition (e.g. changing the propagation distance in propagation-based imaging, performing phase stepping in grating interferometry, or switching from illuminating one edge to the other in edge illumination). This eliminates dead times, hence allowing faster scans. Finally, the necessity to take data at a large number of tomographic view angles could be relaxed through better suited tomographic reconstruction algorithms. It is well known in standard x-ray tomography that fewer view angles are required if iterative (algebraic or statistical) reconstruction algorithms are used instead of analytic ones like filtered back-projection. In fact, much recent research has been dedicated to extending such algorithms to x-ray phase contrast tomography [34, 35]. Additionally, some new algorithms even incorporate the phase retrieval step directly into the reconstruction process, based on a single input projection and without making any assumptions on the sample or the imaging geometry [36, 37], thus relaxing the number of required images even further. As a welcome side effect, reducing the number of tomographic view angles can also lower the delivered radiation dose. The problem of small fields of view in the very high-resolution setups could be overcome by performing region-of-interest tomography, scanning multiple areas of the sample and stitching the images together.

In summary, the recent literature suggests that the remaining shortcomings of x-ray phase contrast tomography (long scan times, small fields of view in some methods) could be overcome in due course. Considering also that most criteria are

already met (non-destructive sample preparation, provision of 3D images, high spatial resolutions and high image contrast, relatively small experimental setups), one can conclude that x-ray phase contrast tomography is indeed well suited to tissue engineering research. Looking forward, it can be anticipated that x-ray phase contrast tomography will ultimately be used for some, if not all imaging tasks listed in Fig. 15.1. Most notably, the fact that no slicing or staining of the sample is required, which is the key difference to the methods most commonly used within the tissue engineering community (histology and electron microscopy), makes it a long-sought solution for imaging scaffolds prior to and after implantation into small animal models. This is a vital requirement for advancing from small-scale in vitro work to more extensive pre-clinical studies. Moreover, the intrinsic volumetric nature of the images allows gaining a precise understanding of the scaffolds' microarchitecture in three dimensions. As already mentioned in the introduction, this is required to develop the knowledge necessary to fabricate synthetic scaffolds that could eventually replicate naturally derived ones. Synthetic scaffolds have the advantage that they are man-made, can be produced on a semi-industrial scale and, hence, made widely available to the population. Finally, due to its high spatial resolution and contrast capabilities, x-ray phase contrast tomography could ultimately become a tool for routine quality control of tissue engineered implants, and as a result solve some of the controversies around patient safety that are sometimes associated with the field.

References

1. Appel AA, Anastasio MA, Larson JC, Brey EM (2013) Imaging challenges in biomaterials and tissue engineering. Biomaterials 34:6615–6630
2. Bravin A, Coan P, Suortti P (2013) X-ray phase-contrast imaging: from pre-clinical applications towards clinics. Phys Med Biol 58:R1–R35
3. Olivo A, Castelli E (2014) X-ray phase contrast imaging: from synchrotrons to conventional sources. Riv Del Nuovo Cimento 37:467–508
4. Munro PRT (2017) Coherent x-ray imaging across length scales. Contemp Phys 58:140–159
5. Cloetens P, Ludwig W, Baruchel J, Van Dyck D, Van Landuyt J, Guigay JP, Schlenker M (1999) Holotomography: quantitative phase tomography with micrometre resolution using hard synchrotron x-rays. Appl Phys Lett 75:2912–2914
6. Paganin D, Mayo SC, Gureyev TE, Miller PR, Wilkins SW (2002) Simultaneous phase and amplitude extraction from a single defocused image of a homogeneous object. J Microsc 206:33–40
7. Olivo A, Speller R (2006) Experimental validation of a simple model capable of predicting the phase contrast imaging capabilities of any x-ray imaging system. Phys Med Biol 51:3015–3030
8. Pfeiffer F, Weitkamp T, Bunk O, David C (2006) Phase retrieval and differential phase-contrast imaging with low-brilliance x-ray sources. Nat Phys 2:258–261
9. Thuering T, Stampanoni M (2014) Performance and optimization of x-ray grating interferometry. Phil Trans R Soc A 372:20130027
10. Olivo A, Speller R (2007a) A coded-aperture technique allowing x-ray phase contrast imaging with conventional sources. Appl Phys Lett 91:074106
11. Munro PR, Hagen CK, Szafraniec MB, Olivo A (2013) A simplified approach to quantitative coded aperture x-ray phase imaging. Opt Express 21:11187–11201

12. Diemoz PC, Endrizzi M, Zapata CE, Pesic ZD, Rau C, Bravin A, Robinson IK, Olivo A (2013a) X-ray phase-contrast imaging with nanoradian angular resolution. Phys Rev Lett 110:138105
13. Endrizzi M, Vittoria FA, Kallon G, Basta D, Diemoz PC, Vincenzi A, Delogu P, Bellazzini R, Olivo A (2015) Achromatic approach to phase-based multi-modal imaging with conventional x-ray sources. Opt Express 23:16473–16480
14. Olivo A, Speller R (2007b) Modelling of a novel x-ray phase contrast imaging technique based on coded apertures. Phys Med Biol 52:6555–6573
15. Zysk AM, Garson AB III, Xu Q, Brey EM, Zhou W, Brankov JG, Wernick MN, Kuszak JR, Anastasio MA (2012) Non-destructive volumetric imaging of tissue microstructure with benchtop x-ray phase-contrast tomography and critical point drying. Biomed Opt Express 3:1924–1932
16. Appel AA, Larson JC, Somo S, Zhong Z, Spicer PP, Kasper FK, Garson AB III, Zysk AM, Mikos AG, Anastasio MA, Brey EM (2012) Imaging of poly(α-hydroxy-ester) scaffolds with x-ray phase-contrast microcomputed tomography. Tissue Eng: Part C 18:859–865
17. Appel AA, Larson JC, Garson AB III, Guan H, Zhong Z, Nguyen BB, Fisher JP, Anastasio MA, Brey EM (2015) X-ray phase contrast imaging of calcified tissue and biomaterial structure in bioreactor engineered tissues. Biotechnol Bioeng 112:612–620
18. Krenkel M, Toepperwien M, Dullin C, Alves F, Salditt T (2016) Propagation-based phase-contrast tomography for high-resolution lung imaging with laboratory sources. AIP Adv 6:035007
19. Appel AA, Ibarra V, Somo SI, Larson JC, Garson AB III, Guan H, McQuilling JP, Zhong Z, Anastasio MA, Opara EC, Brey EM (2016) Imaging of hydrogel microsphere structure and foreign body response based on endogenous x-ray phase contrast. Tissue Eng: Part C 22:1038–1048
20. Appel AA, Anastasio MA, Brey EM (2011) Potential for imaging engineered tissues with x-ray phase contrast. Tissue Eng: Part B 17:321–330
21. Toepperwien M, Krenkel M, Vincenz D, Stoeber F, Oelschlegl AM, Goldschmidt J, Salditt T (2017) Three-dimensional mouse brain cytoarchitecture revealed by laboratory-based x-ray phase-contrast tomography. Sci Rep 7:42847
22. Witte YD, Boone M, Vlassenbroeck J, Dierick M, Hoorebeke LV (2009) Bronnikov-aided correction for x-ray computed tomography. J Opt Soc Am A 26:890–894
23. Tapfer A, Braren R, Bech M, Willner M, Zanette I, Weitkamp T, Trajkovic-Arsic M, Siveke JT, Settles M, Aichler M, Walch A, Pfeiffer F (2013) X-ray phase-contrast CT of a pancreatic ductal adenocarcinoma mouse model. PLoS One 8:e58439
24. Hagen CK, Maghsoudlou P, Totonelli G, Diemoz PC, Endrizzi M, Rigon L, Menk RH, Arfelli F, Dreossi D, Brun E, Coan P, Bravin A, De Coppi P, Olivo A (2015) High contrast microstructural visualization of natural acellular matrices by means of phase-based x-ray tomography. Sci Rep 5:18156
25. Ignatyev K, Munro PR, Speller RD, Olivo A (2011) Effects of signal diffusion on x-ray phase contrast images. Rev Sci Instrum 82:073702
26. Bradley RS, Robinson IK, Yusuf M (2017) 3D x-ray nanotomography of cells grown on electrospun scaffolds. Macromol Biosci 17:1600236
27. Birnbacher L, Willner M, Velroyen A, Marschner M, Hipp A, Meiser J, Koch F, Schroeter T, Kunka D, Mohr J, Pfeiffer F, Herzen J (2016) Experimental realisation of high-sensitivity laboratory x-ray grating-based phase-contrast computed tomography. Sci Rep 6:24022
28. Tapfer A, Bech M, Velroyen A, Meiser J, Mohr J, Walter M, Schulz J, Pauwels B, Bruyndonckx P, Liu X, Sasov A, Pfeiffer F (2012) Experimental results from a preclinical x-ray phase-contrast scanner. Proc Natl Acad Sci 109:15691–15696
29. Diemoz PC, Hagen CK, Endrizzi M, Olivo A (2013b) Sensitivity of laboratory based implementations of edge illumination x-ray phase contrast imaging. Appl Phys Lett 103:244104
30. Diemoz PC, Vittoria FA, Olivo A (2014) Spatial resolution of edge illumination x-ray phase-contrast imaging. Opt Express 22:15514–15529
31. Hemberg O, Otendal M, Hertz HM (2003) Liquid-metal-jet anode electron-impact x-ray source. Appl Phys Lett 83:1483–1485

32. Diemoz PC, Hagen CK, Endrizzi M, Minuti M, Bellazzini R, Urbani L, De Coppi P, Olivo A (2017) Single-shot x-ray phase-contrast computed tomography with nonmicrofocal laboratory sources. Phys Rev Appl 7:044029
33. Bevins N, Zambelli J, Li K, Qui Z, Chen G (2012) Multicontrast x-ray computed tomography imaging using Talbot-Lau interferometry without phase stepping. Med Phys 39:424–428
34. Xu Q, Sidky EY, Pan X, Stampanoni M, Modregger P, Anastasio MA (2012) Investigation of discrete imaging models and iterative image reconstruction in differential x-ray phase-contrast tomography. Opt Express 20:10724–10749
35. Fu J, Schleede S, Tan R, Chen L, Bech M, Achterhold K, Gifford M, Loewen R, Ruth R, Pfeiffer F (2013) An algebraic iterative reconstruction technique for differential x-ray phase-contrast computed tomography. Z Med Phys 23:186–193
36. Brendel B, Von Teuffenbach M, Noel PB, Pfeiffer F, Koehler T (2016) Penalized maximum likelihood reconstruction for x-ray differential phase-contrast tomography. Med Phys 43:188–194
37. Chen Y, Guan H, Hagen CK, Olivo A, Anastasio MA (2017) Single-shot edge illumination x-ray phase-contrast enabled by joint image reconstruction. Opt Lett 42:619–622